The Micro-Optical Ring Electrode: A Sensor for Multiple Actinide Ions

Linnett, Gary

This dissertation is submitted for the degree of
Doctor of Engineering

November 2021

School of Engineering

“Seek the balance,
Work the science,
Through diligence,
Moderate the middle”
Puscifer

Declaration

This thesis has not been submitted in support of an application for another degree at this or any other university. It is the result of my own work and includes nothing that is the outcome of work done in collaboration except where specifically indicated. Many of the ideas in this thesis were the product of discussion with my supervisor Dr Fabrice Andrieux.

Abstract

This thesis researches the development of the Micro-Optical Ring Electrode (MORE) for the analysis of trans-uranium elements in aqueous mixtures. The MORE is a photo-electrochemical device based on a ring microelectrode that uses the insulator interior to the ring as a light guide. This single device exploits the unique photophysical and electrochemical properties of multiple analytes present in mixtures to quantify them. This study aims to develop a protocol for the analysis of ions of uranium, neptunium and plutonium. These elements are most relevant to the nuclear industry, especially in the areas of decommissioning and fuel-reprocessing, where speedy and safe identification of radioactive contaminants is essential.

Non-radioactive surrogates were used to test whether the MORE could generate photocurrents from ions with similar chemical properties to their radioactive counterparts. The results obtained by the successful generation of photocurrents were compared to the mathematical model proposed by (Andrieux, Boxall and O'Hare, 2006a). Depleted uranium was used as a surrogate for active uranium whilst non-radioactive surrogates vanadium and cerium was used for neptunium and plutonium. Upon successful detection of a photocurrent from the surrogates the optimum parameters to give the largest photocurrent magnitude possible were established. For uranium these parameters were an illumination wavelength of 410 nm, a working electrode potential of 0.7 V and the electron acceptor ethanol at a concentration of 200 mmol dm^{-3}. For vanadium these parameters were an illumination wavelength of 350 nm, a working electrode potential of 0.5 V and the electron acceptor iron (III) chloride at a concentration of 100 mmol dm^{-3}. No photocurrents were generated for cerium. A preliminary study into the ability of the MORE to detect photocurrents generated by individual ions in a mixture of uranium and ruthenium was also carried out.

The surface finish at the tip of the MORE was shown to influence the magnitude of the generated photocurrents with a rougher finish resulting in larger photocurrents.

Acknowledgements

I would like to express my gratitude to my PhD supervisor Dr Fabrice Andrieux for his faith in me to deliver this project and his continued guidance, support and patience.

I am very grateful to the EPRSC and Sellafield Ltd for funding this project and I extend my thanks to Nick Atherton and Dr Xavier Poteau for agreeing to be my industrial supervisors.

I wish to thank all the staff and students of Lancaster University for creating a welcoming environment for me to undertake this project. I am especially grateful to the staff and students in the Lancaster University Engineering department without whom this project would not be possible; in particular I would like to thank Dr Wilbraham, Michael Chimes and Peter Jones.

I am grateful to the support given to me by Dr Sara Baldock of Lancaster University Chemistry Department, Dr Alexander Robson of Lancaster University Physics Department and Dr Oliver Payton of Bristol University who have all contributed data that has helped with the progression of this project.

I wish to extend a special thank you to my Mother, Maureen and to Paul for their continuous support and belief in me. A very special thanks goes to Dr Stephanie Evans for her support and guidance during the writing of my thesis.

Contents

Tables

Figures

GLOSSARY OF TERMS

Symbol	Meaning	Unit
Roman symbols		
a	Inner diameter of the ring electrode	m
b	Outer diameter of the ring electrode	m
C	The bulk concentration of the electro-active species	mol m^{-3}
D_s	Diffusion coefficient	m^2 s^{-1}
E	Potential	V
E°	Standard redox potential	V
F	Faraday constant (96484.6)	C mol^{-1}
$i_{diff,lim}$	Diffusion limited current	A
I_{ph}	Flux of light at electrode surface	mol photons m^{-2} s^{-1}
i_{ph}	Photocurrent	A
$I_{R,ss}$	Diffusion Limited Current	A
$k_{0,}$ k_2	Pseudo-first-order rate constants	(s^{-1})
k_1	Second- order rate constant	(m^3 mol^{-1} s^{-1})
l_0	Characteristic length, a function of ring dimension	m
n	Number of electrons exchanged in a redox reaction	none
[S]	Concentration of sensitizer	mol m^{-3}

[A]	Concentration of acceptor	mol m^{-3}
U	Dimensionless concentration of the photoexcited species	none
Greek symbols		
λ	Wavelength	nm
ρ	Dimensionless radial distance from the center of the optical disc	none
X	the dimensionless kinetic length	none
ε	Extinction coefficient	none
φ	Quantum yield	$m^3 mol^{-1} cm^{-1}$
τ	Dimensionless time	none

ABBREVIATIONS

Abbreviation	Definition
A	Surface Area (cm^2)
CA	Chronoamperometry
CV	Cyclic Voltammetry
DIN	Deutsches Institut für Normung
ECL	Electro-chemiluminescence
FIA	Flow Injection Analysis
GRiN	Graphene Ring Nanoelectrode
HS-AFM	High Speed Atomic Force Microscopy
ICP-MS	Induced Coupled Plasma Mass Spectrometry
$K_3[Fe(CN)_6]$	Potassium hexacyanoferrate (III)
KCl	Potassium Chloride
MORE	Micro-Optical Ring Electrode
NNL	National Nuclear Laboratory
NOVA 2.0	electrochemistry software from Metrohm Autolab
OTTLE	Optically Transparent Thin Layer Electrodes
OTE	Optically Transparent Electrode
PCE	Photophysical-Chemical-Electrochemical
PE	Photophysical-Electrochemical

R^2	is a statistical measure of how close the data are to the fitted regression line
RODRE	Rotating Optical Disc Ring Electrode
SCE	Standard Calomel Electrode
SEM	Scanning Electron Microscopy
TBP	tributyl phosphate
XANES	X-ray absorption near edge structure

1 Literature Review

1.1 Introduction

The aim of this project is to build on previous work to further develop the Micro Optical Ring Electrode (MORE) as a photoelectrochemical sensor for nuclear applications. Work has been carried out to investigate the ability of the MORE to identify and quantify a range of trans uranium elements both in isolation and in mixtures. Uranium, neptunium and plutonium are the most encountered actinides in the nuclear industry therefore this project will focus on the detection of these. Detection is achieved by taking advantage of each element's unique photochemical and electrochemical characteristics. Such a sensor would be of great value to both the decommissioning and fuel-reprocessing sector within the nuclear industry, where safe identification of radioactive contaminants is essential. The MORE has numerous advantages over current detection methods such as Induced Coupled Plasma Mass Spectrometry (ICP-MS) and scintillation counting. The MORE can be used in-situ and will therefore remove the need for sampling, this will save time, money and reduce radiological risk.

1.2 Electrochemistry and Photochemistry

1.2.1 Electrochemistry

An electrochemical cell enables the transfer of electrons across an electrolyte / electrode interface resulting in the establishment of a current. The current can either be used directly to generate energy or monitored by a sensor. An electrochemical cell is composed of two or three electronic conductors (electrodes) and an ionic conductor (electrolyte). Charge moves through the electrode and circuit via the transfer of electrons and is carried through the electrolyte by ions.

A current can be generated when an electric potential is applied between two electrodes. The chemical reaction occurring in an electrochemical cell is the product of two independent half reactions which describe the chemical changes happening at each of the electrodes. For electrochemical studies, interest is typically focused on the chemical reaction at one electrode, which is defined as the working electrode. The other electrode often has a stable and well-defined potential and is known as the reference electrode.

Since the potential at the reference electrode is fixed, any changes in the cell potential occur at the working electrode.

It is possible to have individual half-cells containing an electrode surrounded by an electrolyte, which is separated by the accumulation of electrical charges present at the boundary of an electrode and electrolyte when they are in contact with each other (Helmholtz double layer). The electrolyte contains a species which will either be reduced or oxidised. A redox reaction between the electrode and electrolyte occurs within the double layer, thus creating a potential difference. An example of a half-cell is the iron (II) / iron (III) system which is based on the following reaction:

$$Fe^{3+}(aq) + e^{-} \leftrightarrow Fe^{2+}(aq)$$

Equation 1.1:
Iron (III) to iron (II) redox reaction

The redox reaction takes place at a platinum electrode which is placed in a solution containing two aqueous ions of the same element. Iron (II) can be reduced to form iron (III), and iron (III) can be oxidised to form iron (II). The direction of this reaction depends on how easily each species gains an electron; this is defined as the redox potential.

1.2.2 Photochemistry

Photochemistry is the study of the chemical effects due to absorption of electromagnetic radiation in the ultraviolet, visible and infrared regions. Photochemical reactions enable large activation barriers to be negated in a short period of time thus allowing reactions to occur that would not be accessible via thermal processes.

There are two fundamental principles that are crucial to understanding photochemistry.

1) The Grotthuss-Draper law that states only light which is absorbed by a system can bring about a photochemical change.
2) The Stark-Einstein law that states for each photon of light absorbed by a chemical system, only one molecule is activated for a subsequent reaction.

During a photochemical process photoexcitation occurs when a reactant enters a transient excited state due to the absorption of a photon. The chemical and physical properties of the reactant are noticeably different from that of the original unexcited state. This excited state is short lived due to a sequence of events that will either return the reactant to its original ground state or result in the formation of a new chemical species which will eventually reach its own ground state. Fluorescence and phosphorescence are examples of a simple photochemical process whereby emission of

light is due to the release of energy as a photon when the electron returns to the ground state following excitation.

For incident photons with energies in the range of UV-Vis (n-IR), the energy is sufficient to promote an electron from the ground state to an excited state. Quantum mechanics dictates that electrons bound to an atom can only exist at certain energy levels. If the absorbed energy is equal to or greater than the difference between two energy levels, an electron present at the lower energy level will be promoted to the higher energy level with the reactant now being in an excited state. The energy of the incident photon can be calculated with Equation 1.2:

$$E = \frac{hc}{\lambda}$$

E	Photon energy (J)
h	Plank constant (6.62607015×10^{-34} J·s)
c	Speed of light (3×10^{8} ms^{-1})
λ	Wavelength of light (nm)

Equation 1.2: Photon energy equation

The excited electron can either participate in electron transfer processes or lose the gained energy by de-exciting to a lower state by the release of a photon. Various examples of photochemical reactions can be found throughout nature, including photosynthesis (Equation 1.3), human formation of vitamin D and bioluminescence in fireflies.

$$6CO_2 + 6H_2O + \text{sunlight} \rightarrow C_6H_{12}O_6 + 6O_2$$

Equation 1.3 Photosynthesis

For photons with energies higher than the UV-Vis (n-IR) range, molecular vibrations occur which do not involve the excitation of an electron but can instead result in a thermal reaction. Thermal decomposition is an example of a thermal reaction, the introduction of heat initiates chemical decomposition. Examples of thermal decomposition include calcium carbonate decomposing into calcium oxide and carbon dioxide (Equation 1.4), and the decomposition of water molecules at 2000^{o}C.

$$CaCO_3 + \text{heat} \rightarrow CaO + CO_2$$

Equation 1.4: Thermal decomposition of calcium carbonate

1.3 Introduction to the MORE

The Micro Optical Ring Electrode (MORE, Figure 1.1) is a microelectrode that consists of a central cylindrical fibre optic support (inner insulator) surrounded by a concentric gold layer. The fibre optic delivers monochromated light to a solution containing the analytes of interest. Upon illumination a series of photochemical reactions occur, the products of which can be detected at the electrochemical sensor, in this case the gold layer. Careful selection of the illumination wavelength and operating electrode potential offers a dual means of determining the concentration of the target analyte in the solution of interest.

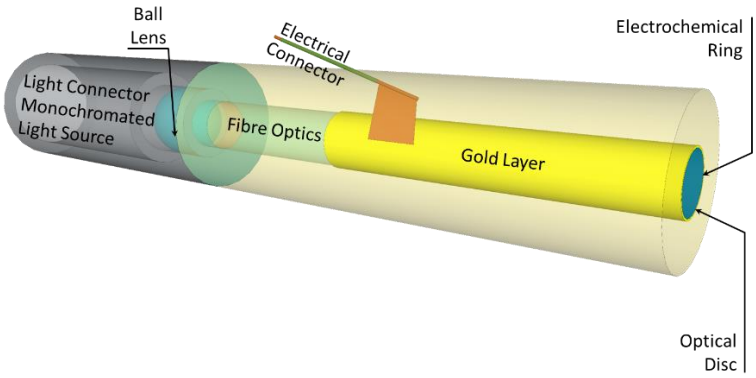

Figure 1.1: Schematic diagram of the MORE

(Andrieux, Boxall and O'Hare, 2006b).

1.3.1 Mechanism of detection

Mechanisms of photocurrent detection at the MORE have been previously explored by (Andrieux, Boxall and O'Hare, 2006a) who found that photocurrents are detected at the MORE as a result of one of two general mechanisms: in a Photophysical – Electrochemical (PE) system and in a Photophysical-Chemical – Electrochemical (PCE) system.

When the MORE is used in a Photophysical – Electrochemical (PE) capacity the sensitizer (S) is photoexcited and detected directly by the MORE. However, when the MORE is used in a Photophysical-Chemical – Electrochemical (PCE) capacity, the sensitizer is photoexcited and undergoes a chemical reaction, the products of which are detected at the MORE. The involvement of a chemical reaction can be exploited to improve detection, for example if the photoexcited sensitizer is short lived (Figure 1.2).

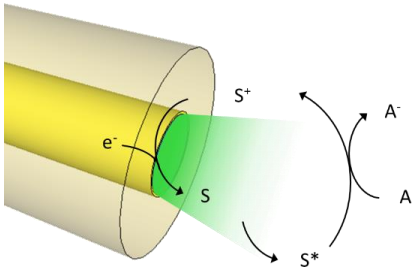

$$S \xrightarrow{(h\nu)k_0} S^*$$

$$S^* + A \xrightarrow{k_1} S^+ + A^-$$

$$S^+ + A^- \xrightarrow{k_2} S + A$$

Figure 1.2: Photocurrent detection mechanism.

1.3.2 Previous work

Previous work studying the MORE have shown positive results for its ability to investigate complex photochemical systems (Pennarun, 1999). For example, the MORE was successfully used to examine the photoelectrochemistry of methylene blue. Methylene blue is a chemical compound that is capable of being photoactivated to produce a singlet oxygen. This form of oxygen is highly cytotoxic and therefore has various uses in the medical industry for example that of a photodynamic therapy that can target cancerous cells. When investigating the photochemistry of methylene blue the MORE was successful in detecting a photocurrent generated by the formation of a triplet excited state. Furthermore, when in the presence of a reducing agent, the MORE was able to provide significant insights into the difference between the homogenous and heterogeneous chemistry of methylene blue (Pennarun, 1999).

The ruthenium-iron system has also been used to demonstrate the ability of the MORE to measure spectral response. Results showed that the photocurrent action spectrum mimicked that of the UV- visible spectrum for ruthenium. The correlation between the photocurrent action spectrum and the UV-visible spectrum suggests that different analytes could be identified within a mixture by tuning the illumination wavelength to match that of the absorption peak of the target analyte. A semi-analytical mathematical model of photocurrent response has also been derived (Equation 1.5) (Andrieux, Boxall and O'Hare, 2006b).

$$i_{ph} = \frac{nFD_s\pi\varphi I_{ph}\varepsilon[S]}{1.03k_2}\left[\frac{k_1[A]}{k_0 + k_1[A]}\right]\sqrt{\frac{a}{X_k}}\sqrt{b^2 - a^2}\,\frac{3}{2\Gamma\left({}^2/_3\right)}\int_0^{(k_2t)^{2/3}} e^{-z^{3/2}}\,dz$$

Equation 1.5: Mathematical model devised to calculate photocurrent magnitude detected by the MORE depending on the below variables

Where:

n	Number of electrons exchanged
F	Faradays constant
D_s	Diffusion coefficient for species S ($m^2\ s^{-1}$)
[S]	Concentration of sensitizer (mol m^{-3})
[A]	Concentration of acceptor (mol m^{-3})
φ	Quantum yield ($m^3\ mol^{-1}\ cm^{-1}$)
I_{ph}	Flux of light at electrode surface ((mol photons) $m^{-2}\ s^{-1}$)
k_0, k_2	Pseudo-first-order rate constants (s^{-1})
k_1	Second- order rate constant ($m^3\ mol^{-1}\ s^{-1}$)
X	Dimensionless kinetic length
ε	Extinction coefficient at λ

1.3.3 Mathematical expressions for the diffusion limited current

Symanski and Bruckenstein (1988) developed a mathematical expression for an approximation of the steady state current at a thin microelectrode:

$$I_{R,ss} = nF\mathrm{Ds}Cl_0$$

Equation 1.6

Where

n Number of electrons exchanged during the redox reaction.
F Faraday constant (96484.6 $C.mol^{-1}$)
D_s The diffusion coefficient of species being studied
C The bulk concentration of the electro-active species
l_0 The characteristic length of the ring electrode

An expression for l_0 has been given by Smythe (1951):

$$(l_0) = \frac{\pi^2(a+b)}{\ln\left(16\left(\frac{b+a}{b-a}\right)\right)}$$

Equation 1.7

Where

a Inner radius (of gold ring)
b Out radius (of gold ring)
l_0 Characteristic length of the ring electrode

This expression is only applicable for very thin electrode rings where $\frac{b-a}{b} \ll 1$. Whilst this expression is only an approximation, it is generally regarded as the most accurate expression derived to calculate the steady state current at the electrode tip.

A mathematical model for the diffusion-limited current at the surface of micro-ring electrodes was characterised by (Szabo, 1887). At long times, the time dependence of the diffusion-limited current is given by the asymptotic semi-analytical expression:

$$i_{diff,lim} = nF\mathrm{Ds}Cl_0(1 + \frac{l_0}{\sqrt{4\pi^3 Dt}})$$

Equation 1.8:

Where

n	Number of electrons exchanged during the redox reaction.
F	Faraday constant (96484.6 $C.mol^{-1}$)
D_s	The diffusion coefficient of species being studied
C	The bulk concentration of the electro-active species
l_0	The characteristic length of the ring electrode
t	Time in seconds

Once the MORE has been manufactured, its ring thickness can be determined by electrochemical means using the above mathematical model (Equation 1.8). This is achieved by recording a chronoamperogram in a model solution.

1.4 Actinides

When in solution, actinides display a large variation in oxidation states, ranging from +2 to +7, these are summarized in Table 1.1. Lower oxidation states become stable in an acidic environment, whereas higher oxidation states require basic solutions to stabilise the ions. The maximum oxidation state that can be found in compounds of the early actinides correlates to the total number of electrons available in the 7s, 6d and 5f orbitals. The stability of high oxidation states starts to decrease after uranium with the +3 state dominating for the later actinides (Bursten, Rhodes and Strittmatter, 1989).

	Oxidation State					
Actinide	+2	+3	+4	+5	+6	+7
Actinium		✓				
Thorium	✓	✓	✓			
Protactinium		✓	✓	✓		
Uranium		✓	✓	✓	✓	
Neptunium		✓	✓	✓	✓	✓
Plutonium		✓	✓	✓	✓	✓
Americium	✓	✓	✓	✓	✓	
Curium		✓	✓			
Berkelium		✓	✓			
Californium	✓	✓				
Einsteinium	✓	✓				
Fermium	✓	✓				
Mendelevium	✓	✓				
Nobelium	✓	✓				
Lawrencium		✓				

Table 1.1: The known oxidation states of the actinides

Studies concerning the coordination chemistry of the actinides has been limited, due to their elevated level of radioactivity, limited availability and very short half-lives. Uranium is the most studied of the actinides due to its abundance, long lifetimes and being a relatively weak alpha emitter (Seaborg, 1990).

The uranium fuel cycle is the most commonly encountered fuel cycle within the nuclear industry. Uranium, neptunium and plutonium are radioactive actinide elements that are frequently found within the uranium fuel cycle, they are therefore of keen interest for study (World Nuclear Association, 2020).

1.4.1 Uranium

Uranium is the heaviest known element that occurs in macroscopic quantities in nature, with a lifetime comparable to that of the age of the earth. Natural uranium consists of three isotopes, uranium-234 (0.005%), uranium-235 (0.711%) and uranium-238 (99.284%). The varying abundance of the three isotopes in nature is caused by differing half-lives and all three naturally occurring isotopes of uranium are unstable. Artificial isotopes uranium-236, uranium-233 and uranium-232 are generated in nuclear reactors via transmutation of uranium-235 and thorium-232 (World Nuclear Association, 2018).

1.4.1.1 Uranium Oxidation States

Uranium can exist in four oxidation states U(III), U(IV), U(V) and U(VI), with most compounds being in either the +4 or +6 states. Uranium (III) is unstable in aqueous solutions and is readily oxidised by water resulting in hydrogen and Uranium (IV) (Equation 1.9 A). Uranium (V) is also unstable in an aqueous solution, except in hydrofluoric acid due to the formation of the UF_6^- ion. Uranium (IV) becomes unstable in the presence of oxygen (for example when exposed to the air), as the oxygen oxidises uranium (IV) to produce uranium (VI) (Equation 1.9 B), also known as uranyl. Reduction of uranyl (VI) to uranyl (V) is also possible via two mechanisms; weakening the U=O bond through oxo functionalisation (Schnaars, Wu and Hayton, 2011) or the addition of a mild reducing agent with a reduction potential of 0.16 V in perchloric acid at 298 K (Liddle, 2015). Uranyl is the most thermodynamically stable of the four oxidised uranium ions and is therefore the most encountered species of uranium present in an aqueous solution. It is for this reason that the MORE will focus primarily on the detection of uranyl ions (Morss, 2020).

A $$U(III) \rightarrow U(IV) + e^-$$

$$E_0 = -0.607 + 0.0591 \log \frac{U(IV)}{U(III)}$$

B $$U(IV) + 2H_2O \rightarrow U(VI) + 4H^+ + 2e^-$$

$$E_0 = 0.333 - 0.1182ph + 0.0295log \frac{U(VI)}{U(IV)}$$

Equation 1.9: Uranium redox reactions and standard redox potentials (Pourbaix, 1974)

1.4.1.2 Uranium Photochemistry and Electrochemistry

In this thesis, we will use the MORE to detect the presence of uranyl ions in acidic aqueous solutions. Not only is the uranyl ion stable in acidic aqueous solutions, such as those encountered in nuclear fuel reprocessing, but it's photochemical and electrochemical behaviours are already well established.

Under anaerobic conditions one electron reduction of uranyl (VI) to uranyl (V) is achieved by minerals and microbes (Lovley *et al.*, 1991; Renshaw *et al.*, 2005). Under these conditions uranyl (V) disproportionates into uranyl (VI) and uranium (IV).

Uranyl (V) is an important intermediate in photochemical processes involving uranyl (VI). Uranyl (VI) become photochemically active when exposed to UV and near-UV light resulting in the generation of photoexcited uranyl (VI). Photoexcited uranyl (VI) is long lived (≤ µs) and highly oxidising (Yong *et al.*, 2013). In the ground state, uranyl

has a standard redox potential of 0.06 V (U(VI) to U(V)) (Kern and Orlemann, 1949), however once photoexcitation occurs the redox potential is estimated to be 2.6-2.7 V (Burrows and Kemp, 1974a; Buchachenko and Khudyakov, 1991). Ligand to metal charge transfer arising from U(5f) ← O(2p) transitions generate the uranyl (V) intermediate which contains a highly reactive oxyl radical. Quenching of the uranyl (V) intermediate can be achieved by H atom abstraction if the quencher is aliphatic (Wang, Bakac and Espenson, 1995; Fonseca *et al.*, 2004) or via electron transfer if the quencher is unsaturated (Mao and Bakac, 1996; Sarakha, Bolte and Burrows, 1997).

Several classification of uranyl photoreactions have been proposed according to their mechanism (Yusov and Shilov, 2000).

Intramolecular reactions proceeding by an electron transfer takes place in the decomposition of uranyl oxalate with the reaction ending with evolution of CO_2:

$$UO_2C_2O_4 + 2\ H^+ + h\nu \rightarrow UO_2^{\ 2+} + CO_2 + CO + H_2O \text{ (pH 0)}$$

$$UO_2C_2O_4 + H_2O + h\nu \rightarrow UO_2^{\ 2+} + HCOO^- + CO_2 + OH^- \text{ (pH 7)}$$

Intermolecular reactions whose primary step is abstraction of a hydrogen atom from the substrate:

$$(UO_2^{2+*}) + SH_2 \rightarrow UO_2H^{2+} + SH,$$
$$UO_2H^{2+} \rightarrow UO_2^{+} + H^+ \text{ solv},$$

Where SH_2 is the substrate. This mechanism is observed in the reactions of photoexcited uranyl with alcohols:

$$(UO_2^{\ 2+*}) + RCH_2OH \rightarrow UO_2H^{2+} + RCHOH.$$

Photoreduction of uranyl in a solution with ethanol in sulphuric acid resulting in the formation of uranium (IV) has been demonstrated (Nagaishi *et al.*, 1996, 2002a). The yield of uranium (IV) increased linearly with increasing number of photons absorbed by the solution. Both experiment and density functional theory calculations demonstrate that in protic solutions photoexcited uranyl ions can undergo photoreduction and subsequently oxidise other organic substrates such as acids, alkanes, arenes and DNA (Burrows, 1990; Tsushima, 2009; George, Whittaker and Stearns, 2011).

Quenching of the luminescence of uranyl by aromatic hydrocarbons and variable-valence metal ions in the lowest oxidation state can be achieved by reversible electron transfer. Evidence for electron transfer in reactions of photoexcited uranyl with Mn^{2+} (Burrows *et al.*, 1976), $Ru(bpy)_3^{2+}$ (Rosenfeld-Grünwald and Rabanl, 1980) and Ce (III)

(Meyer *et al.*, 1982) utilizing pulse photolysis has been observed. An increase in the concentration of $Ru(bpy)_3^{2+}$ was correlated with the rate of deactivation of uranyl.

Out of the four common types of photochemical reactions that can occur when dealing with metal complexes (substitution, isomerization, redox reactions, and photocatalysis or photosensitization), the uranyl ion tends to favour redox reactions and photocatalysis (Gangwer, 1977). The preference of uranyl ions to undergo redox and photocatalysis reactions again makes it an ideal candidate for detection by the MORE.

1.4.1.3 Uranyl electronic absorption spectrum

The UV-visible spectrum of the uranyl ion has been studied in detail and presents five peaks between 338 and 500 nm resulting in the well-recognised glove shape (Figure 1.3). The maximum absorption peak is observed at 413.8 nm with an extinction coefficient of 7.9 L mol^{-1} cm^{-1} (Burrows and Kemp, 1974a). Between 400 and 500 nm light absorbance is the result of a transfer of an electron from the higher molecular orbital situated on one of the oxygen atoms to the non-bonding 5f orbital on the uranium atom (Yusov and Shilov, 2000). The peak observed at 490 nm is due to an zero phonon-phonon transition and therefore a measure of the energy gap between the ground state and excited state (Yusov and Shilov, 2000).

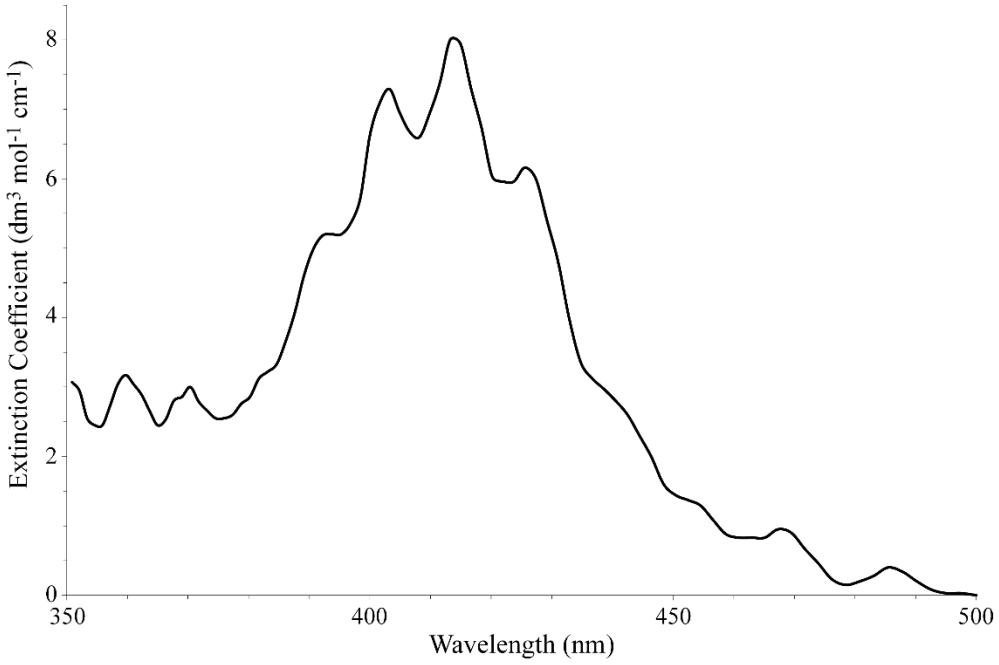

Figure 1.3: Electronic absorbance spectrum of uranyl between 350 and 500 nm (Burrows and Kemp, 1974a).

1.4.2 Neptunium

Neptunium (Np) was the first trans-uranium element discovered by E.M. McMillian at the University of California in 1939 (Seaborg, 1990). The discovery of neptunium occurred during part of an experiment studying nuclear fission which had been discovered the previous year. McMillian was attempting to measure the energies of two recoiling fragments generated by the fission of uranium. His studies found the presence of an unexpected radioactive product, one that did not recoil in the same manner as the uranium fission products. McMillian concluded that this product had been created due to a neutron being absorbed by an isotope of uranium (Equation 1.10).

A $$^{238}_{92}\mathrm{U} + \mathrm{n} \rightarrow {}^{239}_{92}\mathrm{U} + \gamma$$

B $$^{239}_{92}\mathrm{U} \rightarrow {}^{239}_{93}\mathrm{Np} + \beta^{-}$$

Equation 1.10: Mechanism for neptunium formation.

1.4.2.1 Oxidation States of Neptunium

There are five possible oxidation states neptunium can exhibit when in solution, these range from neptunium (III) to neptunium (VII). Neptunium (III) oxidises slowly in the presence of oxygen to form neptunium (IV) (Equation 1.11 A). Both neptunium (V) and neptunium (VI) are stable in either an acidic or basic solution. Neptunium (VII) is a strong oxidising agent and is only stable in an alkaline solution (Clark *et al.*, 1981; Williams *et al.*, 1997). Neptunium (IV) is stable in aqueous solution, however, it will be oxidised at an extremely slow rate by oxygen to form neptunium (V) (Hindman, Magnusson and LaChapelle, 1949; Burney and Harbour, 1974) (Equation 1.11 B).

A $$Np(III) \rightarrow Np(IV) + e^{-}$$

$$E_0 = 0.152 + 0.591log\frac{Np(III)}{Np(IV)}$$

B $$Np(IV) + 2H_2O \rightarrow Np(V) + 4H^{+} + e^{-}$$

$$E_0 = 0.749 - 0.2364pH + 0.0591log\frac{Np(V)}{Np(IV)}$$

Equation 1.11: Neptunium redox reaction and standard redox potentials (Pourbaix, 1974)

1.4.2.2 Optical properties of Neptunium (IV)

When in aqueous solution, neptunium (IV) appears yellow green in colour and absorbs strongly in the near infrared region of the electromagnetic spectrum. As seen in Figure 1.4 neptunium (IV) absorbs at several wavelengths between 650 and 1050 nm. The absorbance spectrum is dominated by two large peaks; both have an extinction coefficient of 83 L mol^{-1} cm^{-1} at wavelengths of 723 and 964 nm and are due to f-f transitions (Gangwer, 1977; Park *et al.*, 2018).

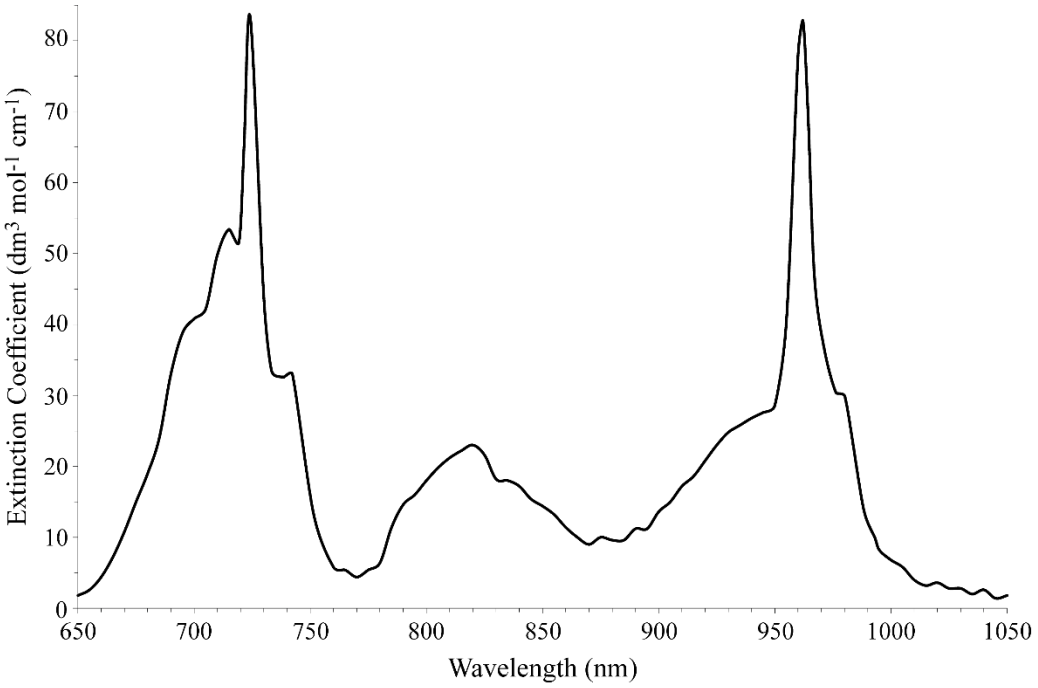

Figure 1.4: Electronic absorbance spectrum of neptunium (IV) (Gangwer, 1977).

1.4.3 Plutonium

As with neptunium, experiments conducted at the University of California were responsible for the discovery of the next trans-uranium element, plutonium (Seaborg, 1990). Just one year after the discovery of uranium, Seaborg used the 60-inch cyclotron to bombard uranium with deuterons (Seaborg, 1990) which resulted in the generation of a new isotope of neptunium which subsequently decayed via beta emission to form plutonium (Equation 1.12).

A $^{238}_{92}U + {}^{2}_{1}H \rightarrow {}^{238}_{93}Np + 2{}^{1}_{0}n$

B $^{238}_{93}Np \rightarrow {}^{238}_{94}Pu + \beta^{-}$

Equation 1.12: Mechanism for plutonium formation.

1.4.3.1 Oxidation States of Plutonium

When in an aqueous solution, plutonium can exist in five oxidation states ranging from plutonium (III) to plutonium (VII) (Clark, 2000). A unique property of plutonium is that the first four oxidation states can all be present at one time when plutonium is in a thermodynamically stable water system (Lide, 2007). The most thermodynamically stable ion of plutonium is plutonium (IV). Plutonium (III) is also stable however it can be slowly oxidised to plutonium (IV) via alpha radiation which is present due to other plutonium ions (Equation 1.13 A). Plutonium (IV) is only stable in small quantities when in concentrated acidic solutions. Plutonium (IV) disproportionates to plutonium (III) and plutonium (VI) when in weak acidic solutions (Equation 1.13 B) (Clark, 2000). Plutonium (V) is stable in acidic solutions between a pH of 2 and 6. When plutonium (V) is present as the plutonyl ion in a higher or lower pH, disproportionation occurs resulting in the generation of plutonium (IV) and plutonium (VI) (Equation 1.13 C). Plutonium (V) is produced via the reduction of plutonium (VI) in dilute acids (Clark, 2000). Plutonium (VI) is stable in aqueous solutions however, as with plutonium (III) it can be altered by alpha radiation present due to plutonium isotopes with plutonium (IV) undergoing reduction in this instance. Plutonium (VII) is a strong oxidising agent that has the ability to oxidise water and produce oxygen when in a solution with a pH less than 7 (Clark, 2000).

A $$Pu(III) \rightarrow Pu(IV) + e^-$$

$$E_0 = 0.967 + 0.0591log\frac{Pu(IV)}{Pu(III)}$$

B $$Pu(IV) + 2H_2O \rightarrow Pu(VI) + 4H^+ + 2e^-$$

$$E_0 = 1.042 - 0.1182pH + 0.0295log\frac{Pu(VI)}{Pu(IV)}$$

C $$2Pu(V) + 4H^+ \rightarrow Pu(IV) + Pu(VI) + 2H_2O$$

Equation 1.13: Plutonium redox reaction and standard redox potentials

(Pourbaix, 1974)

1.4.3.2 Electronic absorption spectra of Plutonium (III) and (IV)

When in aqueous solution, plutonium (III) appears purple in colour whilst plutonium (IV) appears as a yellow-brown colour (Clark, 2000).

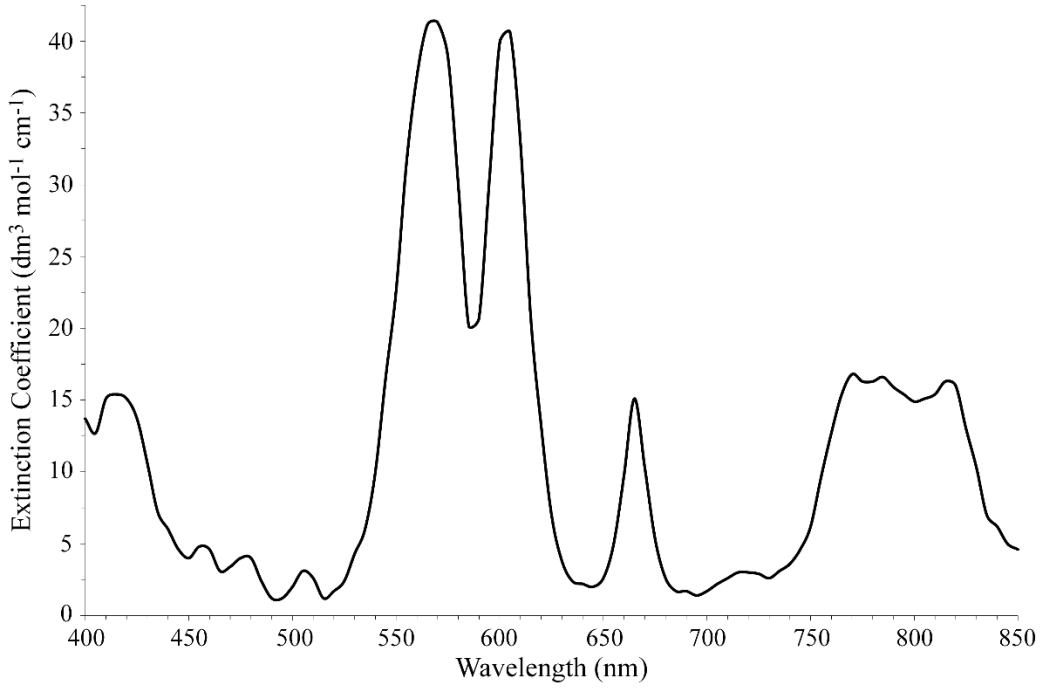

Figure 1.5: Electronic absorbance spectrum of Pu (III) aqua ion (Clark, 2000).

As seen in Figure 1.5, plutonium (III) exhibits a number of absorbance peaks at wavelengths between 400 and 850 nm. As with neptunium (IV) (Figure 1.4), the

absorbance spectrum for plutonium (III) contains two absorbance peaks which are considerably larger than the rest. These larger peaks observed at 570 and 605 nm both have an extinction coefficient of 41 L mol^{-1}. cm^{-1} (Clark, 2000).

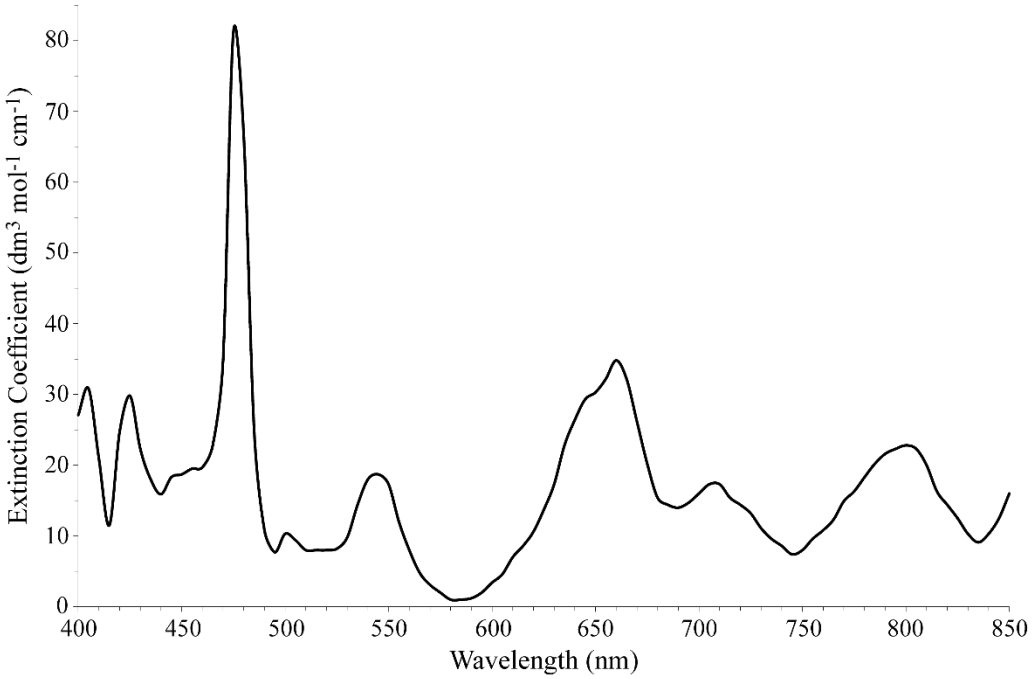

Figure 1.6: Electronic absorbance spectrum of Pu(IV) aqua ion (Clark, 2000).

As shown in Figure 1.6, plutonium (IV) has a number of absorption peaks between 400 and 850 nm. The largest absorption peak is observed at 477 nm and has an extinction coefficient of 81 L mol^{-1} cm^{-1} (Clark, 2000).

1.4.4 Actinide Ion Detection

Various methods of actinide detection have been developed which include luminescence, colorimetric analysis, and X-ray absorption near edge structure (XANES).

Pulsed photoacoustic spectroscopy has been used to detect oxidation state specific analysis of uranium (U(IV) and U(VI) in aqueous solutions down to the micromole region. Piezoelectric transducer, pulsed laser radiation and a differential methods were used to reduce solvent and window absorption (Schrepp *et al.*, 1983).

A colorimetirc actinide sensor using the expanded porphyrin, isoamethyrin (hexaphyrin (1.0.1.0.0.0)) undergoes a readily discernible colour change in the presence of uranyl,

neptunyl and plutonyl cations (Sessler *et al.*, 2004). Semi-quantitative studies carried out with uranyl – acetate in a 1:1 mixture of methanol and dischloromethane suggest a detection limit of less than 28 ppb using UV-vis spectroscopic analysis of the Soret-like band (Sessler *et al.*, 2004).

More recently proof of concept work has shown success with multiple colorimetric agents for uranium and plutonium (Riddle and Demmer, 2020). Colorimetric agents such as 1-(2-pyridylazo)-2-naphthol have been used in combination with 2-(5-bromo-2-pyridylazo)-5,5-diethylaminophenol to increase the intensity of visual colour change and selectively of the actinide of interest. Results included simple separation stages, use of a sprayed colorimetric agent and a colorimetric agent wet wipe. These are used to produce a colour change in the presence of actinides uranium, plutonium and potentially thorium (Riddle and Demmer, 2020).

The use of crystal optics and a laboratory-based X-ray source has demonstrated that X-ray absorption spectroscopy measurements at the uranium L_3 edge can be easily obtained. The XANES spectra were usually composed of one intense peak known as the so-called white line. The oxidation state of the uranium ion determines the energy position and intensity of the white line (Bès *et al.*, 2018).

1.5 Nuclear waste reprocessing

Spent nuclear fuel contains significant amounts of uranium and plutonium which are considered important resources for a number of applications, including the manufacture of new nuclear fuel via recycling. Fresh nuclear fuel consists of two isotopes of uranium, uranium-235 which has been enriched to 3-5% (initially at 0.8%) with the rest being uranium-238. Uranium-235 is a fissile material that undergoes nuclear fission in most reactors. During nuclear fission of uranium-235, uranium-236(~0.4%), plutonium-239 (~0.9%) and additional fission products (~3.3%) are produced (World Nuclear, 2020) . Fission products are the two atomic fragments produced when an atomic nucleus undergoes nuclear fission (e.g. strontium, xenon, barium, krypton). The generation of these fission products reduces the efficiency of the nuclear reactor. Due to the high neutron cross section the generated fission products readily absorb free neutrons, thus reducing neutron availability to uranium-235 and therefore decreasing its ability to undergo nuclear fission. The reduction in energy output from the nuclear fuel rods means that they must be replaced before all of the uranium has been fully utilized (*Microscopic Cross-section | Definition & Examples | nuclear-power.net*, 2020).

Spent fuel thus contains unreacted uranium-235 as well as useful secondary products such as, plutonium-239 and uranium-236 which can be made into MOX fuel. Plutonium is produced via transmutation due to the absorption of a neutron by uranium-238, whilst

uranium-236 is produced due to a failed fission of uranium-235 (World Nuclear Association, 2017).

In addition to the useful secondary products, when uranium-235 undergoes fission two lighter atoms are produced with approximate atomic masses ranging from 90-100 and 130-140. These fission products are extremely radioactive with short half-lives (Radioactivity, 2018). Before any uranium or plutonium contained in the 'spent fuel' can be considered an asset, they must first be separated from these toxic fission products. The procedure developed to achieve this is known as PUREX (Plutonium-Uranium Reduction EXtraction).

1.5.1 PUREX

The Plutonium Uranium Redox EXtraction (PUREX) process is the primary method used by the majority of spent nuclear fuel reprocessing facilities. Spent fuel contains the actinides uranium and plutonium and a mixture of minor actinides for example americium, neptunium and curium (Selvaduray, Goldstein and Anderson, 1979; Veliscek-Carolan, 2016). The aim of PUREX is to extract uranium and plutonium and is based on liquid-liquid extraction ion-exchange developed as part of the Manhattan project. The first large scale PUREX operation started in 1956 at the Hanford Works Site (Gerber, 1993).

The first step in the PUREX process is to immerse fuel rods in ponds of water to allow for most of the fission products with short half-lives to decay, this typically takes around three months (World Nuclear Association, 2020). Following their time in the ponds the fuel rods are dissolved in nitric acid (3-6 Molar) producing a mixture of uranyl nitrate ($UO_2(NO_3)_2$), plutonium (IV) nitrate ($Pu(NO_3)_4$) along with other metal nitrates (Veliscek-Carolan, 2016). Plutonium (IV) and uranium (VI) are separated through a solvent extraction process utilizing tributyl phosphate (TBP) and kerosene (Veliscek-Carolan, 2016). TBP has several desirable properties which makes it ideal for this process including its good radiolytic and chemical stability and low aqueous solubility. The density of TBP is similar to that of water, therefore dilution with a non-polar, low density dilute is required to achieve phase separation. Phase separation is accomplished through the addition of kerosene. Uranium (VI) and plutonium (IV) ions can be extracted in the kerosene phase as the TBP–fission product complexes remain in the aqueous phase. Plutonium is subsequently separated from uranium by treatment of the kerosene solution with a reducing agent (hydrazine) which converts the plutonium to the +3 oxidation state. Plutonium (III) can then pass into the aqueous phase which is extracted away from the kerosene phase. The uranium is separated from the kerosene solution via back-extraction into nitric acid. The purity of the extraction products is

measured to ensure the process has been successful (Veliscek-Carolan, 2016). The PUREX process is summarized in Figure 1.7.

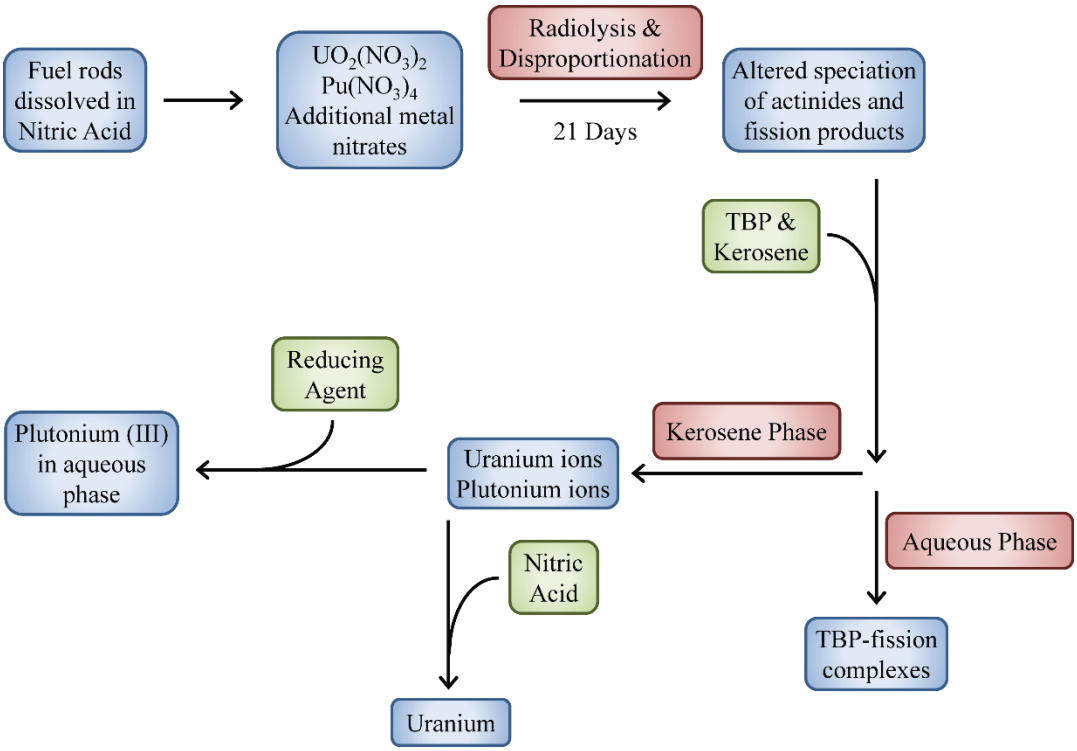

Figure 1.7: PUREX process

1.6 Surrogates for Neptunium and Plutonium Experimentation

Whilst the overall aims of this project are to test whether the MORE can detect ions of uranium, neptunium and plutonium in solution, initial experiments will be conducted using surrogates for neptunium and plutonium due to their radioactive nature and thus limited accessibility. The use of surrogates will allow for the development of experimental experience and technique. Successful demonstration of the MORE using surrogates will lead to experiments using neptunium and plutonium, carried out in collaboration with the National Nuclear Laboratory (NNL).

The requirements for selecting a surrogate include it being in the same oxidation state, a hard acid cation and that it has a similar radius to the ion of interest (Choppin, 2007). The non-radioactive surrogates chosen were depleted uranium, vanadium (V) and cerium (Ce) for uranium, neptunium and plutonium respectively. The surrogates for

neptunium (IV) and plutonium (III, IV) were chosen because of their similar thermodynamic properties to their radioactive counterparts. The similarity in oxidation state at similar narrow pH range, water solubility and redox potentials can be seen by comparing Pourbaix diagrams of neptunium and plutonium to vanadium and cerium respectively (Figure 1.8). Cerium (IV) has been used as a surrogate for plutonium in previous studies (Marra *et al.*, 2012); however caution must be taken with regards to the control of the tetravalent oxidation state (Choppin, 2007). Vanadium has been used as a surrogate in previous studies also (Chimes *et al.*, 2018).

A

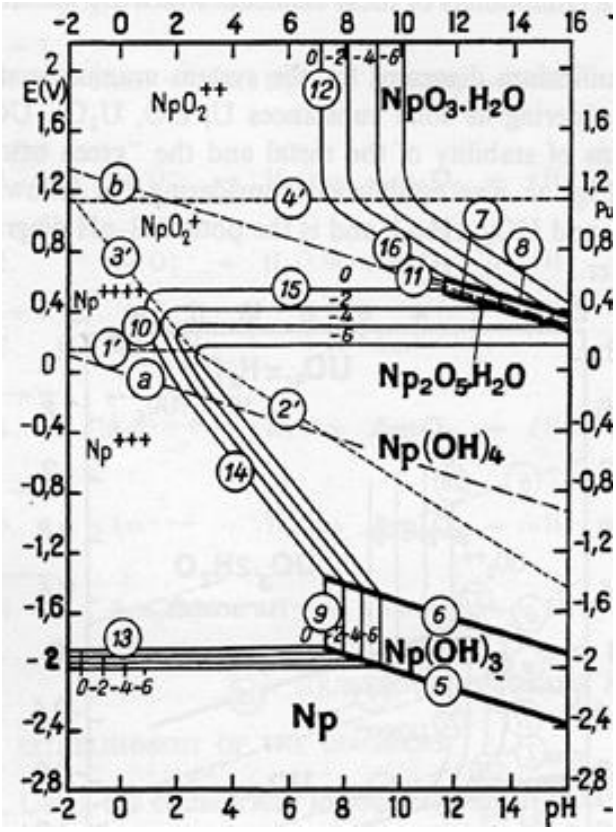
E(V)
pH
NpO_2^{++}
$NpO_3.H_2O$
NpO_2^+
Np^{++++}
$Np_2O_5H_2O$
$Np(OH)_4$
Np^{+++}
$Np(OH)_3^-$
Np

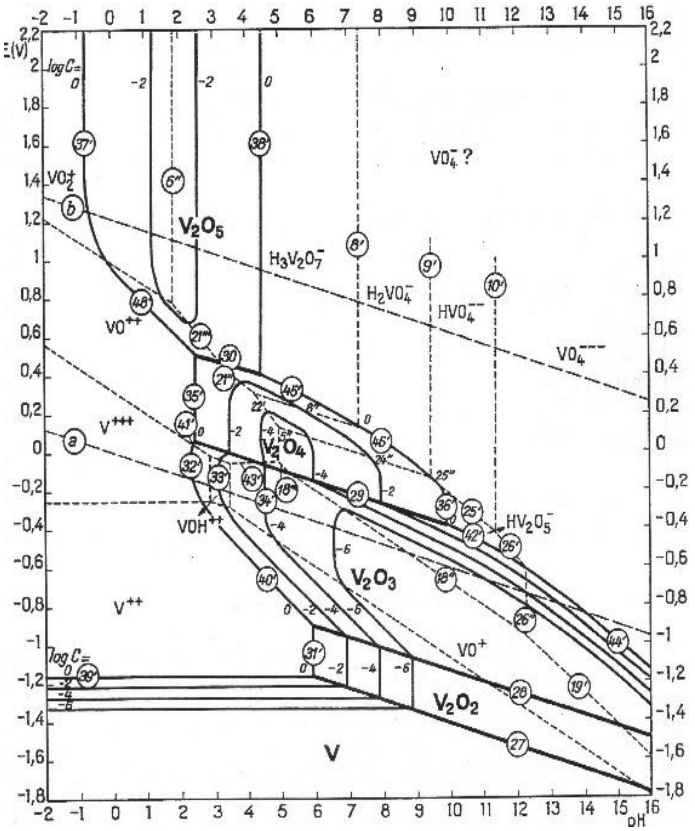
E(V)
pH
VO_2^+
V_2O_5
$H_3V_2O_7^-$
VO_4^- ?
$H_2VO_4^-$
HVO_4^{--}
VO_4^{---}
VO^{++}
V^{+++}
V_2O_4
$HV_2O_5^-$
VOH^{++}
V_2O_3
V^{++}
VO^+
V_2O_2
V

B

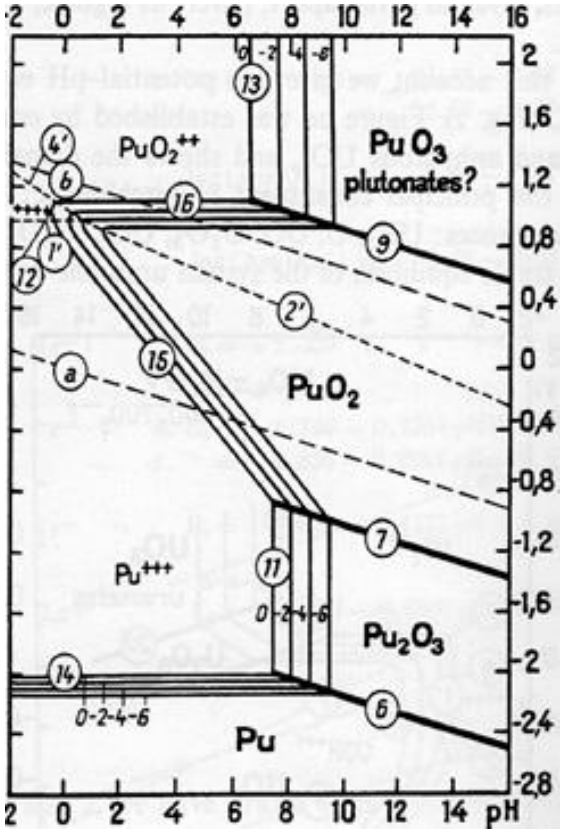
PuO2++
Pu O3
plutonates?
PuO2
Pu+++
Pu2O3
Pu
pH

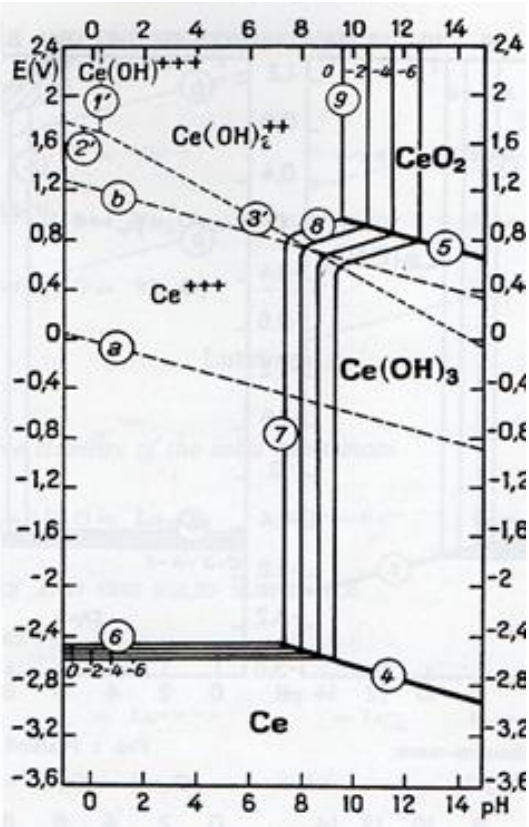
E(V)
Ce(OH)+++
Ce(OH)2++
CeO2
Ce+++
Ce(OH)3
Ce
pH

Figure 1.8**:** Pourbaix diagrams (Pourbaix, 1974)

A) Comparison between neptunium (Np) and vanadium (V).
B) Comparison between plutonium (Pu) and cerium (Ce).

1.6.1 Vanadium

Naturally occurring vanadium is composed of one stable isotope, ^{51}V, and one radioactive isotope, ^{50}V which has a half-life of $1.5x10^{17}$ years and a natural abundance of 0.25%. A total of 24 artificial radioisotopes have also been characterized with mass numbers ranging from 40 to 65. The most stable of these isotopes are ^{49}V (half-life of 330 days) and ^{48}V (half-life of 16 days). Vanadium has a rich and varied chemistry due to the variety of easily accessible oxidation states that it can exist in.

1.6.1.1 Oxidation States of Vanadium

Vanadium can exist in four possible oxidation states ranging from vanadium (II) to vanadium (V). When present in aqueous solution, vanadium forms metal aquo complexes consisting of four colours., lilac $(V(H_2O)_6)^{2+}$, green $(V(H_2O)_6)^{3+}$, blue $(VO(H_2O)_5)^{2+}$ and yellow VO_3^-. Vanadium (II) compounds are reducing agents whereas vanadium (V) compounds are oxidizing agents, Vanadium (IV) compounds typically exist as vanadyl derivatives containing the VO^{2+} centre (Holleman, 1985).

1.6.1.2 Vanadium Photochemistry and Electrochemistry

Electrochemical studies on vanadium compounds began in the early 1970s to understand the structure of new compounds when present in a solution. During initial experiments complexes were not in isolation but investigated in solution. A study by Good and Sawyer (1976) on oxido-vanadium (IV) gluconate demonstrated that a one-electron oxidation occurred at 0.118 V (vs SCE) at pH 6 and at -0.280 V in 0.5 M NaOH.

In the higher oxidation states of +4 and +5, vanadium is highly oxophilic that results in oxido – (VO^{2+}, VO^{3+}) and dioxide – (VO_2, VO_2^+) compounds being the most investigated species.

The vanadium redox flow battery (VRFB) utilizes vanadium in all four of its oxidation states with one electrode using the V/IV couple whilst the other electrode uses the III/II couple. Conversion of these oxidation states is illustrated by the reduction of a strongly acidic solution of vanadium (V) compound with zinc dust or amalgam. The VRFB has

excellent electrochemical kinetics and negligible side reaction (Ding *et al.*, 2013). The transfer of electrons in a VRFB occurs as follows:

Positive electrode: $$VO_2^+ + 2H^+ + e^- \rightleftharpoons VO^{2+} + H_2O$$

$$E^0 = +1.01\ V\ vs.SHE$$

Negative electrode: $$V^{2+} \rightleftharpoons V^{3+} + e^-$$

$$E^0 = -0.25\ V\ vs.SHE$$

Overall: $$VO_2^+ + V^{2+} + 2H^+ \rightleftharpoons VO^{2+} + V^{3+} + H_2O$$

$$E^0 = 1.26\ V\ vs.SHE$$

(Zeng *et al.*, 2015)

1.6.2 Cerium

Naturally occurring cerium consists of four isotopes, cerium-140 (88.48%), radioactive cerium-142 (11.08%), cerium-138 (0.25%) and cerium-136 (0.19%). A total of 38 synthetic radioactive isotopes of cerium have been characterized ranging in mass from 199 to 157.

1.6.2.1 Oxidation States of Cerium

There are two possible oxidation states for cerium, +3 and +4 states. Cerium (IV) oxide can be reduced to cerium (III) oxide with hydrogen gas .

1.6.2.2 Cerium Photochemistry and Electrochemistry

Cerium (III) has ultraviolet absorption bands with relatively high intensity when compared to the other lanthanides.

Cerium is a highly electropositive metal that reacts slowly with water producing cerium (III) hydroxide and hydrogen gas. Cerium dissolves readily in dilute sulphuric acid to form solutions containing the colourless cerium (III). Cerium (IV) solutions can be prepared by a redox reaction between cerium (III) and the strong oxidising agents peroxodisulfate or bismuthate. The redox potential for cerium (IV)/cerium (III) depends on conditions due to the relative ease of complexation, though +1.72 V (vs SHE) is typically used as a represented value. The redox potential for cerium (III)/cerium (IV) is -2.34 V (vs SHE). Cerium is notable as the only lanthanide that has significant aqueous and coordination chemistry in the +4 oxidation state (Marsac *et al.*, 2017).

Due to ligand to metal charge transfer transitions, aqueous cerium (IV) solutions are orange-yellow (Kandrashkin, Asano and Van Der Est, 2006)(Farid and Edelmann, 2012). Aqueous cerium (IV) is metastable in water (Marsac *et al.*, 2017) and is a strong oxidising agent that oxidizes hydrochloric acid to give chlorine gas. During the Belousov-Zhabotinsky reaction, cerium oscillates between the +4 and +3 oxidation states to catalyse the reaction. Cerium (IV) sulphate salts are regularly used as standard reagents for volumetric analysis in cerimetric titrations (Gschneidner, 2006). When using cerium (IV), the nitrate complex is the most commonly encountered and is a strong oxidising agent.

The cerium (III)/ cerium (IV) redox couple is used in zinc-cerium batteries. This type of redox flow battery was first developed by Plurion Inc during the 2000s. It is a rechargeable battery where both negative zinc and positive cerium electrolytes are circulated through an electrochemical flow reactor during operation and stored in two separate compartments.

1.7 Electrochemical sensors

1.7.1 Microelectrodes

A microelectrode is defined as an electrode with one or more of its dimensions being in the micrometre or sub-micrometre range with a typical micro-disc electrode having a diameter less than 50 µm (Pennarun, 1999). This small size allows for several advantages:

- They can be utilised in small sample volumes and provide good spatial resolution.
- Their mathematical behaviour is predictable which can allow calibration less use.
- Measurements in aprotic solvents are possible due to the small electrolysis current incurring a small ohmic drop.
- Their material flux is enhanced with respect to their macroscopic analogues due to their convergent diffusion fields that lead to higher current densities.
- They have a higher faradaic to charging current ratio.
- They have an increase in the mass transport to and from the electrode surface, this allows for steady state to be quickly achieved resulting in a short response time of less than a 1µs which allows for the monitoring of dynamic processes.
- They are relative cheap and easy to fabricate.

The advantages of microelectrodes have resulted in their acceptance as one of the best means to investigate a wide number of fields in analytical chemistry. In most incidents

the use of microelectrodes involves amperometry detection, which can be defined as the measurement of a current that flows at the electrode surface due to a redox reaction. It is possible not only to relate these currents to the concentrations of the species being reduced/oxidised at the electrode surface but also to the concentrations in the bulk whole solution.

1.7.2 Optical sensors and techniques

Optical sensors deliver light to a region of interest, this light can be used in one of two ways:

1. To investigate the composition of a solution or to evaluate an analyte, e.g. UV-Visible spectroscopy.
2. To initiate the selective formation of an analyte that is then detected by other means, e.g. fluorescence sensors.

1.7.2.1 Photochemical sensors

A basic example of an optical sensor is a light guide with one end attached to a reagent (optode). If when immersed in a solution, the reagent forms a reversible complex with an analyte the optical properties of the complex will be different compared to that of the uncomplexed reagent. Observed changes in the optical properties could include a shift in the wavelength of the maximum absorption peak or the fluorescence of light with a differing wavelength (Ache, 1993). The primary purpose of an optical sensor is to extract quantitative information via a spectroscopic measurement implemented directly in the sample. Such sensors have been utilized in the selective detection of ions, gases and small molecular species.

For most optical photochemical sensors, fibre optics are used to facilitate the delivery of light to the sensing area that is exposed to the sample of interest. A significant advantage fibre that optic-based sensors have is the ability to continuously monitor the level of analyte in a sample that could be a great distance from the instrument or in an inaccessible or dangerous area such as in a glove box to test radioactive material.

A pH sensor with a fluorescent pH indicator (acryloylfluorescein) immobilised at one end of a fibre optic is one of the simplest examples of an ion-selective based optical sensor (Tan, Shi and Kopelman, 1992). The pH measurement is based on differences in the luminescence properties of the acid-base conjugate pair of the immobilised dye. Such sensors have been built with millisecond response times (Tan, Shi and Kopelman, 1992). This technology is based on nanofabricated optical fibre tips and near field photoinitiated polymerisation. The polymer acts to increase the sensor surface area which aids to counterbalance the weak signal produced by a submicron sensor.

The development of a fibre optic sensor for the detection of a range of ions has led to the design of different systems. One example of this is to immobilise an indicator molecule that discriminately binds the ion of interest at the tip of the device. A fluorescence-based fibre optic biosensor capable of detecting zinc (II) at nanomolar concentrations has been developed (Thompson and Jones, 1993). This device exploits the fact that dansylamide binds to the carbonic anhydrase enzyme only when zinc is located in the active site of the enzyme emitting a blue florescence (Thompson and Jones, 1993). Without zinc, dansylamide does not bind to the enzyme and the resulting emission is a green-yellow fluorescence. By measuring the ratio of the fluorescence intensities at two wavelengths corresponding to emission from the bound and free forms of dansylamide, the occupancy of the active site of the enzyme by zinc was obtained.

Several optical sensor designs have been reported with the most common type employing a distal-type probe in which the indicator chemistry is immobilised at the tip. A device for DNA sequencing based on an axial optical fibre beam excitation scheme for a multiplexed fluorescence detector for capillary electrophoresis has been developed (Taylor and Young, 1993). The excitation laser is coupled to optical fibres that are inserted into capillary tubes. Ten of these tubes are monitored simultaneously during electrophoresis.

As an alternative to immobilising a substance onto the end of a fibre optic, a controlled-release polymer system can be used to deliver reagents to the sensing area of the optical fibre. Essentially, this technique requires the use of a reservoir that passively releases polymers to the sensing area of fibre optic. Such a device has been used for herbicide monitoring and for optical immunosensors (Barnard and Walt, 1991, 1992). Fibre-optic based microprobes have also been used successfully for investigating chlorophyll fluorescence with a high degree of accuracy and spatial resolution (Schreiber *et al.*, 1996). A fibre taper was fabricated while heating a fibre end via a small flame with fibre tips of 10-30μm in diameter were prepared by cutting the taper with a small knife.

A sensing element can also be used that contains a polymer crossed linked to an optical fibre (Seitz, 1993). The polymer swells or shrinks when it interfaces with the analyte. The swelling and shrinking of the polymer alter the distance between the fibre optics and the polymer. This change in distance is measured by the intensity of light reflected by the polymer to the fibre optic, with a shorter distance resulting in lower intensity.

1.7.2.2 Photo-electrochemical sensors

When an optical sensing device is combined with an electrode the resulting device can be used to investigate the electrochemistry of a photoactive species of interest. A combined optical sensor and electrode allows for the collection of electrochemical data

relating to the excited state of a photo-active molecule. Such devices have found applications in both analytical research and energy conservation.

A rotating optical disc-ring electrode was used by Johnson and co-workers (Johnson and Resnick, 1972) which was subsequently developed by Albery and Bartlett (Albery and Bartlett, 1985). Based on the conventional Rotating Ring Disc Electrode (RRDE) it utilized a central quartz disc through which light would penetrate an electrolyte solution. Photo-chemically generated products are detected by a concentric ring electrode which surrounds the disc. Teflon is used to sheathe the electrode with its end-surface in the plane of the ring electrode and the quartz disc. The photoelectrode is rotated about an axis perpendicular to and passing through the centre of the quartz disc, light is then shone through the quartz disc which is collimated to the axis of rotation. This RRDE design was used to study the photolysis of benzophenone in alkaline media (Lubbers *et al.*, 1974), it also proved useful for studying charge transfer phenomena in colloidal suspensions of semi-conductor particles (TiO_2) (Riefkohl *et al.*, 1987).

The central quartz was replaced by (Van Dyke and Cheng, 1988) with two fibre optics encased in an electrically conducting graphite loaded epoxy resin electrode allowing the optical discs and the electrode surface to be in the same plane. This design results in a reduced size and improved temporal and special features for the electrode, it was used for spectro-electrochemcial measurements of small samples and places difficult to reach. The overall size of the electrode was not stated however the fibre optics used in the construction had a diameter of 100 μm and proved small enough to conduct experiments within the brains of both rats and dogs. Van Dyke and Cheng, (1989) also manufactured an electrode for measuring stationary fluorescence on electrochemically preconditioned samples. The tip of a disposable pipette was used to seal a bundle of fibre optics. Six of the fibres situated around the circumference were selected to function as the emission collection arm of the electrode whilst another six fibres were used to function as the excitation arm of the electrode. A cylindrical working electrode with a diameter of 5 mm was used to electrochemically condition the probe and surrounded the fibre optical bundle and pipette configuration. To allow for flow injection analysis a cylindrical platinum working electrode was drilled with several holes with a dimeter of 0.5 mm which resulted in a ‘cage’ for the passage of solution.

(Kuhn, Weber and SG, (1990) further developed this design through the addition of an auxiliary/pseudo-reference electrode. A fibre optic of 200 μm diameter was encased by a 15 μm thick gold ring which itself was surrounded by a silver ring with an outer diameter of 2 mm and an inner diameter of 1.6 mm. The ring response was characterised and the electro-generated chemiluminescence detected from a solution of ruthenium (II) tris-(2,2’-bipyridine) in the presence of persulfate. Reduction of the ruthenium species occurred at the electrode surface resulting in a series of chemical reactions which

eventually generated excited ruthenium (II) tris-(2,2'-bipyridine) ($Ru(bipy)_3^{2+}$). The decay of the excited ruthenium species causes the observed luminescence. Special attention was given to cleaning the electrode which required the deliberate formation of an oxide layer on the metal surface which was then removed. This cleaning procedure assured that results were reproducible.

A purpose-built device for detecting hydrogen peroxide generated from photochemical reduction of oxygen has also been manufactured (Cohen and Weber, 1993). Photoexcitation of $Ru(bipy)_3^{2+}$ in oxygen containing samples was achieved via the fibre optic. Reduction of oxygen to hydrogen peroxide was achieved via a redox reaction of the photoexcited $Ru(bipy)_3^{2+}$ with reductants present in serum and urine (e.g. uric acid) served as electron donors regenerating $Ru(bipy)_3^{2+}$. When used invitro, triethanolamine was added to the solution to reduce $Ru(bipy)_3^{3+}$ and regenerate $Ru(bipy)_3^{2+}$. When an enzyme (catalase) for which hydrogen peroxide is a substrate is added to the solution, the electrochemical signal subsequently decreases. The components of this probe consist of a large gold coated optical fibre with a diameter of 510 µm and a ring thickness of 35 µm. Convective heating effects were achieved by connecting to an argon ion laser.

A fibre optic multi photon ionisation detector for polycyclic aromatic hydrocarbons was manufactured by Yamada (1992). Two gold electrodes fixed at the end of a fused silica fibre optic replaced the gold ring. The fibre optic allowed the delivery of 355 nm pulsed laser light which resulted in a measurable current.

A platinum electrode was surrounded with bundles of fibre optics allowing the measurement of the photosynthetic activity of algae (Takeuchi, Yokoyama and Y, 1993). This was achieved by using the electrode as a Clark-type oxygen sensor which could measure the resulting oxygen produced by photosynthesis produced by shining light through the fibre optics.

Similar devices have also been used in the detection of electro-chemiluminescence (ECL). No light source is need and mon chromatic light is not required, stray light can be easily eliminated. This results in increased sensitivity of the electrode. ECL analysis requires the correlation between the light intensity of the response and the concentration of the analyte. Analysis can be performed either directly when the analyte luminesces itself or indirectly through combination with other reagents. ECL has been used for immunoassays as it allows for the determination of the specific binding of two molecules, one of which is labelled with a molecular species capable of chemiluminescence (Deaver, 1995). A buffered solution of tripropylamine and an N-hydroxysuccinimide ester of ruthenium(II) tris-(2,2'-bipyridine) chelate for labelling proteins and haptens was used. The reaction between the Nhydroxysuccinimide ester of ruthenium(II) tris-(2,2'-bipyridine) and enzymes added to the solution freed $Ru(bipy)_3^{2+}$

ions that could be oxidised at the electrode surface. Excited $Ru(bipy)_3^{2+}$ was produced in the presence of electro generated excited tripropylamine species. Relaxation of $Ru(bipy)_3^{2+}$ from its excited state resulted in the emission of a photon with a wavelength of 620 nm. The concentration of the protein can be calculated via the intensity of the emitted photon. Possible ECL from sacrificial electro active species must be accounted for in the calculations.

Images that characterise the electrochemical reactivity of the surfaces of electrodes such as pyrolytic (Bowling *et al.*, 1989) and platinum (Pharr *et al.*, 1990; Engstrom, Nohr and Vitt, 1994) have been created using ECL. Sensitive microscope-based imaging was used in conjunction with the reaction of luminol in alkaline peroxide. Luminol is a chemical that exhibits chemiluminescence with a blue glow when mixed with an appropriate oxidising agent. This allowed for the monitoring the course of electron transfer at various regions on the electrode surface. The electron transfer kinetics of the luminol system are considerably more favourable in defect rich regions of the electrode surface. Luminol, 5-amino-2,3- dihydro-1,4-phthalazinedione, with an oxidant under alkaline conditions is possibly the best-known chemiluminescent reaction in aqueous solutions.

A rotating disc electrode was used to study this system Haapakka and Kankare, (1982). Oxidation of the luminol occurs at the ring with the disc being utilized to generate hydrogen peroxide from oxygen present in solution. As the electrode rotates, the generated hydrogen peroxide gathers at the ring where an ECL reaction takes place. Chemiluminescence was shown to generate from the reaction of the radical product of the one electron oxidation of luminol with the superoxide radical ion O2 which is generated at the ring electrode surface (Lind, Mereniji and Erikan, 1983). The product of this reaction is 3-aminophthalate, which has been identified as the photon emitting species. A photo multiplier tube was required to detect the emitted light. Haapakka concluded that the intensity of the chemiluminescence of luminol was highly dependent on the electrode materials. Further investigation into this feature found that glassy carbon was the most active electrode material for the oxidation of luminol and gold the least (Vitt and Johnson, 1991).

Of particular relevance to this project, MORE- like devices collected in arrays was used for ECL measurements (Szunerits and Walt, 2002). Approximately 600 optical fibres were bundled together and cleaned with piranha solution before ‘sensitisation’ in a solution of $SnCl_2$. A layer of silver was then deposited from a solution of $AgNO_3$, while surface bound Sn^{2+} was oxidised to Sn^{4+}. The silver coated fibres were then submerged in an aqueous solution of sodium gold sulphite, sodium sulphite and formaldehyde, where the silver catalytically oxidised formaldehyde while the gold was concurrently reduced to the metal form. The device was immersed in a 25% nitric acid solution which

dissolved any residual particles. The resulting gold coated fibres were then potted in epoxy resin and cured at 100°C. Silver glue was used to establish an electrical contact with the gold layer. The thickness of the gold layer was found to be approximately 1µm. ECL at the ring electrode array was demonstrated through oxidation of $Ru(bipy)_3^{2+}$ in tri-n-propylamine at pH=7, with the generated light collected and detected via the optical fibre bundle.

1.8 Aims of this project

1.8.1 The MORE as a Single Analyte Sensor

This project will expand on the work carried out by (Andrieux, Boxall and O'Hare, 2006b) that demonstrated that the MORE can detect a single analyte of Ru(bipy)32+ in solution. This project will focus on whether the MORE can detect the presence of uranyl, vanadium (IV) and cerium (III) ions. Once the experimental techniques have been established using vanadium (IV) and cerium (III) as surrogates, the project will be expanded to determine whether active analytes of neptunium (IV) and plutonium (III) and (IV) ions can be detected by the MORE.

1.8.2 The MORE as a Multi Analyte Sensor

As we have seen in the previous sections uranium (VI), neptunium (IV) and plutonium (III) and (IV) ions all have maximum absorbance peaks at different wavelengths of the electromagnetic spectrum (413.8, 723/964, 570/605 and 477 nm respectively). This can be seen clearly when the absorbance spectra for each analyte are plotted together as seen in Figure 1.9.

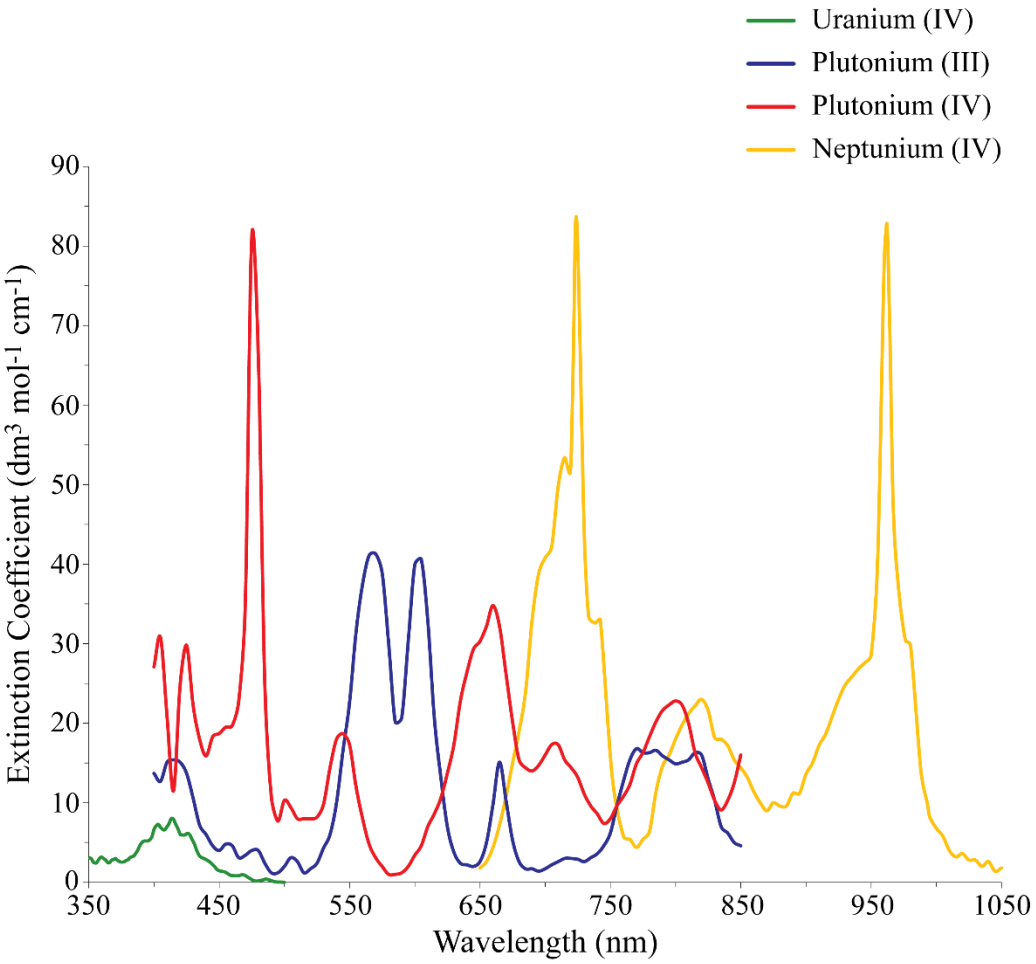

Figure 1.9: Comparison of electronic absorbance spectra for uranium (VI), neptunium (IV), plutonium (III) and plutonium (IV) aqua ions.

It is the unique absorption properties of each element that can be exploited by the MORE to allow the detection of each individual analyte in a mixture. Detection of an individual element could be achieved due to the MOREs ability to deliver light at specific desired wavelengths. For example, if the target analyte was neptunium (IV) in a mixture containing all four uranium (VI), neptunium (IV) and plutonium (III) and (IV) ions we could illuminate that mixture with light at a wavelength of 725 nm. Only the target analyte neptunium (IV) would enter an excited state that would create a photocurrent detectable by the MORE. To detect additional ions in the mixture the above process would be repeated altering the illumination wavelength each time to match that of a desired target analyte.

The possibility of interference between different analytes in a mixture will be investigated. This will be done by measuring the photocurrents generated by ions in a

single solution at various wavelengths. Close attention will be given to wavelengths in the range of the maximum absorbance of other target analytes. The results generated from this will determine if signal-deconvolution techniques will be required and will also establish the limits of detection for each analyte.

2 Materials and Methods

2.1 Reagents

Distilled water was produced in house using a Millipore direct-q 3 UV water purification system (ZRQSVP3WW, Merck, Darmstadt, Germany) to a conductivity of 18.2 MΩ·cm at 25°C. Prior to electrochemical experiments all solutions were purged for 15 minutes with nitrogen (white spot grade, BOC Ltd, Guilford, UK) to remove any dissolved oxygen.

Tris(2,2'-bipyridyl)dichlororuthenium(II) hexahydrate, hydrogen peroxide, sulphuric acid, potassium hydroxide, nitric acid, propan-2-ol, (3-mercaptopropyl) trimethoxysilane, iron (III) chloride, potassium hexacyanoferrate (III), vanadium (IV) oxide sulfate hydrate, cerium (III) chloride, ethanol and platinum wire (E5P1330-1EA) were all purchased from Sigma-Aldrich (Dorset, UK). Uranium was purchased from SPEXCertiPrep (Rickmansworth, UK) at a concentration of 10.00 g/l in 5% nitric acid.

2.1.1 Manufacturing the MORE

MOREs were fabricated according to an adapted procedure from Andrieux et al (2005). The electrode consists of four components: a fibre optic core, a conductive gold layer, an electrical contact and an insulating epoxy sheath. A light source is subsequently attached to the rear of the electrode and contains a ball lens to focus light emitted from an external source through the fibre optic.

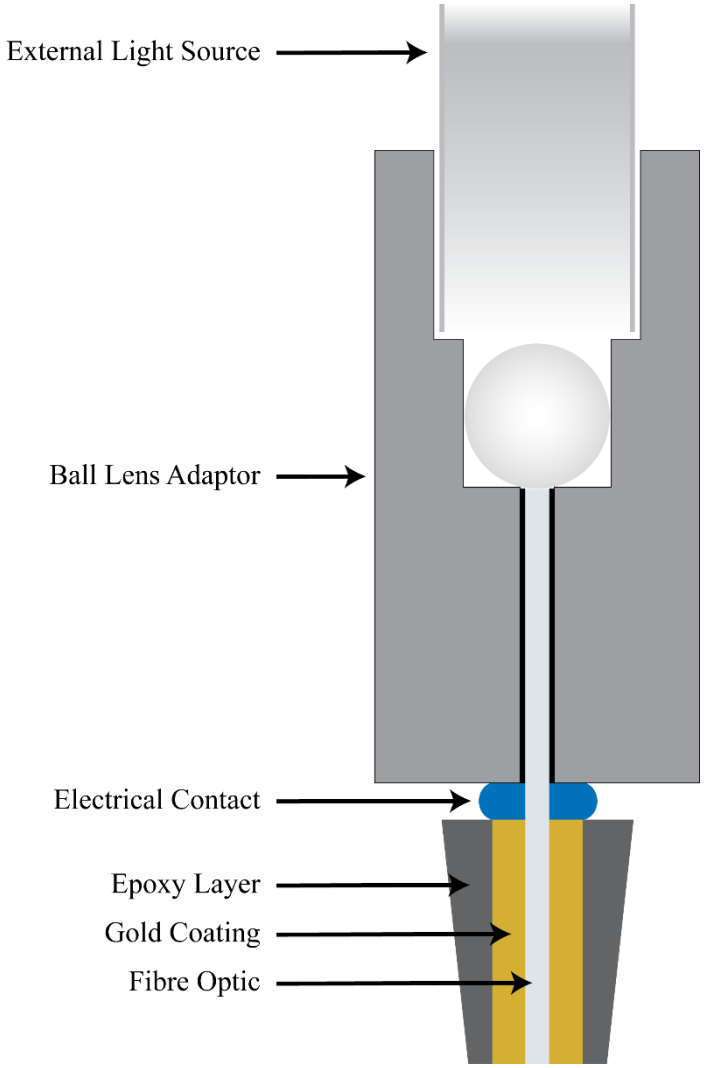

Figure 2.1: Illustration of the MORE

2.1.2 Fibre optic preparation

The MORE was constructed around a 200 µm diameter fibre optic which acted as the light guide (Horbia scientific, UK, model HO200/220). Fibres from Horiba Scientific were selected for their good transmittance properties across the UV, visible and infrared range (Figure 2.2). The fibre optic cable was cut into 5 cm sections using a fibre optic cutting block (Edmund Optics, 54-013). The fibres were then submerged overnight in piranha solution (hydrogen peroxide (1:3 v/v) and sulphuric acid (2:3 v/v). Following overnight incubation, the piranha solution containing the fibres was heated to 75ºC for at least two hours and until the outer cladding, along with any organic material, had

dissolved. The stripped fibres were then rinsed with distilled water and stored in a desiccator.

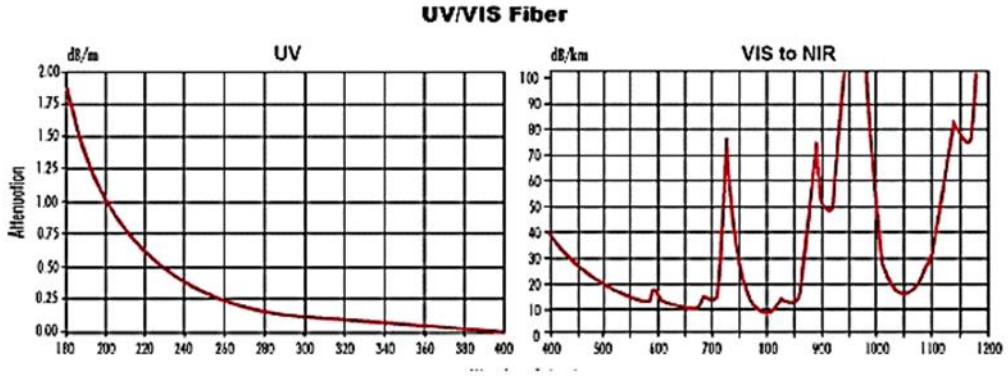

Figure 2.2: Transmittance properties of fibre optics used to manufacture MOREs (Horiba scientific).

In an additional cleaning stage, the fibres were placed in nitric acid (5 mol dm^{-3}) and ultra-sonicated for 15 minutes. The fibres were then placed in potassium hydroxide (5 mol dm^{-3}) overnight. The following day the fibres were transferred to nitric acid (5 mol dm^{-3}) and ultra-sonicated for 15 minutes. This process resulted in a roughened surface on the fibre and facilitated the silanisation procedure whereby silane was used as a molecular adhesive between the glass of the fibre and the deposited gold (see 2.1.3) (Goss, 1990). In addition to an adhesive, the silane acted to extend the lifetime of the fibre by reducing the risk of cracks forming between the fibre optic and gold layers during experimentation. Secondly, if delamination between the electrode material and the insulator were to occur; the hydrophobic properties of the silane layer over the surface of the barrel of the fibre would prevent any solution from penetrating gaps between the fibre surface and the gold coating. It is important to prevent solution interacting with the conductor at any region other than the tip as additional interaction would increase the non-faradaic current, thus compromising both the signal-to-noise ratio and the reproducibility of results.

To coat the fibres in silane, a mixture of propan-2-ol (40 g), (3-mercaptopropyl)trimethoxysilane (1 g) and water (1 g) was prepared and brought to reflux (Goss, 1990). The exposed fibres were placed into the mixture for 10 minutes while reflux was maintained. The fibres were then removed from the silane solution and cured in an oven at 100^{o}C for eight minutes. The silanisation procedure was repeated twice and, once complete, the treated fibres were transferred to a desiccator loaded with silica gel to remove any moisture.

2.1.3 Gold coating

Reflecting the work carried out by Andrieux (2005) gold was chosen as the conductive layer for the MORE due to its inert properties. A Quorum Technologies sputter coater (serial 942U7-26, Laughton, UK) equipped with a rotating stage (RS 336-315 12v d.c. 60 r.p.m.) and modified to accommodate 6 fibres was used to coat the fibre optics with gold (Figure 2.3). Using a rotary pump (Edwards RV3 vacuum pump,) and a gold target (SC510-314A,), a thin layer of gold was deposited on the barrel of the optical fibres. The fibres were loaded onto the stage and a vacuum of 0.02 mbar was established within the chamber prior to an 800 V bias being applied between the stage and the target for six minutes.

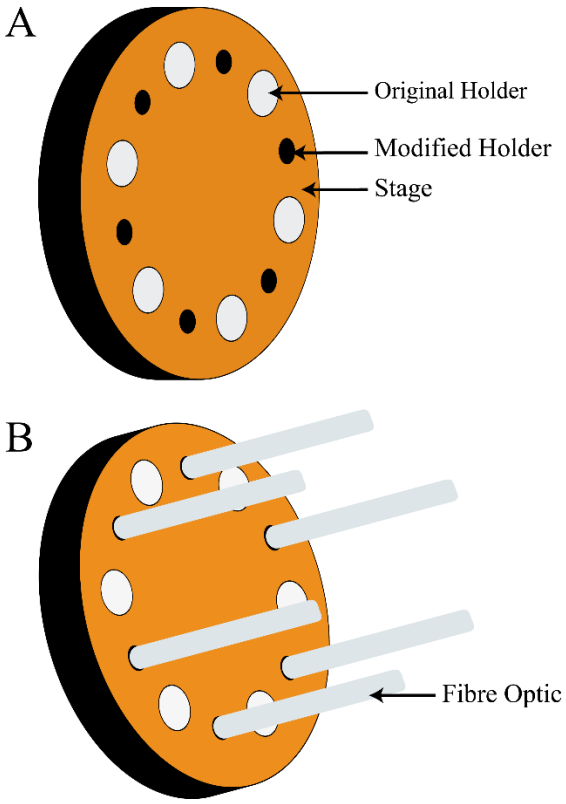

Figure 2.3: Illustration of the rotary device used to coat fibres with gold

A: Modified rotary device
B: Modified rotary device with fibre optics inserted

2.1.4 Electrical and light connector

The electrical contact to the gold layer was achieved by positioning a commercially available connector (Multi-contact plug 2mm, 1085442, Farnell, UK) onto the optical

fibre. Silver loaded epoxy (CW2400, Farnell, UK) was used to secure the contact between the connector and the gold layer and was cured at 100^{o}C for 10 minutes. The non-gold coated end of the fibre optic was inserted into a sheath (Fibre Optic Splice Protection Sheath size 23 mm, Hilltop Products, UK) to provide robustness and allow for simple attachment of the MORE to the aluminium light guide (Figure 2.4).

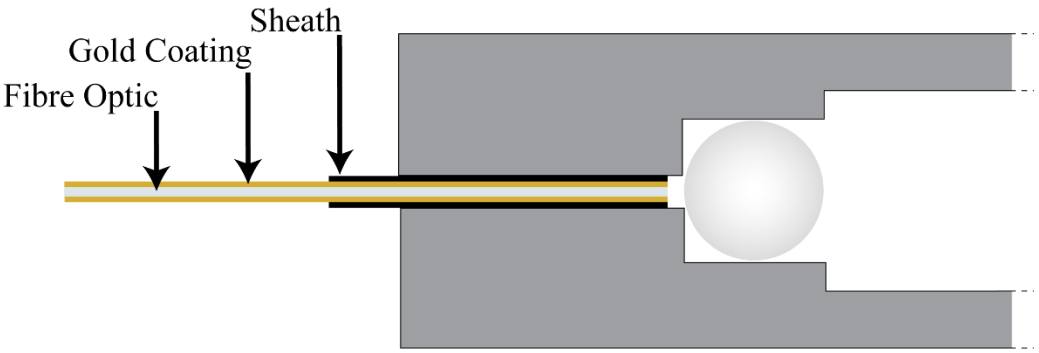

Figure 2.4: Illustration of the connection between the fibre optic and the light guide

This diagram demonstrates how the gold coated fibre optic of the MORE connects to aluminium light guide with use of a fibre optic sheath.

To further increase robustness of the MORE and to insulate the gold coated fibre optic, the treated fibres were potted in araldite resin (1759533 RS Components, Farnell, UK). Two volumes of resin (2020/A) were mixed with one volume of the hardener (2020/B) as per the manufacturer's instructions. The amount of air introduced into the mixture was kept to a minimum. The araldite was poured into a 5 mL pipette tip to which a coated fibre was inserted. Great care was made to ensure the araldite resin was as free from air bubbles as possible. The presence of bubbles at the tip of the MORE could result in additional exposure of the electrode to the electrolyte and, as mentioned previously, increasing the surface area of the electrode exposed to the solution of interest could cause errors in the electrochemical analysis. To reduce the possibility of air bubbles forming in the epoxy, the gold coated fibre optic was suspended in the araldite and left to cure slowly at room temperature for 48 hours. This slow curing time gave any bubbles present an opportunity to rise to the surface of the resin and away from the electrode tip

The final stage in producing the MORE was to attach a light connector to enable the delivery of light through the fibre optic to the tip of the MORE. The exposed end of the fibre optic was attached to an aluminium light connector (manufactured in house) which included a recess for a 5.0 mm diameter ball lens (43-712, N-BK7 ball lens, Edmund

Optics, England) held in place with optical glue (NOA88, Edmund Optics, England) (Figure 2.4).

2.1.5 Final steps and surface treatment

Upon construction of the MORE, the very tip of the electrode was sawn off using a small hacksaw. Removing the tip of the MORE exposed a concentric system consisting of the fibre optic, gold, and araldite (Figure 2.5).

The sawn electrodes were polished on decreasing grades of abrasive materials including silicon-carbide paper (120, 600 and 1200 grade, Screwfix, UK), and diamond slurry (6, 3 and 1 µm (Moleroda Finishing Systems, UK)) on a micro cloth (Buehler, UK). Between each polishing step, the electrode was carefully rinsed with distilled water to remove any abrasive particles.

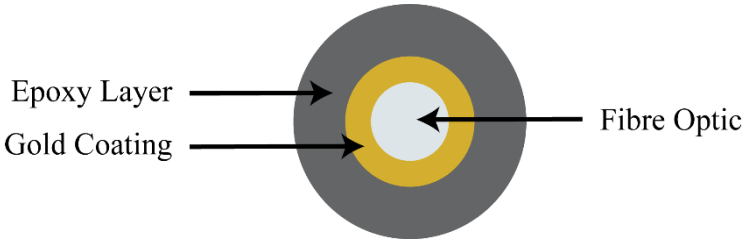

Figure 2.5: Cross-section of the tip of the MORE

2.1.6 Calibration of the MORE

A current is generated within the microelectrode from a solution due to the mass transport of an electrochemically active species to the electrode surface. This mass transport can occur due to three possible mechanisms:

1. Migration: an electromagnetic force causes the movement of the charged species to the electrode.
2. Diffusion: a concentration gradient in the solution causes the movement of the species from a region of high concentration to a region of low concentration.
3. Convection: movement is due to natural or forced convection (e.g. stirring).

During electrochemical experiments, it is necessary to limit the mass transport mechanism. Limiting mass transport allows for greater control of the experiment and allows the system to be more mathematically tractable. For microelectrode experiments the dominant mechanism of mass transport is typically diffusion due to its efficiency. Transport by migration can be negated by the addition of a high concentration of a supporting electrolyte that is non-electro-active in the potential region of interest. After

initially stirring the solution and leaving it to settle, convection can be controlled by performing electrochemical experiment under non-stirred conditions.

The integrity of the electrode seal can be investigated by measurement of the diffusion-limited current of the MORE, it will also allow for calculation of the dimensions of the ring.

2.2 Electrochemistry at the MORE

Electrochemical measurements were carried out using a three-electrode cell in which the MORE served as the working electrode, a Saturated Calomel Electrode (Rusell pH, UK) as the reference electrode and a platinum wire as the auxiliary electrode (Figure 2.6). The electrochemical cell was housed in an earthed faraday cage to reduce noise and exclude ambient light from the system. The electrochemical cell was driven by a potentiostat (PGSTAT128N, Metrohm Autolab, UK) connected to a personal desktop computer via an Autolab interface card and operating NOVA 2.0 software to control the electrochemical cell and collect data. The reference and counter electrodes of the electrochemical cell were connected to the Autolab by means of a DIN (Deusches Industrinorm) connector at the front of the potentiostat module. The working electrode (MORE) was connected via a coaxial cable to the input of the potentiostat. The light source (S/N 3240-A101OB, Photon Technology International, Canada) was connected to the MORE by an external optical fibre light guide that was connected to the aluminium light connector of the MORE.

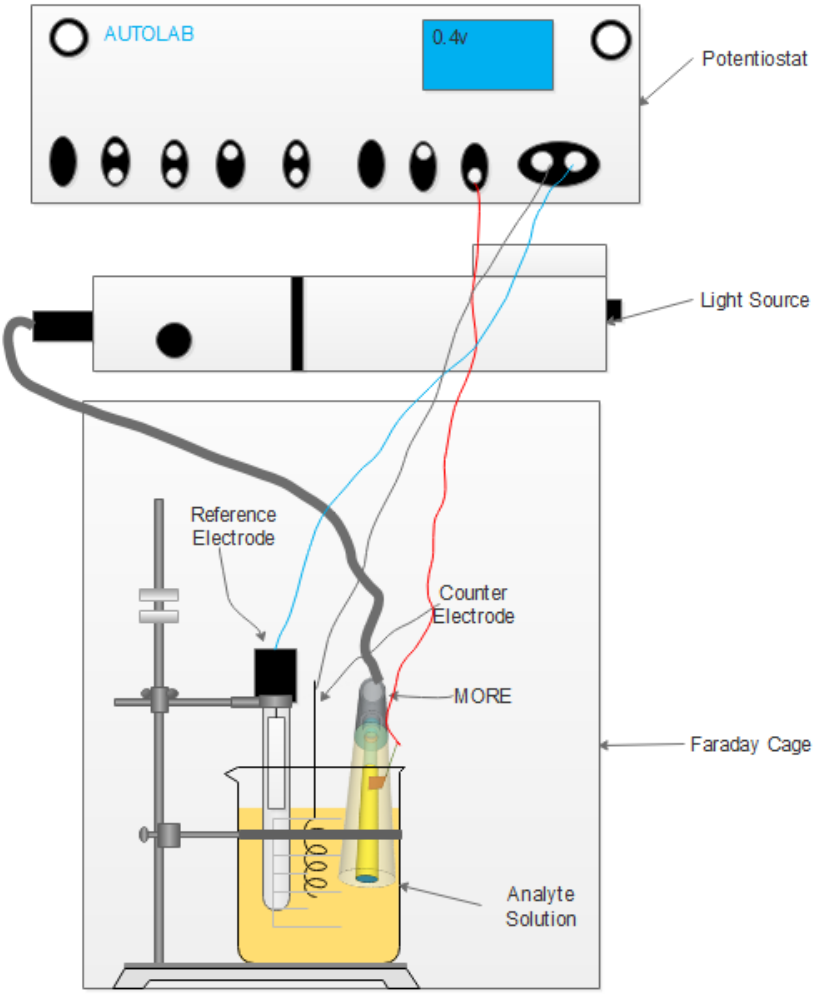

Figure 2.6: Experimental Setup of the MORE electrochemical cell

Diagram illustrating the electrochemical cell set up and how the working electrode (MORE), reference electrode and auxiliary electrode were connected to the potentiostat.

2.2.1 Electrochemistry using a Rotating Disc Electrode

For experiments that required a rotating disc electrode, the experimental setup was carried out as described in Section 2.1.6 but a rotating disc electrode with a surface area (A) of 0.1963 cm^2 replaced the MORE as the working electrode.

2.3 Microscopy

2.3.1 Scanning Electron Microscopy

Scanning electron microscopy (SEM) was carried out in collaboration with Dr Richard Wilbraham and Dr Sara Baldock (Lancaster University). Short sections of the tip of the MORE and gold coated fibre optics were sent to Dr Wilbraham and Dr Baldock respectively. SEM images generated by Dr Baldock were gathered using a field emission scanning electron microscope (JSM-7800F, JEOL, England).

2.3.2 Atomic Force Microscopy

High Speed Atomic Force Microscopy (HS-AFM) was performed in collaboration with Dr Oliver Payton (Bristol University). Short sections from the tip of the MORE were sent to Dr Payton who subsequently imaged the samples. This is a description of the process provided by Dr Payton: MORE samples were mounted on a 12.5 mm diameter SEM stub with a 3.2 x 8 mm pin. The sample was adhered to the stub using silver epoxy. Analysis of the resulting images was carried out by Dr Payton.

2.4 Statistics

2.4.1 Error bars

All photocurrent magnitudes were recorded during a minimum of three light on/light off cycles resulting in at least six results for the photocurrent magnitude. The average of all photocurrents recorded was calculated and plotted. Error bars denote the standard deviation which was calculated from all magnitudes recorded in a single photocurrent experiment.

2.4.2 Chi squared

A Chi Squared Test was used to determine how closely the experimental data matched that of the theoretically predicted results as calculated by the mathematical model. A p-value greater than 0.05 was deemed statistically insignificant. The p-value was determined by utilizing the online tool at *Chi-Square Calculator*.

$$X^2 = \sum \frac{(O - E)^2}{E}$$

$$D_f = N - 1$$

X	Test Statistic
O	Observed Value
E	Expected Value
D_f	Degrees of Freedom
N	Sample Size

Equation 2.1: Chi Squared Test

3 Calibration of the MORE and Surrogate Parameters

3.1 Cyclic Voltammetry and Chronoamperogram

3.1.1 Cyclic voltammetry

To test whether the constructed MOREs were able to work as a functional electrode a cyclic voltammogram was generated using potassium hexacyanoferrate (III) (10 mmol dm^{-3}) and potassium chloride (0.1 mmol dm^{-3}) dissolved in water (Figure 3.1). The working potential of the MORE was observed at 0.3 V (Figure 3.1). The observed working potential was comparable to the known literature value for the redox reaction between potassium hexacyanoferrate (III) and potassium chloride which is 0.3 V (Bard and Faulkner, 2004).

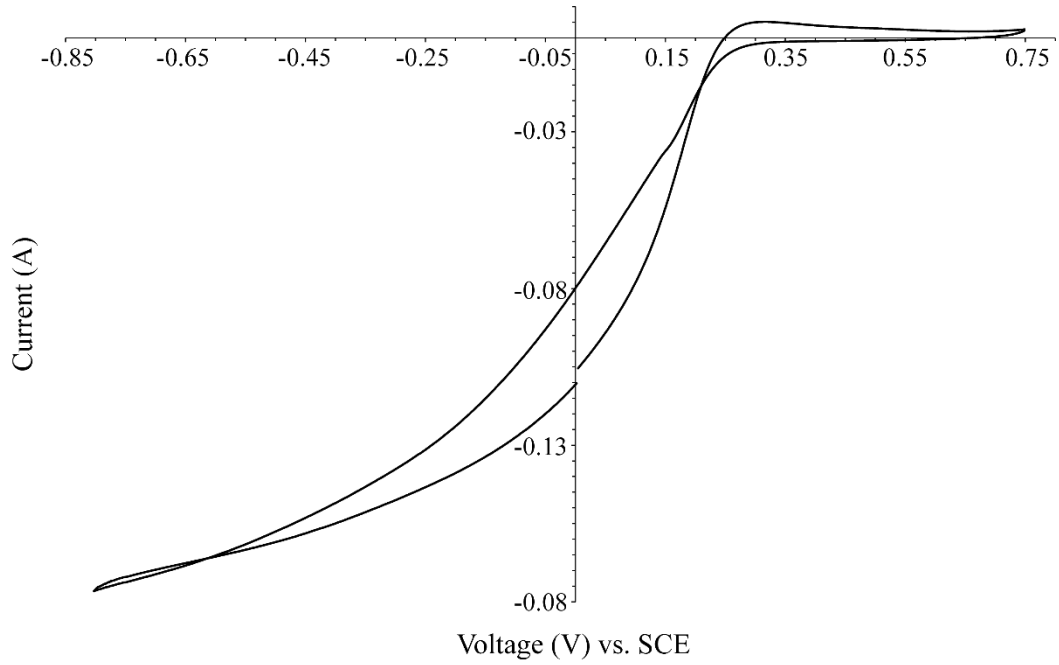

Figure 3.1: Cyclic Voltammogram at the MORE

The recorded cyclic voltammogram of $K_3[Fe(CN)_6]$ (10 mmol dm^{-3}) and KCl (0.1 mol dm^{-3}) with a scan rate of 1 mvs^{-1}. Performed using MORE 4.

Measuring a cyclic voltammogram demonstrated that the MORE could detect and generate a current. The cyclic voltammetry also provided information regarding the quality of the seal between the fibre optic and araldite insulators and the gold conductor. If the seal between the electrode and the insulator is intact the following features should be observed:

1. A thin CV that indicates a non-faradaic process due to capacitive charging at the electrode surface being limited.
2. The half wave potential would be consistent with values expected from the literature.
3. The CV reaches a plateau after the half wave potential.

These three features were all observed in Figure 3.1 confirming that the manufacturing method used to construct the MORE was reliable. A cyclic voltammogram was recorded for each individual MORE fabricated and the above features checked to ensure a robust construction.

3.1.2 Chronoamperogram

Chronoamperogram experiments were carried out using the electrochemical cell setup described in Section 2.1.6. The diffusion limited current of potassium hexacyanoferrate (III) (3, 5, 7 and 10 mmol dm^{-3}) in the presence of potassium chloride (0.1 mol dm^{-3}) was measured. Potassium hexacyanoferrate (III) and potassium chloride were chosen for this experiment because the values for both the standard potential and the diffusion coefficient are well established in the literature (Bard and Faulkner, 2004).

Figure 3.2A shows a chronoamperogram recorded in a solution of potassium hexacyanoferrate (III) (10 mmol dm^{-3}) and potassium chloride (0.1 mol dm^{-3}). Initially a rapid increase in the current was observed that plateaued after approximately 15 seconds indicating that a diffusion limited current was attained. Currents recorded in 3, 5 and 7 mmol dm^{-3} potassium hexacyanoferrate (III) all followed the trend observed for 10 mmol dm^{-3} potassium hexacyanoferrate (III). The diffusion limited current measured between 50 and 300 seconds, when a steady state was observed, the data was averaged and plotted against potassium hexacyanoferrate (III) concentration (Figure 3.2B). The diffusion limited current as a function of potassium hexacyanoferrate (III) concentration generated a straight-line graph (Figure 3.2B).

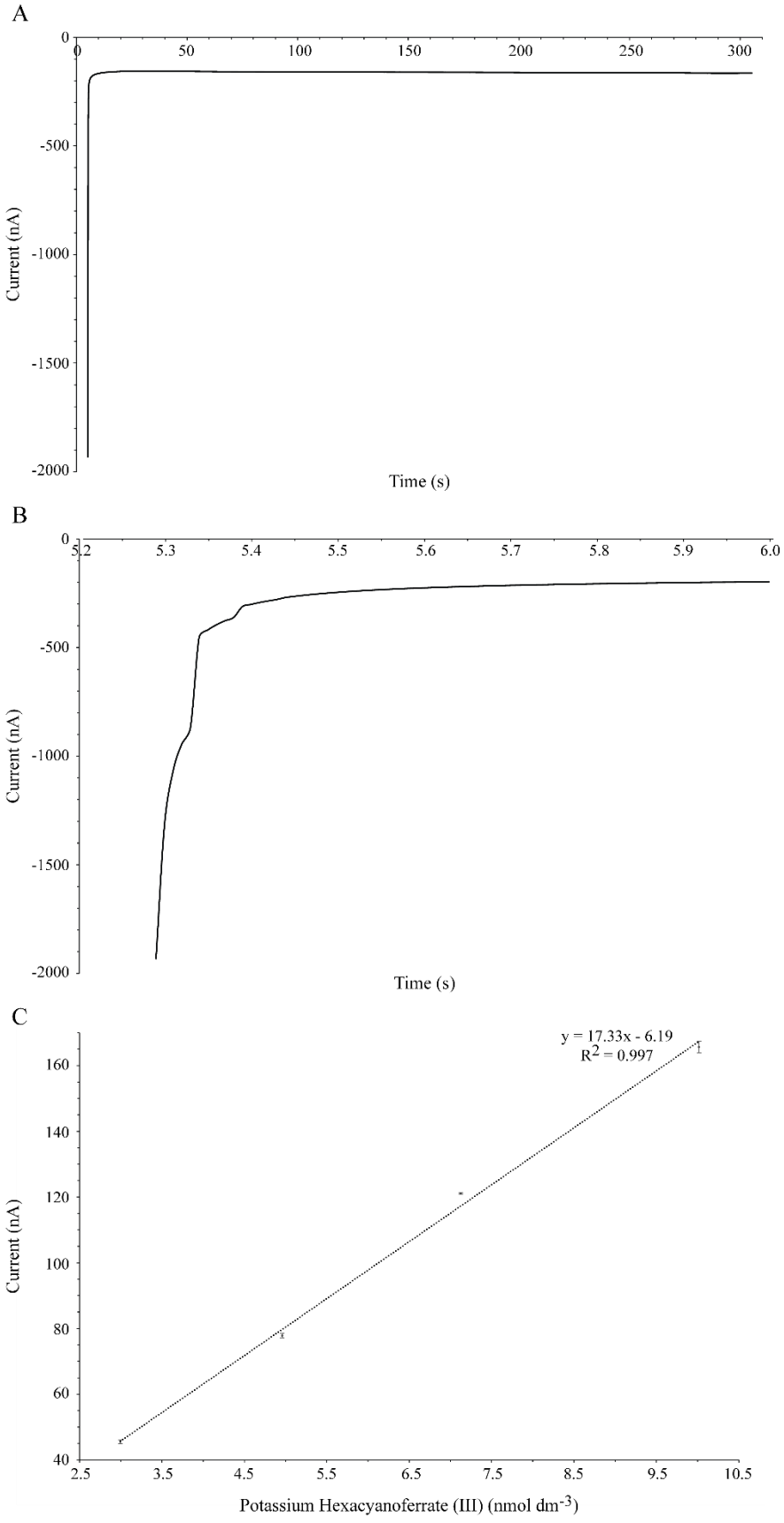
A
0
-500
-1000
-1500
-2000
Current (nA)
0
50
100
150
200
250
300
Time (s)
B
0
-500
-1000
-1500
-2000
Current (nA)
5.2
5.3
5.4
5.5
5.6
5.7
5.8
5.9
6.0
Time (s)
C
y = 17.33x - 6.19
R2 = 0.997
160
140
120
100
80
60
40
Current (nA)
2.5
3.5
4.5
5.5
6.5
7.5
8.5
9.5
10.5
Potassium Hexacyanoferrate (III) (nmol dm-3)

Figure 3.2: Electrochemical recordings at the MORE

A: Chronoamperogram of a solution containing potassium hexacyanoferrate(III) (10 mmol dm^{-3}) and potassium chloride (0.1 mol dm^{-3}). E = -0.3 V vs SCE for 300 s recorded using MORE 4.
B: The initial rise of Figure 3.2A.
C: Diffusion limited current as a function of potassium hexacyanoferrate(III) concentration recorded at the MORE (MORE 4). Error bars denote standard deviation.

3.2 Calculating the thickness of the gold ring of the MORE

In order to use the mathematical model explaining the sensitizer/acceptor behaviour and the MORE (Andrieux, Boxall and O'Hare, 2006a), the thickness of the gold ring must be known. The gold ring thickness can be calculated by determining the characteristic length of the ring electrode using **Equation 3.1**(Smythe, 1951). However, before Equation 3.1 can be used the characteristic length (l_0) must first be calculated via the mathematical expression for the diffusion limited current ($I_{R,ss}$) devised by Symanski and Bruckenstein (1988) (Equation 3.2).

$$(l_0) = \frac{\pi^2(a+b)}{\ln\left(16\left(\frac{b+a}{b-a}\right)\right)}$$

Equation 3.1

Where:

a	Inner radius (of gold ring)
b	Out radius (of gold ring)
l_0	Characteristic length of the ring electrode

$$I_{R,ss} = nFDCl_0$$

Equation 3.2

Where:

$I_{R,ss}$	Diffusion limited current
n	Number of electrons exchanged during the redox reaction (taken as 1)
F	Faraday constant (96484.6 $C.mol^{-1}$)
D	The diffusion coefficient of species being studied
C	The bulk concentration of the electro-active species
l_0	The characteristic length of the ring electrode

The diffusion limited current was established experimentally using the chronoamperogram experiments carried out above (Figure 3.2B). The gradient of the observed straight line in Figure 3.2B is equivalent to the diffusion limited current divided by the concentration of analyte used. The calculated gradient was therefore substituted into Equation 3.2 giving Equation 3.3.

$$Gradient = nFDl_0$$

Equation 3.3

Where:

n	Number of electrons exchanged during the redox reaction (taken as 1)
F	Faraday constant (96484.6 C.mol^{-1})
D	The diffusion coefficient of species being studied
l_0	The characteristic length of the ring electrode

To calculate l_0,Equation 3.3 was further rearranged to give Equation 3.4.

$$l_0 = \frac{Gradient}{nFD}$$

Equation 3.4

Where:

n	Number of electrons exchanged during the redox reaction (taken as 1)
F	Faraday constant (96484.6 C.mol^{-1})
D	The diffusion coefficient of species being studied
l_0	The characteristic length of the ring electrode

The value of the characteristic length of the electrode (l_0) is unique for each MORE. Upon calculating l_0, Equation 3.1 was used to calculate the thickness of the gold ring for each MORE used. The inner radius (a) is known from the dimension of the fibre optic (100 µm). Determining the outer radius (b) mathematically through the use of Equation 3.1 allowed for the calculation of the gold ring thickness of each MORE by subsequently subtracting the inner radius (a) from the calculated outer radius (b).

The gold ring thickness was calculated for three individual MOREs manufactured, each with a sputter coating time of six minutes. The thinnest gold ring thickness was calculated to be 1.3 µm and the thicknesses was 3.3 µm. The average gold ring thickness calculated for the MOREs was 2.5 ± 0.89 µm ($\pm$ standard deviation).

3.3 Measuring a photocurrent at the MORE

Measuring the cyclic voltammetry demonstrated that the fabricated MOREs were functional with regards to detecting a current (Figure 3.1). However, the aim of this project was to use the MORE to detect photocurrents resulting from the transfer of photoexcited electrons. To determine if the fabricated MOREs could detect a photocurrent an experiment was set up using a solution containing tris(2,2'-bipyridyl)ruthenium (II) chloride hexahydrate ($Ru(bipy)_3^{2+}$) (10 mmol dm^{-3}) serving as the sensitizer, and iron (III) chloride (5 mmol dm^{-3}) serving as the acceptor, dissolved in water. Prior to exposure to the MORE, the solution was bubbled with nitrogen for 15 minutes to remove any dissolved oxygen. This is due to how electrochemically active oxygen is and therefore will prevent oxygen impacting on any of the results.

It has previously been shown that a working potential of 0.5 V (vs SCE) is adequate to generate a photocurrent via the photoexcitation of $Ru(bipy)_3^{2+}$ and subsequent electron transfer to iron (III) ((Andrieux, Boxall and O'Hare, 2006a). To establish a steady state within the solution the experiment was left to run for approximately 200 seconds in the dark before the light was switched on. Following illumination, a decrease in the current was immediately observed and this reduced current remained constant for the duration that the light was switched on (100 seconds) (Figure 3.3). When the light was switched off again, the current returned to its initial value (Figure 3.3).

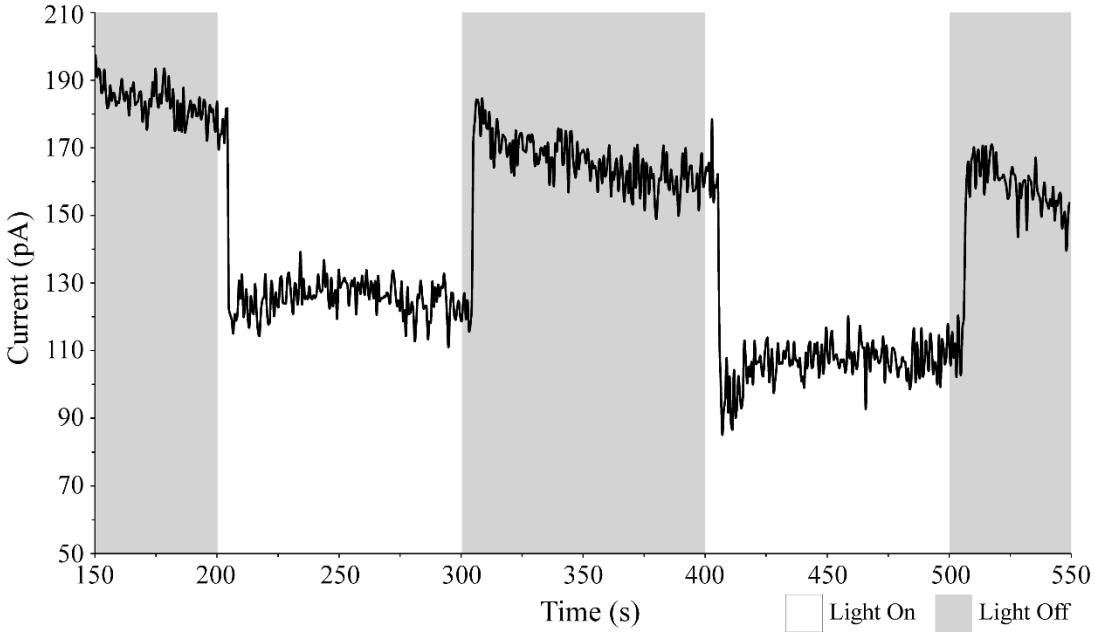

Figure 3.3: Photocurrent from a ruthenium solution

Photocurrent generated using white light in deaerated solution containing $Ru(bipy)_3^{2+}$ (10 mmol dm^{-3}) and $FeCl_3$ (5 mmol dm^{-3}) at pH 1.83 with a working potential of 0.5 V vs SCE.

The photocurrents measured by the MORE were in the region of 80 pA, they were reproducible and demonstrated that the fabricated MORE was functional in terms of initiating and detecting a photocurrent. The results seen here compare favorably with previous work carried out on the $Ru(bipy)_3^{2+}$ / iron(III) chloride system that also demonstrated a photocurrent with a magnitude of ~80 pA for a $Ru(bipy)_3^{2+}$ (10 mmol dm^{-3}) and iron (III) chloride (5 mmol dm^{-3}) setup (Andrieux, Boxall and O'Hare, 2006a).

3.4 Drift Correction

When performing electrochemical experiments, it is common to observe a drift in the current measured. This drift is attributed to noise (and subsequent residual current) generated in the equipment required for experimentation. Drift is an important consideration not only when measuring currents in the nano Amp range but especially when measuring minute changes in current, i.e. during photocurrent detection. When measuring minute changes in current a large drift could have the potential to obscure photocurrents, thus making it appear as though no photocurrent had occurred.

When performing photocurrent experiments with the MORE drift was observed (an example of which can be seen in Figure 3.4A). To compensate for drift a baseline correction was applied. Drift compensation was accomplished by selecting only those data points immediately prior to the light being turned on. These data points were selected to assume the trend of the photocurrent had the light not been turned on and off. By selecting only those points prior to re-illumination any change in current occurring due to the change in light conditions is ignored. Removal of these data points eliminated the rise and fall of the photocurrent signal. Removal of data generated by photocurrents resulted in a smaller number of data points. This reduced number of data points were compared to various trendlines that modelled the extent of drift occuring; whichever trendline had the highest R^2 value was subsequently selected Equation 3.4B. The trendline generated was due to the background drift. The equation associated with the selected trendline was then subtracted from the raw data, resulting in a reduction in the recorded drift. Figure 3.4C shows the baseline corrected photocurrent of the raw data shown in Figure 3.4A.

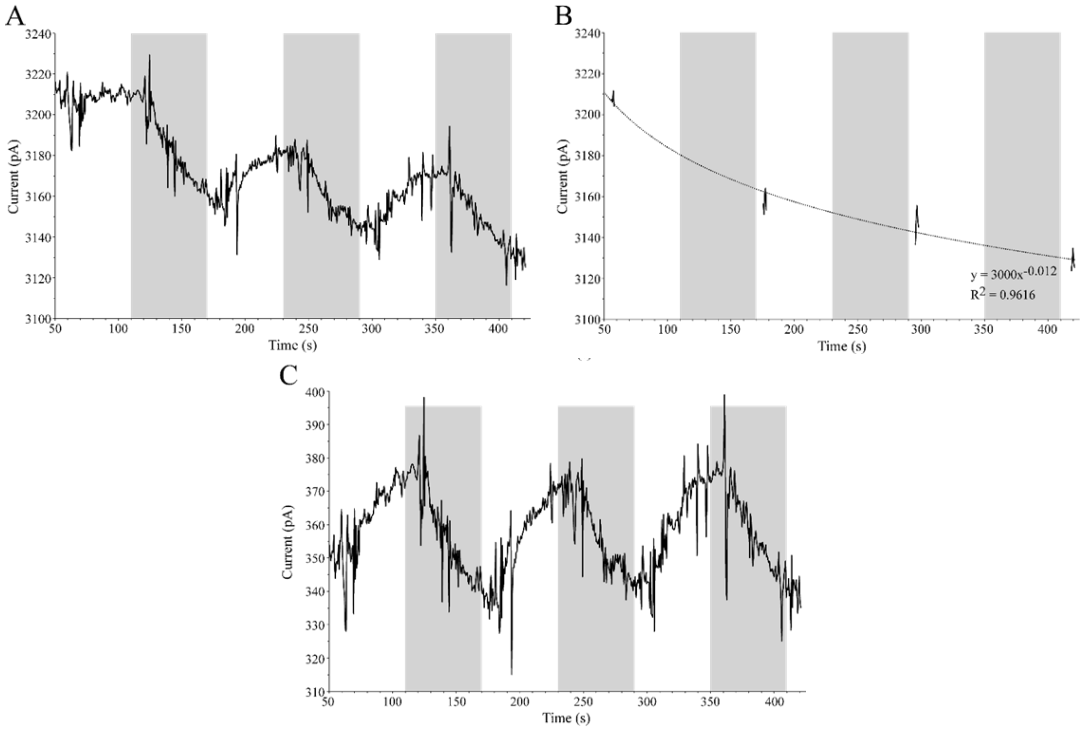

Figure 3.4: Photocurrent of the Micro-Optical Ring Electrode before and after a baseline correction to correct for drift.

A: Photocurrent with drift. Recorded using MORE 4 in a deaerated solution containing UO_2^{2+} (17.52 mMol dm^{-3}) and EtOH (100 mMol dm^{-3}) at a pH of 0.20 using white light illumination and a working potential of 0.7 V vs. SCE.
B: The data from (A) but only showing data points immediately prior to the light being turned on.
C: A recalculation of the current observed in (A) but accounting for the drift by correcting using the gradient determined in (B).

Removal of drift allows for a more accurate determination of the photocurrent measured by the MORE. The baseline drift correction set our above was applied to any photocurrent measurements in which drift was observed.

3.5 Impact of surface finish on recorded photocurrents

In the first instance MOREs were tested with an unpolished tip and photocurrents were observed. The mathematical model outlined by Andrieux, Boxall and O'Hare, (2006a) assumes that the ring is uniformly illuminated at the tip of the MORE with the optical

fibre, gold ring, and araldite resin all in the same plane. To achieve this the MORE needed to be polished to a smooth near mirror finish.

To create MOREs that had a near-mirror finish at the tip three grades of silicon carbide paper were used followed by polishing with diamond slurry. Previous work by Andrieux, Boxall and O'Hare, (2006a) demonstrated that photoexcitation of a solution of $Ru(bipy)_3^{2+}$ in the presence of iron (III) chloride resulted in the generation of a photocurrent. To test the ability of a highly polished MORE to detect a photocurrent a deaerated solution of $(Ru(bipy)_3^{2+}$ (10 mmol dm^{-3}) (the sensitizer) and iron (III) chloride (5 mmol dm^{-3}) (the acceptor) was set up. Following set up of the MORE electrochemical cell in the mixed solution it was left in the dark for 100 seconds to establish a steady state. Following illumination, no photocurrent was observed yet a considerable amount of drift could be seen (Figure 3.5). The light was cycled on and off at 50 second intervals twice yet no photocurrent was observed during any period of illumination (Figure 3.5).

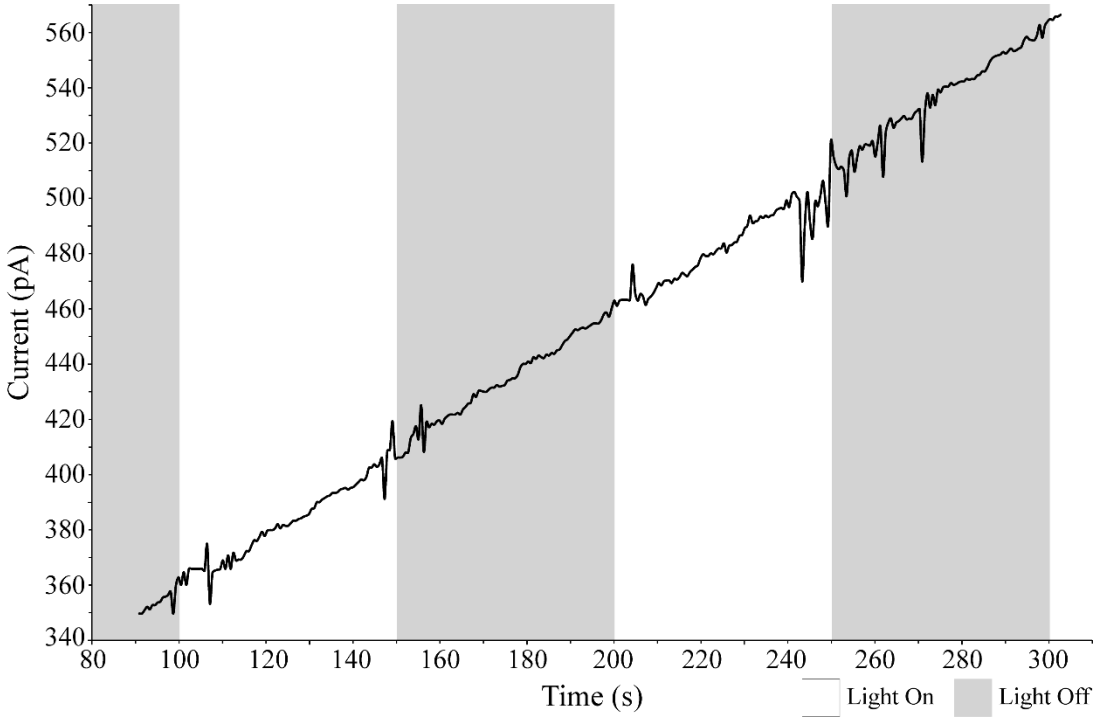

Figure 3.5: Measuring the photocurrent generated by a MORE with a smooth tip

A solution containing $Ru(bipy)_3^{2+}$ (10 mmol dm^{-3}) and Fe^{3+}(5 mmol dm^{-3}) at a pH of 1.83 was illuminated with white light at 50 s intervals. The working potential was 0.5 V vs SCE. The current was measured using MORE 4.

To understand why the highly polished MORE failed to detect a photocurrent a series of experiments were carried out to investigate whether the surface finish of the MORE impacted the generation and/or detection of a photocurrent. An experiment was set up in which the photocurrent generated by a solution of $Ru(bipy)_3^{2+}$ (10 mmol dm^{-3}) and iron (III) chloride (5 mmol dm^{-3}) was measured using the same unique MORE that had undergone different rounds of polishing with silicon carbide paper. Three different grades of silicon carbide paper were used. Initially the MORE tip was polished with the roughest grade of silicon carbide paper (120 grade), the MORE was placed in the $Ru(bipy)_3^{2+}$ (10 mmol dm^{-3}) / iron (III) chloride (5 mmol dm^{-3}) solution and the current measured during two cycles of light on / light off. The MORE tip was then polished with the second roughest silicon carbide paper (600 grade) which should result in a smoother finish at the tip of the MORE compared to the 120 grade paper. The current was measured again in the $Ru(bipy)_3^{2+}$ (10 mmol dm^{-3}) / iron (III) chloride (5 mmol dm^{-3}) solution. Finally, the MORE tip was polished with the finest grade of silicon carbide paper (1200 grade) and the current measured. The results shown in Figure 3.6 demonstrate that polishing the tip of the MORE with the roughest grade of silicon carbide paper (120 grade) resulted in a MORE that could detect a photocurrent. Additional polishing with the second roughest grade of paper (600 grade) also resulted in a MORE that was able to detect a photocurrent, albeit with a smaller magnitude compared to that generated by the MORE with a rougher surface finish (Figure 3.6). When the MORE had been polished with the finest grade of silicon carbide paper (1200 grade) no photocurrent was detected (Figure 3.6). It would appear that subsequent polishing and a smoother finish at the tip of the MORE results in a diminished photocurrent size to the point that no photocurrent can be detected (Figure 3.6).

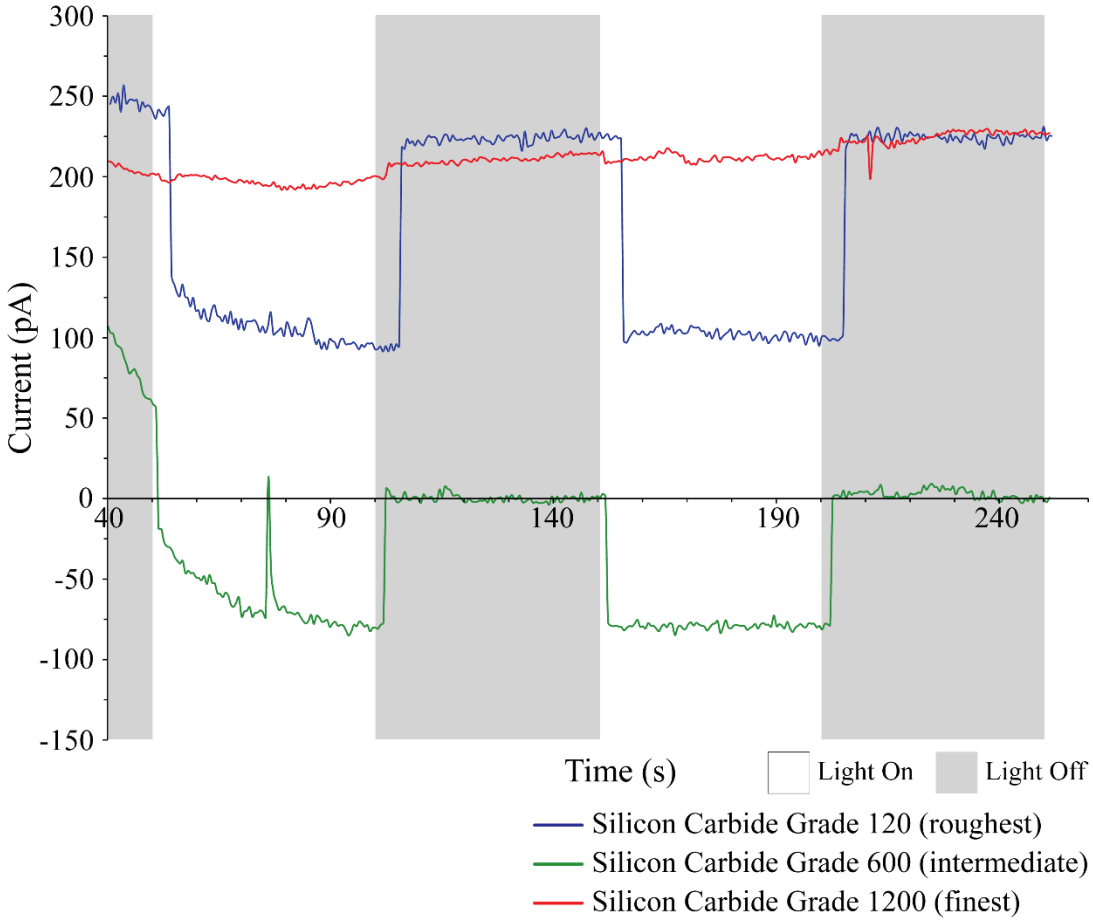

Figure 3.6: Measuring the current following various rounds of polishing at the tip of the MORE

The current in a solution of $Ru(bipy)_3^{2+}$ (10 mmol dm^{-3}) and iron (III) chloride (5 mmol dm^{-3}) was measured using MORE 4 following various rounds of polishing. White light was used to illuminate the solution and the working potential applied was 0.5 V vs SCE. The pH of the solution was 1.83.

To ensure that the effects observed in Figure 3.6 were not specific to the individual MORE used in that experiment the effects of surface finish were tested on an additional three MOREs. The experiments were set up as explained previously in that the same individual MORE and reaction solution were used to measure the photocurrent following polishing of the MORE tip on increasingly finer grades of silicon carbide paper. The results shown in Figure 3.7 demonstrate that as the particle size of silicon carbide paper decreased, and a smoother finish was obtained at the tip of the MORE, the magnitude of the photocurrent observed also decreased. It would therefore appear that a rough finish at the MORE tip correlates with an increase in the size of

photocurrent detected. A large variation in photocurrent magnitude was observed between different MOREs, this is likely due to variations in the size of the gold ring being exposed to the photoexcited products.

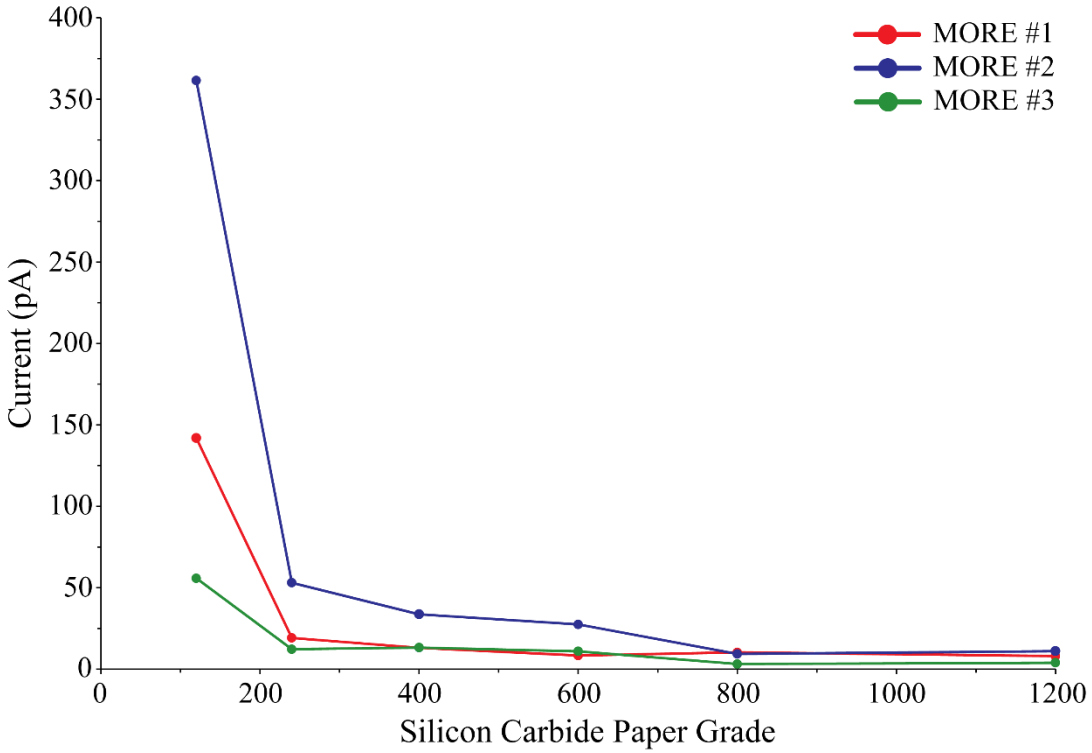

Figure 3.7: Testing the effect of surface finish on current detection in multiple MOREs

The current in a solution of $Ru(bipy)_3^{2+}$ (10 mmol dm^{-3}) and iron (III) chloride (5 mmol dm^{-3}) was measured using MORE constructs 1, 2 or 3 following various rounds of polishing. White light was used to illuminate the solution and the working potential applied was 0.5 V vs SCE. The pH of the solution was 1.83.

3.5.1 Surface finish investigation – Scanning Electron Microscopy

To understand why a rough finish at the MORE tip increased the size of the photocurrent observed, it is useful to consider the configuration of the electrode tip. Scanning electron microscopy (SEM) was used to image the tip of a polished MORE. Initial attempts to image the electrode tip using a scanning electron microscope were unsuccessful due to the large size of the araldite resin layer relative to the gold ring. A considerable amount of charging was observed on the araldite resin which made the gold ring impossible to examine (Figure 3.8).

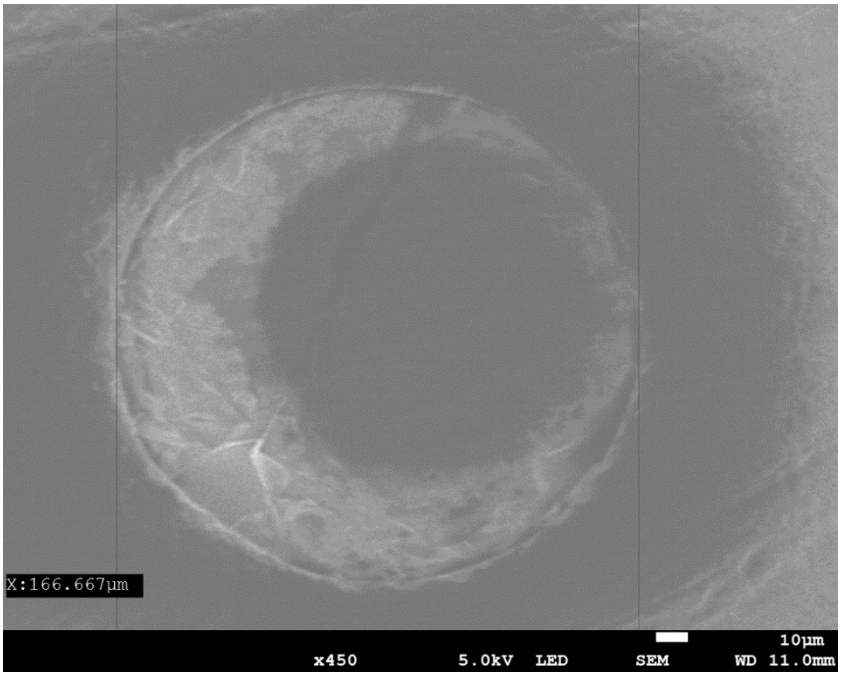

Figure 3.8: SEM image of the tip of a MORE embedded in epoxy showing excessive charging.

To reduce the interference caused by the epoxy resin a gold coated fibre optic was produced under identical conditions as conventional MOREs but lacking the outer araldite insulating layer. Imaging of the uninsulated gold coated fibre optic allowed for the imaging of both the fibre optic and the gold ring (Figure 3.9). Images of the uninsulated fibre also indicated that the thickness of the gold ring was approximately 0.238 µm (Figure 3.9).

Whilst the SEM images of the MORE tip gave an indication of the size of the gold ring present in the MORE, they were not able to explain why the photocurrent varied depending on the surface finish.

A B

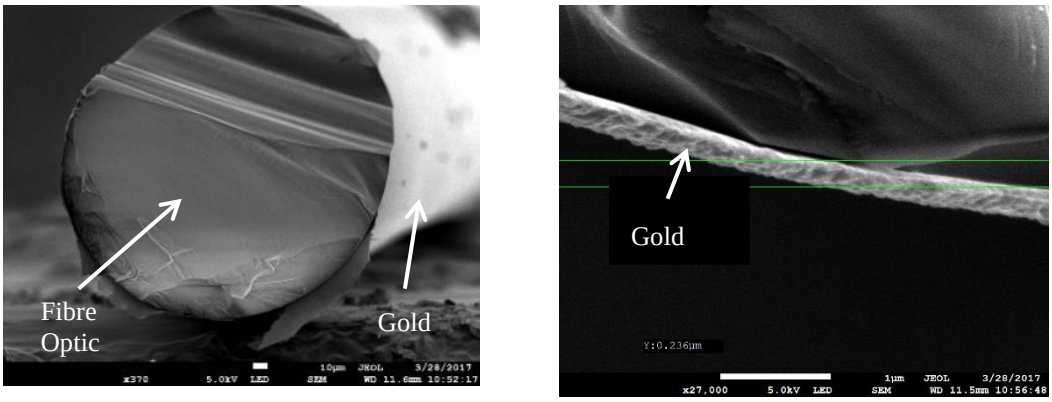

Figure 3.9: SEM image of a gold coated fibre optic

A: SEM image gold coated fibre optic taken with a JEOL field emission scanning electron microscope (JSM-7800F), scale bar of 10µm.
B: SEM image section of gold ring taken with a JEOL field emission scanning electron microscope (JSM-7800F), showing a ring thickness of approximately 0.236µm, scale bar of 10µm.

Images produced by Dr. Baldock, Experimental Officer in Microscopy & Nanofabrication, Department of Chemistry.

3.5.2 Surface finish investigation – Atomic Force Microscopy

To fully understand why the surface finish impacted photocurrent detection an image of the complete MORE tip was needed. High-speed atomic force microscopy (HS-AFM) was used to image the tip of a highly polished complete MORE. HS-AFM is a type of scanning probe microscope, as such a physical probe is used to 'feel' the surface in three dimensions and can form a map of the sample topography. Atomic Force Microscopy is ideal when looking at very small (micrometer) topographical changes on an otherwise flat surface. Although quite forgiving the maximum topography height measurable in a single frame by HS-AFM is 1 µm (personal communication Dr Oliver Payton, Bristol University). Unlike for SEM there is no need for the sample to be conductive or to be imaged in a vacuum. Samples were mounted on a 12.5 mm diameter SEM stub with a 3.2 mm pin 8 mm long and adhered using non-flexible glue with low volatile content, in this instance silver epoxy was used to adhere the sample to the mount. When using HS-AFM the sample must be as flat as possible with the mass and size kept to a minimum as the HS-AFM moves the sample thousands of times a second. Once the sample had been prepared it was imaged and analysed by Dr Oliver Payton at

Bristol University. Figure 3.10 shows the mounted MORE tip during imaging using the HS-AFM, the circular fibre optic is clearly seen at the tip of the cantilever.

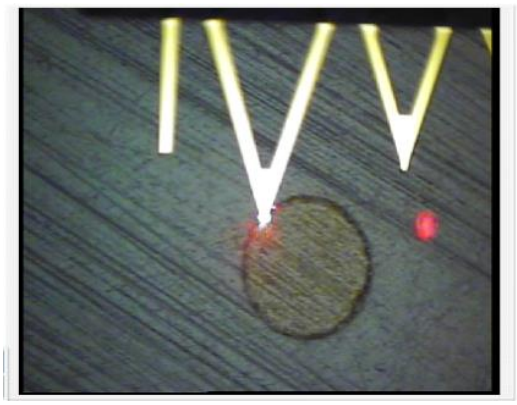

Figure 3.10: Mounted MORE whilst it is being imaged using HS-AFM.

For scale, the longest cantilever is 310 microns from base to tip.

Image produced by Dr Oliver Payton at Bristol University.

When imaged by HS-AFM it was found that the surface roughness was similar between the three components of the MORE suggesting that the polishing tools were leaving the same surface finish regardless of the material making up each of the layers. The similarity in surface finish of the fibre optic, gold coating and araldite insulation meant that when a single HS-AFM image was being analysed it was difficult to determine which layer was being examined. However, at the boundary between the fibre optic and the gold coating it was discovered that the gold coating was rarely level with the top of the fibre optic. The gold coating was often recessed by greater than 4 μm compared to that of the fibre optic (Figure 3.11). It must be noted that the ring seen surrounding the fibre optic in Figure 3.10 is not from the gold coating, it is instead due to the cladding around the optical fibre. The fibre optic cladding is required to enable total internal reflection of light along the fibre and has a different refractive index to that of the core of the fibre optic. Despite the boundaries between the three layers being obscure an attempt to measure the thickness of the gold layer was made. From the HS-AFM images it was estimated that the thickness of the gold layer was 5.15 μm (Figure 3.11), approximately 20 times larger than the size determined using the SEM images. It is likely that it was the size of the fibre optic cladding that was being measured from the AFM images and not the gold ring.

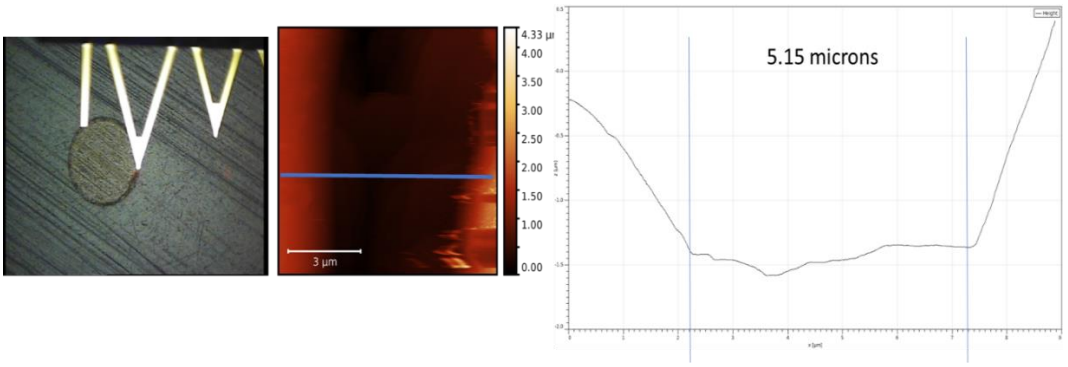

Figure 3.11: AFM data the thickness of the recorded recess.

Image produced and analyzed by Dr Oliver Payton at Bristol University.

Although the MORE sample was highly polished before HS-AFM analysis, the surface was in fact still very rough and given the large height variations the tip was hard to image accurately. The HS-AFM typically measures surface variances of few hundred nano meters, yet some topographical changes found on the MORE sample analyzed were over 4 µm in size.

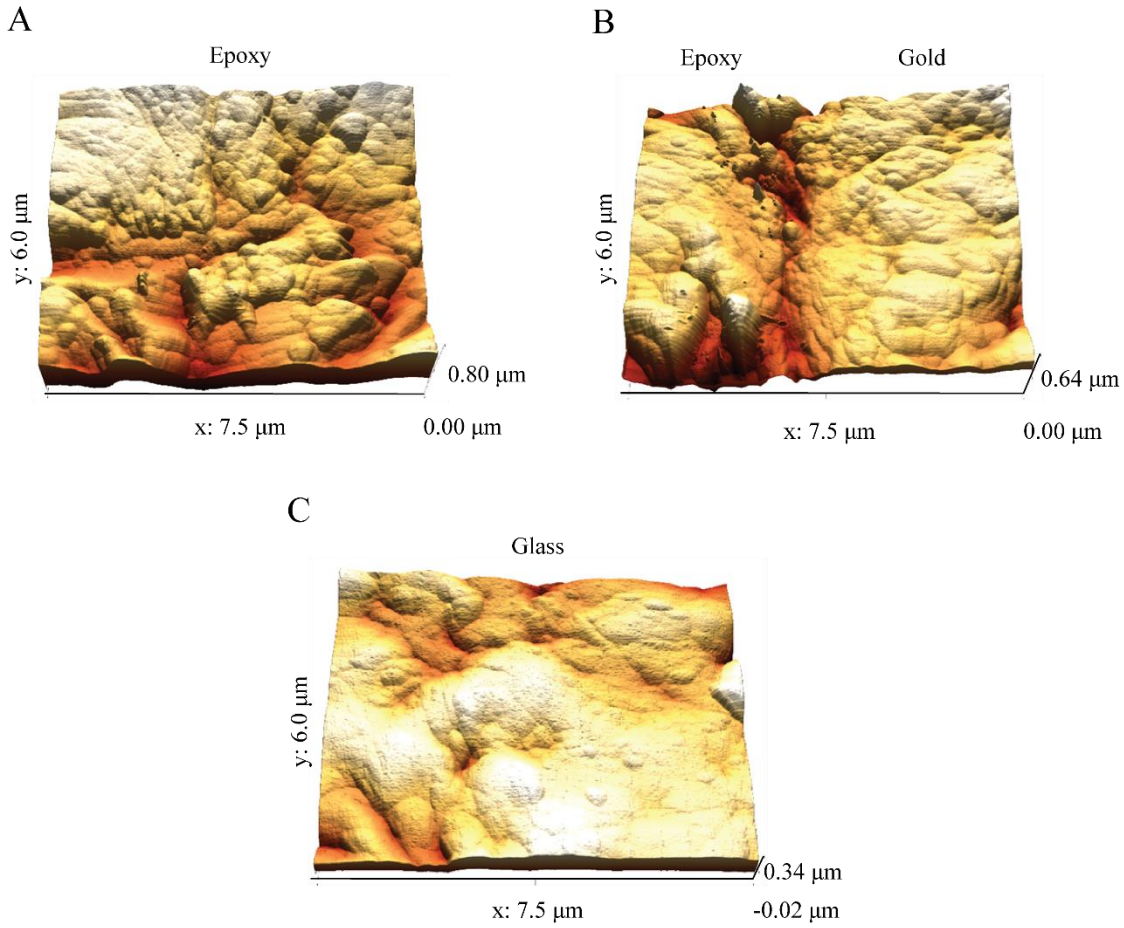

Figure 3.12: High Speed Atomic Force Microscopy on various sections of the tip of a highly polished MORE.

A: AFM image showing the araldite epoxy layer.
B: AFM image showing the araldite epoxy layer on the left and the gold layer on the right.
C: AFM image showing the glass of the fibre optic.

As observed by HS-AFM the flat edge of the gold ring is not level with either the araldite resin or the fibre optic glass, resulting in a recess between the flat plane of the gold and the flat plane of the resin / glass (Figure 3.12). Due to the limitations of the depth to which HS-AFM can measure the depth of the recess observed in this MORE tip could not be determined.

Through the use of both SEM and HS-AFM to observe the tip of a highly polished MORE it would appear that the surface finish is rougher than anticipated. It appears that the gold ring, which is required to detect the photocurrent generated in solution, is set

within a recess below the end point of the fibre optic and the araldite resin insulation (Figure 3.13B). The area within the recess will contain reaction products in solution that are less likely to be photoexcited as the illuminating light will be emitted below the recessed solution (Figure 3.13B). It is possible that a rougher finish at the tip of the MORE would result in scattering of the light emitted at the end of the fibre optic thus generating more photoexcited products that can diffuse to the gold ring, which itself could have a rougher finish and therefore an increased surface area (Figure 3.13C). If more photoexcited products could interact with the gold ring of the MORE a larger photocurrent should be observed.

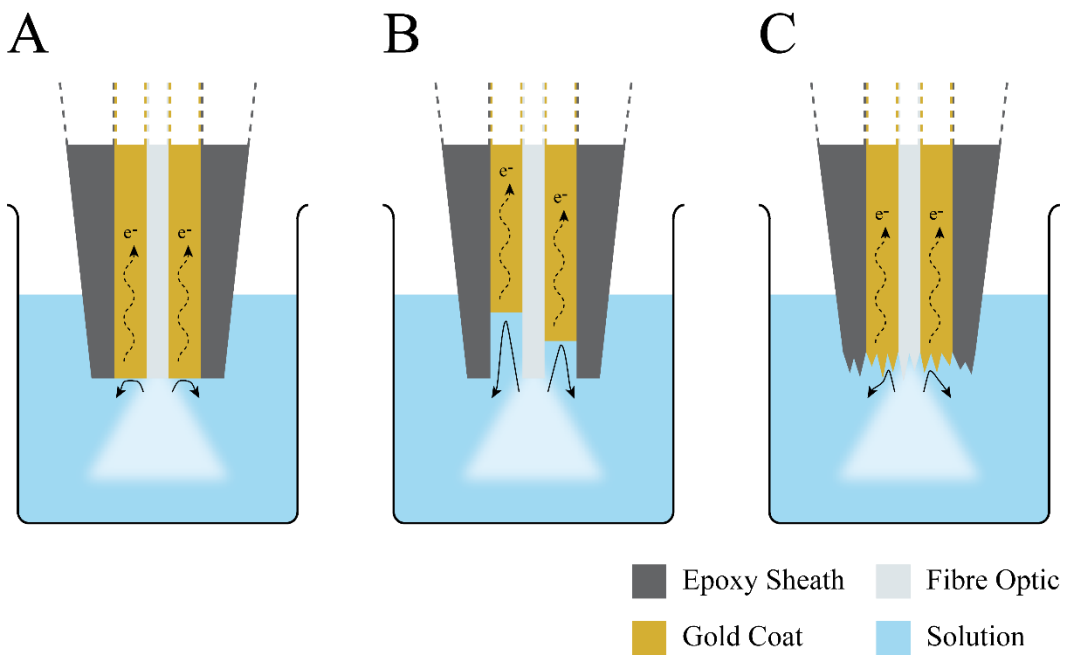

Figure 3.13: Illustration demonstrating how surface finish can impact functionality of the MORE

A: A MORE with a smooth mirror finish.
B: A highly polished MORE with a recess of the gold layer.
C: A roughly polished MORE.

3.5.3 Ion milling

If a reduction in the observed photocurrent when using a highly polished MORE is due to the gold ring sitting in a recess, the removal of the recess should result in an increase in photocurrent detected. To achieve the smoothest finish possible with all three layers of the MORE in the same plane an ion beam was used to polish the tip of the MORE.

An ion beam can be used as an alternative to manually polishing a surface. Ion milling and subsequent scanning probe microscopy were carried out by Dr Alexander Robson of the University of Lancaster Physics department. Before and after ion milling the surface of the MORE was imaged using a MultiMode 8 Scanning Probe microscope. As seen in Figure 3.14B, performing ion milling at the tip of the MORE resulted in a substantially smoother finish compared to that achieved using silicon carbide paper and diamond slurry prior to ion milling (Figure 3.14A). To test whether ion milling had achieved a near-mirror finish with all three materials at the tip of the MORE in the same plane various points around the edge of the electrode were measured using the MultiMode 8 Scanning Probe microscope.

A B

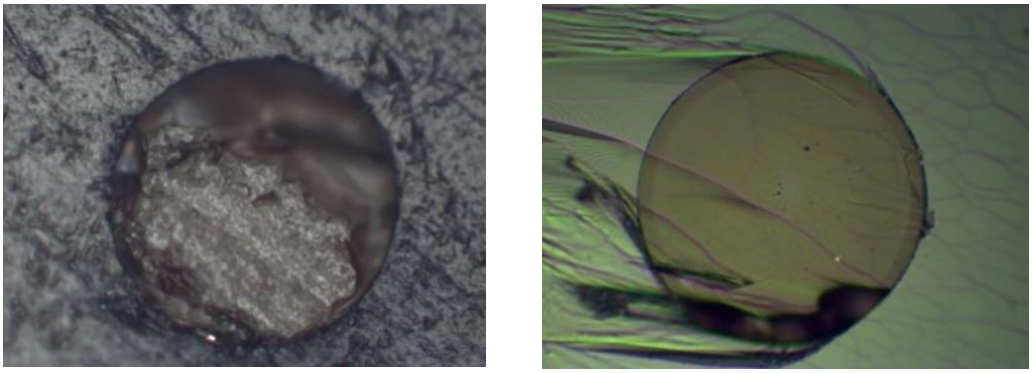

Figure 3.14: The Effects of Ion Milling.

A: Before Ion Beam Milling
B: After Ion Beam Milling

Images produced by Dr Robson of the University of Lancaster Physics department.

A

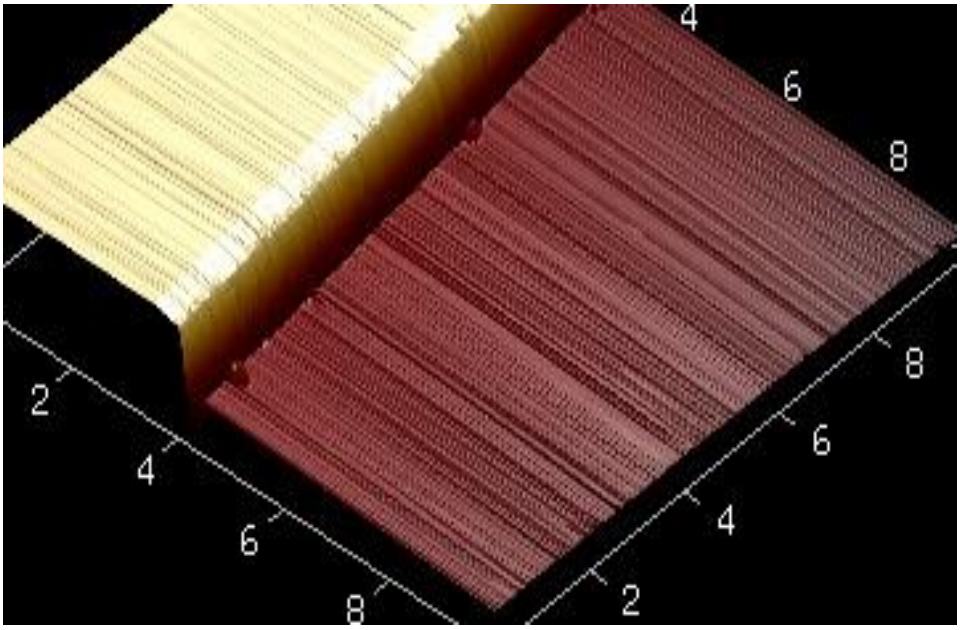

Figure 3.15: Micrograph showing recess feature.

As shown in Figure 3.15 it would appear that ion milling the tip of the MORE resulted in a smooth finish for each individual component of the MORE. However, due to the varying hardness of the MORE components they were still not present in the same plane. A recess was observed at the tip of the MORE with a width of approximately 750 μm. It is possible that this recess indicates where the gold layer of the MORE lies due to gold being particularly susceptible to abrasion. It is therefore possible that the width of the recess could be used as an estimate for the thickness of the gold ring.

Fredrich Mohs, a mineralogist devised a scale of hardness based on the ability of one mineral to scratch another: Mohs Scale of Hardness (Frost, 2006). Talc is regarded as the softest material as it can be scratched by all other materials and thus has a Mohs hardness rating of one, diamond is the hardest material with an Mohs hardness rating of 10 (Frost, 2006). The absolute hardness for the materials at the tip of the MORE based on the Mohs scale are as follows; silica 7 (glass of fibre optic), gold 2.5 and resin 6.5. Whilst the silica and resin are comparable in terms of their hardness rating, gold has a much lower rating and would therefore be more susceptible to erosion by the polishing process. It is likely that the use of silica carbonate paper followed by diamond slurry has a much stronger impact on the gold layer than on the silica or the resin of the MORE, resulting in increased erosion of the gold ring. Similar findings have been reported by (Lee and Bard, 2002) when trying to polish different components of differing scales of hardness in the same plane.

3.5.4 Impact of diamond slurry on the surface finish

The original construction of the MORE required that the final polish be carried out using diamond slurry paste. It has been noted previously that diamond polishing paste is not readily removed from surfaces following extensive washing (Dr R Wilbraham, personal communication). Despite repeatedly washing an electrode that had been polished using a diamond slurry paste with ethanol, silicon particles could still be observed via SEM imagery on the surface of the electrode (Figure 3.16, personal communication Dr Wilbraham).

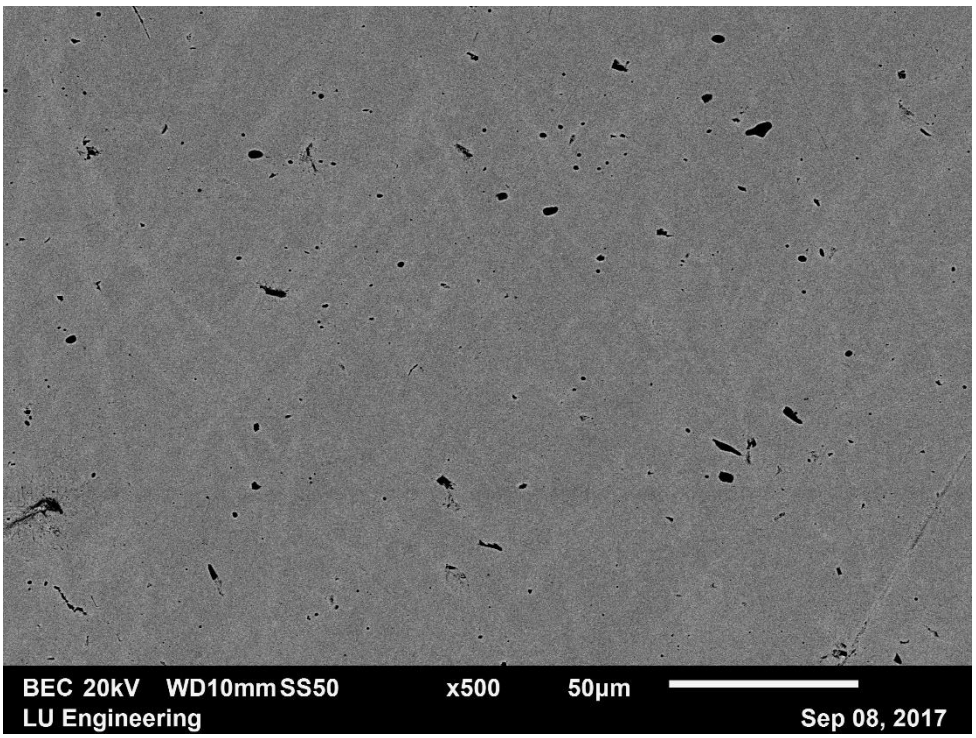

Figure 3.16 SEM image of an electrode that had been polished with diamond slurry paste.

A compositional image that shows all the silicon particles (left over diamond paste) in black versus the grey of the steel despite repeated ethanol washes following polishing.

Image provided by Dr Wilbraham, Engineering Department, Lancaster University.

Due to the difficulty in completely removing the diamond polishing paste, coupled with the presence of a recess at the tip of the MORE, it is likely that during the polishing process the recess became clogged with the polishing paste. Clogging of the recess in

which the gold ring resided would greatly reduce the amount of gold available as a conducting layer. The production of a recess and its potential clogging with diamond slurry paste may explain why highly polished MOREs cease to be functional; the products of photoexcitation would not have access to the conducting layer therefore no photocurrent would be generated. With the particle size of the silicon-carbide papers being much larger than that of the diamond slurry, clogging of the recess with silicon-carbide particles would be unlikely. As shown in Figure 3.7, MOREs that had only been exposed to the first round of silicon carbide polishing paper gave the strongest photocurrent and there was a negative correlation between the grade of silicon carbide polishing paper used and photocurrent magnitude detected. MOREs that had been finished with a diamond slurry paste polish failed to detect any photocurrent regardless of whether the tip had been washed in ethanol and distilled water or not (Figure 3.5). It was therefore deemed unnecessary to highly polish the tip of the MORE and all subsequent experiments were carried out using MOREs with a 'rough' polished tip.

3.5.5 Calculating the thickness of the gold ring of the MORE following different rounds of polishing

Having discovered that increased degrees of polishing at the tip of the MORE appears to result in a recess forming in the gold layer, it was predicted that the surface area, i.e. the thickness of the gold ring, reduced with increased grades of silicon carbide paper. Using the same methods outlined in section 3.2**Error! Reference source not found.** the thickness of the gold ring was calculated electrochemically for an individual MORE polished with different grades of silicon carbide polishing papers.

A MORE was polished with the roughest grade of silicon carbide paper (60 grade). The thickness of the gold ring was determined experimentally by recording the diffusion limited current for different concentrations of potassium hexacyanoferrate (III) (3, 5, 7 and 10 mmol dm^{-3}) in the presence of potassium chloride (0.1 mol dm^{-3}). From the diffusion limited current results, the characteristic length (l_0) of the gold ring was determined using Equation 3.4. Following calculation of l_0 the thickness of the gold ring was calculated using Equation 3.1. This process was repeated with same MORE polished with silicon carbide paper of grades 400, 800 and 1200. The thickness of the gold ring was calculated between each polishing step resulting in four different gold ring thickness calculations for the same MORE after each grade of silicon carbide paper used.

Figure 3.17 shows the averaged results of electrochemically sizing the thickness of the gold ring for three different MOREs. The calculated thickness of the gold ring decreased as a finer grade of silicon carbide polishing paper was used to polish the MORE (Figure 3.17). The same MORE was used to determine the gold ring thickness after each

polishing step therefore, it is unlikely that the actual thickness of the gold ring had changed. Instead, it is likely that it is the exposed surface area of the gold conductive layer that is being calculated and with each polishing step the amount of gold available to the electrolyte is reduced.

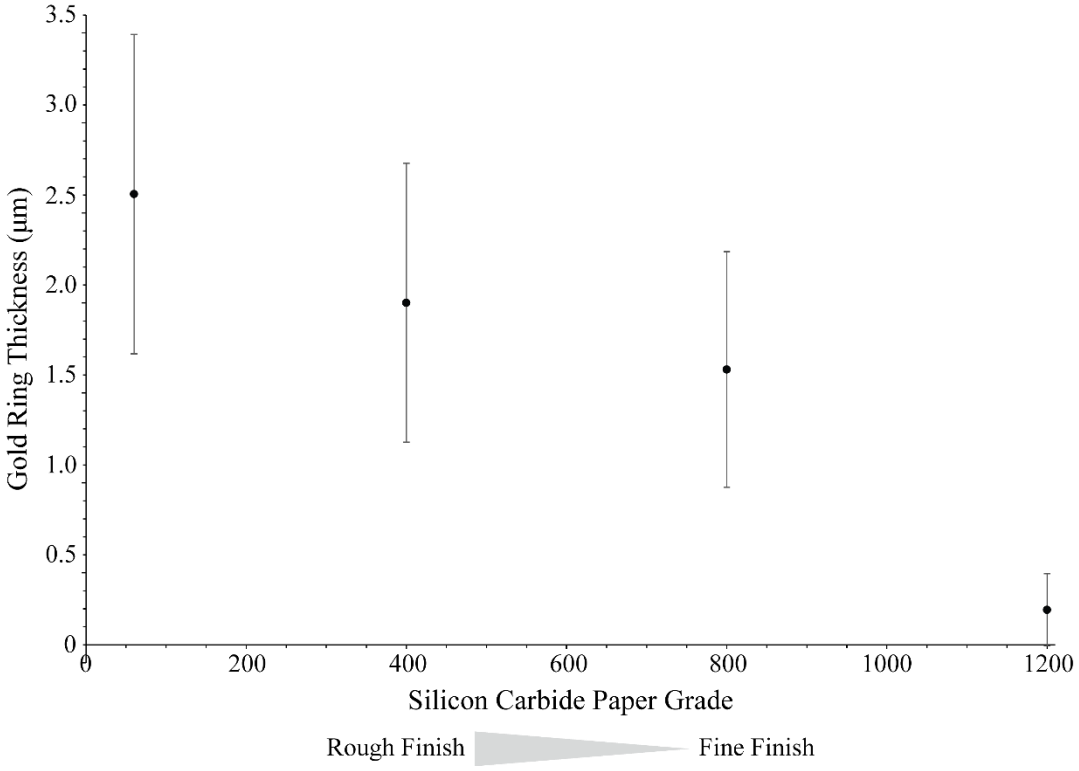

Figure 3.17: Electrochemical sizing of the gold ring of the MORE following polishing with different grades of silicon carbide paper

The current in a solution of $Ru(bipy)_3^{2+}$ (10 mmol dm^{-3}) and iron (III) chloride (5 mmol dm^{-3}) was measured using three individual MOREs following various rounds of polishing. White light was used to illuminate the solution and a working potential of 0.5 V vs SCE was applied. The pH of of the solution was 1.83.

3.6 Determination of the light intensity

The magnitude of photocurrent detected by the MORE is dependent on both the intensity of the light emitted by the MORE and the amount of light absorbed by the sensitizer. A higher intensity of light emitted by the MORE should result in a larger number of photoexcited sensitizer molecules generated thus resulting in a larger magnitude of photocurrent. Considering the impact of light intensity on photocurrent

generation it is useful to determine the intensity of the light entering the system. Whilst assembling MOREs small variations in the light coupling through the ball lens will occur which will influence the intensity of light emitted. Therefore, the light intensity of each MORE used must be measured. Measuring the emitted light intensity was achieved using a Kipp and Zonen CA-2 thermopile and meteon irradiance meter. The fibre optic light source (S/N 3240-A101OB, Photon Technology International, Canada) was left on for 30 minutes before any measurements were taken and the thermopile was left to cool down for 15 minutes between each measurement. Results were recorded for the two MOREs that were used in the majority of the experiments carried out in this thesis. Emitted intensities were measured using white light and light at 350 and 410 nm; these wavelengths were chosen due to results presented in later chapters.

Initially the intensity of white light emitted by the light source alone and after passing through MORE 1 and MORE 4 was measured. It was found that the intensity of light emitted by MORE 1 was ≈270 times less intense than that of the light source alone (3,514 µV to 13 µV) and MORE 4 emitted ≈293 times less intense light than that of the light source (3,514 µV to 12 µV) (Table 3.1). The intensity of light emitted by the light source was then measured for light at 350 and 410 nm. A 31.38 fold reduction in intensity (3,514 µV to 112 µV) and 23.27 fold reduction (3,514 µV to 151 µV) was measured for the light source alone at 350 and 410 nm respectively (Table 3.1). When the intensity of light passing through the MOREs was measured at 350 and 410 nm it was found that the emitted light was below the limit of detection for the thermophile. However, the intensity of light emitted by the MOREs at 350 and 410 nm wavelengths could be calculated based on the observed fold change in intensity of white light when it passed through each MORE. It was therefore calculated that the intensity of light emitted by MORE 1 at 350 nm would be 0.4143 µV and 0.5586 µV at 410 nm (Table 3.1). The light emitted by MORE 4 at 350 nm was calculated to be 0.3825 µV and 0.5157 µV at 410 nm (Table 3.1).

Wavelength (nm)	Light Source Light Intensity (µV) (Measured)	MORE 1 Light Intensity (µV) (Measured or *Calculated)*	MORE 4 Light Intensity (µV) (Measured or *Calculated)*
White	3,514	13	12
350	112	*0.4143*	*0.3825*
410	151	*0.5586*	*0.5157*

Table 3.1: Recorded or calculated light intensity emitted by the light source, MORE 1 and MORE 4.

To use the mathematical model the intensity of light emitted by the MORE needs to be in units of mole photon flux (mol s^{-1} m^{-2}). The results obtained by the thermophile were converted from µV to Joules per meter squared (Jm^{-2}) via a conversion factor (40.75) specifically calibrated for the thermophile used to generate the results above. The energy per mole was calculated for each wavelength measured using Equation 3.5 (Table 3.2). The mole photon flux was then calculated by dividing the light intensity results (in Jm^{-2}) by the energy per mole specific for each wavelength to identify the intensity of light emitted by each MORE in the units required to be utilised in the mathematical model (mol s^{-1} m^{-2}). The results for each MORE at 350 and 410 nm wavelengths are summarised in Table 3.2.

	Wavelength (nm)	Intensity of Light emitted (μV) (calculated)	Intensity of Light emitted (Jm^{-2})	Energy per Mole ($Jmol^{-1}$)	Mole Photon Flux (mol s^{-1} m^{-2})
MORE 1	350	0.4143	16.88	3.42×10^5	4.94×10^{-5}
MORE 1	410	0.5586	22.76	2.92×10^5	7.8×10^{-5}
MORE 4	350	0.3825	15.59	3.42×10^5	4.56×10^{-5}
MORE 4	410	0.5157	21.01	2.92×10^5	7.2×10^{-5}

Table 3.2: Conversion of emitted light intensity for MORE 1 and MORE 4 from μV to mol s^{-1} m^{-2}.

$$E = \frac{hc}{\lambda} N_A$$

Equation 3.5: Equation for photon energy.
Modified to give results in J mol^{-1}.

Where:

E	Energy (Js^{-1})
h	Planck's Constant $(6.63 \times 10^{-34} J \cdot s)$
c	Speed of light $(3 \times 10^8\ ms^{-1})$
$\boldsymbol{\lambda}$	Wavelength (nm)
$\boldsymbol{N_A}$	Avagadros Constant $(6.02 \times 10^{23}\ mole^{-1})$

3.7 Summary

Polishing the tip of the MORE without resulting in a recess forming at the gold layer of the MORE has proven difficult. The three materials used to construct the tip of the MORE all have different levels of hardness and so when polished together the materials will be removed at different rates.

It has been demonstrated that a roughly finished MORE generated a larger photocurrent than the same MORE that had undergone additional rounds of polishing (Figure 3.6). Further to this it would appear that polishing with finer grades of silicon carbide paper reduces the amount of gold available to the electroactive species (Figure 3.17). Based on the SEM and HS-AFM imaging it would appear that the reduction in photocurrent observed from a highly polished MORE is the result of excessive erosion of the gold layer that is either then clogged with diamond slurry or is too deep for photoexcited products to access the conductive gold surface before the photoexcited electron returns to its original state. Therefore, all subsequent experiments were carried out on MOREs that had a rough surface finish.

3.8 Determining the surrogate parameters

Whilst the aims of this project are to detect a photocurrent produced by the radioactive elements uranium, neptunium and plutonium, surrogates will be used in the first instance. Depleted uranium will be used as a surrogate for uranium, vanadium will be used as a surrogate for neptunium and cerium will be used as a surrogate for plutonium. The use of surrogates will allow for the development of experimental technique and experience before moving on to radioactive samples. Before photo-electrochemical experiments with surrogates can be performed, several parameters must first be obtained.

The diffusion coefficient is a physical constant dependant on the size of a molecule and is indicative of its diffusion mobility. When predicting the concentration of target analyte using the mathematical model introduced in Literature Review, the diffusion coefficient of each analyte is required. No literature value for the diffusion coefficient could be found for either vanadium or cerium, therefore these would need to be experimentally determined. To ensure the diffusion coefficient values obtained for vanadium and cerium were accurate the same experiment was carried out using potassium hexacyanoferrate, the obtained value of which was compared with that well documented in the literature (Bard and Faulkner, 2001).

3.8.1 Diffusion coefficients for surrogates

The diffusion coefficient of an electroactive species can be determined with the use of a rotating disc electrode (RDE) and the Levich equation (Bard and Faulkner, 2001) (Equation 3.6). To calculate the diffusion coefficient the following must be identified: the diffusion limited current, the area of the electrode, the bulk concentration of the electroactive species, the viscosity of the solution and the rotation speed of the electrode.

Recording the diffusion-limited current of an analyte of interest at a known concentration over a range of rotation speeds allows for the calculation of the diffusion coefficient via the slope of the graph: $\frac{i_{diff}}{1.555nFC_{bulk}\,v^{-1/6}}\,VS.\,\omega^{1/2}$ which is equal to $D^{2/3}$ where D is expressed in centimetre squared per second units ($cm^2\,s^{-1}$).

$$i_{diff} = 1.555nFAC_{bulk}\,D^{2/3}\,v^{-1/6}\,\omega^{1/2}$$

Equation 3.6

Where:

i_{diff}	Diffusion limited current (A)
n	Number of electrons exchanged during redox
F	Faraday constant (96484.5 C mol^{-1})
A	Area of the electrode (cm^2)
C_{bulk}	Bulk concentration of the electroactive species (mol cm^{-3})
D	Diffusion coefficient of the electroactive species ($cm^2\,s^{-1}$)
v	Viscosity of the solution ($cm^2\,s^{-1}$)
ω	the rotation speed of the electrode (Hz (s^{-1}))

3.8.1.1 Diffusion coefficient of potassium hexacyanoferrate

Before calculating the diffusion coefficient of vanadium and cerium the diffusion coefficient of potassium hexacyanoferrate was calculated and compared to the published value (Bard and Faulkner, 2001). The diffusion limited current was recorded in a solution of potassium hexacyanoferrate (10 mmol dm^{-3}) using a rotating disc electrode with a surface area (A) of 0.1963 cm^2. Rotation speeds used were 200, 400, 600, 800, 1000, 1400 1800 and 2200 rotations per minute (RPM). The viscosity (v) of

the solution was taken to be that of water at 20°C: 10^{-2} cm^2 s^{-1}. The electrochemical process involved the transfer of one electron, therefore n=1.

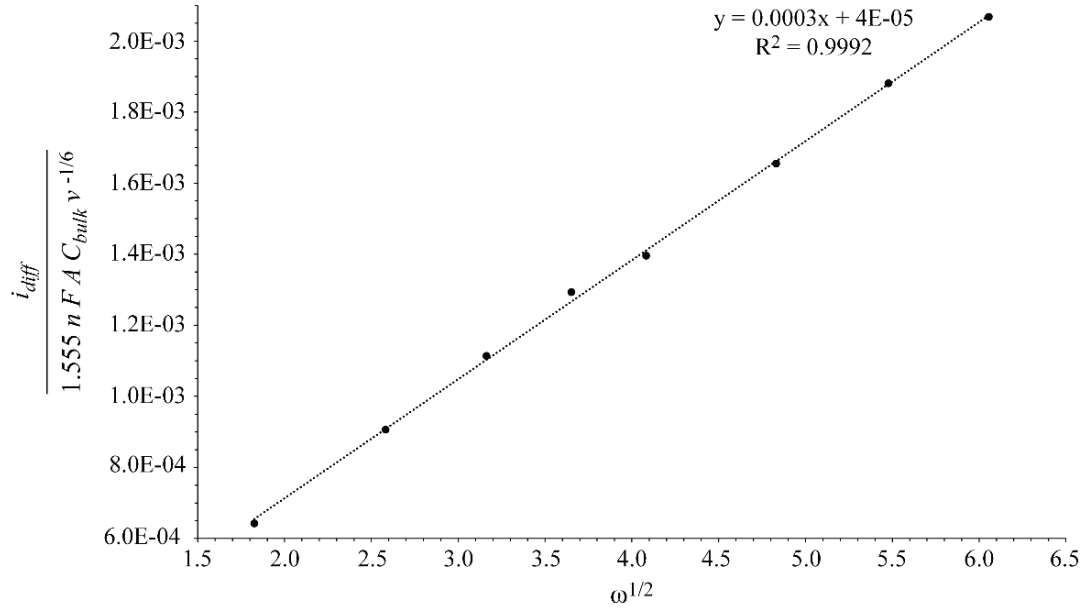

Figure 3.18: Experimental determination of the diffusion coefficient of potassium hexacyanoferrate.

Following the measurement of the diffusion limited current the diffusion coefficient for potassium hexacyanoferrate was calculated to be 6.1×10^{-6} cm^2 s^{-1}. The standard literature value for the diffusion coefficient for potassium hexacyanoferrate is 7.6×10^{-6} cm^2 s^{-1}. (Bard and Faulkner, 2001) our observed value of $6.1 \times 10^{-6} cm^2$ s^{-1} is comparable to the standard literature value.

Having found that the diffusion coefficient for potassium hexacyanoferrate determined was comparable to the published standard gave confidence that the calculated diffusion coefficients for each surrogate would be accurate.

3.8.1.2 Diffusion coefficient of vanadium (IV) oxide sulphate hydrate

The procedure used to determine the diffusion coefficient of potassium hexacyanoferrate was repeated with vanadium (IV) oxide sulphate hydrate (10 mmol dm^{-3}) used in place of the potassium hexacyanoferrate. The current was recorded at each of the following rotation speeds; 100, 200, 300, 400, 500, 600, 700, 800, 900, 1000, 1200, 1400, 1800 and 1400 RPM. To calculate the diffusion coefficient for vanadium

(IV) oxide sulphate hydrate the slope of the line of best fit was determined (Figure 3.19). Though not as linear as that seen for potassium hexacyanoferrate (Figure 3.18) a positive correlation was still observed (Figure 3.19). The diffusion coefficient for vanadium (IV) oxide sulphate hydrate was calculated as 3.3×10^{-8} cm^2 s^{-1}.

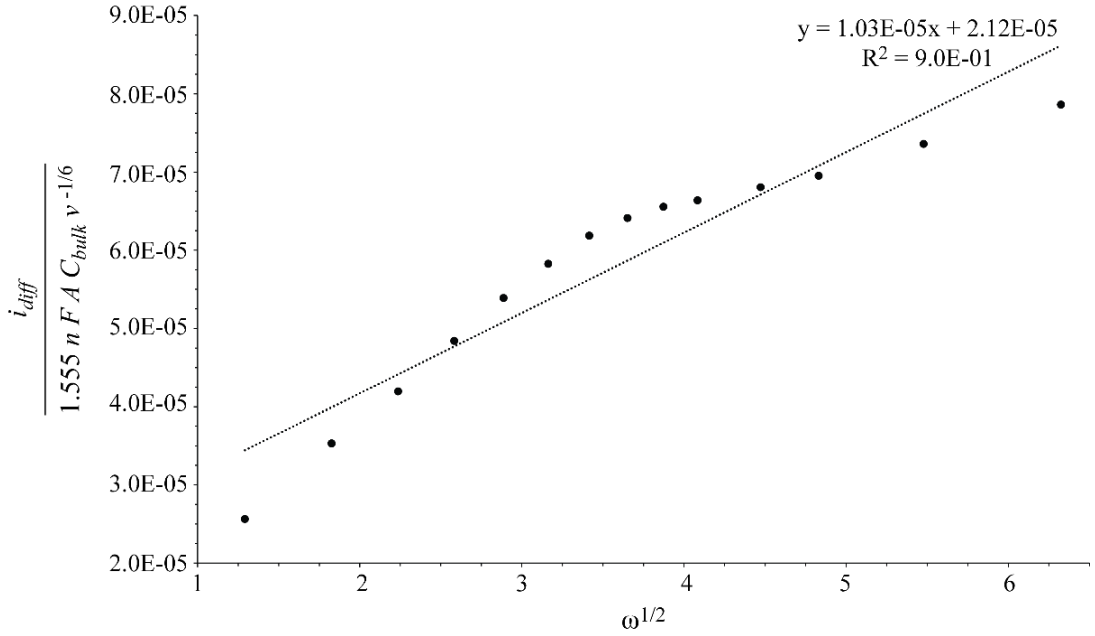

Figure 3.19: Experimental determination of the diffusion coefficient of vanadium (IV) oxide sulphate hydrate.

3.8.1.3 Diffusion coefficient of cerium (III) chloride

The procedure to determine the diffusion coefficient of potassium hexacyanoferrate was again repeated, this time substituting cerium (III) chloride (10 mmol dm^{-3}) in place of potassium hexacyanoferrate. The current generated by cerium (III) chloride was measured using a rotating electrode at the following rotation speeds; 100, 200, 300, 400, 500, 600, 700, 800, 900, 1000, 1200, 1400, 1800 and 1400 RPM. The diffusion coefficient for cerium (III) chloride was subsequently calculated and found it to be 3.36×10^{-7} cm^2 s^{-1}. This is comparable with literature values of 0.5×10^{-6} cm^2 s^{-1} (Leung *et al.*, 2011) and 0.28×10^{-7} cm^2 s^{-1}, 3.43×10^{-7} cm^2 s^{-1} (Baker *et al.*, 2017).

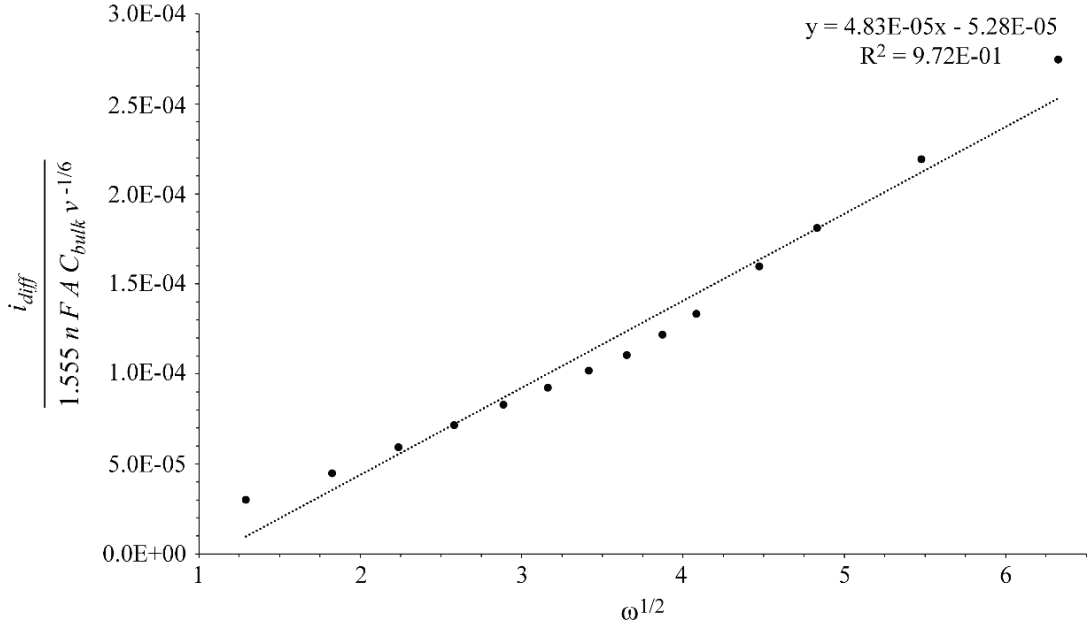

Figure 3.20: Experimental determination of the diffusion coefficient of cerium (III) chloride.

3.9 Absorbance Spectrum of surrogates

The absorbance spectrum for each surrogate was obtained using a spectrophotometer (Spectro-115U, Gamry, USA) with data being analysed in Gamry Echem Analyst software. Absorbance was recorded at wavelengths between 200 and 800 nm (unless otherwise specified) at 0.4 nm increments. The absorbance spectrum was measured at various concentrations (5, 10, 15, 20, 50 and 75 mmol dm^{-3}) allowing the Beer Lambert law to be observed. As seen in Figure 3.22 a linear increase in the maximum absorbance was observed as the analyte concentration increased. Using the Beer Lambert law, the extinction coefficient (ε) was calculated at each wavelength using **Equation 3.7**, where the path optical length is l and relates to the cuvette used to gather the absorbance spectrum (1 cm in this instance), and c is the concentration of the attenuating species.

$$A = \varepsilon l c$$

Equation 3.7

Where:

A	Absorbance
ε	Extinction coefficient
l	Path length
c	Concentration

The absorbance spectrum of a substance should show at least one absorbance peak which will determine if photoexcitation is possible. Ideally any excitation peaks would be above 350 nm as any peaks below this would not be identified due to attenuation of light by materials used to construct the MORE. The transmittance properties of the fibre optic used to manufacture the MORE demonstrates that light attenuation starts to increase at wavelengths lower than 300 nm (**Figure 2.2**). The ball lens used to focus the light to the fibre optic has a wavelength transmittance range of 350-2200 nm (Edmund Optics). The transmittance percentage of the optical glue used to hold the ball lens in place starts to fall below 350 nm (Figure 3.21).

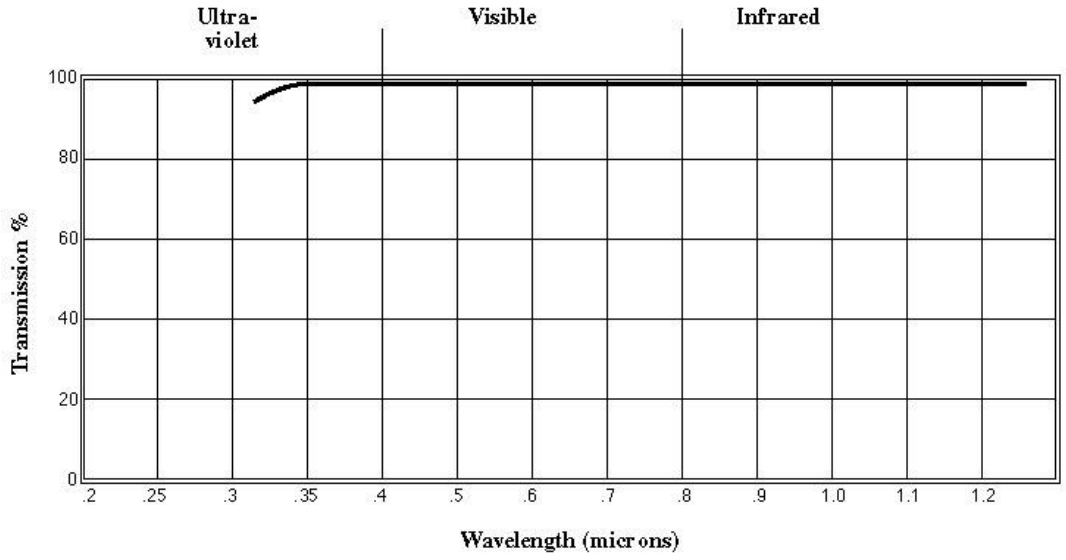

Figure 3.21 Spectral Transmission of NOA 88 Optical Glue (Norland Products).

3.9.1 Measuring the absorbance spectrum for Vanadium (IV) oxide sulphate hydrate

A vanadium (IV) oxide sulphate hydrate solution (75 mmol dm^{-3}) was prepared in water with a pH of 1.76 (buffered with sulfuric acid) and the absorbance spectrum measured between 200 and 850 nm. The vanadium (IV) oxide sulphate hydrate solution was diluted to ~ 50 mmol dm^{-3} and the absorbance spectrum measured again. The dilution and recording of the absorbance spectrum for vanadium (IV) oxide sulphate hydrate solution was repeated until the absorbance spectrum for each required concentration had been collected (75, 50, 20, 15, 10 and 5 mmol dm^{-3}). The absorbance spectrum for each concentration of vanadium oxide sulphate hydrate can be seen in Figure 3.22 A. As explained above the peaks observed below 350 nm were discounted as they are mostly due to absorbance of light from components of the MORE. The most characteristic absorption band for vanadium (IV) oxide sulphate hydrate was observed at 770 nm (Figure 3.22A). Using the absorbance peak and Equation 3.7 an extinction coefficient of 13.28 L mol^{-1} cm^{-1} was calculated for vanadium (IV) oxide sulphate hydrate. This suggests that if a photocurrent is generated by vanadium (IV) oxide sulphate hydrate, photoexcitation would occur at a wavelength of 770 nm. The absorption peak at 770 nm is due to the transition from the E_2 ground state to the E_1 excited state (Gruen and Mcbeth, 1962).

A

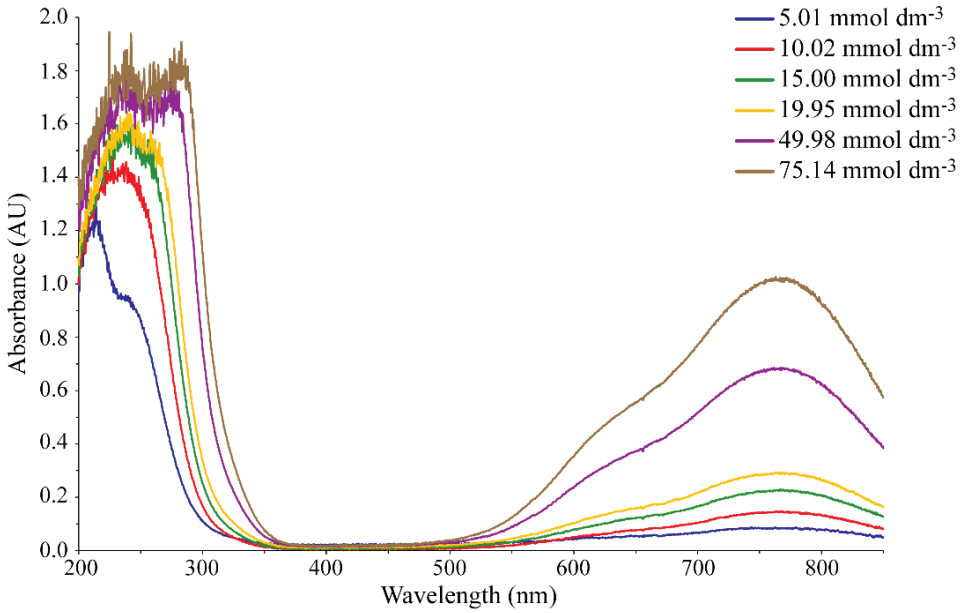

B

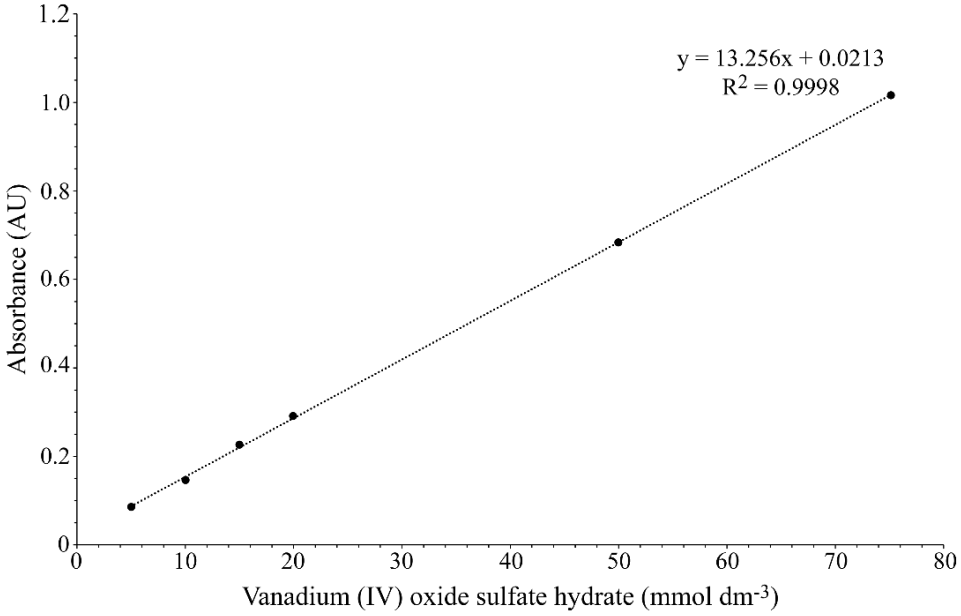

Figure 3.22: Absorbance spectrum of vanadium (IV) oxide sulphate hydrate at various concentrations

A: Absorbance spectrum for various concentrations of vanadium (IV) oxide sulphate hydrate across a range of wavelengths.
B: The absorbance against concentration for vanadium (IV) oxide sulphate hydrate at a wavelength of 770 nm.

Figure 3.22A shows the absorbance measured at 770 nm at each concentration of vanadium (IV) oxide sulphate hydrate tested. A linear increase between concentration and absorbance was observed with the resulting slope producing an R^2 of 0.9992. The linear correlation seen in Figure 3.22B is in keeping with the Beer Lambert law and therefore validates these results.

3.9.2 Measuring the absorbance spectrum for cerium (III) chloride

A cerium (III) chloride solution (75 mmol dm^{-3}) was prepared in water with a pH of 1.82 (adjusted with hydrochloric acid) and the absorbance spectrum measured. The cerium (III) chloride solution was diluted to a concentration of 50 mmol dm^{-3} and the absorbance spectrum collected once again. The dilution and recording of the absorbance spectrum for cerium (III) chloride solution was repeated until the absorbance spectrum for each required concentration had been measured (75, 50, 20, 15, 10 and 5 mmol dm^{-3}). Figure 3.23 shows that the maximum absorbance peak for cerium (III) chloride was observed at 297 nm. Plotting the maximum absorbance value observed against cerium (III) chloride concentration resulted in an extinction coefficient of 10.26 L mol^{-1} cm^{-1} calculated using Equation 3.7.

Figure 3.23B shows the absorbance measured at 297 nm for each concentration of cerium (III) chloride measured. A linear increase of absorbance with concentration was observed and the line of best fit resulted in a slope with R^2 of 0.9971. This confirms the Beer Lambert law and validates our results.

The absorbance of cerium (III) chloride at 297 nm may pose issues regarding the generation and detection of a photocurrent by the MORE. As discussed above, absorbance of light below 350nm is increased by the materials of the MORE yet cerium (III) chloride would require a wavelength of 297 nm to generate a photocurrent.

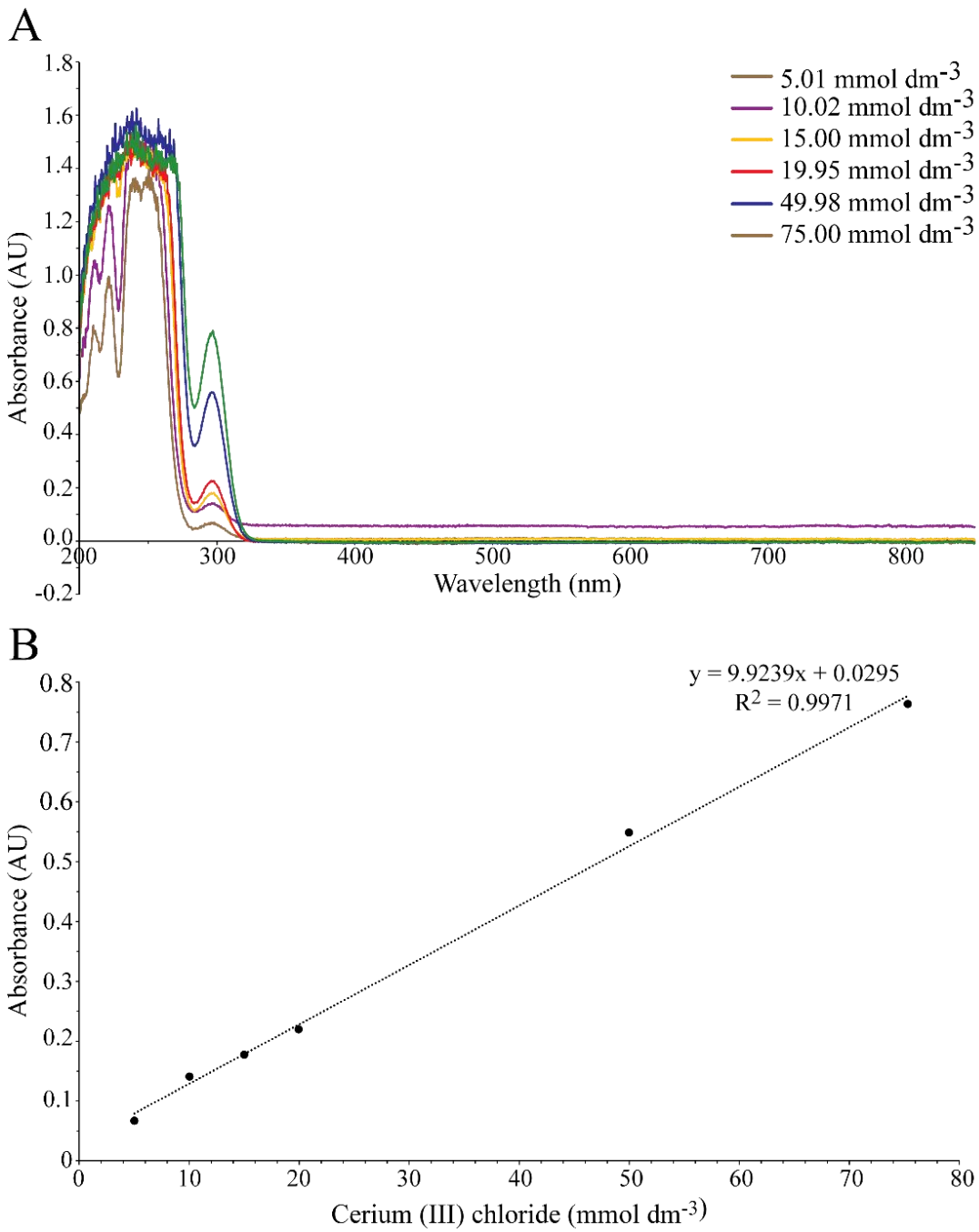

Figure 3.23: Absorbance spectrum for various concentrations of cerium (III) chloride.

A: Absorbance spectrum for various concentrations of cerium (III) chloride across a range of wavelengths.
B: The absorbance against concentration for cerium (III) chloride at a wavelength of 297 nm.

3.10 Conclusion

This Chapter has investigated the ability of the MORE to function as both an electrode and a photoelectrochemical sensor. Constructed MOREs were tested for their ability to generate and produce a photocurrent from tris(2,2'-bipyridyl)dichlororuthenium (II) hexahydrate ($Ru(bipy)_3^{2+}$) (10 mmol dm^{-3}) serving as the sensitizer, and iron (III) chloride (5 mmol dm^{-3}) serving as the acceptor, a system that has previously been used to test for the presence of a photocurrent (Andrieux, Boxall and O'Hare, 2006a). Photocurrents with a magnitude of ~80 pA were successfully generated and measured in this system using the fabricated MOREs. A drift removal procedure was also introduced which greatly improved the accuracy of photocurrents where large drifts were observed.

The surface finish appears to have a strong impact on the functionality of the MORE. The smoother a MORE was polished, the weaker the photocurrent detected. Using SEM and HS-AFM it was found that increased polishing of the MORE resulted in excessive erosion of the conductive gold layer of the MORE. It is possible that the reduction in the available surface area of the gold layer results in loss of function of highly polished MOREs. The mathematical model set out in (Andrieux, Boxall and O'Hare, 2006a) assumes that a cylindrical beam of light is emitted from the end of the MORE and that all three layers of the tip are in the same plane, a result of finely polishing to give a near-mirror finish. However, having discovered that polishing the tip to a smooth finish impinges photocurrent detection the following experiments used MOREs that had been polished to a rough finish to increase the magnitude of the photocurrent detected. When using Andrieux's mathematical model (2006), accounts will have to be made for the fact that the surface finish is not near-mirror finish and the potential impact this will have on the emittance of light from the end of the fibre optic.

The mathematical model used to calculate the behaviour of the MORE (Andrieux, Boxall and O'Hare, 2006a) also requires that the thickness of the conductive layer is known i.e. the area exposed to the electrochemical solution. As part of the investigation into why the surface finish was impacting the photocurrent detected the thickness of the gold layer was measured using SEM and HS-AFM imaging and electrochemical experimentation. Both imaging processes struggled to accurately capture the surface of the MORE tip, however predictions were made regarding the thickness of the gold ring. Large variances were present in the measured thickness of the gold ring between the SEM and HS-AFM images. The ring thickness determined by SEM was ~0.238 µm (3.5.1) compared to ~5.15 µm found using HS-AFM (3.5.2). Electrochemical experimentation estimated the gold ring thickness to be ~2.5 µm for the roughest finish

that then decreased to ~0.19 μm with smoothest finish. Further study will need to be carried out to accurately measure the thickness of the gold ring to increase the accuracy of the mathematical model (Andrieux, Boxall and O'Hare, 2006a).

The initial parameters required for photocurrent generation by the surrogates vanadium and cerium were also determined. The diffusion coefficient was established for each surrogate which is needed to use the mathematical model devised to explain the behaviour of the MORE (Andrieux 2006). The absorbance spectrum was also measured for each surrogate and indicated the illumination region that should result in photoexcited ions. Having established these parameters photocurrent generation and detection experiments of the surrogates using the MORE were carried out and the results are presented later in this thesis.

4 Uranyl

4.1 Introduction

This chapter covers a range of experiments designed to test whether the MORE can be used to generate a photocurrent from a solution of uranyl ions. If successful, the optimal parameters such as the illumination wavelength, operating working potential and scavenger concentration will be investigated. Both the limits of detection and kinetics of the reaction will also be studied.

4.2 Cyclic Voltammetry

Uranyl in the form of $UO_2(OOCH_3)_2$ (99%) at a concentration of 42 mmol dm^{-3} dissolved in 5% nitric acid with a pH of 0.20 was used to perform the following experiments at room temperature.

Cyclic voltammetry was performed to identify regions of oxygen and hydrogen evolution along with any electrochemical processes associated with uranyl in dark conditions. To achieve this, the working electrode potential was cycled between uranyl in nitric acid solvent stability limits Figure 4.1. shows a typical scan of such an experiment recorded at the MORE and several electrochemical processes can be observed. During the forward scan two reduction peaks were observed at approximately 0.4 and 0.55 V. The peak at 0.4 V may be attributed to the reduction of uranyl to UO_2^+ which occurs at 0.303 V vs SCE (Weik and Weik, 2000). The peak at 0.55 V may be attributed to the reduction of uranyl to U^{4+} which occurs at 0.568 V vs SCE (Weik and Weik, 2000). The backward scan identified two oxidation peaks at 0.7 and 0.4 V. The oxidation peak at 0.7 V may be due to gold oxide stripping. Oxygen evolution can be seen initiating at approximately 0.9 V with hydrogen evolution beginning at approximately 0.1 V. These values were consistent during subsequent runs.

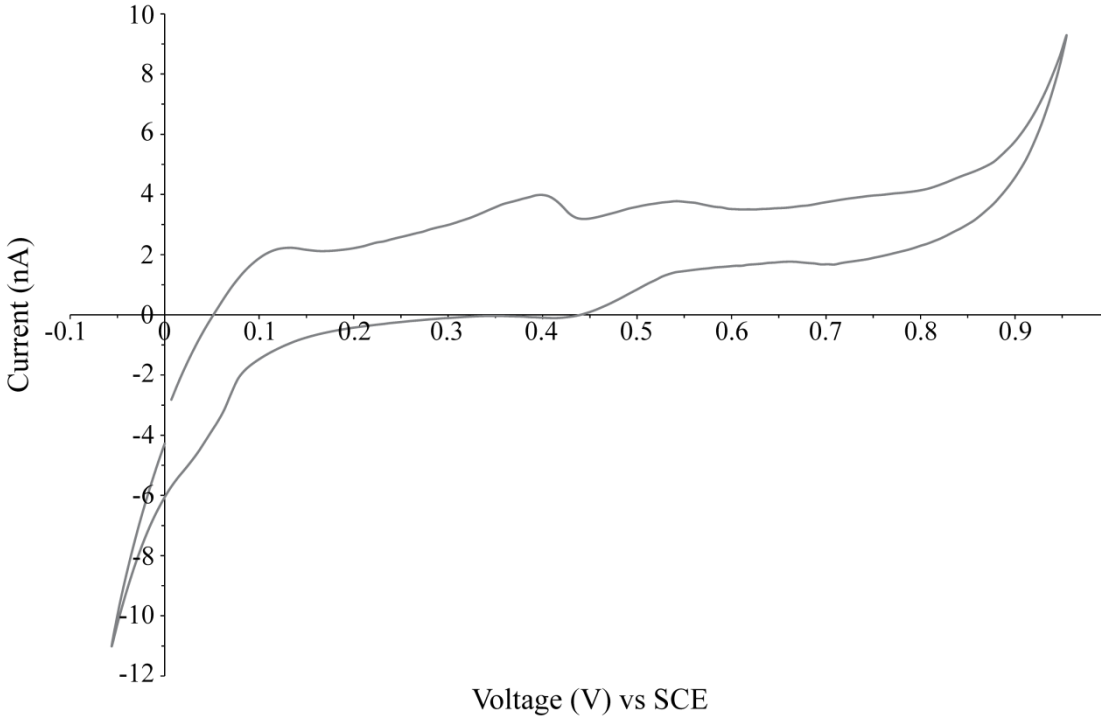

Figure 4.1: Cyclic voltammetry recorded at the Micro-Optical Ring Electrode.

A deaerated stock solution of UO_2^{2+} (42 mmol dm^{-3}) with a pH of 0.20 was prepared and cyclic voltammetry recorded at a scan rate of 1 mVs^{-1}.

4.3 Generating and detecting a uranyl photocurrent

Initially, photocurrent generating experiments were performed in the absence of a scavenger to test whether a uranyl photocurrent could be detected under the Photophysical-Electrochemical mechanism. As seen in Figure 4.2 uranyl failed to generate a photocurrent, indicating that the Photophysical-Electrochemical mechanism cannot detect uranyl ions alone.

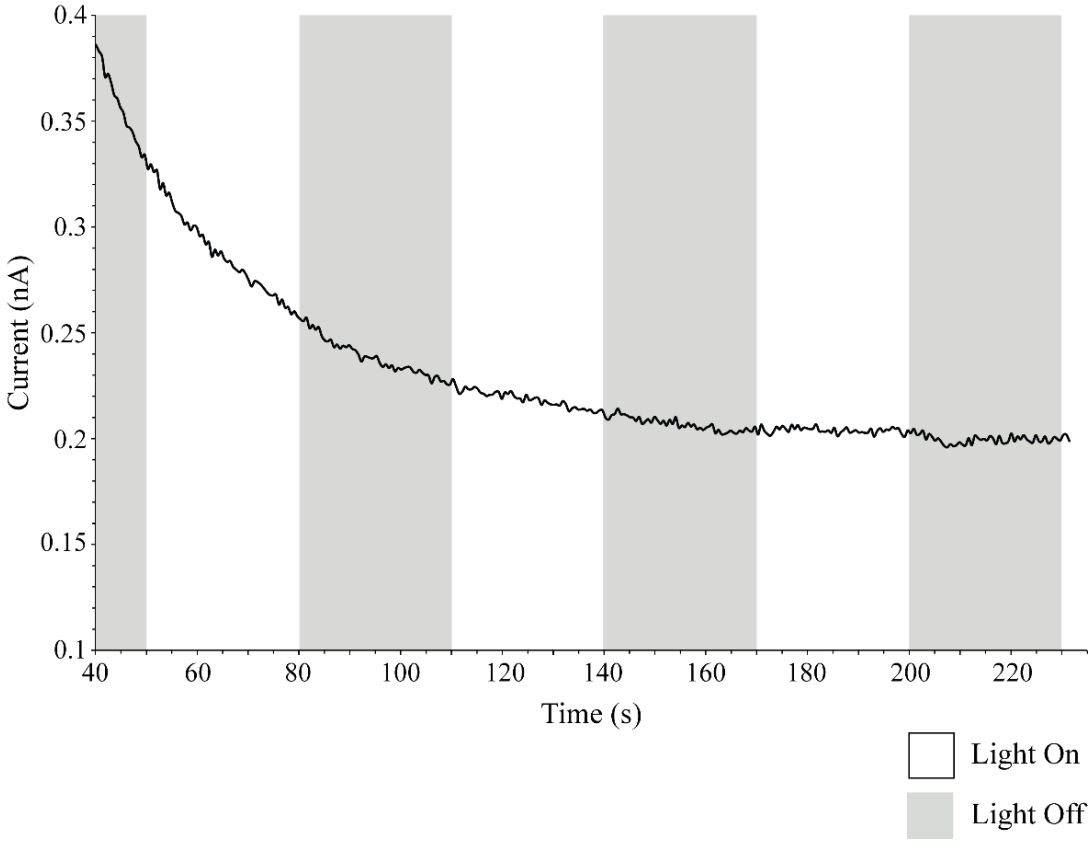

Figure 4.2: Chronoamperometer recorded at the Micro-Optical Ring Electrode

The currents was measured using MORE 4 during 30 s cycles of darkness and white light in a deaerated solution containing UO_2^{2+} (42 mmol dm^{-3}) at pH 0.20 with a working potential of 0.7 V vs SCE.

Based on the well documented ability of photoexcited uranyl ions to oxidise small organic molecules ethanol was selected as the scavenger (Nagaishi *et al.*, 1996, 2002b; George, Whittaker and Stearns, 2011). To test whether the addition of ethanol as an electron scavenger would result in the generation of a photocurrent, an excess of ethanol (100 mmol L^{-1}) was added to the uranyl solution. When illuminated the uranyl / ethanol solution generated a detectable photocurrent and a typical chronoamperogram recorded using the full UV-visible spectrum (white light) is presented in Figure 4.3.

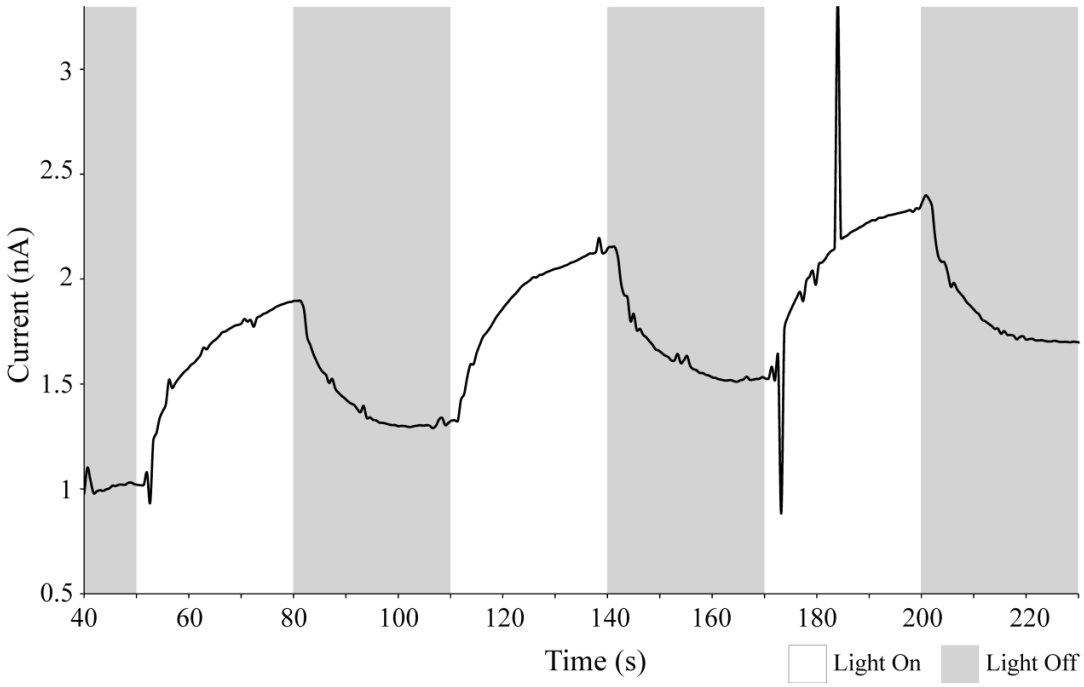

Figure 4.3: Chronoamperometer recorded at the Micro-Optical Ring Electrode

The currents was measured using MORE 4 during 30 s cycles of darkness and white light in a deaerated solution containing UO_2^{2+} (42 mmol dm^{-3}) and EtOH (100 $mmol^{-3}$) at pH 0.20 with a working potential of 0.7 V vs SCE.

A dearated solution of uranyl (42 mmol dm^{-3}) in ethanol (100 mmol dm^{-3}) at pH 0.2 (adjusted using nitric acid) was prepared and subjected to white light illumination. Following a 50 second stabilisation period in the dark, light was cycled on and off at 30 second intervals and the current recorded throughout. A working potential of 0.7 V vs SCE was applied to the MORE and the current was recorded as a function of time. A voltage of 0.7 V was chosen as this appeared to be a relatively flat area in the cyclic voltammogram indicating no redox processes were occurring in the dark. Figure 4.3 demonstrates that once illuminated the system underwent an oxidative process. In the dark, the current returned to its original value, though it must be noted that the signal drifted slightly upwards throughout the duration of the experiment. A drift removal procedure was adopted for experiments where drift was notable as described in The MORE as a Multi Analyte Sensor

As we have seen in the previous sections uranium (VI), neptunium (IV) and plutonium (III) and (IV) ions all have maximum absorbance peaks at different wavelengths of the electromagnetic spectrum (413.8, 723/964, 570/605 and 477 nm respectively). This can

be seen clearly when the absorbance spectra for each analyte are plotted together as seen in Figure 1.9.

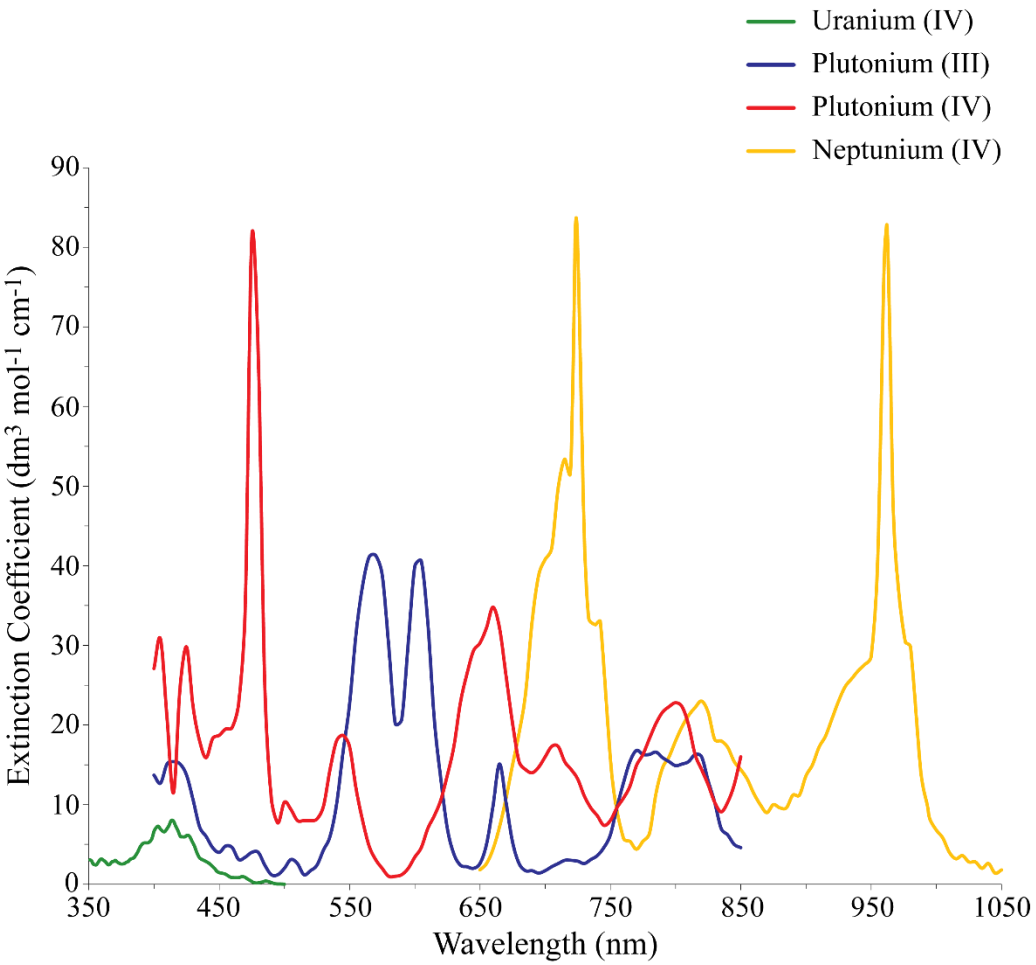

Figure 1.9: Comparison of electronic absorbance spectra for uranium (VI), neptunium (IV), plutonium (III) and plutonium (IV) aqua ions.

It is the unique absorption properties of each element that can be exploited by the MORE to allow the detection of each individual analyte in a mixture. Detection of an individual element could be achieved due to the MOREs ability to deliver light at specific desired wavelengths. For example, if the target analyte was neptunium (IV) in a mixture containing all four uranium (VI), neptunium (IV) and plutonium (III) and (IV) ions we could illuminate that mixture with light at a wavelength of 725 nm. Only the target analyte neptunium (IV) would enter an excited state that would create a photocurrent detectable by the MORE. To detect additional ions in the mixture the above process would be repeated altering the illumination wavelength each time to match that of a desired target analyte.

The possibility of interference between different analytes in a mixture will be investigated. This will be done by measuring the photocurrents generated by ions in a single solution at various wavelengths. Close attention will be given to wavelengths in the range of the maximum absorbance of other target analytes. The results generated from this will determine if signal-deconvolution techniques will be required and will also establish the limits of detection for each analyte.

Materials and Methods. The amplitude of the photocurrent was measured for each light on / light off transient. The three light on transient measurements and the three light off transient measurements were averaged, and the standard deviation was calculated for each light on and light off transient state.

As seen in Figure 4.3, the light on transient was associated with a reproducible oxidation current both in terms of the rise time (related to the kinetics of the system) and the amplitude which was measured at 717 pA ± 128 pA. This oxidation current is likely to be the result of a sensitization reaction, resulting from the transfer of energy from the excited uranyl ion to the acceptor. Photoreactions with alcohols always coincide with the reduction of the uranyl ion. The quantum yields of photoreduction of the uranyl ion with alcohols is relatively high ranging between 0.3 and 0.7 units (Bell and Buxton, 1974, 1975; Natarajan *et al.*, 1992). The reaction of photoexcited uranyl ions with methanol produces CH_2OH (Burrows and Kemp, 1974b; Buchachenko and Khudyakov, 1991). With the knowledge that uranyl is highly oxidizing and that uranium (IV) is stable in aqueous solution, it is likely that the photocurrent observed in Figure 4.3 is due to the uranyl being reduced by ethanol to which is subsequently oxidized at the gold ring. During this reaction the ethanol is converted to acetic acid (AcOH) (Figure 4.4). This reduction of uranyl would result in an oxidation current consistent with the results observed in Figure 4.3.

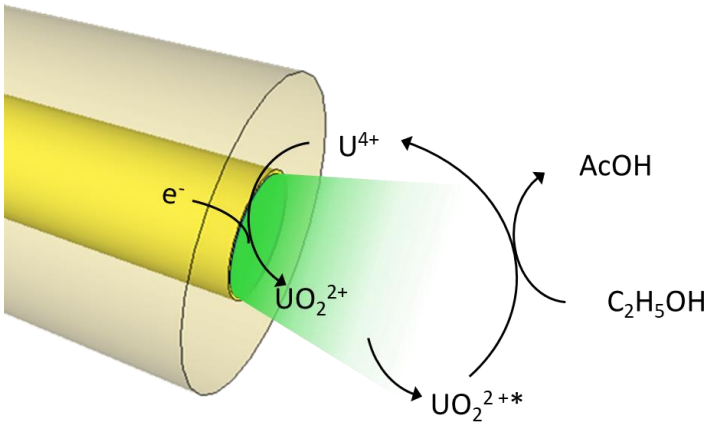

Figure 4.4: Proposed mechanism for photocurrent generation utilizing uranyl as the sensitizer and ethanol as the acceptor.

4.4 Optimum conditions for uranyl detection.

To establish the optimum conditions for the detection of uranyl in solution, a study was conducted to determine several key parameters which would enable the detection of the largest photocurrent possible. The parameters tested included the potential applied to the MORE, the wavelength of light for photoexcitation and the concentration of the acceptor in the reaction to determine the optimum conditions with which to detect uranyl.

4.4.1 Optimum working potential

The MORE can distinguish between analytes via two modes of discrimination; the illumination wavelength and the working electrode potential used to record the electrochemical processes. It is therefore necessary to study the amplitude of the photocurrent as a function of working electrode potential; this will determine the optimum operating electrode potential to be applied to the MORE that should generate the maximum photocurrent in the presence of the uranyl ion. Chronoamperometry experiments were carried out in a solution containing UO_2^{2+} (42 mmol dm^{-3}) and ethanol (100 mmol dm^{-3}) at pH 0.2 using white light while varying the working electrode potential by 100 mV increments between 0.2 and 0.7 V. This range was chosen based on the results in Figure 4.1 where the cyclic voltammetry of a uranyl solution demonstrated oxygen evolution at 0.8 V and hydrogen evolution at 0.1 V. Photocurrents were therefore measured between working potentials of 0.2 and 0.7 V vs SCE to reduce the impact of hydrogen and oxygen evolution respectively. As seen in Figure 4.5, photoexcited ions were successfully detected at all Volts measured. The largest

photocurrent was generated with an electrode operating working potential of 0.7 V vs SCE with a magnitude of 122 pA (Figure 4.5).

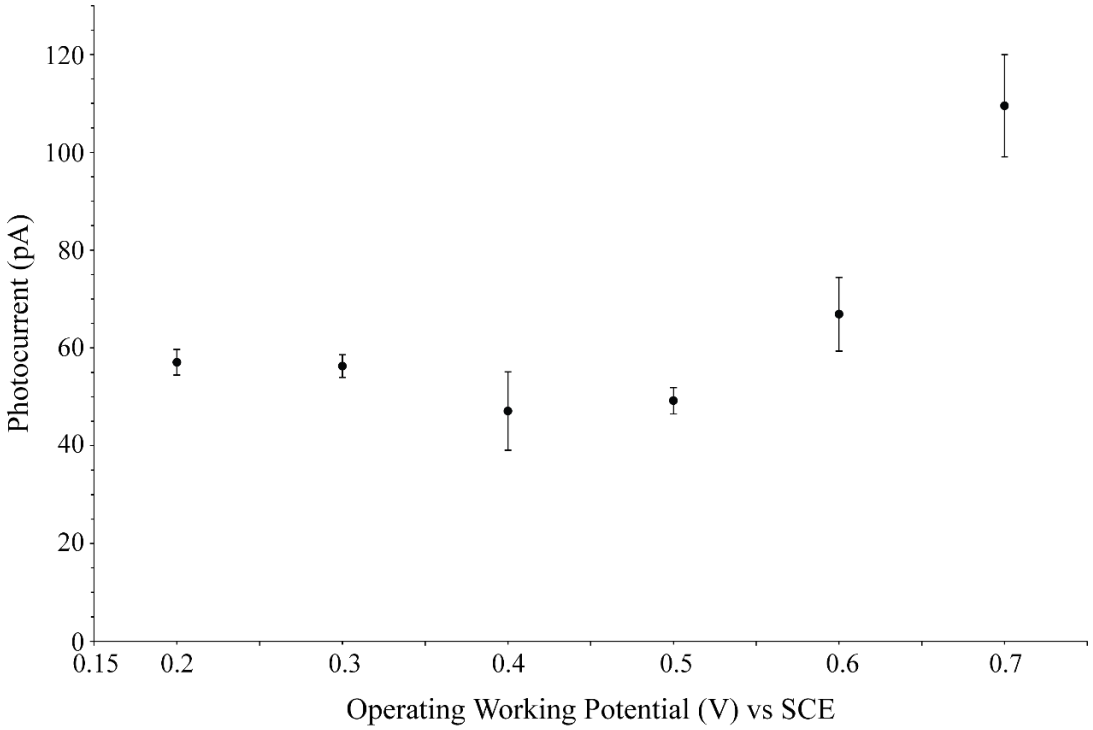

Figure 4.5: Photocurrent magnitude as a function of working potential

Currents were measured using MORE 4 in a deaerated solution containing UO_2^{2+} (40 mmol dm^{-3}) and EtOH (100 $mmol^{-3}$) at pH 0.11. Working potentials between 0.1 and 0.7 V vs SCE were used.

4.4.2 Photocurrent wavelength dependence

Once the optimum working electrode potential had been established, the next step was to determine the optimum illumination wavelength. The photocurrent generating experiment carried out for Figure 4.3 was repeated while varying the wavelength of the incident light to cover the range of the main peaks observed on the uranyl absorbance spectrum (340-500 nm) in 10 nm increments.

The magnitude of the photocurrent generated by uranyl ions was determined at each wavelength tested; three cycles of light on and light off were carried out for each

wavelength. The average of the three light on and light off photocurrents can be seen in Figure 4.6 which shows the recorded photocurrents, together with the absorption spectrum of the uranyl ion.

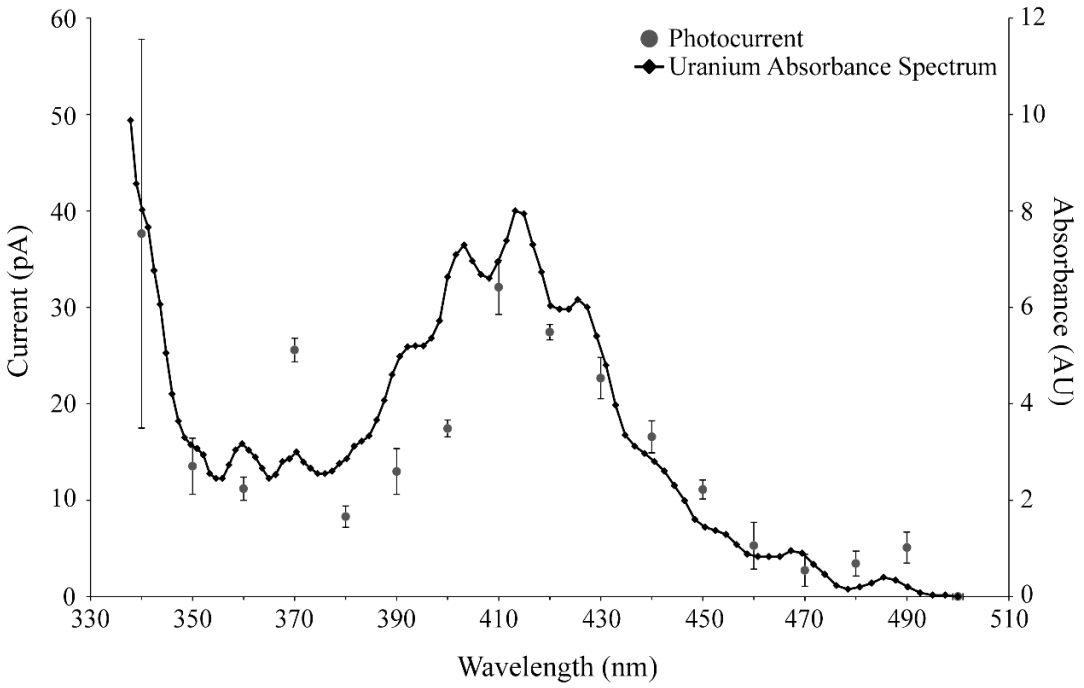

Figure 4.6: Photocurrent generation at various illumination wavelengths and compared to the absorbance spectrum of uranyl.

Currents were measured at various illumination wavelengths using MORE 4 in a deaerated solution containing UO_2^{2+} (42 mmol dm^{-3}) and EtOH (100 $mmol^{-3}$) at pH 0.2 with a working potential of 0.7 V vs SCE.
Uranium absorbance spectrum provided by Dr Andreux (personal communication).

Figure 4.6 demonstrates that the wavelength-dependent photocurrent closely follows that of the UV-visible spectrum of the uranyl ion, with the maximum photocurrent observed at 410 nm which corresponds closely with the lambda max value on the absorbance spectrum. At wavelengths in the range of 400-500 nm the photocurrent action spectrum matches the trend of the absorbance spectrum. Yusov and Shilov (2000) demonstrated that the absorbance of light by uranyl at wavelengths between 400 and 500 nm was a result of the transfer of an electron from the higher molecular orbital of the oxygen atom to the non-bonding 5f orbital of the uranium ion (Yusov and Shilov, 2000). Absorption of light by uranyl at 490 nm however is the result of a pure electronic transition (Yusov and Shilov, 2000). The correlation of the photocurrent action spectrum and absorbance spectrum indicates that the photocurrent is the result of the photoexcitation of uranyl and that the efficiency of this process is maximised by the

formation of the charge transfer complex. These results also support the suggestion from Andrieux (2005, 2006) that the MORE may be deployed as a spectrophotoelectrochemcial probe to fully characterise mixtures of analytes.

4.4.3 Optimum scavenger concentration

According to the semi-analytical model for the behaviour of the MORE presented in Chapter 1 (Equation 1.8:) any generated photocurrent is dependent on the concentration of the scavenger. Once an adequate electron acceptor had been identified, in this instance ethanol, it was possible to determine the optimum concentration that led to the largest photocurrent. By varying the ethanol concentration and recording the corresponding photocurrent, the optimum concentration of ethanol that supported the photochemical reaction was determined. Figure 4.7 shows the amplitude of the photocurrent measured at the MORE as a function of ethanol (scavenger) concentration. At the lower range of concentrations tested (50, 100 and 150 mmol dm^{-3}), the photocurrent increased steadily reaching a maximum of 1,448 pA at an ethanol concentration of 200 mmol dm^{-3}. A further photocurrent was recorded in the presence of 250 mmol dm^{-3} ethanol which showed a slight decrease in the photocurrent magnitude recorded to 1,352 pA. Due to the overlap in error bars for photocurrents recorded with 200 and 250 mmol dm^{-3} ethanol it is possible that the maximum photocurrent magnitude had in fact been reached with the addition of 200 mmol dm^{-3}, as predicted by the mathematical model (explained in 1.1.1). To determine if this hypothesis is correct, further experiments would need to be carried out measuring the photocurrent magnitude in the presence of ethanol at concentrations higher than 250 mmol dm^{-3}.

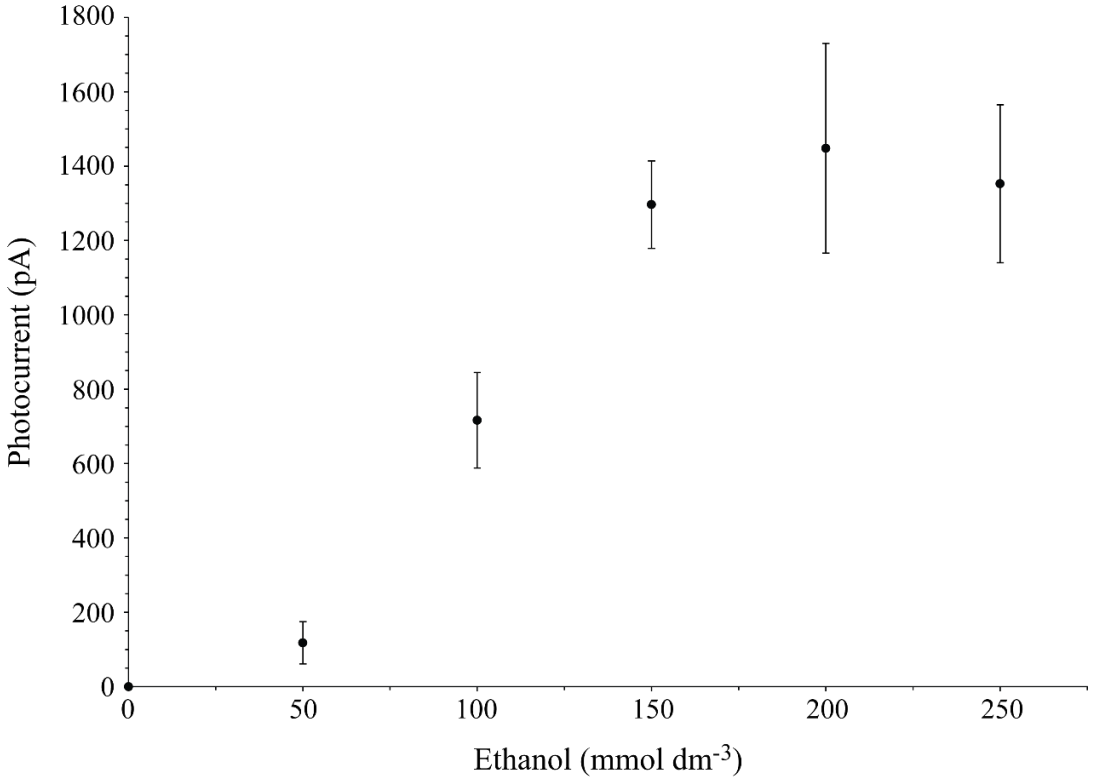

Figure 4.7: Photocurrent magnitude in the presence of various concentrations of ethanol

Currents were measured in white light using MORE 4 in a deaerated solution containing UO_2^{2+} (42 mmol dm^{-3}) and EtOH at various concentrations. The solution was at pH 0.2 and a working potential of 0.7 V vs SCE was applied.

4.5 Limits of detection

Once the optimum conditions for detecting uranyl had been established, the lowest concentration of uranyl that could generate a photocurrent detectable by the MORE was tested. To determine the limits of detection ethanol (200 mmol dm^{-3}) was added to a uranyl solution with an initial concentration of 39.53 mmol dm^{-3}. A chronoamperometry was set up as discussed above with a voltage of 0.7 V vs SCE applied for 230 seconds. The light was switched on after 50 seconds for a duration of 30 seconds after which it was switched off. The light was cycled on and off at 30 second internals for a total of three times and the average photocurrent magnitude calculated. The uranyl solution was then diluted, bubbled with nitrogen for 15 minutes and the experiment repeated. The uranyl solution was further diluted until no photocurrent could be detected.

Figure 4.8 shows how the detected photocurrent varied with uranyl concentration. A decrease in uranyl concentration resulted in a decrease in the magnitude of the photocurrent detected (Figure 4.8). The lowest concentration of uranyl that produced a photocurrent detectable by the MORE was 7.52 mmol dm^{-3}, generating a photocurrent of 9.8 pA. No photocurrent was recorded using a uranyl solution at a concentration of 2.52 mmol dm^{-3}. This result suggests that the lowest concentration of uranyl that the MORE can detect is between 2.52 and 7.52 mmol dm^{-3}.

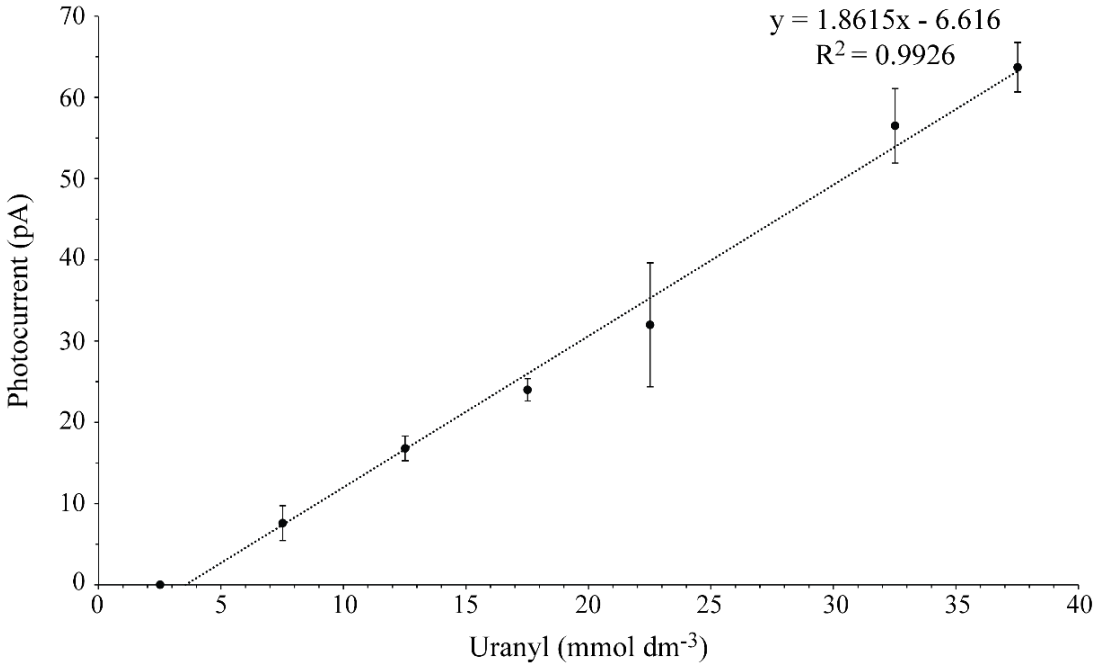

Figure 4.8: Photocurrent detection at various concentrations of uranyl

Currents were measured in white light using MORE 4 in a deaerated solution containing UO_2^{2+} at various concentrations and EtOH (200 $mmol^{-3}$) at pH 0.2 with a working potential of 0.7 V vs SCE.

Although no photocurrent was measurable at 2.52 mmol dm^{-3}, a considerable amount of drift was present during these experiments. Therefore, a photocurrent may have been generated but hidden due to the amount of drift present. With the elimination of this drift it may be possible to detect photocurrents at concentrations of uranyl less than 7.52 mmol dm^{-3}.

4.6 Application of mathematical model for uranyl

Application of the mathematical model will be conducted in two parts. First the dependence of the photocurrent on acceptor concentration will be considered, followed by the dependence of the photocurrent on the sensitizer concentration.

4.6.1 Photocurrent as a function of acceptor concentration

The mathematical model described in chapter 1 1.1.1 predicts that the measured photocurrent can be described by Equation 4.1.

$$i_{ph} = \frac{nFD_s\pi\varphi I_{ph}\varepsilon[S]}{1.03k_2}\sqrt{\frac{a}{X_k}}\sqrt{b^2-a^2}\left[\frac{k_1[A]}{k_0+k_1[A]}\right]$$

Equation 4.1: Mathematical model devised to explain the behaviour of the MORE

Please refer to Equation 1.5 for definitions

The relationship between the dependence of the photocurrent generated by uranyl on the scavenger concentration (ethanol) at concentrations between 0 and 250 mmol dm^{-3} can be seen in Figure 4.7. A linear relationship is initially seen with the photocurrent plateauing between 150 and 250 mmol dm^{-3}.

Rearranging Equation 4.1 gives Equation 4.2:

$$\frac{1}{i_{ph}} = \left(\frac{nFD_s\pi\,\varphi I_{ph}\varepsilon[S]}{1.03k_2}\sqrt{\frac{a}{X_k}}\sqrt{b^2-a^2}\right)^{-1}\left[1+\frac{k_0}{k_1[A]}\right]$$

Equation 4.2

When $\frac{1}{i_{ph}}$ is plotted as a function of $\frac{1}{[Ethanol]}$ a straight line should be generated with an intercept equal to $\frac{1.03k_2\sqrt{X_{k_2}}}{nFD_s\,\pi\varphi I_{ph}\varepsilon[S]\sqrt{b^2-a^3}}$ and a slope equal to $\frac{k_0}{k_1}\,\frac{1.03k_2\sqrt{X_{k_2}}}{nFD_s\,\pi\varphi I_{ph}\varepsilon[S]\sqrt{b^2-a^3}}$ this can be seen in Figure 4.9. The ratio of the slope to the intercept results in a value for the $\frac{k_0}{k_1}$ ratio which corresponds to the reciprocal of the Stervn-Volmer constant $\frac{1}{K_{SV}}$

defined by Lin and Sutin (1976). This procedure was applied to the uranyl photocurrent as a function of ethanol concentration between 0 and 250 mmol dm^{-3}.

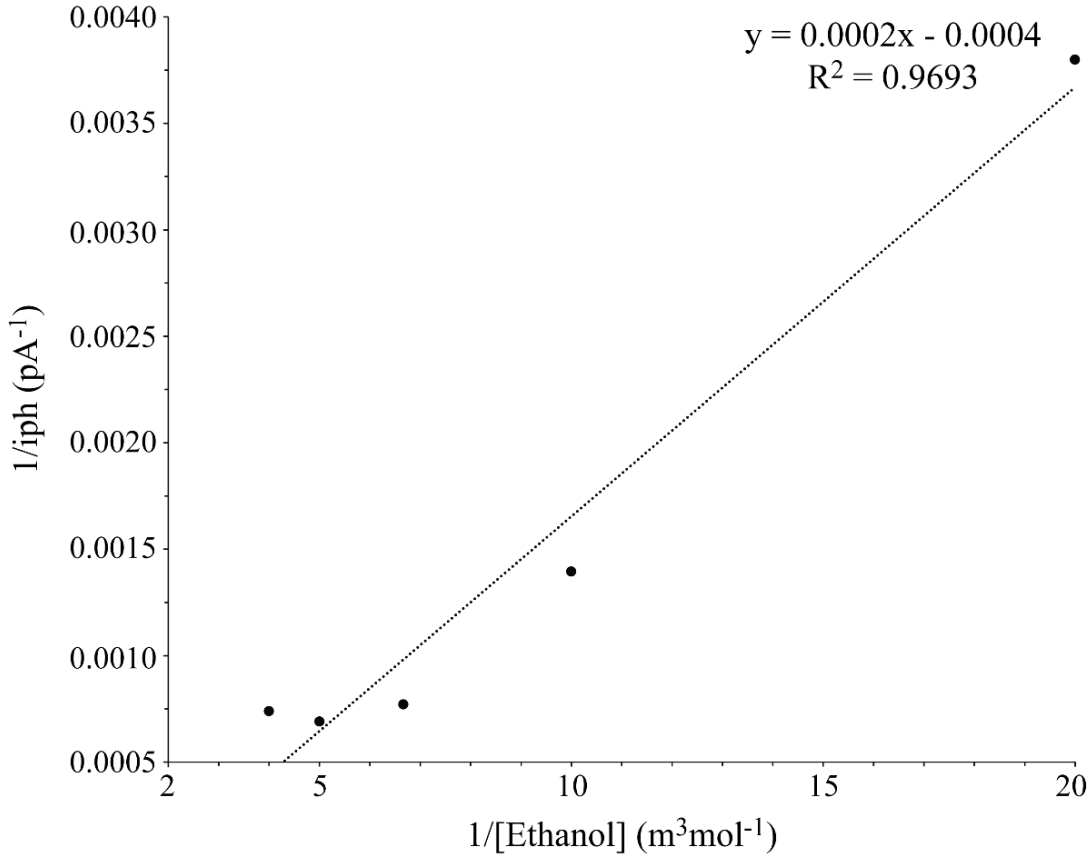

Figure 4.9: Reciprocal of photocurrent as a function of the reciprocal of ethanol concentration

The reciprocal photocurrents observed in Figure 4.8 were plotted against the reciprocal ethanol concentration and the line of best fit determined.

The model predicts that the reciprocal current is linearly dependent on the reciprocal of the scavenger concentration. Figure 4.9 confirms this prediction with a ratio of the slope to the intercept being equal to 0.558 m^3 mol giving a Stern-Volmer constant (K_{SV}) of 1.79 m^3 mol^{-1}.

4.6.2 Photocurrent as a function of Sensitizer (uranyl) concentration

The mathematical model (Equation 4.1) predicts that at a constant acceptor concentration the magnitude of the photocurrent should linearly depend on the

concentration of the sensitizer (uranyl). The observed photocurrent as a function of sensitizer concentration in the presence of a constant concentration of acceptor (ethanol (100 mmol dm^{-3})) is shown in Figure 4.8 and an R^2 value of 0.9926 was observed when a line of best fit was plotted. Knowing the slope of the line of best fit for the plotted photocurrent as a function of sensitizer concentration along with the value of $\frac{k_1}{k_0}$ and all other experimental parameters it is possible to use Equation 4.1 to determine the value of $\frac{\varphi}{k_2^{3/4}}$. Furthermore, if the value of k_2 is known it would be possible to calculate a value for the quantum yield of the photoexcitation of uranyl.

4.6.2.1 Determining the k_2 Value

The accuracy of the mathematical model can be determined by plotting the photocurrent normalised to its value at $t \to \infty$, as a function of time and comparing this with the predicted shape of the transient response of the MORE, using Equation 4.3. Figure 4.10 shows the results for three different photocurrents generated using uranyl solutions at a concentration of 39.53 mmol dm^{-3} where the theoretical normalised photocurrent is given by:

$$\frac{i}{i_{t=\infty}} = \frac{3}{2\Gamma(2/3)} \int_0^{(k_2 t)^{2/3}} e^{-z^{2/3}}\, dz$$

Equation 4.3

Adjusting the value of k_2 in Equation 4.3 varies the gradient of the rising portion of the transient. Once the theoretical and experimental values coincide (see Figure 4.10) a value of k_2 can be determined. Comparing the theoretical current with those experimentally observed generated a of k_2 value of 0.05 s^{-1}. A chi squared statistical analysis was carried out to assess whether there was any statistically significant difference between the theoretical and experimental photocurrents. Three experimental photocurrents were independently compared to the theoretical photocurrent and a p-value of 1 was obtained for all three comparisons. This suggests that all three experimental photocurrents are significantly similar to the theoretical.

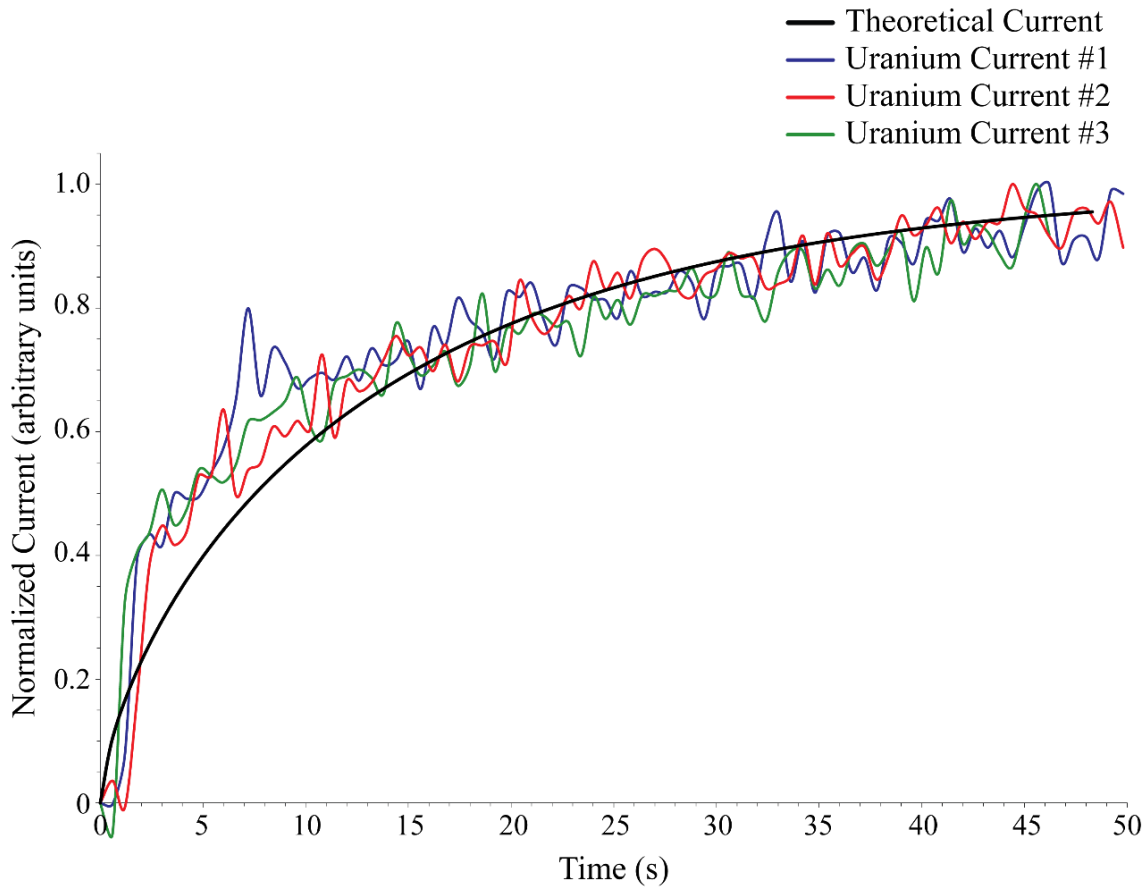

Figure 4.10: Theoretical and experimental transient response of the MORE with a normalised current.

The current was measured using MORE 4 during 50 s cycles of darkness and 410 nm wavelength of light in a deaerated solution of UO_2^{2+} (42 mmol dm-3) and EtOH (200 mmol^{-3}) at pH 0.2 with a working potential of 0.7 V vs SCE. The experiment was repeated three times and compared to the mathematical model values to determine k_2.

4.6.2.2 Calculating the photoexcitation quantum efficiency of uranyl

Once a value for k_2 was determined it was possible to calculate a value for the quantum efficiency of photoexcited uranyl. According to Equation 4.1 the steady state photocurrent is linearly dependant on the concentration of the sensitizer with a slope equal to $\frac{nFD_s\pi\varphi I_{ph}\varepsilon[S]}{1.03k_2}\sqrt{\frac{a}{X_k}}\sqrt{b^2-a^2}\left[\frac{k_1[A]}{k_0+k_1[A]}\right]$. As all the variables in this equation, expect for φ, are known it is possible to calculate a value for the quantum yield of photogenerated uranyl. This is achieved by plotting the photocurrent as a function of sensitizer concentration as shown in Figure 4.8. For this set of data, the quantum yield

of photoexcitation was estimated to be 7.55 x 10^{-6}. The accuracy of this value will be impaired due to a lack of a definitive ring thickness and the mathematical model not incorporating the effects of surface finish on the generated photocurrent.

4.7 Conclusion

This chapter has detailed the results gathered relating to uranyl photocurrent detection. A photocurrent was successfully generated and measured. The following optimal parameters were also identified; a working potential at 0.7 V vs SCE, an illumination wavelength at 410 nm and an electron scavenger (ethanol) concentration at 200 mmol dm^{-3}. The limits of detection were also determined to be between 2.52 and 7.52 mmol dm^{-3}. The kinetics of the system was also established by comparing the theoretical current with those experimentally observed which generated a of k_2 value of 0.05 s^{-1}. An estimation of the quantum yield of photogenerated uranyl was also calculated to be 7.55 x 10^{-6}.

5 Cerium and Vanadium

5.1 Cerium (III) chloride

5.1.1 Cyclic Voltammetry

Cyclic voltammetry was carried out to identify regions of oxygen and hydrogen evolution along with electrochemical processes associated with cerium (III) chloride under dark conditions. Figure 5.1 shows a cyclic voltammogram for cerium (III) chloride recorded at the MORE. The forward scan showed two oxidation peaks at ~0.2 V and 0.4 V whilst the backward scan showed two reduction peaks at ~0.65 V and 0.2 V (Figure 5.1). There are no obvious redox processes relating to cerium at these regions (Weik and Weik, 2000). Oxygen evolution can be seen initiating at approximately 0.8 V whilst hydrogen evolution can be seen at approximately -0.2 V (Figure 5.1).

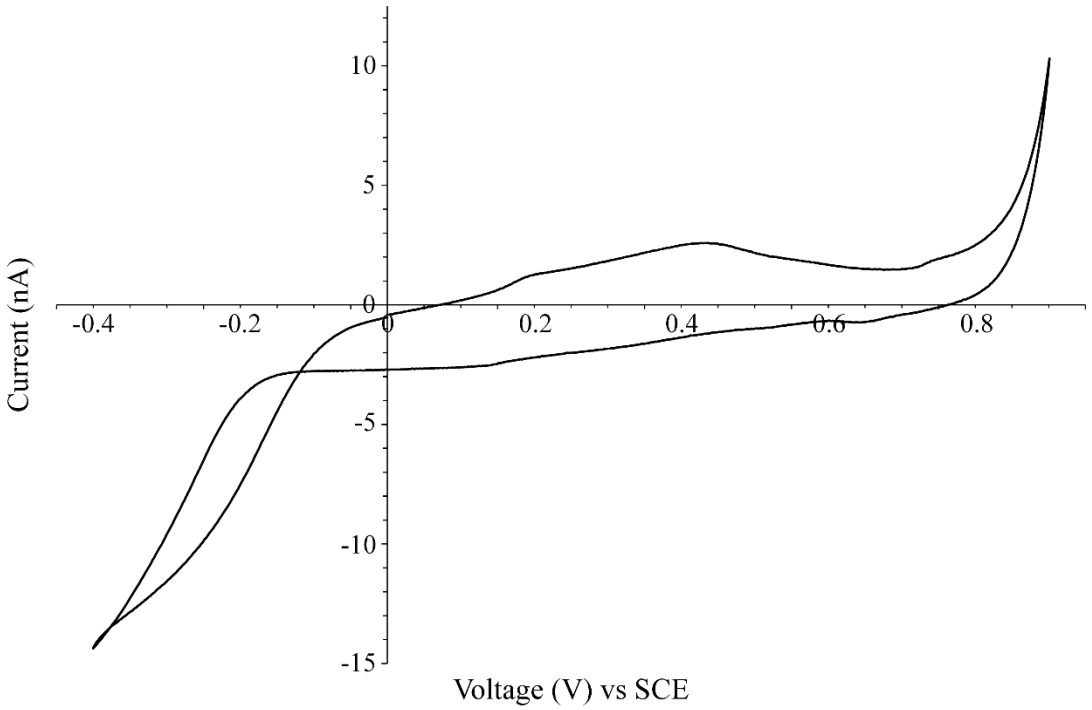

Figure 5.1: Cyclic Voltammetry of Cerium (III) Chloride

The current was measured using MORE 4 in white light in a deaerated solution of $CeCl_3$ (10 mmol dm^{-3}) and KCl (100 mmol dm^{-3}) at a pH of 1.76. A range of working potentials between -0.4 and 1.2 V vs SCE were tested with a scan rate of 1 mVs^{-1}.

5.1.2 Cerium photocurrent

The presence of a detectable photocurrent was tested in a solution of cerium (III) chloride (10 mmol dm^{-3}) in the absence of any electron acceptor using white light to photoexcite electrons. The working potential was varied in 0.1 V increments from -0.4 to 0.8 V as this was the region between hydrogen and oxygen evolution obtained during the cyclic voltammetry (Figure 5.1). No photocurrents were observed from cerium (III) chloride in the absence of a scavenger under any of the conditions tested. An example of an amperometry recorded in a cerium (III) chloride solution can be seen in Figure 5.2. Whilst it is possible that the lack of a detectable photocurrent was due to the overlap of the excitation wavelength with the wavelength of light attenuated by components of the MORE, it is also possible that cerium (III) chloride required an electron acceptor to aid photocurrent generation.

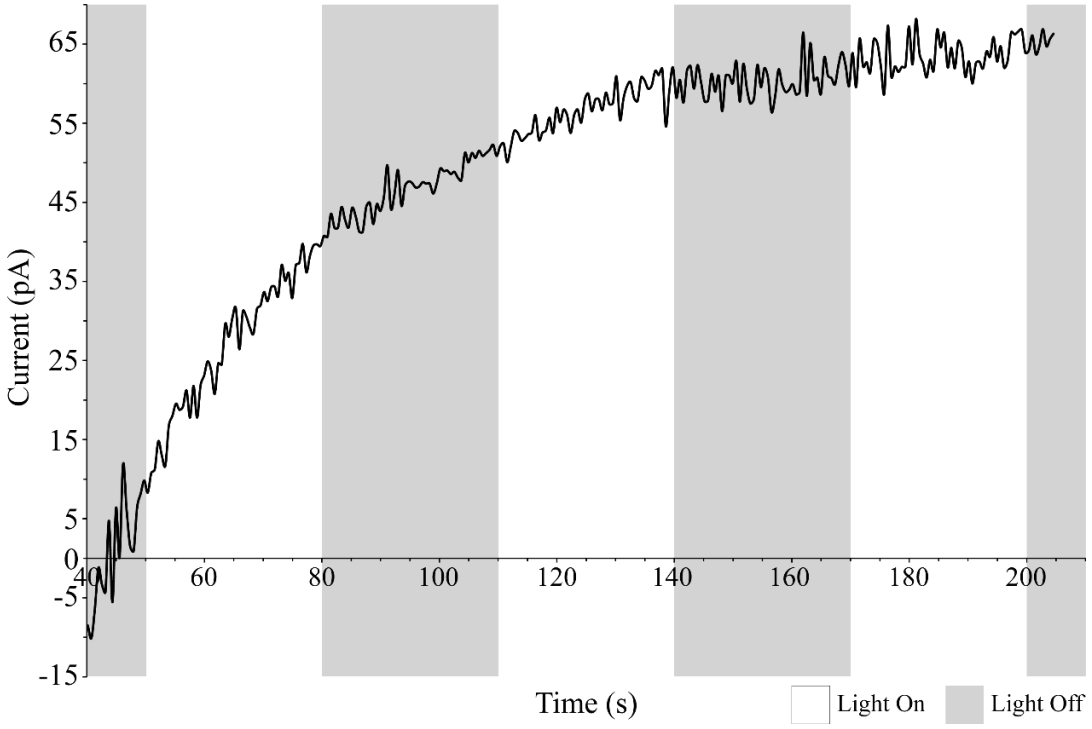

Figure 5.2: Chronoamperometry of a cerium (III) chloride solution

The current was measured using MORE 4 during 30 s cycles of darkness and white light in a deaerated solution of $CeCl_3$ (10 mmol dm^{-3}) and KCl (200 mmol dm^{-3}) at a pH of 1.76 with a working potential of 0.4 V vs SCE.

Cerium has not been studied to the same extent as ruthenium or uranyl. As a result of this an element of a 'trial and error' approach was undertaken whilst trying to identify a suitable electron acceptor. Initially the ability of cerium (III) chloride was tested in the presence of ethanol, which had previously been used as an electron acceptor for uranyl. The working potential was varied in 0.1 V increments from -0.4 to 0.8 V vs SCE to avoid hydrogen and oxygen evolution (-0.2 and 0.8 V respectively) identified during the cyclic voltammetry (Figure 5.1). When tested with the MORE no photocurrent was detected from the cerium (III) chloride (10 mmol dm^{-3}) / ethanol (100 mmol dm^{-3}) solution at any working potential tested. An example of a recorded current can be seen in Figure 5.3, measured using a working potential of 0.4 V vs SCE. It would therefore appear that ethanol is not a suitable electron scavenger to promote photocurrent generation by cerium (III) chloride. Whilst ethanol was a suitable electron acceptor to help generate a detectable photocurrent from uranyl ions (section 4.3), Andrieux et al (2006) demonstrated that iron (III) chloride promoted the generation of a photocurrent in a solution of $Ru(bipy)_3^{2+}$.

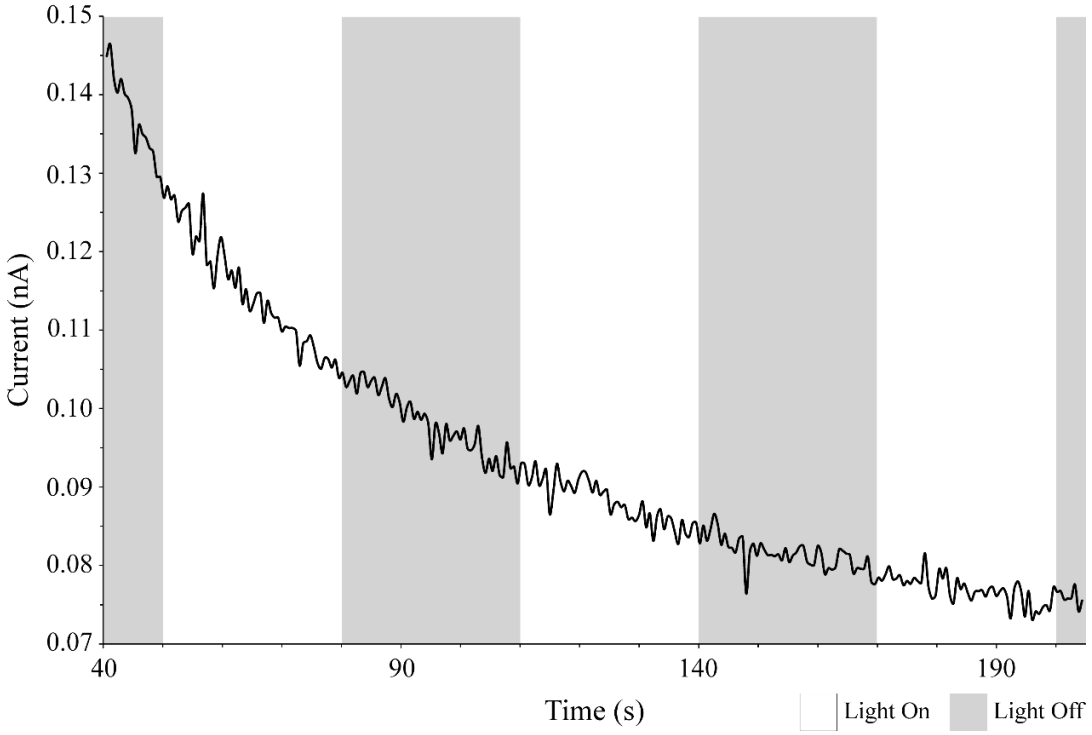

Figure 5.3: Chronoamperometry of cerium (III) chloride in the presence of ethanol

The current was measured using MORE 4 during 30 s cycles of darkness and white light in a deaerated solution of $CeCl_3$ (10 mmol dm^{-3}), ethanol (100 mmol dm^{-3}) and KCl (200 mmol dm^{-3}) at a pH of 1.76 with a working potential of 0.4 V vs SCE.

A solution of cerium (III) chloride (10 mmol dm^{-3}) and iron (III) chloride (100 mmol dm^{-3}) was set up and photocurrent generation was tested by the MORE between -0.4 and 0.8 V vs SCE in 0.1 V increments. As seen in

Figure 5.4 in the presence of iron (III) chloride (100 mmol dm^{-3}) and with a working potential of 0.4 V vs SCE no photocurrent was detected. This result was representative of all working potentials tested. It would therefore appear that iron (III) chloride is not a suitable electron acceptor for cerium (III) chloride.

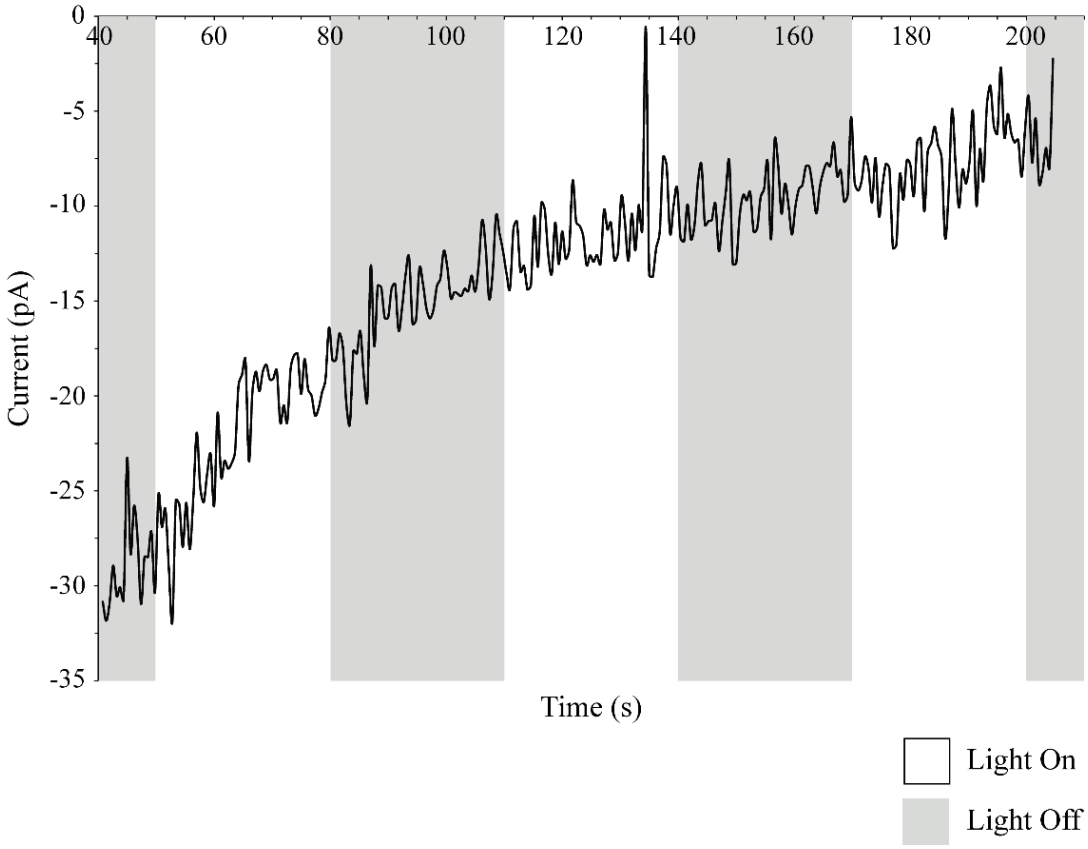

Figure 5.4: Chronoamperometry of cerium (III) chloride in the presence of iron (III) chloride

The current was measured using MORE 4 during 30 s cycles of darkness and white light in a deaerated solution of $CeCl_3$ (10 mmol dm^{-3}), iron (III) chloride (100 mmol dm^{-3}) and KCl (200 mmol dm^{-3}) at a pH of 1.76 with a working potential of 0.4 V vs SCE.

Cerium (III) chloride was chosen to act as a surrogate for the detection of a photocurrent generated by plutonium by the MORE. However, it was discovered that the only absorbance peak for cerium (III) chloride was at 297 nm (Figure 3.23), a wavelength that coincided with the region of light absorbed by components of the MORE. Despite this overlap the ability of the MORE to detect a photocurrent from cerium (III) chloride was tested. No photocurrent could be detected from cerium (III) chloride either alone or in the presence of electron acceptors ethanol or iron (III) chloride. An alternative surrogate for plutonium will have to be identified to allow further work with the MORE to continue. The alternative surrogate would have to have an absorption peak, and therefore excitation wavelength, above 350 nm to avoid light attenuation by the MORE.

5.2 Vanadium (IV) oxide sulphate hydrate

5.2.1 Cyclic Voltammetry

Cyclic voltammetry was carried out to identify regions of oxygen and hydrogen evolution along with electrochemical processes associated with vanadium (IV) oxide sulphate hydrate under dark conditions. To achieve this, the working electrode potential was cycled between the solvent stability limits. Figure 5.5 shows a typical scan of such an experiment recorded by the MORE in a solution of Vanadium (IV) oxide sulphate hydrate (40 mmol dm^{-3}). During the forward scan one oxidation peak was seen at approximately 0.4 V vs SCE (Figure 5.5). The backward scan identified two reduction peaks at 0.7 and 0.5 V vs SCE (Figure 5.5). The only redox reaction that vanadium undergoes in this region occurs at a redox potential of approximately 0.578 V vs SCE and is the reduction of VO^{2+} to V^{3+}(Weik and Weik, 2000).

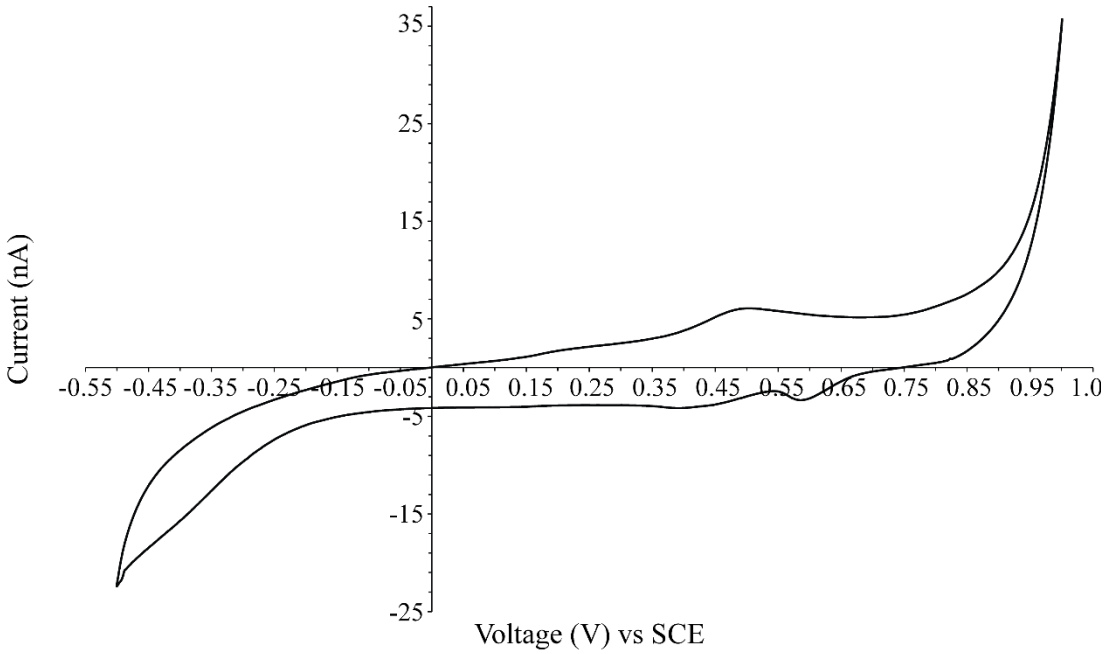

Figure 5.5: Cyclic Voltammetry of Vanadium (IV)

The current was measured using MORE 4 in white light in a deaerated solution of V(IV) (40 mmol dm^{-3}) and KCl (200 mmol dm^{-3}) at a pH of 1.77. A voltage range of -0.5 to 1 V vs SCE was scanned at a range of 10 mVs^{-1}.

5.2.2 Vanadium photocurrent

Experiments were carried out to determine whether the MORE was able to detect the presence of vanadium in solution via generation of a photocurrent using vanadium (IV) oxide sulphate hydrate as the sensitizer. The initial test was undertaken in the absence of an acceptor to determine if vanadium alone was able to generate a photocurrent. When tested, no photocurrent was observed in a solution of vanadium (IV). It would therefore appear that vanadium (IV) cannot produce a photocurrent in the absence of an electron scavenger (Photophysical-Electrochemical mechanism) (Figure 5.6).

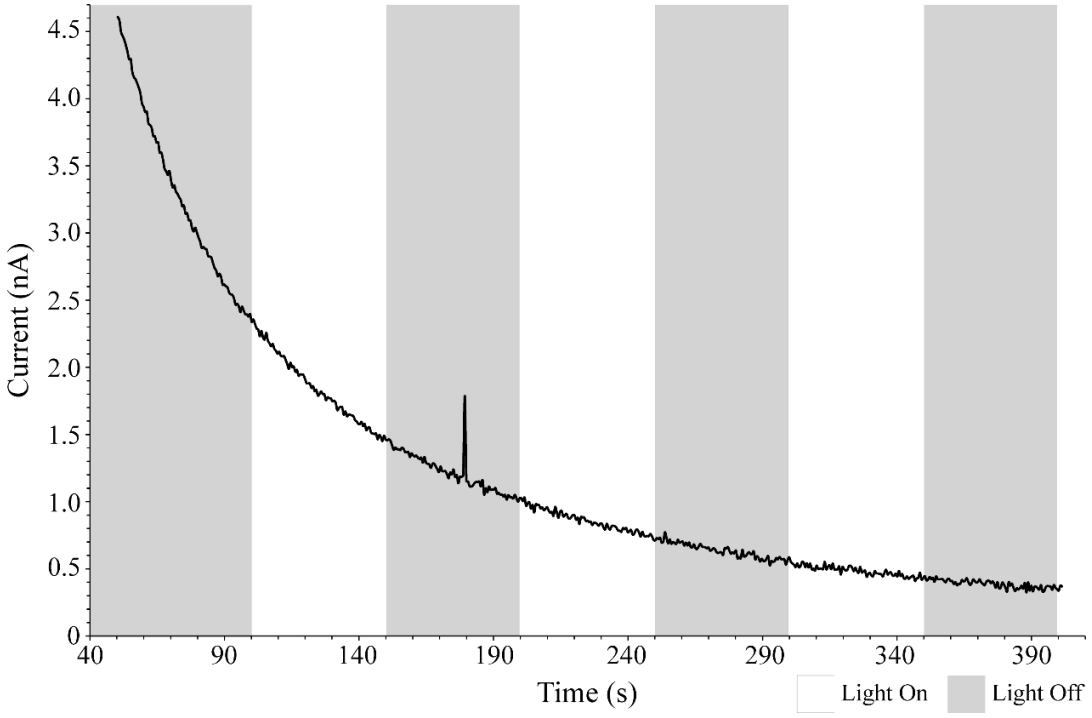

Figure 5.6: Chronoamperometry of vanadium (IV)

The current was measured using MORE 4 during 30 s cycles of darkness and white light in a deaerated solution of V(IV) (40 mmol dm^{-3}) and KCl (200 mmol dm^{-3}) at a pH of 0.47 and a working potential of 0.4 V vs SCE.

As with cerium, vanadium has not been studied to the same extent as uranyl or ruthenium. As a result of this an element of 'trial and error' was undertaken whilst attempting to identify a suitable electron acceptor. Uranyl has been shown to oxidise small organic molecules such as ethanol (Nagaishi *et al.*, 1996) which was therefore selected to promote the generation of a photocurrent in a uranyl containing solutions. We therefore tested whether ethanol would also act as an acceptor for vanadium and

promote the generation of a photocurrent. A solution of vanadium (IV) (40 mmol dm^{-3}) and ethanol (200 mmol dm^{-3}) was tested for photocurrent detection by the MORE. It would appear that despite the presence of ethanol in the solution no photocurrents were observed from a vanadium solution (Figure 5.7).

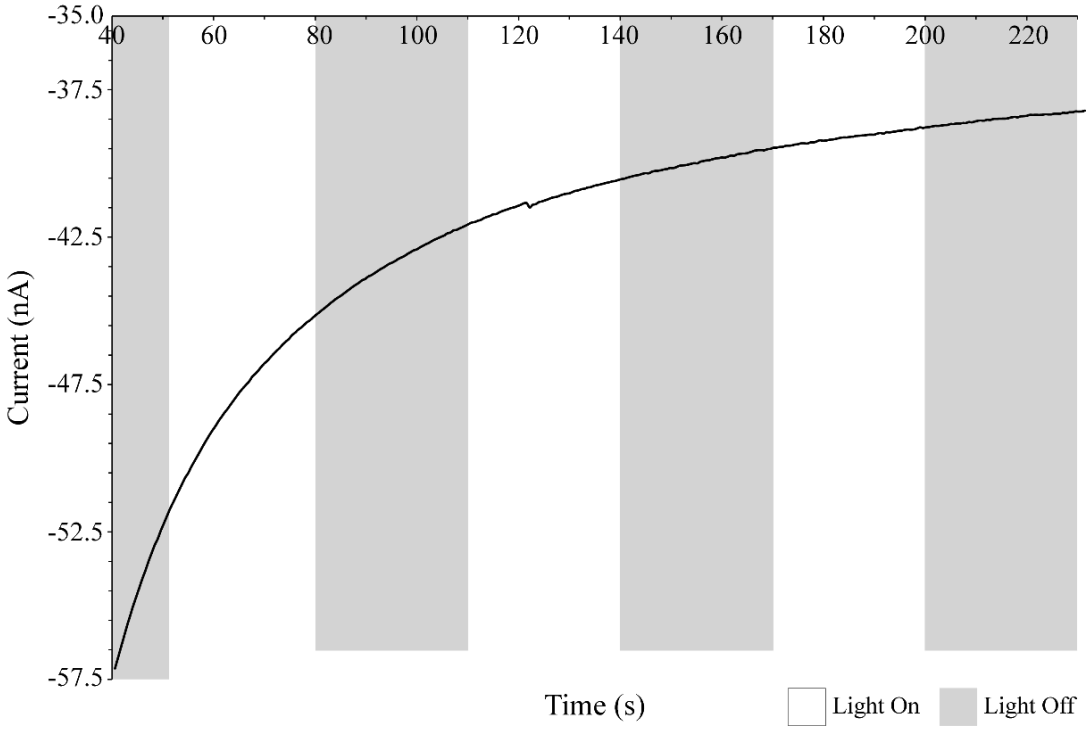

Figure 5.7: Chronoamperometry of vanadium (IV) in the presence of ethanol

The current was measured using MORE 4 during 30 s cycles of darkness and white light in a deaerated solution of V(IV) (40 mmol dm^{-3}), ethanol (200 mmol dm^{-3}) and KCl (200 mmol dm^{-3}) at a pH of 0.08 and a working potential of 0.4 V vs SCE.

Iron (III) chloride is an alternative electron acceptor to ethanol that has previously been used to generate a ruthenium photocurrent (Andrieux et al 2005). Andrieux et al (2005) showed that in the presence of iron (III) chloride a ruthenium photocurrent was observed at an optimum voltage of 0.5 V vs SCE. As illustrated by the cyclic voltammetry, it appears that vanadium (IV) oxide sulphate hydrate undergoes a reduction process at 0.5 V vs SCE (Figure 5.5). We therefore tested whether iron (III) chloride would act as an electron acceptor for photoexcited vanadium (IV) oxide sulphate hydrate and generate a photocurrent.

A solution of vanadium (IV) oxide sulphate hydrate (40 mmol dm^{-3}) and iron (III) chloride (200 mmol dm^{-3}) was prepared and tested for the production of a photocurrent. A working potential of 0.5 V vs. SCE was applied to the MORE with the current recorded as a function of time. As seen in Figure 5.8, the presence of iron (III) chloride in the vanadium (IV) oxide sulphate hydrate solution produced a detectable photocurrent. To allow the current to reach a steady state the MORE was placed in the vanadium and iron (III) chloride solution for 50 seconds prior to the light being switched on. Following illumination, a photocurrent was generated which was observed as immediate decrease in the current and remained until the light was switched off at 150 seconds (Figure 5.8). This light on / light off cycle was repeated, and a second photocurrent was observed during the second light on phase between 250 and 350 seconds (Figure 5.8). As seen in Figure 5.8, once illuminated a negative current was generated suggesting that the vanadium ions underwent a reduction process. When in the dark, the current returned to its original value with little to no drift observed (Figure 5.8).

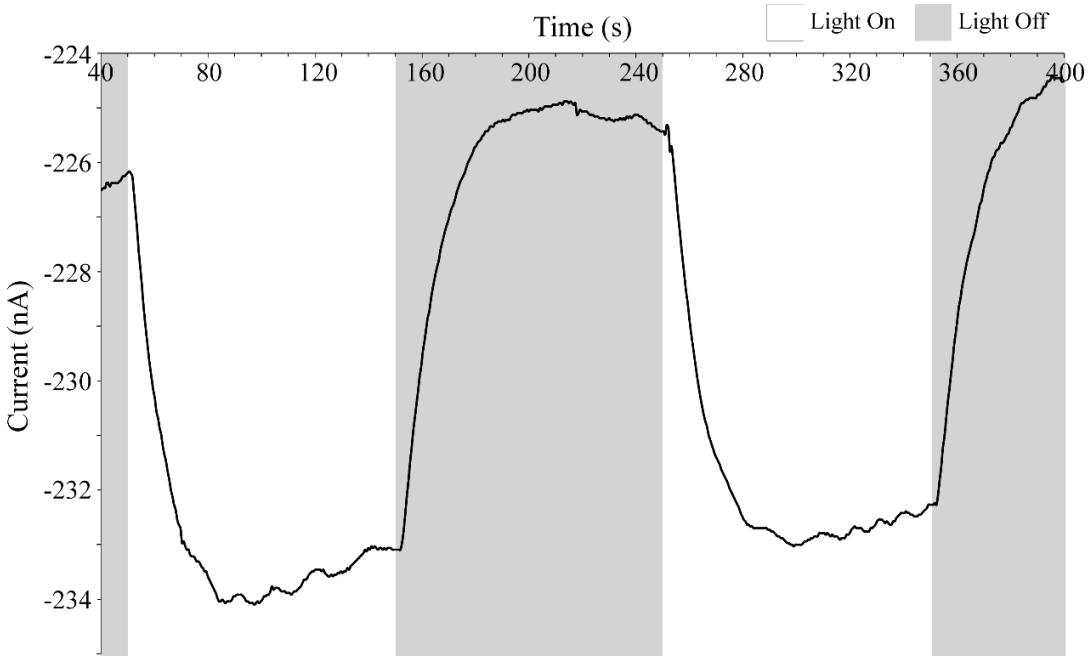

Figure 5.8: Chronoamperometry of vanadium (IV) in the presence of iron (III) chloride

The current was measured using MORE 4 during 100 s cycles of darkness and white light in a deaerated solution of V(IV) (40 mmol dm^{-3}), $FeCl_3$ (200 mmol dm^{-3}) and KCl (200 mmol dm^{-3}) at a pH of 0.14 and a working potential of 0.4 V vs SCE.

Figure 5.8 demonstrates that the light on transient of a vanadium photocurrent solution is associated with a reproducible reduction in the detected current in relation to both the rise time (kinetics of the system) and the amplitude which is measured at 7.5 nA ± 0.56 nA (Figure 5.8). This reduction of the current is likely to be the result of a sensitization reaction which initiates from the transfer of energy from the excited vanadium ion.

5.2.3 Determining the optimum conditions for detection of a vanadium photocurrent

Having successfully detected a photocurrent following the photoexcitation of vanadium the parameters required to achieve the maximum photocurrent possible were optimised. These parameters included determining: the potential applied to the MORE, the wavelength of illumination for photoexcitation and the concentration of acceptor in the reaction.

5.2.4 Photocurrent wavelength dependence

The full absorbance spectrum tested for vanadium (IV) oxide sulphate hydrate ranged from 300 to 800 nm with a major peak identified at 765 nm (Figure 3.22). The presence of a photocurrent was tested across the full 300 to 800 nm absorbance spectrum of vanadium (IV) oxide sulphate hydrate at 10 nm increments.

For each wavelength tested the amplitude of three photocurrents were recorded and the average calculated. As seen in Figure 5.9, photocurrents were observed from a vanadium (IV) oxide sulphate hydrate (40 mmol dm^{-3}) and iron (III) chloride (100 mmol dm^{-3}) solution illuminated with light between wavelengths of 330 to 410 nm. The largest photocurrent was recorded at an illumination wavelength of 350 nm (0.8 nA) (Figure 5.9). No photocurrents were observed between 550 to 800 nm despite the presence of at least one major peak and a potential shoulder on the vanadium (IV) oxide sulphate hydrate absorbance spectrum (Figure 5.9, Figure 3.22). It is possible that the lack of any observed photocurrent between 550 and 800 nm is due to the energy from the illuminating light creating molecular vibrations within the vanadium complexes. Molecular vibrations would absorb the light energy, and thus generate an absorbance peak, but would not result in the photoexcitation of individual electrons required for a photocurrent.

A

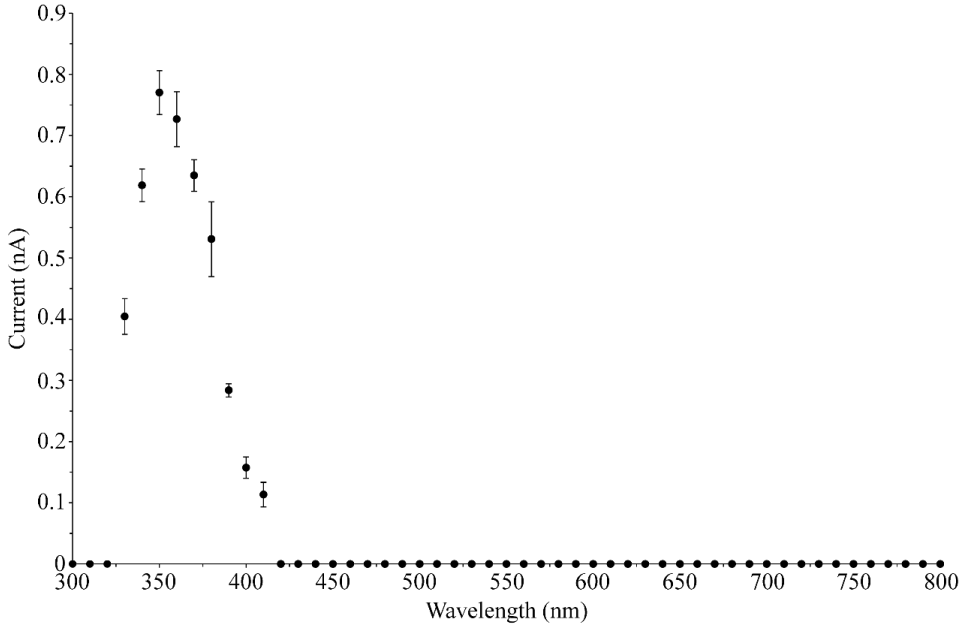

B

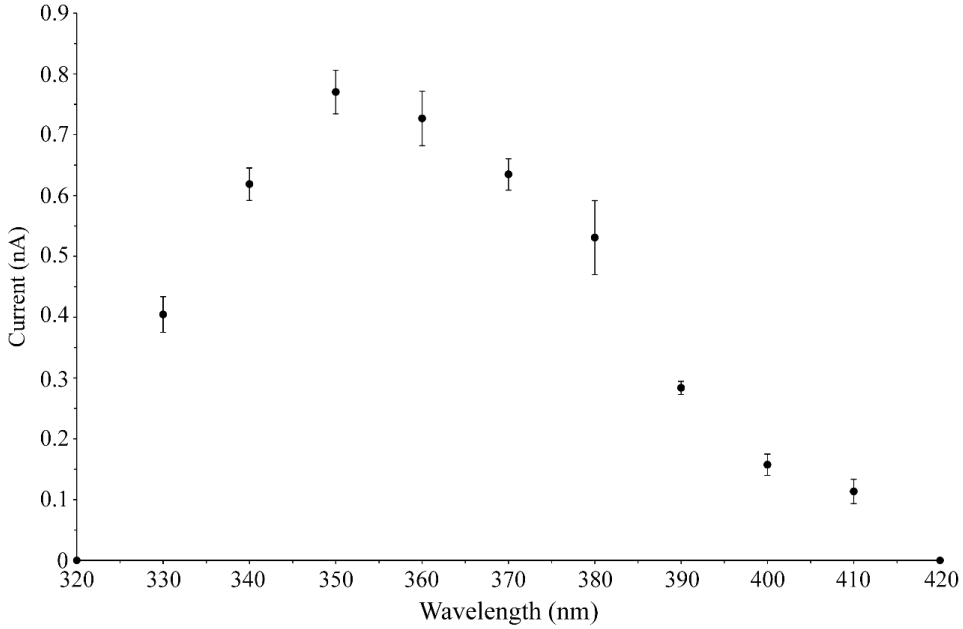

Figure 5.9: Photocurrent as a function of illumination wavelength

Currents were measured using MORE 4 during 30 s cycles of darkness and various wavelengths of light in a deaerated solution of V(IV) (40 mmol dm^{-3}), $FeCl_3$ (200 mmol dm^{-3}) and KCl (200 mmol dm^{-3}) at a pH of 0.14 and a working potential of 0.5 V vs SCE.

A: Photocurrent detection between 300 and 800 nm wavelengths.

B: Photocurrent detection between 320 and 420 nm wavelengths.

Once a photocurrent as a function of wavelength was established for the vanadium (IV) solution, the illumination wavelengths that produced a photocurrent and the absorbance spectrum for vanadium (IV) were compared. If the observed photocurrent was being generated by the vanadium (IV) ions the illumination wavelengths required to generate the photocurrent should correlate with wavelengths at which vanadium absorbs light. However, as demonstrated in Figure 5.10 when the wavelengths at which a photocurrent was generated and the absorbance spectra were compared it was clear that the two did not coincide. The optimum wavelength for photocurrent generation by vanadium (IV) oxide sulphate hydrate was recorded at 350 nm. The absorbance peak for vanadium (IV) closest to 350 nm was at less than 300 nm and as discussed in section 3.9, light in the region of 200 to 300 nm is largely attenuated by the components of the MORE. No photocurrents were detected from vanadium (IV) oxide sulphate hydrate at wavelengths above 410 nm, however the wavelength of maximum absorbance (λ max) for vanadium (IV) is observed at 765 nm which is considerably different from the wavelengths at which a photocurrent was observed.

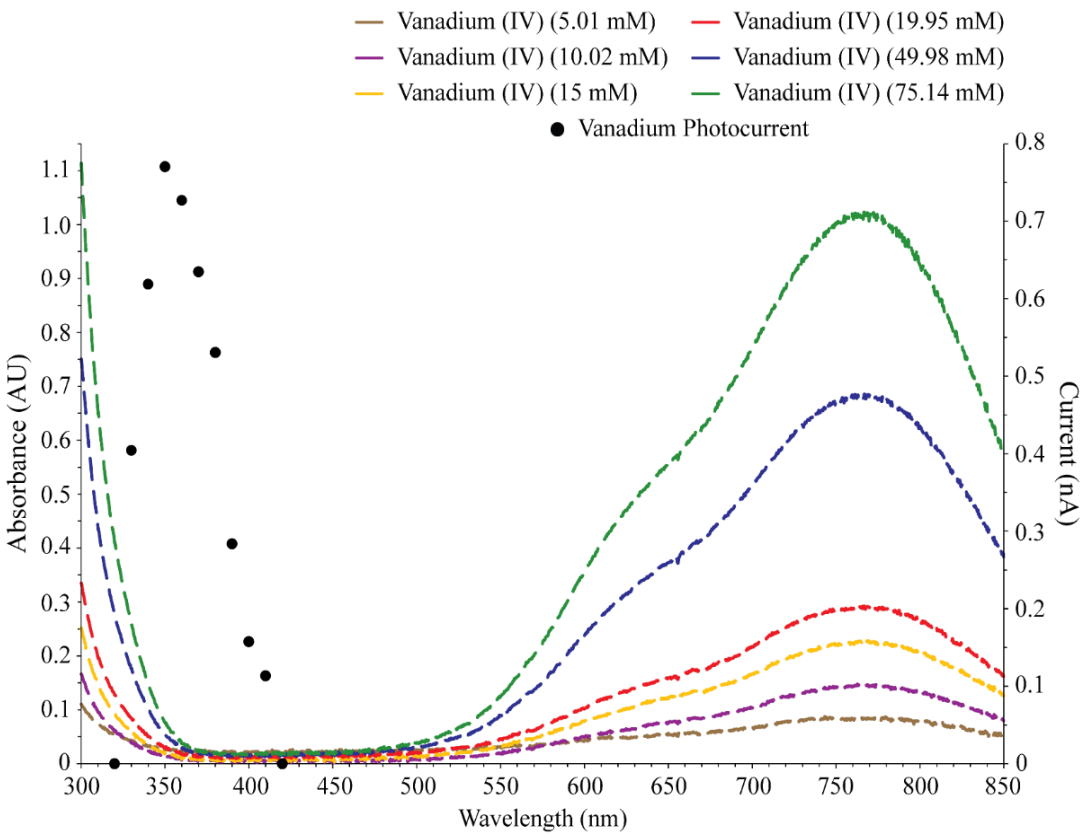

Figure 5.10: Observed photocurrent and absorbance spectrum for vanadium (IV) oxide sulphate hydrate.

The observed photocurrent action spectrum generated at wavelengths between 320 and 420 nm from Figure 5.9 was plotted against the absorbance spectrum for vanadium (IV) oxide sulphate hydrate from Figure 3.22.

The difference between the observed photocurrent as a function of wavelength and the absorbance spectrum for vanadium (IV) suggests that the detected photocurrent is not due to the photoexcitation of vanadium (IV) ions.

5.2.5 Identifying the sensitizer during photocurrent generation

5.2.5.1 Vanadium (III) and vanadium (V) ions

Given the mismatch between the vanadium (IV) absorbance spectrum and the photocurrent action spectrum for these experiments, it is important to consider whether the possible oxidation or reduction of vanadium (IV) may have led to the generation of these photocurrents. The photocurrent action spectrum was compared to the absorbance

spectrum for both vanadium (III) and (V) ions (Figure 5.11, Figure 5.12). No correlation was observed between the range of wavelengths required to generate a photocurrent and the absorbance peaks for vanadium (III) chloride suggesting that the generated photocurrent was not due to the photoexcitation of vanadium (III) ions (Figure 5.11). A strong correlation however was observed between the absorbance spectrum of vanadium (V) and the photocurrent action spectrum recorded (Figure 5.12). This correlation suggests that the generated photocurrent could be due to the photoexcitation of vanadium (V) ions. What was initially a solution of solely vanadium (IV) ions had likely transformed into a mixture of both vanadium (V) and vanadium (IV) ions.

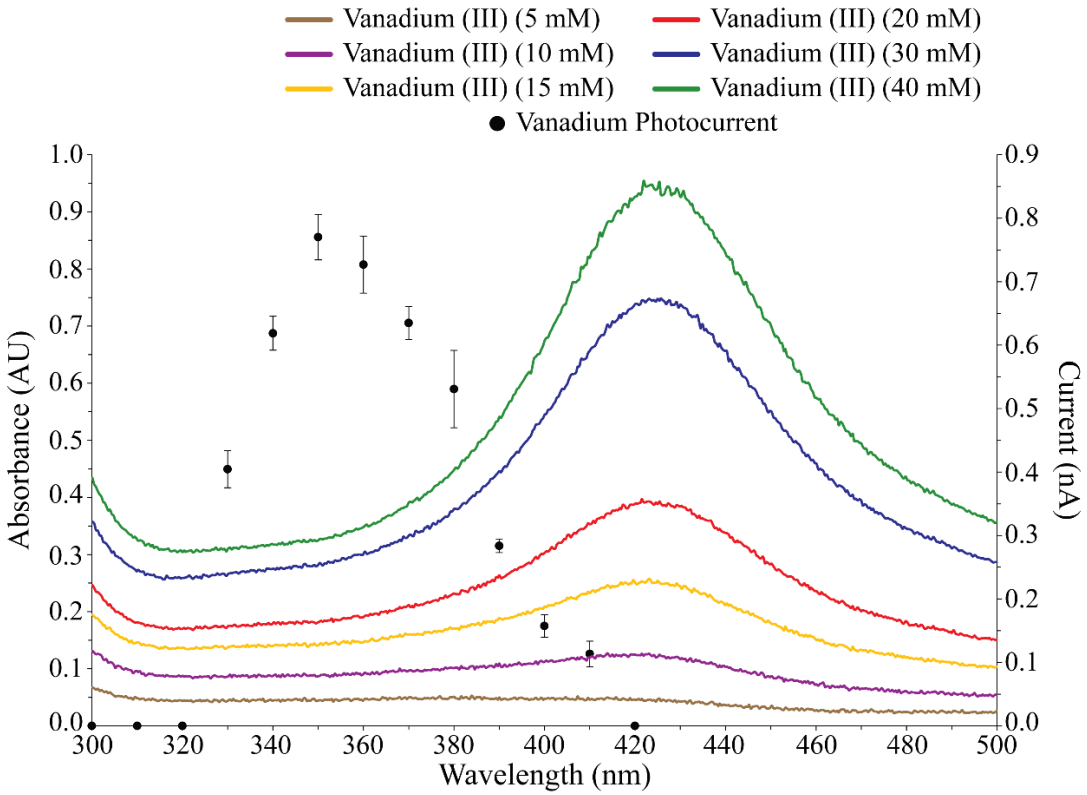

Figure 5.11: Observed photocurrent action spectrum and absorbance spectrum for vanadium (III) chloride

The observed photocurrent action spectrum generated at wavelengths between 320 and 420 nm from Figure 5.9 was plotted against the absorbance spectrum of vanadium (III) chloride at various concentrations.

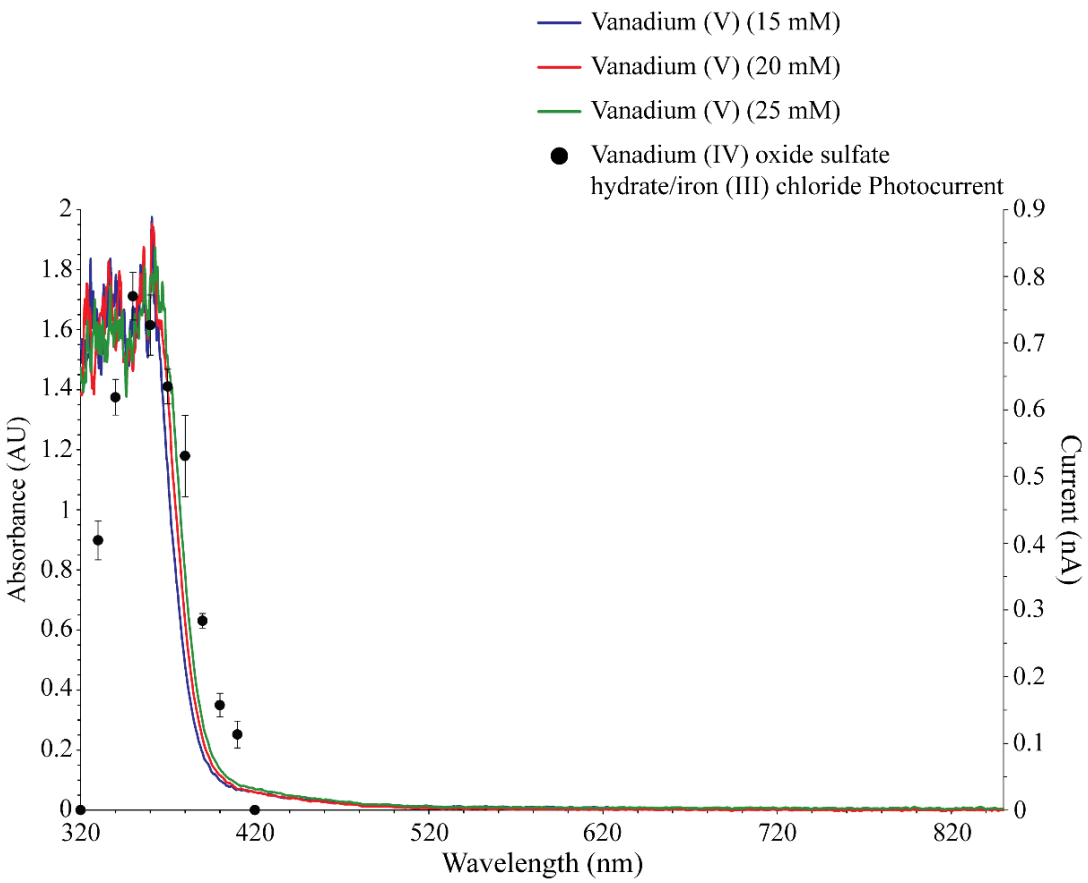

Figure 5.12: Observed photocurrent action spectrum and absorbance spectrum for vanadium (IV) ions

The observed photocurrent action spectrum generated at wavelengths between 320 and 420 nm from Figure 5.9 was plotted against the absorbance spectrum of vanadium (IV) ions provided by M. Chimes (personal communication).

The prediction that vanadium (IV) ions had undergone a redox reaction is supported by the information found in the vanadium Pourbaix diagram (Figure 5.13). The vanadium Pourbaix diagram indicates that vanadium will undergo a change in oxidation state from vanadium (IV) to vanadium (V) at approximately pH 0 in aqueous conditions (Figure 5.13). The photocurrents observed in Figure 5.9 were generated in a solution containing sulphuric acid and had a low pH of 0.14. However, reduction of vanadium (IV) to vanadium (V) will only occur in the presence of the right oxidant. The material data safety sheet for vanadium (IV) oxide sulfate hydrate (Sigma Aldrich) states to avoid moisture and strong oxidizing agents (Section 10: stability and reactivity). Vanadium (IV) oxide sulphate hydrate was stored as a stock solution consisting of 200 mmol dm^{-3} vanadium (IV) oxide sulfate hydrate in 25 ml of water with an adjusted pH to 0.08 via

the addition of nitric acid. It is possible that a redox reaction occurred between the vanadium (IV) ions and dissolved oxygen in the solution resulting in the partial conversion of vanadium (IV) ions to vanadium (V) ions. This stock solution was subsequently used to prepare all vanadium photocurrent solutions.

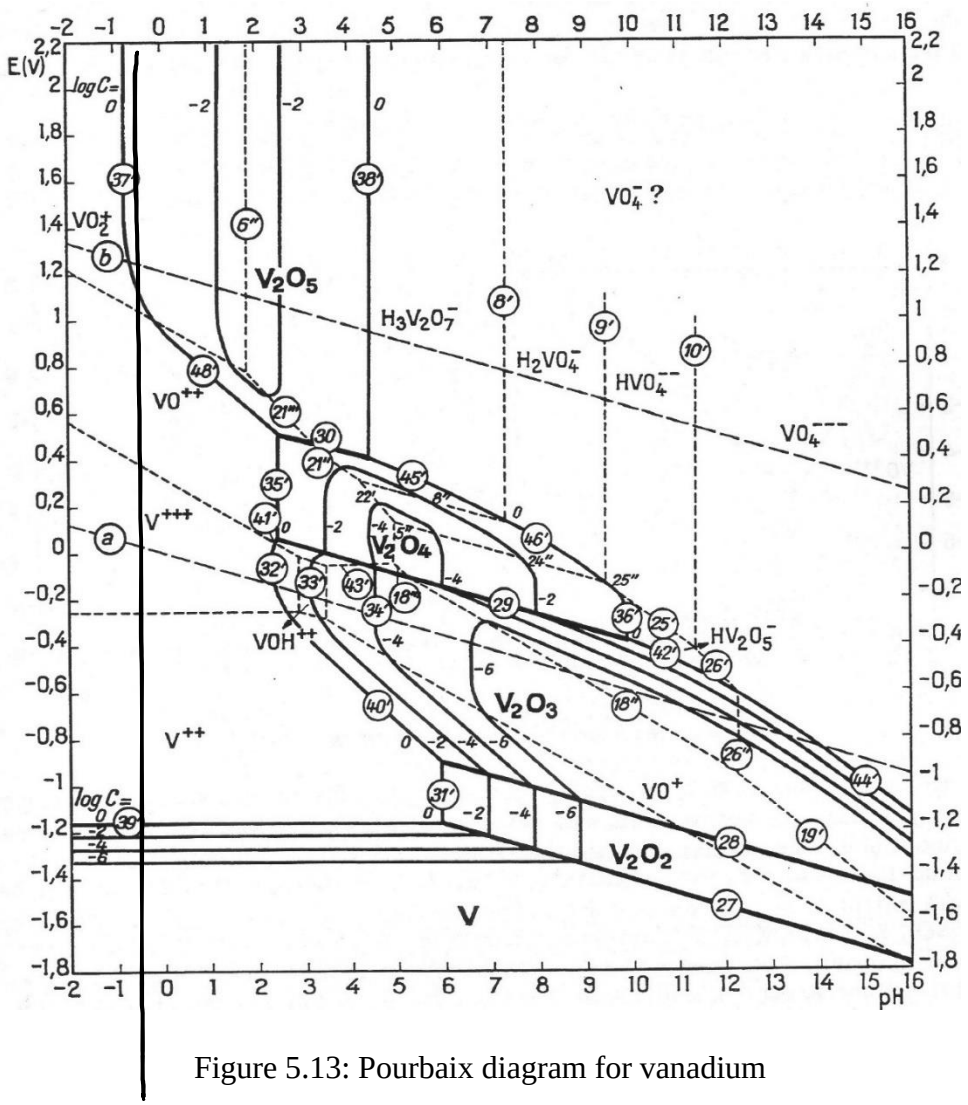

Figure 5.13: Pourbaix diagram for vanadium

(Pourbaix, 1974).

5.2.6 Estimating vanadium (V) concentration

Having discovered that the photocurrent observed in a solution of vanadium (IV) oxide sulphate hydrate solution and iron (III) chloride is likely being generated by vanadium (V) ions, the proportion of vanadium (IV):vanadium (V) ions in the solution used to

measure photocurrents was calculated. To achieve this, the absorption spectrum of the stock vanadium (IV) oxide sulphate hydrate solution was measured (Figure 5.14).

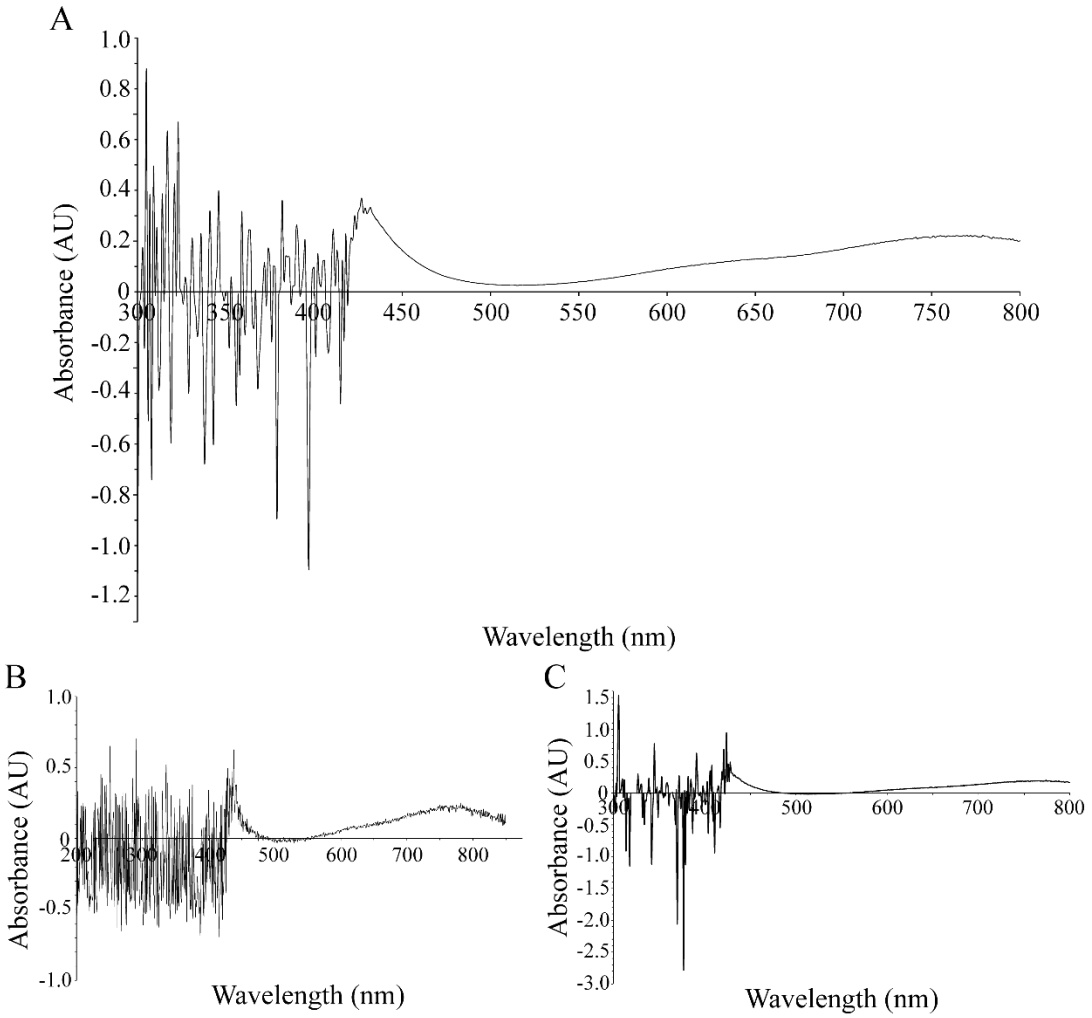

Figure 5.14: Absorbance spectrum of the vanadium stock solution showing poor spectra in the UV region due to an excess of Fe saturating the detector. A, B and C were obtained using different spectrometers.

The absorbance spectrum for the vanadium (IV) oxide sulphate hydrate stock solution at a presumed concentration of 40 mmol dm^{-3} in the presence of iron (III) chloride (200 mmol dm^{-3}) was measured across a range of 300 to 800 nm.

The absorbance peaks for both vanadium (IV) and vanadium (V) were established at various concentrations (Figure 5.10 and Figure 5.12) and both displayed a linear correlation between the maximum absorbance value and concentration. By measuring

the absorbance spectrum for the vanadium (IV) oxide sulphate hydrate stock solution the concentration of vanadium (IV) and vanadium (V) ions based on the strength of the absorption peaks could be calculated. Figure 5.14 shows the absorbance spectrum of the vanadium (IV) oxide sulphate hydrate stock solution at a presumed concentration of 40 mmol dm^{-3} and in the presence of iron (III) chloride (200 mmol dm^{-3}) (vanadium photocurrent solution). An unusual amount of interference was observed between 200 and 450 nm wavelengths. The level of noise observed between 200 and 450 nm unfortunately masked the absorbance spectrum for vanadium (V) which is in the region of 300 to 400 nm (Figure 5.12), this meant it was impossible to identify the absorbance peak for vanadium (V). The interference observed between 200 and 450 nm could be explained due to the inability to prepare and subtract a suitable blank solution from the absorbance spectrum especially as the cuvette absorbs light in the region of 300 nm. The blank used to obtain these spectrums contained water, iron (III) chloride (100 mmol dm^{-3}) and potassium chloride (200 mmol dm^{-3}).

Since the absorbance spectrum for iron (III) chloride shows absorbance in the region of 310 to 430 nm (Figure 5.15) and vanadium (V) absorbs in the region of 350 to 370 nm (Figure 5.12) the presence of both these compounds (and potentially iron (II) chloride too), could help explain the level of the noise observed between 200 and 450 nm. In addition, the absorbance spectrum for iron (III) chloride was generated using a solution at 1 mmol dm^{-3} and generated peaks with a height of 0.7 AU (Figure 5.15). The concentration of iron (III) chloride in the vanadium photocurrent solution was 100 times greater than that used to generate the absorbance spectrum, suggesting that the spectrometer could have become saturated in the absorbance region for iron (III) chloride, contributing to the observed noise in Figure 5.14.

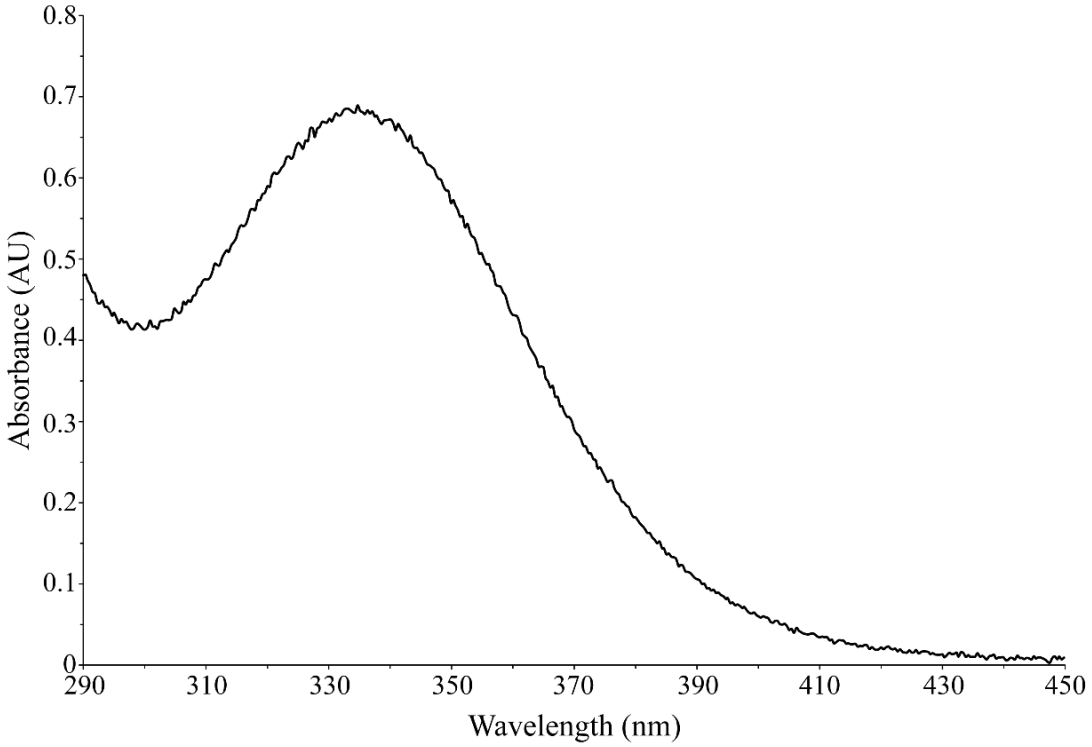

Figure 5.15: Absorbance spectrum of iron (III) chloride

The absorbance spectrum for iron (III) chloride from a 1 mmol dm^{-3} solution dissolved in water with a calculated extinction coefficient of 700 L mol^{-1} cm^{-1} and a pH of 0.08.

Whilst the observed absorbance spectrum for the vanadium photocurrent solution was unusable at wavelengths lower than 450 nm, wavelengths higher than 450 nm gave a clear spectrum (Figure 5.14). The maximum absorbance peak for vanadium (IV) had previously been identified at 765 nm (Figure 3.22) and this peak was easily identified on the absorbance spectrum generated from the mixed vanadium/iron photocurrent solution (Figure 5.14). Figure 5.16 illustrates how the previously established line of best fit Figure 5.16 from the absorbance peaks of various concentrations of vanadium (IV), made it possible to estimate the concentration of vanadium (IV) ions present within the vanadium (IV) oxide sulphate hydrate/iron (III) chloride photocurrent solution. As this relationship is following Beer Lamberts law, the intercept was set to zero. By observing the peak absorbance height of the vanadium photocurrent solution and rearranging the line of best fit equation (Equation 5.1) for x the concentration of vanadium (IV) ions could be estimated.

$$x = \frac{y}{0.0137}$$

Equation 5.1

Where:

x concentration (Mol)

y absorbance

An absorbance peak of 0.299 was recorded at 765 nm in the vanadium photocurrent solution (the maximum absorbance peak for vanadium (IV) oxide sulphate hydrate) (Figure 5.14). Substituting the value of 0.229 for y into Equation 5.1 it is estimated that the concentration of vanadium (IV) ions present in the mixed vanadium/iron photocurrent solution was 21.82 mmol dm^{-3}. The original concentration of vanadium (IV) oxide sulphate hydrate used to create the solution was 40 mmol dm^{-3}; it would therefore appear that a loss of 18.18 mmol dm^{-3} vanadium (IV) ions had occurred. If it is assumed that this loss of vanadium (IV) ions was due to their conversion into vanadium (V) ions, then the concentration of vanadium (V) ions in the vanadium photocurrent solution was estimated to be 18.18 mmol dm^{-3}.

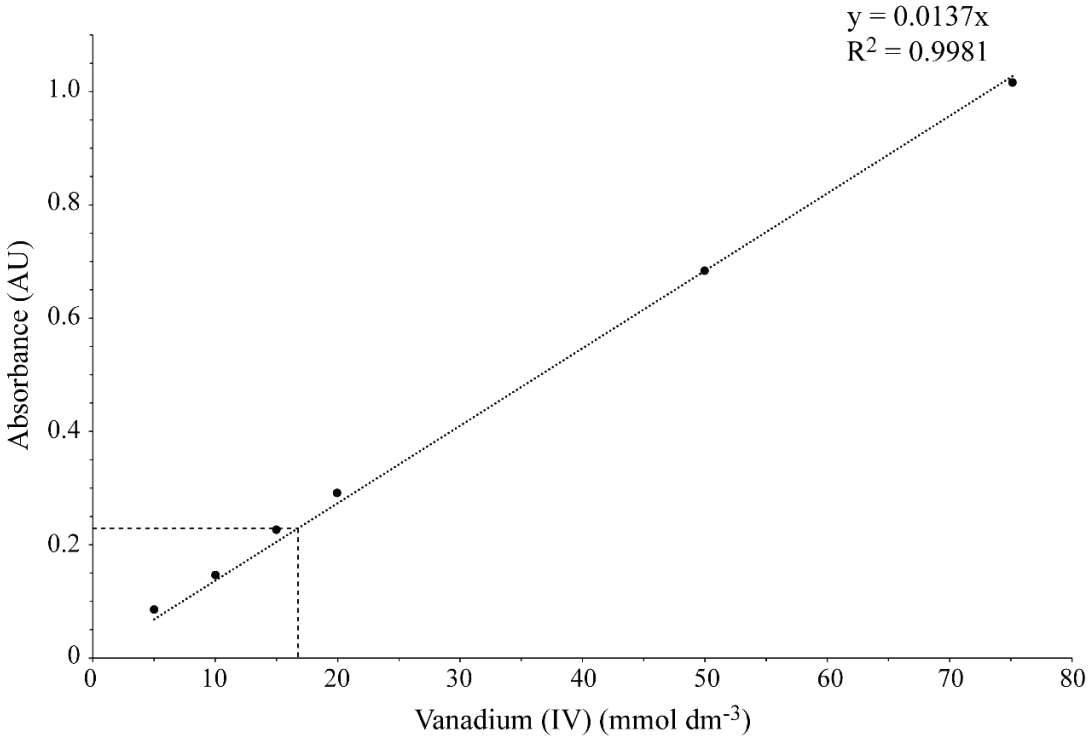

Figure 5.16: The absorbance against concentration for vanadium (IV) oxide sulphate hydrate

By determining where on the line of best fit for the absorbance to concentration gradient the maximum absorbance peak observed in the vanadium photocurrent solution at 765 nm intercepted, a prediction of the concentration of vanadium (IV) ions could be calculated.

5.2.7 Optimum Working Potential

To determine the optimum operating working potential for the vanadium photocurrent solution at the MORE, the amplitude of the photocurrent as a function of working electrode potential was studied. Chronoamperometry experiments were carried out in a solution containing the vanadium (IV) oxide sulphate hydrate stock solution (initially at 40 mmol dm^{-3}), potassium chloride (200 mmol dm^{-3}) and iron (III) chloride (200 mmol dm^{-3}) at a pH of 0.14. As calculated above, it is now predicted that this solution in fact contained a mixture of vanadium (IV) and (V) ions at concentrations of approximately 21.82 mmol dm^{-3} and 18.18 mmol dm^{-3} respectively.

The working electrode potential was varied by 100 mV increments between -0.2 and 0.8 V vs SCE. This range was chosen due to the stability limits of oxygen and hydrogen evolution observed during cyclic voltammetry measurements of vanadium (IV) (Figure

5.5). Under white light illumination conditions, a photocurrent was detected at working electrode potentials between 0.4 and 0.6 V vs. SCE. The maximum photocurrent observed was recorded at 0.4 V vs. SCE (Figure 5.17).

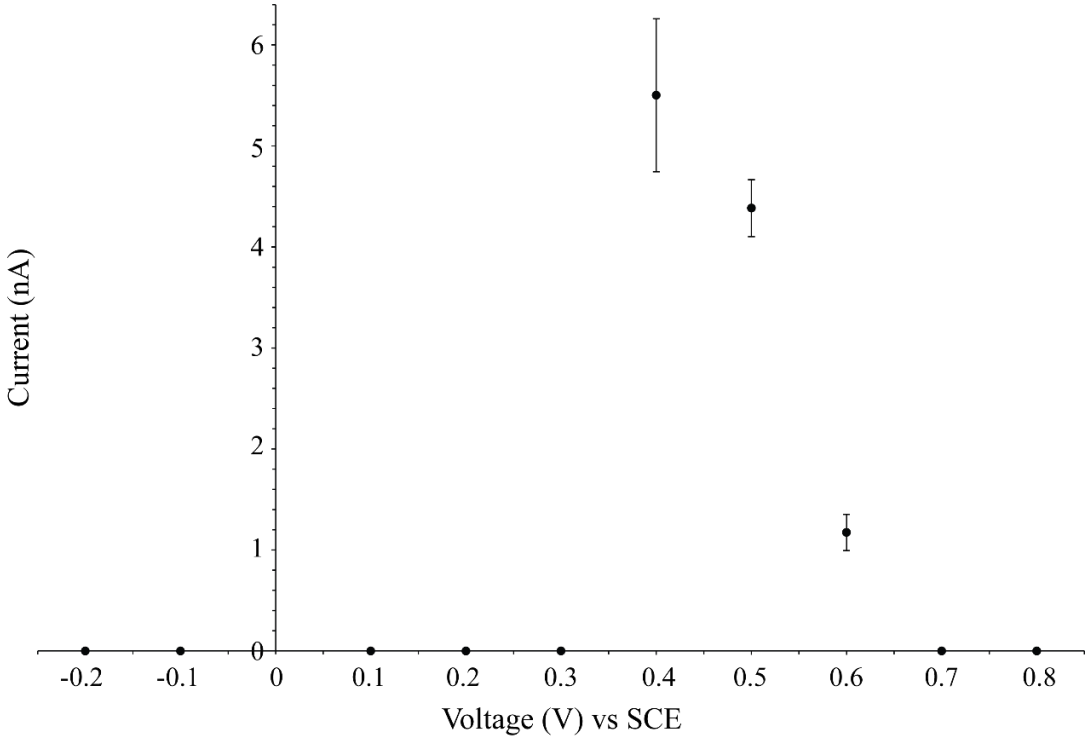

Figure 5.17: Photocurrent generation at a range of working potentials in white light

The current was measured using MORE 1 during 30 s cycles of darkness and white light in a deaerated solution of vanadium photocurrent solution (initially at 40 mmol dm^{-3}), $FeCl_3$ (200 mmol dm^{-3}) and KCl (200 mmol dm^{-3}) at a pH of 0.14 across a range of working potentials.

Figure 5.18 shows the photocurrent recorded under monochromatic illumination at λ = 350 nm as a function of working electrode potential. This wavelength was chosen because it had previously been determined to be the optimal illumination wavelength for this system (Figure 5.9). A photocurrent was successfully detected at working electrode potentials ranging between 0.4 and 0.7 V vs. SCE, with the highest photocurrent detected at a working electrode potential of 0.5 V vs. SCE (Figure 5.18).

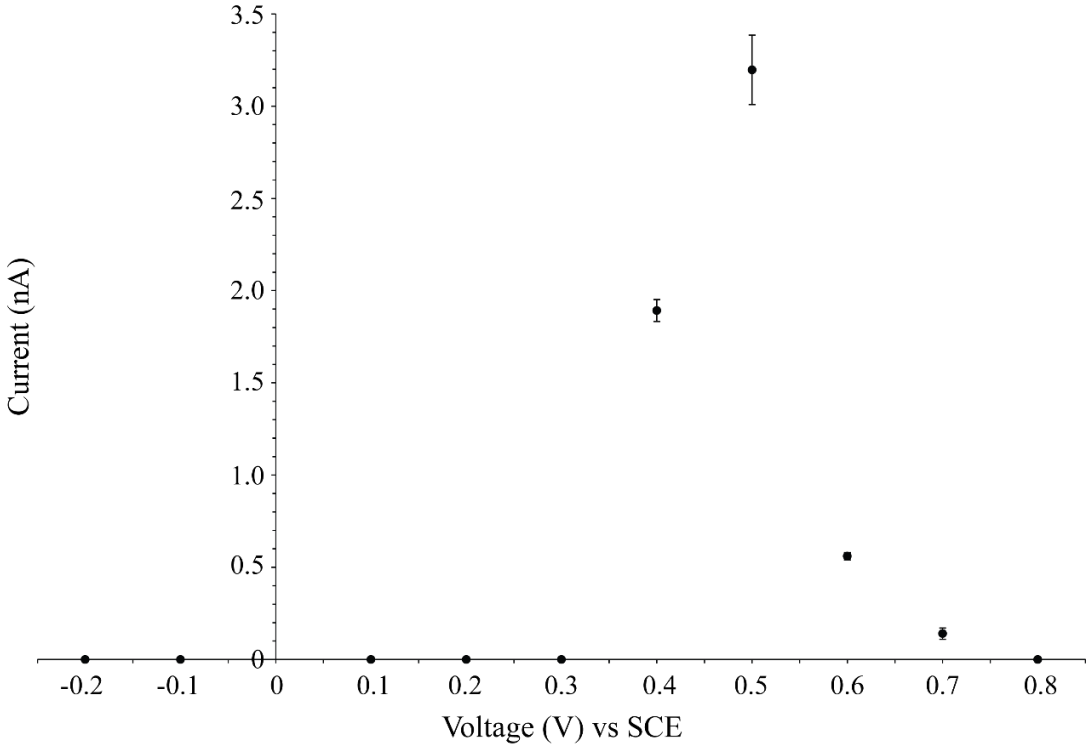

Figure 5.18: Photocurrent generation at a range of working potentials in 350 nm light

The current was measured using MORE 1 during 30 s cycles of darkness and 350 nm wavelength of light in a deaerated solution of vanadium photocurrent solution (initially at 40 mmol dm^{-3}), $FeCl_3$ (200 mmol dm^{-3}) and KCl (200 mmol dm^{-3}) at a pH of 0.14 across a range of working potentials.

The narrow potential range identified for the detection of vanadium suggests that vanadium could be distinguished from other analytes in a mixture with similar optimum illumination wavelengths, by tuning the working electrode potential.

5.2.8 Optimum Scavenger Concentration

Iron (III) chloride was added to the vanadium solution to act as an electron scavenger and only in the presence of iron (III) chloride was a photocurrent detectable in the vanadium solution (Figure 5.7 versus Figure 5.8). Experiments were carried out to understand the effect of iron (III) concentration on the amplitude of the photocurrent detected. Progressively increasing concentrations of iron (III) chloride at 0, 50, 100, 150 and 200 mmol dm^{-3} were added to vanadium photocurrent solution (40 mmol dm^{-3} of vanadium stock solution), the results are shown in Figure 5.19.

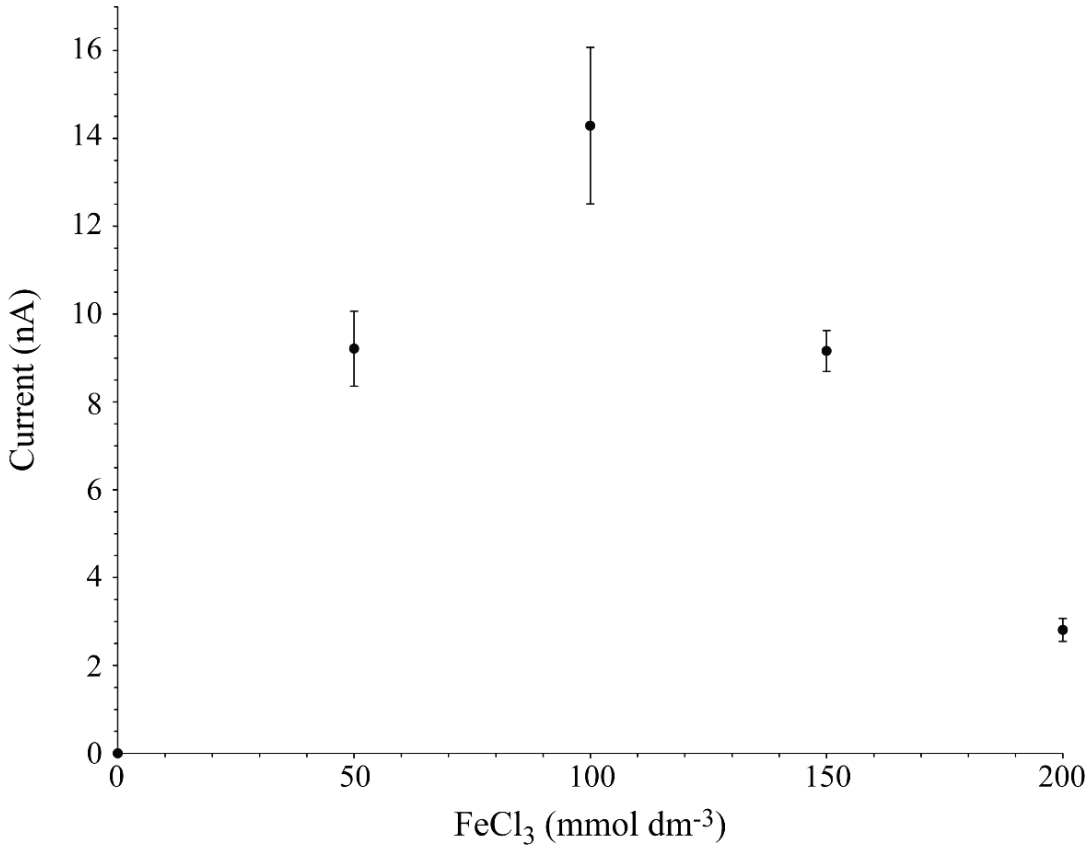

Figure 5.19: Photocurrent detection in various concentrations of iron (III) chloride

The current was measured using MORE 4 during 30 s cycles of darkness and white light in a deaerated solution of vanadium photocurrent solution (initially at 40 mmol dm^{-3}) and KCl (200 mmol dm^{-3}) at a pH of 0.14, a working potential of 0.5 V vs SCE and in the presence of various concentrations of $FeCl_3$.

A photocurrent of magnitude 9.2 nA was successfully generated at an iron (III) concentration of 50 mmol dm^{-3} (Figure 5.19). The maximum photocurrent observed was 14.3 nA with an iron (III) concentration of 100 mmol dm^{-3} (Figure 5.19). At concentrations of iron (III) chloride above 100 mmol dm^{-3} the magnitude of the photocurrent fell with an amplitude of 9.5 nA observed in the presence of 150 mmol dm^{-3} iron (III) and 2.8 nA in the presence of 200 mmol dm^{-3} iron (III) (Figure 5.19).

The mathematical model presented in section 1.1.1, predicts that the photocurrent magnitude would remain steady in the presence of scavenger concentrations greater than the optimum, however the data in Figure 5.19 differs from this prediction. Due to this discrepancy the mathematical model relating to the scavenger and acceptor concentration will not be applied to this data. One possible reason for this behaviour is

the higher concentrations of iron (III) in solution may cause an attenuation of the light, effectively reducing the number of photons available to photoexcite the vanadium ions, which may be caused by the overlap in the absorption peak for iron (III) chloride at 335 nm (Figure 5.15) and that for the photoexcitation of vanadium (V) ions at 350 nm.

The Beer-Lambert equation (Equation 5.2) may be used to estimate the thickness of the absorbance layer to which light penetrated into the solution; that is the distance over which the light intensity dropped to 1/e of the value at the surface of the MORE. The Beer Lambert length was calculated for light absorption in solutions of vanadium (IV/V) ions with varying concentrations of iron (III) chloride. If an increase in iron (III) concentration was impacting the availability of light to the vanadium ions the light absorption thickness calculated by the Beer Lambert equation would decrease.

$$x_\varepsilon = \frac{1}{\varepsilon_\lambda [S]}$$

Equation 5.2

x_ε	Beer Lambert length
ε_λ	Extinction coefficient at wavelength (λ)
$[S]$	Concentration of analyte

The kinetic length (Equation 5.3) is the thickness of the reaction layer, which is the distance the photoexcited sensitizer (S^*) can diffuse before it returns to the non-excited counterpart (S).

$$x_k = \sqrt{\frac{D_s}{k_0}}$$

Equation 5.3

x_k	Kinetic Length
D_s	Diffusion coefficient
k_0	Rate constant

If the Beer Lambert length is greater than the Kinetic Length then the attenuation of the light would have no impact on the photocurrent, whereas if the kinetic length becomes greater than the Beer Lambert length, then the excitation only occurred in part of the

volume. To determine the kinetic length a value of k_0 must be determined. This can be found by determining Stern-Volmer constant which is usually found by plotting 1/photocurrent against 1/acceptor when a linear relationship is seen (section 4.6). As a linear relationship is not seen after 100 mmol dm^{-3} of acceptor (Figure 5.19) it would be worth repeating this experiment with a greater number of acceptor concentrations below 100 mmol dm^{-3}. If a linear relationship is observed then the Stern-Volmer constant can be determined and a value of k_0 and the kinetic length can be calculated.

The presence of iron (III) chloride in the vanadium photocurrent solution at a concentration of 50, 100, 150 or 200 mmol dm^{-3} aided the production of a photocurrent (Figure 5.19). However, the addition of iron (III) chloride at concentrations above 100 mmol dm^{-3} appeared to impede photocurrent generation (Figure 5.19). The Beer Lambert depth was calculated for each of the iron (III) chloride concentrations used in Figure 5.19. The illumination depth (as calculated by the Beer Lambert equation) was subsequently compared to the photocurrent generated in the presence of each concentration of iron (III) chloride (Figure 5.20A and B). A concentration of 100 mmol dm^{-3} iron (III) chloride resulted in the largest photocurrent observed (Figure 5.20B). The calculated illumination volume for a solution with an iron (III) chloride concentration was ~$1.2x10^{-5}$ cm^3. The Beer Lambert length for a solution containing 150 mmol dm^{-3} iron (III) chloride was calculated as ~$8x10^{-6}$ cm^3 (Figure 5.20A)The reduction in Beer Lambert volume in a solution containing 150 mmol dm^{-3} iron (III) chloride compared to 100 mmol dm^{-3} iron (III) chloride coincides with an observed reduction in photocurrent generation (below A and B). Comparing the calculated Beer Lambert lengths and the observed photocurrents suggest that the minimum volume of solution that can be illuminated whilst allowing a steady flow of ions to be photoexcited and generate a photocurrent lies between ~ $1.2x10^{-5}$ cm^3 and ~ $8x10^{-6}$ cm^3 for a vanadium photocurrent solution in the presence of iron (III) chloride.

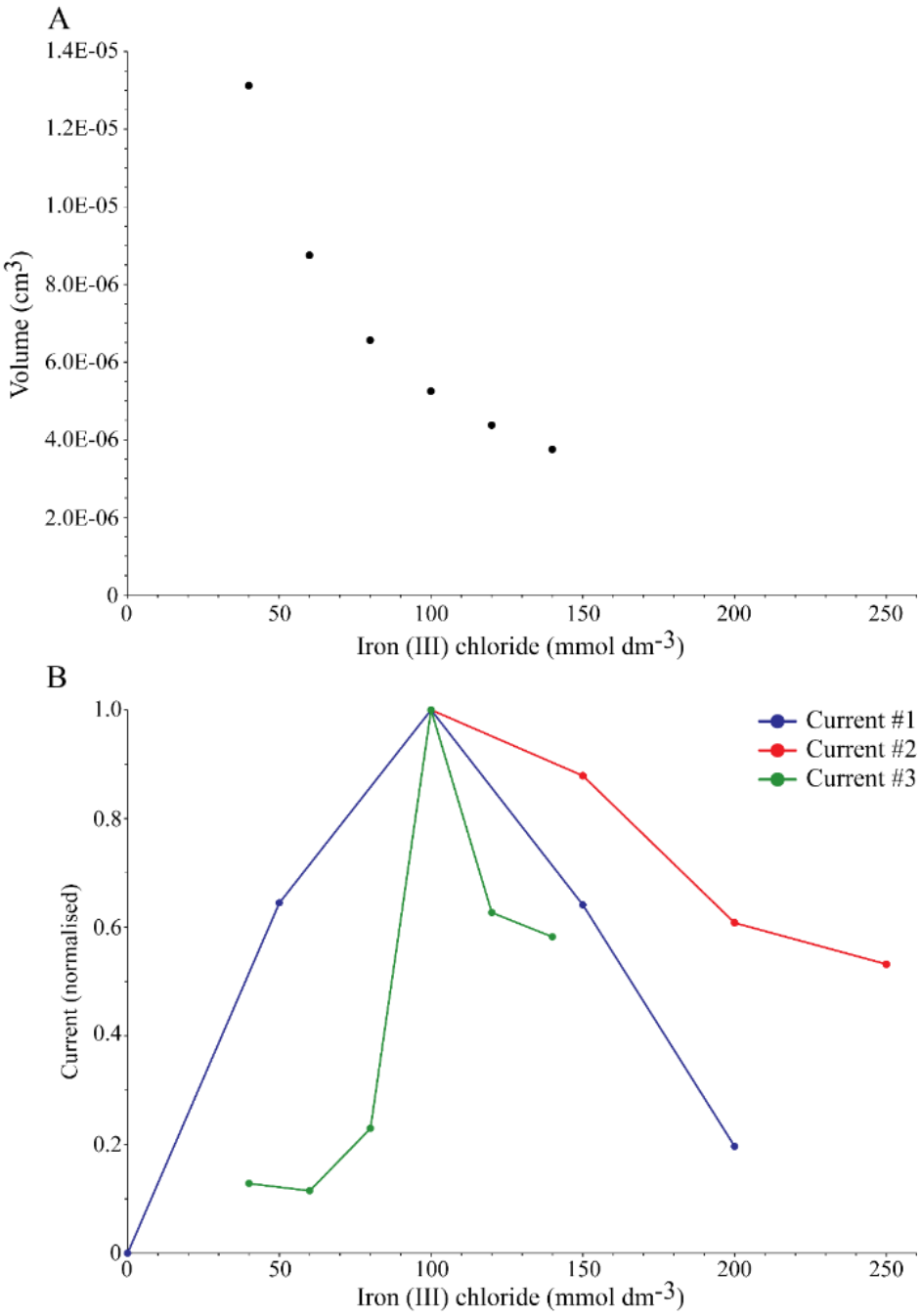

Figure 5.20: Iron (III) concentration as a function of both Beer Lambert length and photocurrent.

A: The Beer Lambert length calculated for various concentrations of iron (III) chloride.
B: Three independent photocurrent generation experiments in various concentrations of iron (III) chloride, normalized to the maximum observed photocurrent per experiment.

5.3 Limits of Detection

Up to this point all the photocurrent experiments have used the same concentration of vanadium stock solution (40 mmol dm^{-3}). However, it would be useful to know the sensitivity of the MORE and establish the lowest concentration of vanadium that can generate a detectable photocurrent.

Photocurrents were measured in a solution containing 35 mmol dm^{-3} vanadium stock solution and iron (III) chloride (100 mmol dm^{-3}). A diluting solution containing potassium chloride (200 mmol dm^{-3}) and iron (III) chloride (100 mmol dm^{-3}) was progressively added to vanadium stock solution after each photocurrent detection to produce a dilution series. A chronoamperometry was established with a voltage of 0.5 V vs SCE applied for the duration of the experiment. To initiate a photocurrent the light was switched on at 50 seconds and left on for an additional 50 seconds after which it was switched off. The light on light off cycle was repeated at least three times to generate at least three separate photocurrents for each concentration tested and the average calculated. Following the production of the chronoamperometry the dilution solution was added to the vanadium stock solution, bubbled with nitrogen for 15 minutes and the experiment repeated. The photocurrent measurement and subsequent dilution of the vanadium stock solution was repeated six more times resulting in photocurrents collected for the vanadium stock solution with concentrations of 35, 30, 25, 20, 15, 10, 5, 2 and 1 mmol dm^{-3}.

As seen in Figure 5.21, a decreasing photocurrent magnitude was observed as the concentration of vanadium stock solution decreased. The maximum concentration of vanadium stock solution (35 mmol dm^{-3}) tested generated the largest photocurrent at 4.3 nA (Figure 5.21). Despite diluting the vanadium stock solution to 1 mmol dm^{-3} the lowest concentration tested that resulted in an attainable photocurrent was 2 mmol dm^{-3} which resulted in a photocurrent of 0.2nA.

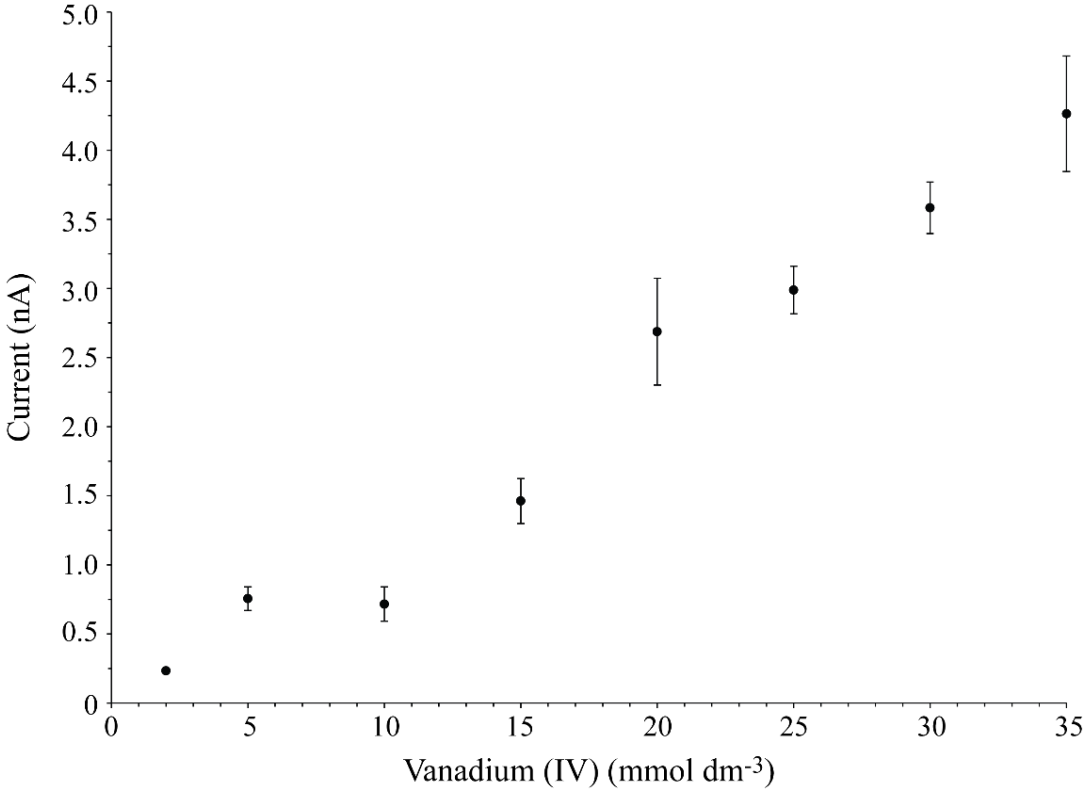

Figure 5.21: Limits of detection recorded at the MORE

The current was measured using MORE 4 during 50 s cycles of darkness and 350 nm wavelength of light in a deaerated solution of vanadium stock solution at an initial concentration of 35 mmol dm^{-3}, $FeCl_3$ (100 mmol dm^{-3}) and KCl (200 mmol dm^{-3}) at a pH of 0.08 and a working potential of 0.5 V vs SCE. Following each photocurrent measurement, the vanadium photocurrent solution was diluted with KCl (200 mmol dm^{-3}) and $FeCl_3$ (100 mmol dm^{-3}) and the photocurrent measurements repeated.

A considerable amount of drift was observed in the chronoamperogram generated with the various concentrations of vanadium stock solution. The presence of drift could have obscured any photocurrent generated from the very lowest concentration of vanadium stock solution tested. The elimination of this drift may improve the sensitivity of the MORE to lower concentrations of sensitizer.

5.3.1 Recalculating the limits of detection to account for the presence of vanadium (V) ions

As mentioned in section 5.2.5 it would appear that vanadium (V) ions, not vanadium (IV) ions are being detected by the MORE. The flux between vanadium (IV) and vanadium (V) ions and the knowledge that it is vanadium (V) ions that are generating the photocurrent means that the observed limit of detection needs to be amended to account for the ratio of vanadium (IV) to vanadium (V) ions. If it is assumed that only vanadium (V) is generating a photocurrent, and that the ratio of the initial concentration of vanadium (IV) to final vanadium (V) ions is approximately 1:0.45 then the initial starting concentration of vanadium (V) ions in the experiment was in fact 15.91 mmol dm^{-3}. Following dilution, the concentration of vanadium (V) ions would have been 13.64, 11.36, 9.09, 6.82, 4.55, 2.27 and 0.91 mmol dm^{-3}. Figure 5.22 shows the observed photocurrent measured in Figure 5.21 but plotted against the calculated concentration of vanadium (V) ions. It would now appear that the limit of detection of the MORE is closer to 0.91 mmol dm^{-3} rather than the 2 mmol dm^{-3} suggested previously (Figure 5.21).

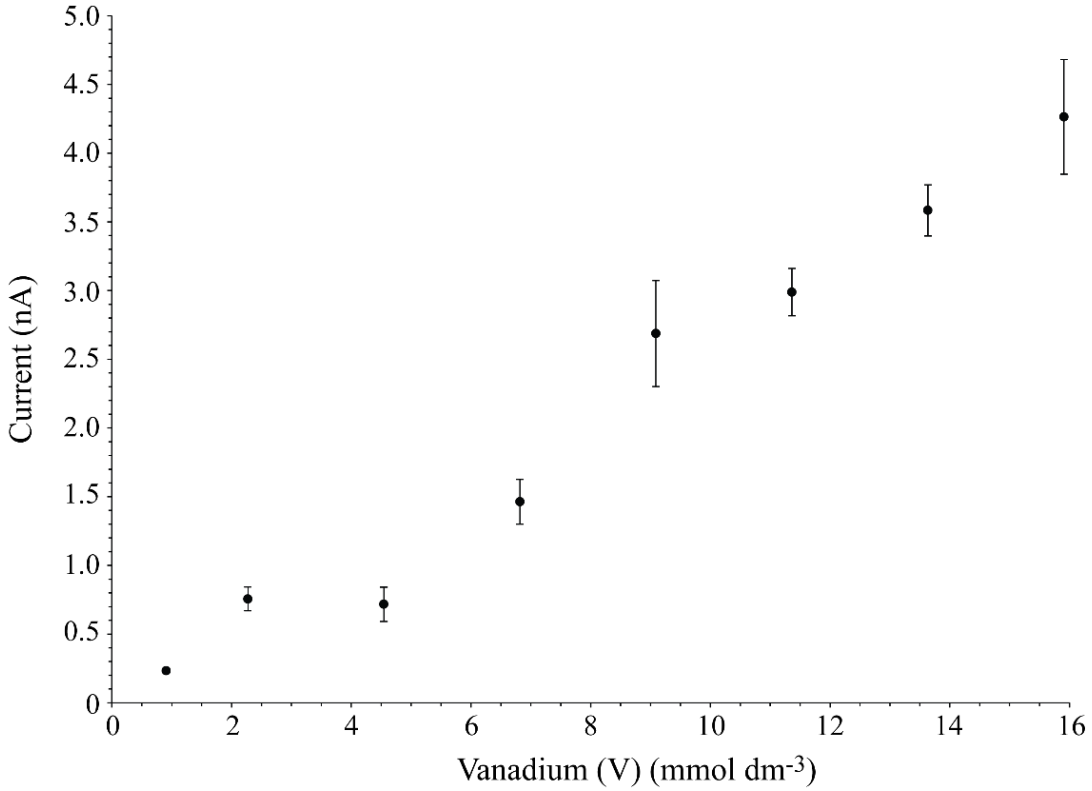

Figure 5.22: Limit of detection of the MORE corrected for the presence of vanadium (V)

The photocurrents generated in Figure 5.21 plotted against the calculated concentration of vanadium (V) ions present in the solution.

5.4 Kinetics

The accuracy of the mathematical model was assessed by plotting the photocurrent normalised to its value as a function of time and comparing the normalised photocurrent with the predicted shape of the transient response of the MORE, using Equation 4.3. Figure 5.23 shows the results for three different photocurrents compared to the theoretical normalised photocurrent given by Equation 4.3.

Adjusting the value of k_2 in Equation 4.3 varies the gradient of the rising portion of the transient. Once the theoretical and experimental values coincide a value of k_2 can be determined. Utilizing these results, the k_2 for vanadium was determined to be 0.062 s^{-1}. A chi squared statistical analysis was carried out to assess whether there was any statistically significant difference between the theoretical and experimental photocurrents. Three experimental photocurrents were independently compared to the theoretical photocurrent and a p-value of 1 was obtained for all three comparisons. This

suggests that all three experimental photocurrents are significantly similar to the theoretically calculated values.

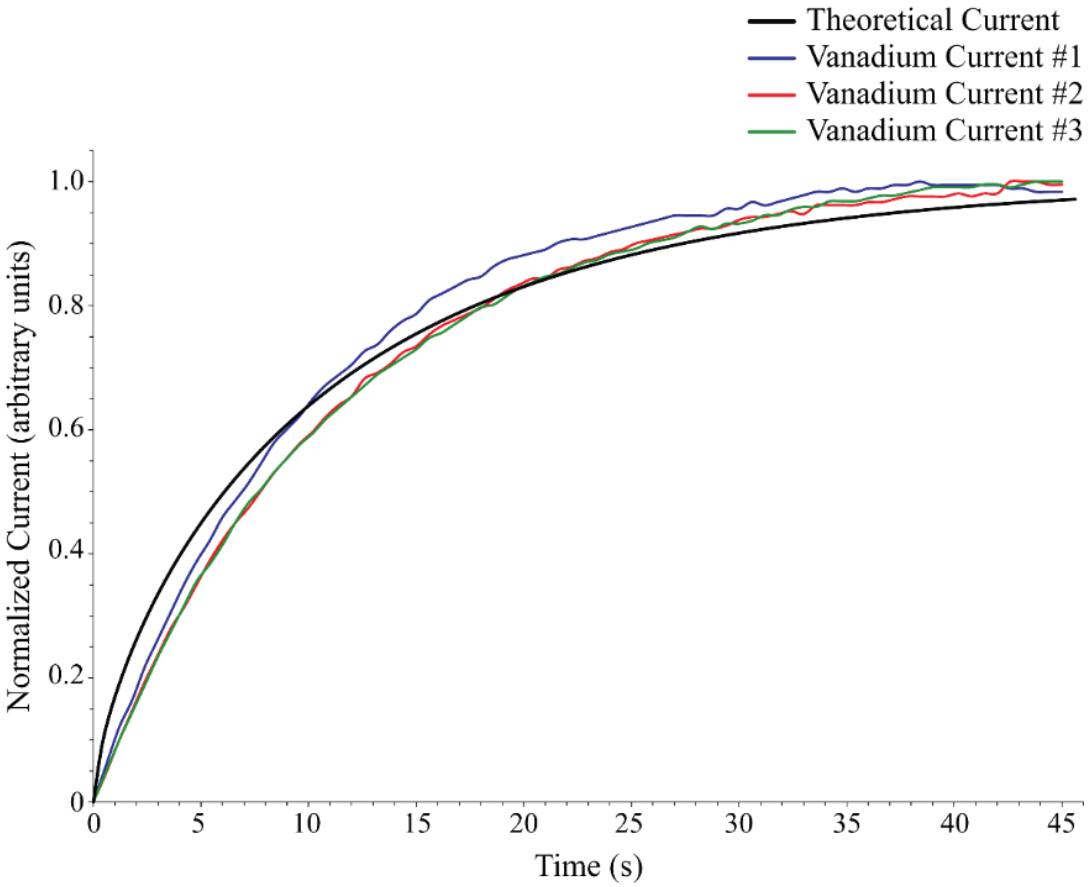

Figure 5.23: Theoretical and experimental transient response of the more with a normalized current

The current was measured using MORE 4 during 50 s cycles of darkness and 350 nm wavelength of light in a deaerated solution of vanadium stock solution (at a presumed concentration of 40 mmol dm^{-3}), $FeCl_3$ (100 mmol dm^{-3}) and KCl (200 mmol dm^{-3}) at a pH of 0.14 and a working potential of 0.5 V vs SCE. The experiment was repeated three times and compared to the mathematical model values to determine k_2.

5.5 Conclusion

This chapter has detailed the results gathered relating to the detection of vanadium photocurrents by the MORE. A successful generation and measurement of photocurrents at a variety of concentrations of vanadium stock solution have been demonstrated. It was also discovered that vanadium (IV) oxide sulphate hydrate likely converts to vanadium (V) when in solution. The following optimal parameters were identified; a working potential at 0.5 V vs SCE, a wavelength at 350 nm and iron (III chloride as an electron scavenger at a concentration of 100 mmol dm^{-3}. The limits of detection were also found to be between 1 and 2 mmol dm^{-3} for the vanadium stock solution which has been corrected to 0.91 mmol dm^{-3} for vanadium (V) ions alone. The kinetics of the system were also established by comparing the theoretical current with those experimentally observed which generated a of k_2 value of 0.062 s^{-1}.

Repeating these experiments starting with a fresh solution of vanadium (V) ions would be beneficial to confirm that it is vanadium (V) responsible for the generated photocurrents. Further investigation into vanadium (IV) oxide sulfate hydrate transforming into vanadium (V) when in solution would also be useful. Once a solution containing vanadium (IV) oxide sulfate hydrate had been made, the absorbance spectrum could be taken at regular intervals to give some insight on the rate of the reduction reaction.

It would also be of benefit to repeat the photocurrent and acceptor concentration experiments with acceptor concentrations below 100 mmol dm^{-3}. If a linear relationship applies then the Stern-Volmer value can be determined and a value of k_0 and the kinetic length can be calculated. This would allow for a comparison between the kinetic length and the Beer Lambert length.

6 Multiple Analyte Studies

6.1 Introduction

This work has shown that the MORE can generate photocurrents with single analytes of uranyl and vanadium with previous work demonstrating photocurrents generated by ruthenium (Andrieux, Boxall and O'Hare, 2006a). An electrode with the ability to identify analytes whilst present in mixtures would be advantageous allowing for broader applications. To detect individual ions in a mixture it is important that the optimal parameters for photocurrent generation of each analyte are sufficiently distinct. These parameters for uranyl and ruthenium are summarized in Table 6.1. Mixtures of vanadium and uranyl, vanadium and ruthenium were also briefly investigated. These experiments failed to generate any photocurrents with a steady state current not being achieved. This resulted in a very noisy signal that may have been due to each analyte/acceptor interfering with one another.

	$Ru(bipy)_3^{2+}$	Uranyl
Wavelength (nm)	460	410
Extinction Coefficient ($L\ mol^{-1}.\ cm^{-1}$)	13,825	7.79
Acceptor Concentration ($mmol\ dm^{-3}$)	5	200
Potential (V)	0.5	0.7
k_2 (s^{-1})	2.5 (Dickinson, 2013)	0.065

Table 6.1: Comparison of various optimal parameters relating to photocurrent generation of $Ru(bipy)_3^{2+}$ and uranyl ions.

6.2 Uranyl and Ruthenium Mixture

To assess whether the MORE could distinguish between two different analytes a deaerated solution containing uranyl (UO_2^{2+}) (40 mmol dm^{-3}), tris(2,2'-bipyridyl)ruthenium (II) chloride hexahydrate ($Ru(bipy)_3^{2+}$) (10 mmol dm^{-3}), iron (III) (5 mmol dm^{-3}) and ethanol (200 mmol dm^{-3}) was prepared.

6.2.1 Generating a photocurrent in a uranyl (VI) and $Ru(bipy)_3^{2+}$ mixture

Initially photocurrents were generated targeting the optimum parameters for uranyl and the optimum parameters for $Ru(bipy)_3^{2+}$. This was done to ensure individual photocurrents would still be generated in a mixed solution. Figure 6.1A shows a photocurrent generated targeting uranyl with a wavelength of 410 nm and an electrode potential of 0.7 V vs SCE. Uranyl generates a positive photocurrent due to an oxidative reaction, however a strong reduction photocurrent is seen in Figure 6.1A. $Ru(bipy)_3^{2+}$ generates a reduction photocurrent, therefore it is possible that the photocurrent observed in Figure 6.1A is in fact due to ruthenium alone despite this experiment using the optimal parameters for uranyl. Figure 6.1B shows a photocurrent generated targeting ruthenium with a wavelength of 460 nm and an electrode potential of 0.5 V vs SCE. This also displays a strong reduction photocurrent typical of those generated by $Ru(bipy)_3^{2+}$.

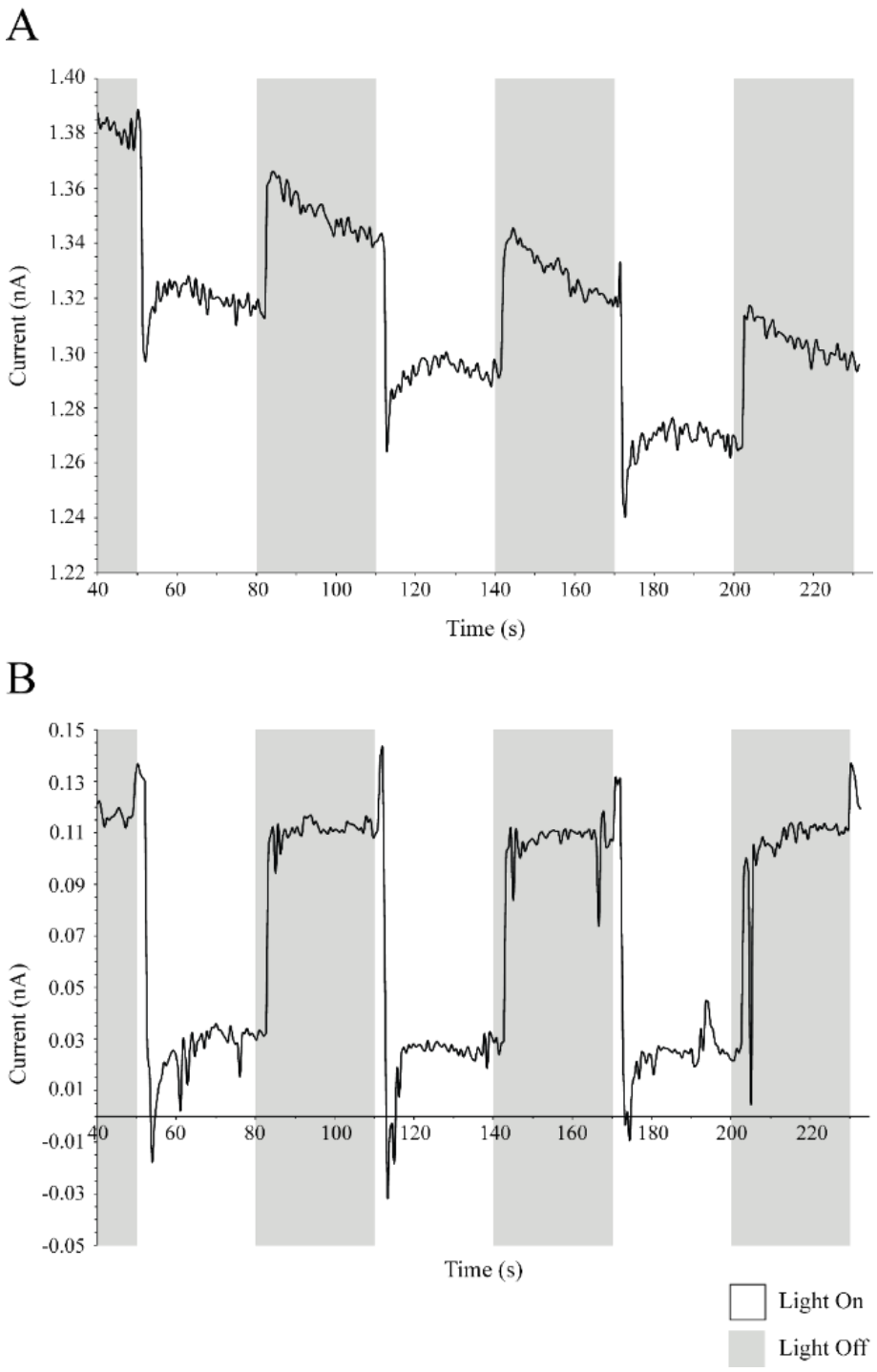

Figure 6.1: Photocurrent detection from a mixture of uranyl and $Ru(bipy)_3^{2+}$

Currents were measured using MORE 4 during 30 s cycles of darkness and targeted wavelength of light in a deaerated solution containing UO_2^{2+} (40 mmol dm^{-3}), $Ru(bipy)_3^{2+}$ (10 mmol dm^{-3}), $FeCl_3$ (200 mmol dm^{-3}) and EtOH (200 mmol dm^{-3}).

A: Targeting uranyl using light at 410 nm and a working potential of 0.7 V vs SCE.
B: Targeting $Ru(bipy)_3^{2+}$ using light at 460 nm and a working potential of 0.5 V vs SCE.

6.2.2 Impact of an additional analyte on photocurrent magnitude

As seen in Figure 6.2 uranyl and $Ru(bipy)_3^{2+}$ have maximum absorbance peaks at different wavelengths. Uranyl has a maximum absorbance peak at approximately 410 nm whereas ruthenium has a maximum absorbance peak at 460 nm.

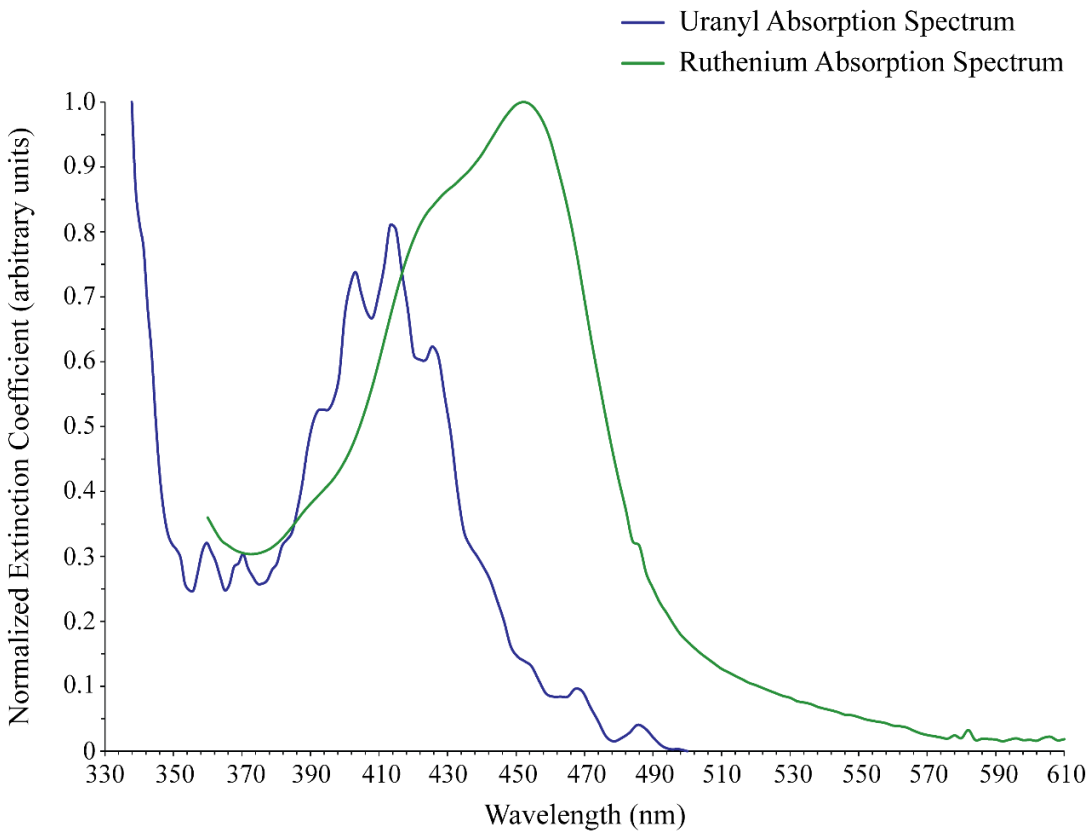

Figure 6.2: Normalized absorption spectrums for $Ru(bipy)_3^{2+}$ and uranyl

The absorbance spectrum for uranyl and $Ru(bipy)_3^{2+}$ were normalized to the maximum value observed for $Ru(bipy)_3^{2+}$.

The uranyl absorption spectrum was compared to the normalized photocurrents generated from a mixture of uranyl (40 mmol dm^{-3}) and $Ru(bipy)_3^{2+}$ (10 mmol dm^{-3}) (Figure 6.3). Different concentration were used due to $Ru(bipy)_3^{2+}$ having a much larger extinction coefficient. If the same concentrations were used there would be little chance of seeing any impact of photocurrents due to uranyl. Uranyl photocurrents are due to an oxidative process as characterized by a positive photocurrent, whereas $Ru(bipy)_3^{2+}$ photocurrents are due to a reductive process and therefore produce a negative photocurrent. Due to the overlap in absorption spectrum of uranyl and $Ru(bipy)_3^{2+}$ both analytes should generate photocurrents within an overlapping range of wavelengths. As

can be seen in Figure 6.3 both photocurrents follow the trend of the $Ru(bipy)_3^{2+}$ absorbance spectrum suggesting uranyl cannot be distinguished.

A

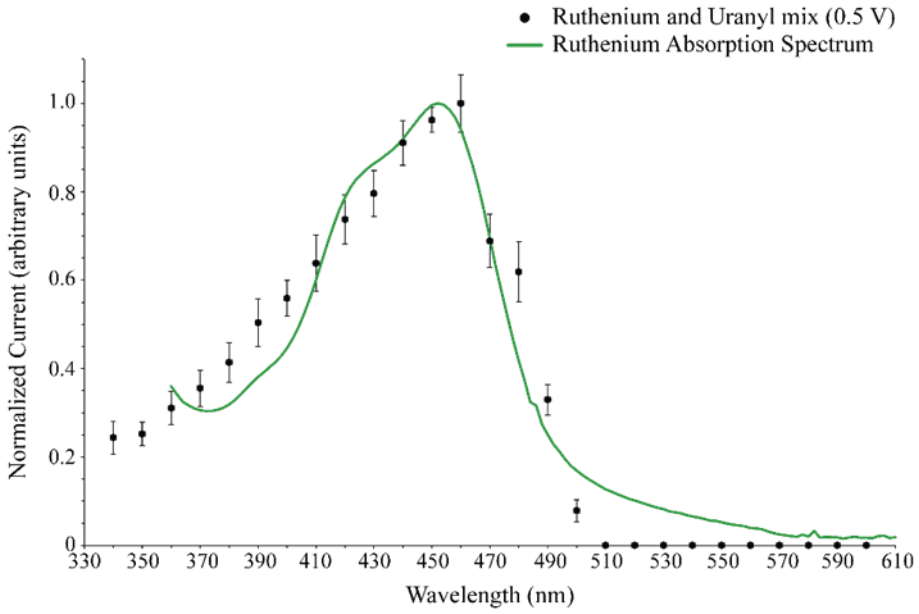

B

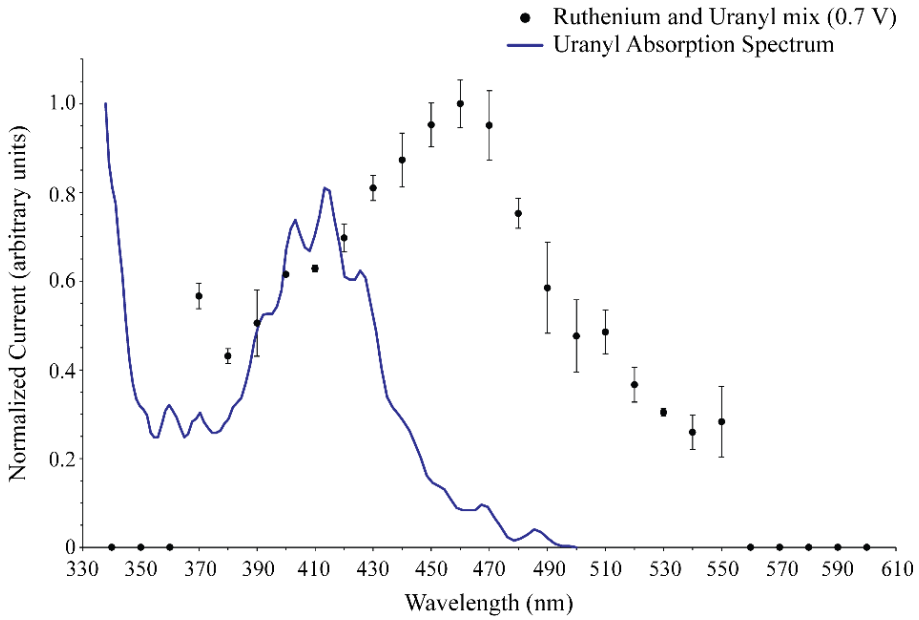

Figure 6.3: Comparison of the photocurrent action spectrum to absorbance spectrum

Currents were measured using MORE 4 during 30 s cycles of darkness and targeted wavelength of light in a deaerated solution containing UO_2^{2+} (40 mmol dm^{-3}), $Ru(bipy)_3^{2+}$ (10 mmol dm^{-3}), $FeCl_3$ (200 mmol dm^{-3}) and EtOH (200 mmol dm^{-3}).

A: Targeting $Ru(bipy)_3^{2+}$ using light at 460 nm and a working potential of 0.5 V vs SCE compared to the ruthenium absorbance spectrum.

B: Targeting uranyl using light at 410 nm and a working potential of 0.7 V vs SCE compared to the uranyl absorbance spectrum.

6.3 Conclusion

These results demonstrate that it was difficult for the MORE to distinguish between two analytes in a mixture. Two key explanations exist that could explain why the MORE was unable to differentiate between a mixture of uranyl and $Ru(bipy)_3^{2+}$. Firstly, both uranyl and $Ru(bipy)_3^{2+}$ have similar maximum absorption wavelengths (410 and 450 nm respectively). Despite the maximum absorption wavelengths being close, yet distinct, it was the case that both uranyl and $Ru(bipy)_3^{2+}$could produce photocurrents at the optimum wavelength of the other. Secondly, in addition to the close proximity of maximum absorbance wavelength, the vast difference in the extinction coefficients of uranyl and $Ru(bipy)_3^{2+}$ meant that photocurrents generated by $Ru(bipy)_3^{2+}$ dominated the recorded current. Diluting the amount of $Ru(bipy)_3^{2+}$ present in the mixture solution may prevent the photocurrents generated by $Ru(bipy)_3^{2+}$ overwhelming those generated by uranyl. If the magnitude of photocurrents generated by the two single analyte solutions were comparable it may be possible to detect the influence of a secondary analyte on photocurrent generation when compared to the single primary analyte solution.

Ideally, when choosing analytes to detect in a mixture it would be preferable if the optimum parameters of maximum absorption and operating working potential were as distinct as possible. If it is not possible for the optimum parameters to sufficiently differ then it would be ideal if the extinction coefficients were comparable to ensure that a photocurrent generated from one analyte did not dominate over the other.

7 Conclusion and Future Work

7.1 Conclusion

The overall aims of this project were to determine whether the MORE was capable of detecting and quantifying uranyl, neptunium (IV), plutonium (III) and plutonium (IV) ions, both individually and combined as a mixed solution. Initially non-radioactive surrogates vanadium (IV) oxide sulphate hydrate and cerium (III) chloride were selected for experimentation. Non-radioactive surrogates were used to test whether the MORE could generate photocurrents from ions with similar chemical properties to their radioactive counterparts. The results obtained by the successful generation of photocurrents were compared to the mathematical model proposed by Andrieux (2005).

7.1.1 Uranium results

The results presented here demonstrate that it is possible for the MORE to detect photocurrents generated by uranyl ions when present in solution. Photocurrent generation by uranyl ions required ethanol as an electron acceptor. It is likely that ethanol acted to reduce photoexcited uranyl to uranium (IV) which was then oxidized at the gold ring. Under the conditions set out in Table 7.1 it was determined that the limit of detection for uranyl was between 2.52 and 7.52 mmol dm^{-3}. The kinetics of the reaction was calculated to be 0.05 s^{-1}. Several parameters can affect the magnitude of a photocurrent detected by the MORE including the wavelength of illumination, the operating working electrode potential and the electron scavenger concentration. The optimal parameters required to generate the largest magnitude photocurrent for the detection uranyl are summarized in Table 7.1.

Sensitizer	Illumination wavelength (nm)	Working potential (V vs SCE)	Electron acceptor	Concentration of electron acceptor (mmol dm^{-3})
Uranyl	410	0.7	ethanol	200

Table 7.1: Optimum parameters for photocurrent generation of uranyl

7.1.2 Cerium results

Cerium (III) chloride was selected for initial experimentation with the MORE as a non-radioactive surrogate for neptunium. The experimental results obtained indicate that it is not possible to detect a photocurrent generated by cerium (III) ions. This is likely due to cerium (III) only having one absorption peak at 297 nm which coincides with the wavelengths of light attenuated by the components of the MORE. In addition, it is possible that to generate a photocurrent cerium (III) chloride requires an electron acceptor different to the ethanol or iron (III) tested here.

7.1.3 Vanadium results

All vanadium experiments carried out with the MORE used an initial solution of vanadium (IV) oxide sulphate hydrate. A photocurrent was successfully detected by the MORE in this solution. The wavelength of illumination that resulted in the largest photocurrent was 350 nm which did not coincide with any absorption peaks associated with vanadium (IV) ions. However, the absorbance peak of vanadium (V) corresponded with the photocurrent action spectra generated by the vanadium photocurrent solution. It was therefore concluded that the observed photocurrent was in fact due to the photoexcitation of vanadium (V) ions only. These results indicate that caution must be taken when selecting a sensitizer as an unexpected redox reaction may occur resulting in a change of oxidation state which could impact photoexcitation and therefore photocurrent generation.

Once the conversion of vanadium (IV) to vanadium (V) ions had been accounted for the limit of detection was calculated as 0.91 mmol dm^{-3}. The mathematical model determined the kinetics of the reaction to be 0.062 s^{-1}. Table 7.2 summarizes the optimal parameters required to generate the largest magnitude photocurrent for the detection vanadium (V) ions.

Sensitizer	Illumination wavelength (nm)	Working potential (V vs SCE)	Electron acceptor	Concentration of electron acceptor (mmol dm^{-3})
Vanadium (V)	350	0.5	Iron (III) chloride	100

Table 7.2: Optimum parameters for photocurrent generation of vanadium (V)

7.1.4 Detection of individual ions in mixtures

In order to detect individual ions in a mixture it is important that the optimal parameters of detection are sufficiently distinct. During experimentation, it was found that the optimum wavelength of illumination for uranium, vanadium and ruthenium were all very similar (410 nm, 350 nm and 460 nm respectively). The similarity in optimal wavelengths meant that identifying the individual photocurrent generated by either uranium or ruthenium in a mixed solution proved difficult. In addition, the relatively large extinction coefficient of $Ru(bipy)_3^{2+}$ (13,825 L mol^{-1} cm^{-1} (Andrieux, Boxall and O'Hare, 2006a)) meant that the photocurrent generated by ruthenium ions dominated and potentially obscured that produced by uranyl.

7.1.5 Surface finish results

This study has shown that the surface finish at the tip of the MORE influences the size of the generated photocurrent. It was found that a smooth finish at the tip of the MORE abolished its ability to generate a photocurrent. However, a rougher surface finish at the tip of the MORE resulted in photocurrents with larger amplitudes. To understand why a rougher surface finish resulted in an increase in photocurrent detected, the tip of the MORE was examined using both SEM and AFM. A recess was found to form at the electrode tip due to excessive abrasion of the gold layer. Whilst the optical fibre and the epoxy coating of the MORE have similar hardness ratings (7 and 6.5 respectively (Frost, 2006)), the gold layer is much softer (2.5 (Frost, 2006)) meaning it is more susceptible to erosion during the polishing procedure.

Microscopy images were also used to estimate the thickness of the gold ring. Cross-sections of the same MORE were analysed by both SEM and AFM. SEM images estimated the ring thickness to be ~0.238 µm whilst the AFM estimated the thickness to be ~5.15 µm. In addition to the microscopy imaging electrochemical sizing experiments were performed and estimated a gold ring thickness of ~2.5 µm. MOREs fabricated by Andrieux et al. (2006) and using the same electrochemical sizing method resulted in an estimated gold ring thickness of ~5 nm (Andrieux, Boxall and O'Hare, 2006a). However, a MORE sample made by Andrieux was analyzed by AFM as part of this investigation and had an estimated ring thickness of ~5.25 µm. The large variation in estimated gold ring thickness of the MOREs means that an accurate method for determining the size of the ring thickness has yet to be determined. An accurate size of the gold ring is required to determine the unknown concentration of analytes of interest using the mathematical model .

7.2 Further Work

7.2.1 Vanadium (V)

Having identified that vanadium (V) ions and not vanadium (IV) ions generate a photocurrent, it would be worth repeating the experiments carried out here with a starting solution of vanadium (V) ions. This would allow for a more accurate determination of the parameters required for a vanadium (V) photocurrent. Once the parameters for photocurrent generation have been established for vanadium (V) it may also be possible to more accurately determine the limit of detection. If the parameters identified for vanadium (V) ions corresponded with those determined in this thesis, it would corroborate the hypothesis that the photocurrent identified in the vanadium solution was indeed due to vanadium (V) ions.

7.2.2 Mathematical Model

This work has demonstrated that the surface finish of the MORE impacts the magnitude of the generated photocurrent. The mathematical model devised by Andrieux, Boxall and O'Hare, (2006b) utilized MOREs fabricated with a smooth surface finish. No experimentation was carried out on the impact of surface finish on photocurrent magnitude and as such the mathematical model does not take surface finish into consideration (Andrieux, Boxall and O'Hare, 2006b). In light of the results presented here, the mathematical model needs to be amended to accommodate the effects of surface finish on photocurrent magnitudes.

7.2.3 Neptunium and Plutonium

Due to difficulty obtaining access to neptunium and plutonium samples, experiments with these ions were not possible. However, given the success of generating photocurrents with uranyl, which has a relatively low extinction coefficient (7.9 L mol^{-1} cm^{-1}) (Burrows and Kemp, 1974b) when compared to neptunium (83 L mol^{-1} cm^{-1}) (Gangwer, 1977) and plutonium (41 L mol^{-1} cm^{-1}) (Clark, 2000), the prospect of detecting photocurrents generated by neptunium and plutonium ions with the MORE seems likely. In addition, the maximum absorbance peaks of neptunium (723 nm and 964 nm) (Gangwer, 1977) and plutonium (570 nm and 605 nm) (Clark, 2000) are sufficiently distinct that it is plausible the individual ions of neptunium and plutonium could be detected in a solution containing a mixture of the two.

7.2.4 Redesign of MORE

Whilst the current MORE design has successfully detected photocurrents, there are some areas for potential improvement. In particular the ability to regulate the tip of the MORE with regards to gold ring thickness and surface finish.

One possibility for a new design is demonstrated in Figure 7.1. The redesigned MORE would introduce a UV-vis-nIR transparent window (e.g. quartz), a thin electrode layer and a low power light source. It would also have integrated counter and reference electrodes resulting in miniaturisation of the device. An example of a low power light source would be the use of LED lights. A potential drawback of the use of LED lights is that they only emit a single wavelength of light; this would not be an issue when sampling analytes of a known illumination wavelength but could cause issues if the redesigned MORE was deployed in a mixture of unknown analytes.

The new design would eliminate the need for a fibre optic core and insulating araldite resin. The new design would not require polishing either, thus eliminating the possibility of a recess forming in the conducting gold layer.

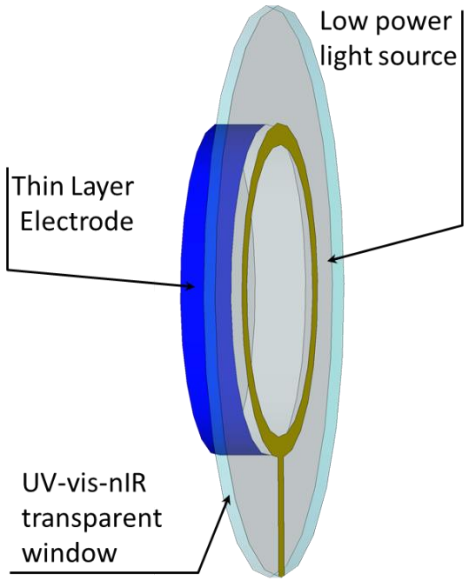

Figure 7.1: Possible redesign of the MORE

7.2.5 Further applications of MORE

7.2.5.1 Americium-241

The MORE could be used to investigate any system that involves a photochemically initiated reaction that results in an electron exchange. One possible application of the MORE could be the detection of americium-241. Amercium-241 has an extinction coefficient of 340 L mol^{-1} cm^{-1} at its maximum absorbance peak at 504 nm (Hall and Herniman, 1954). Currently americium-241 is considered a waste product of the nuclear industry and is generated during beta decay of plutonium-241. During spent nuclear fuel reprocessing americium-241 can be extracted. A number of proposals have been made which plan to turn this waste into an asset by utilizing it as a low output power source

in nuclear space batteries (Sarsfield *et al.*, 2016). Presently plutonium-238 is used for nuclear space batteries and can only be made in reactors dedicated to nuclear weapon manufacturing. However, weapon reactors are now deactivated meaning that a new source of power for nuclear space batteries will be needed. At the National Nuclear Laboratory americium-241 has been harvested from plutonium during spent fuel reprocessing and research is underway into its potential as a fuel for space batteries (Sarsfield *et al.*, 2016). The MORE may be used to confirm extraction has been successful.

7.2.5.2 Applications outside the nuclear industry

Elemental and molecular analysis is required for industries other than the nuclear industry; these include water treatment facilities, pharmaceutical applications and environmental monitoring which currently utilize an ICP-MS for analysis. Theoretically the MORE could be used to detect any analytes of interest providing they have a sufficient absorbance peak and undergo photoexcitation when illuminated.

8 Appendix

8.1 History of Actinides

When neptunium and plutonium were discovered it was believed that their chemical properties would be similar to those of rhenium and osmium. However, chemical tracer experiments demonstrated this to be incorrect (Seaborg, 1990). In 1944, Seaborg proposed that neptunium and plutonium may occupy a second series comparable to that of the lanthanide elements (Seaborg, 1990). As a result, the periodic table was revised to include a second rare earth series called the actinides.

The actinide series of the periodic table contains 15 metallic elements with atomic numbers from 89 (actinium) to 103 (lawrencium). They all decay radioactively into other elements and have complex chemical behaviour due to their outer electron configuration. The actinides have a full 5f electron shell, whereas the lanthanides have a full 4f electron shell. It is this filling of the f shell that results in the actinides and lanthanides having comparable chemical properties. The atomic emission spectra of the actinides are very complex with 100,000 lines having been measured for uranium alone. This complexity arises from the splitting of the energy levels due to interaction of valence electrons with each other and 5f electrons (Seaborg, 1990).

8.2 Electrodes

8.2.1 Geometries

Microelectrode behaviour is dependent on its geometry. There are four main shapes associated with microelectrodes: disc, ring, band and hemispherical. It is possible to obtain a fifth geometry by combining a disc and a ring. A sixth shape is also possible whereby the surface of the electrode is ellipsoidal and is achieved by truncating a disc electrode at an angle, producing a bevelled electrode.

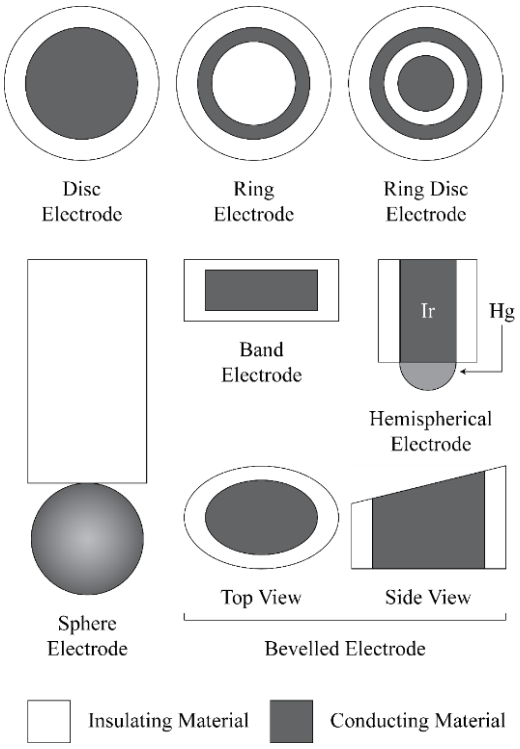

Figure 8.1: Different shapes of microelectrodes.

When microelectrodes of any geometry are connected in parallel the typical low currents associated with microelectrodes can be amplified. The amplification of the signal can be carried out whilst simultaneously retaining the properties of the individual microelectrodes (Wightman and Wipf, 1989).

The circumference of the electrode to the electrode surface is related to the accessibility of the electrode to the electro-active species. Increasing the ratio results in the production of considerably larger current densities and is frequently referred to as the edge effect.

To understand the edge effect, it can be useful to consider a two-dimensional system, in which each dimension is defined by their corresponding axes with their origin at the centre of the electrode. The x-axis is perpendicular to the surface of the electrode whereas the r-axis follows the surface of the electrode. When considering a typical planar macroscopic disc electrode under diffusion control, the current is generated due to semi-infinite linear diffusion of the electro-active species to the electrode surface (Wightman and Wipf, 1989). This means that the majority of the generated current is due to diffusion in the x-axis only with the diffusion to the edge of the electrode providing a marginal contribution to the overall current (Wightman and Wipf, 1989).

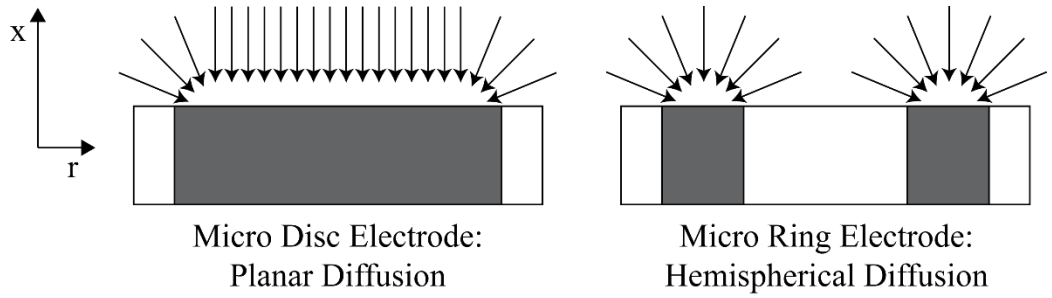

Figure 8.2: Comparison of the available electrode surface area between a disc and ring electrode.

The ratio of the current occurring due to diffusion at the edge of the electrode compared to the centre increases when the dimension of the electrode reduces (Figure 8.2) (Wightman and Wipf, 1989).

Therefore, at the edge of the electrode the electro-active species can access the electrode from along both the x- and the r- axes, thus resulting in a converging diffusion field at the edge of the electrode. When dealing with a disc microelectrode, the field at the edge begins to expand with time producing a hemispherical field over the entire disc (Wightman and Wipf, 1989). Once a hemispherical field occurs the electrode can access the electro-active species from both the x- and r- axis and the disc shape passes a larger current per unit area when compared to an electrode shape that only has access to one-dimension diffusion (Wightman and Wipf, 1989). In addition, since the diffusion field is convergent, a steady state diffusion field is generated at the electrode surface with a corresponding steady state diffusion current (Wightman and Wipf, 1989). This steady state in microelectrodes is obtained in a relatively short space of time when compared to macroelectrodes and results in natural convection becoming insignificant (Wightman and Wipf, 1989).

A ring electrode is essentially a disc electrode from which the section away from the edge has been removed and replaced with an internal edge. The presence of an internal edge results in additional edge enhanced diffusion and an increase in current density. High perimeter-to-area ratio ring microelectrodes can be manufactured to capitalize on the consequence of the convergent diffusion field resulting in high current densities. These ring electrodes would demonstrate high signal-to-background and signal-to-noise ratios when utilized in analytical voltammetry. The charging current is proportional to the electrode area and the faradaic current to the radius. Therefore, switching from a disc to a ring electrode with identical radii reduces the area of the electrode and thus increases the faradaic-to-charging current ratio.

When recording a cyclic voltammogram, (Tallman, 1994) demonstrated that for ring, disc and band electrodes of the same perimeter and area size, the geometry had an insignificant impact on the redox peak, width and position. However, there was a

substantial influence on the redox peak height due to the differences in the diffusion field for each geometry tested.

8.2.2 Microelectrode fabrication

Due to their comparative ease of fabrication, the disc and ring microelectrodes are the most used geometries.

The type of electrode required will determine the method of construction and materials needed. Thoroughly cleaning all components of the electrode is vital in minimizing signal interference regardless of the type of electrode being manufactured. Disc microelectrodes are the easiest to fabricate and as such are the mostly widely used. The process begins by encasing a metal wire (gold, silver or platinum) or a graphite rod into an insulating material (glass, quartz, epoxy resin). Ring microelectrodes require a conducting material (carbon, gold) that is typically deposited on either the inside of the external insulator or the outside of the internal insulator.

8.2.2.1 Disc microelectrodes

Generally, disc electrodes are made by sealing a conductive metal wire into an insulating capillary such as glass, epoxy or polyimide (Wightman and Wipf, 1989; Mossier-Boss and Lieberman, 1999) which is achieved by heating the insulating capillary. It is also possible for a capillary to be pulled from a tube of the insulator containing a metal wire, resulting in sealing the wire in place without the need for additional heating (Pendley and Abruna, 1990). Various other methods of fabrication have also been implemented such as utilizing a Bunsen burner to seal a wire into a borosilicate tube (Howell and Wightman, 1984) resulting in a larger more robust microelectrode. Regardless of which method is used the coefficient of thermal expansion of both the insulating material and electrode material should be of a similar value as this will promote long-term stability of the electrode.

Before the electrode can be used it is important to polish the tip of the device. This is generally accomplished by decreasing grades of silicon-carbide polishing pads followed by polishing cloths with decreasing grades of diamond slurry. Finally, alumina is used to obtain a smooth ‘mirror’ like surface (Wightman and Wipf, 1989). Care must be taken when polishing with alumina as it possesses electrocatalytic properties (Zak and Kuwana, 1983). It is vital that the tip of the electrode is as clean as possible and ultrasonication of the electrode tip is performed in a bath of triply distilled water to help achieve this.

Various methods have been employed to create an electrical contact between the microelectrode and the contact wire. Wightman and Wipf (1989) utilized a silver epoxy to attach the wire forming the electrode to the contact wire. Colloidal metal paint has also been used to secure electrical contact (Tsionsky *et al.*, 1994; Mossier-Boss and

Lieberman, 1999). Woods metal, a low melting point (approx. 60^{o}C) metal alloy consisting of bismuth, cadmium, lead and tin have also been utilized to establish an electrical contact. Small pieces of the Woods metal are deposited inside a glass tube at the bottom of which the electrode wire is sealed. A hot water bath is used to immerse the glass tube which melts the metal. Upon removal of the glass from the water bath it is left to cool, during the setting process a copper wire is placed inside the Woods metal providing an electrical contact (Pennarun, 1999; Shackleford, 2003). To add mechanical strength to the electrode, back filling of the glass tube with an epoxy resin can be employed. Spot welding and soldering (Dittmar *et al.*, 1997) are additional techniques used to establish an electrical contact with the microelectrode.

8.2.2.2 Ring Microelectrodes

Like disc microelectrodes, a variety of techniques can be deployed in the fabrication of ring microelectrodes. When compared to disc microelectrodes, the main difference with ring microelectrodes is that they require an additional insulator on the inside of the electrode material in conjunction with the outside insulator. Depending on the purpose of the electrode a variety of materials can be used as the inner insulator (glass rod, epoxy resin etc). A fibre optic is used as the inner insulator when the microelectrode is to be used in photo-electrochemical experiments (Pennarun, 1999).

The conducting material used will determine what fabrication methods are employed. Thermal evaporation, chemical vapour deposition, plasma sputtering of a metal and ion beam coating are the most common ring microelectrode fabrication methods encountered. To ensure an even coating of the conductive material around the inner insulator the internal substrate is rotated during deposition. The ring electrode is subsequently set in a non-conductive epoxy resin an electrical contact is attached by silver epoxy. Setting the ring microelectrode in an epoxy casing also serves to add robustness to the device. The tip of the electrode can then be polished, as explained previously, exposing the ring electrode (Kim, Scarnulis and Ewing, 1986).

When creating a ring microelectrode for photo-electrochemical detection, commercially available metal-coated fibre optics have been shown to produce active microelectrodes (Kuhn, Weber and SG, 1990; Cohen and Weber, 1993). When using commercially coated fibre optics to create a ring microelectrode, the fibre's coating must first be removed, the fibres can then be set in a nonconductive material, such as epoxy, subsequently polished to expose the metal ring. Electrical contact is established via the attachment of a conductive wire to the exposed length of the fibre away from the tip.

Gold coated fibres have been utilized in the detection of electro-chemiluminescence in solutions of ruthenium(II) tris(2,2'-bipyridine) chloride with persulphate (Kuhn, Weber and SG, 1990). The microelectrode device connected the gold coated optical fibres to a copper wire which was then set in epoxy inside a silver tube. This tube was used as a pseudo reference electrode with the entire assembly inserted into a connector. Both ends

were polished with the diameter of the optical fibre (200µm) used as the light guide with the gold ring electrode (with a thickness of 15 µm) acting as the working electrode.

A similar device utilizing a gold-coated fused silica fibre optic with a layer of electro-polymerised 2-allylphenol atop a gold jacket. A layer of epoxy resin was the applied to the surface of the polymer and the whole assembly was inserted into a Pyrex tube. The constructed electrode was then used to detect hydrogen peroxide that had been generated electrochemically from a photochemical reduction of the ubiquitous substrate precursor, oxygen. The fibre optic allowed for the photoexcitation of $Ru(bipy)_3^{2+}$ in oxygen containing samples, which mediates the overall photoreaction.

8.3 Photo-electrochemical devices

Optical electrodes are required to study photochemically-induced electrochemistry. The following sections will discuss two approaches to optical electrodes: front illumination and back illumination.

8.3.1 Front illumination

Front illumination of an electrode is achieved when light is shone through the electrolyte solution on to the electrode surface. This type of electrodes requires an electrolyte with sufficient transparency to allow for the light to reach the electrode resulting in only a small percentage of the light being absorbed by the photoactive species near to the electrode surface. Front illumination is typically used for purely practical reasons as it requires minimal equipment and installation resulting in a cheap and practical device to investigate photoelectrochemical systems. To maximise the produced photocurrent high absorption near the electrode surface is required, this becomes particular important when dealing with unstable photogenerated products with short lifetimes. A thin layer, flow injection analysis (FIA) cell has been developed for photo electroanalytical chemistry (Elbicki, Morgan and Weber, 1985). This FIA cell has proven popular during photoelectrochemical detection in high-performance liquid chromatography and solar energy conversion (Archer, 1975; Elbicki, Morgan and Weber, 1985; Barisci and Wallace, 1994). To minimise the light energy lost before the light enters the electrolyte solution any kind of barrier between the light source and solution must be avoided (Archer, 1975). This design feature is important for photo-electrochemical (PCE) cells and allows for an increase in the overall efficiency. A titanium dioxide-based semiconductor photoelectrochemical detector has been used for flow injection analysis and liquid chromatography (Brown, Birks and Koval, 1992). This detector requires illumination of the titanium dioxide semiconductor working electrode which is situated along the cylindrical electrochemical cell. Front illumination is also required when studying electrochemical process found in nature such as photosynthesis. Another example is the production of charge carriers and their separation which occurs due to

light induced excitation of photosensitive dyes at the surface of bilayer lipid membranes (Verma and Bhowmik, 1992).

Front illumination is also utilized by optically transparent thin layer electrodes (OTTLE), which has a design based on a thin layer cell configuration. Originally these electrodes consisted of a gold mini grid (a thin gold sheet with approximately 100-2000 perforations per inch) contained between two glass microscope slides separated by 100 µm thick adhesive spacers. The bottom edge of the cell is submerged into a small vessel containing both a secondary and reference electrode which is filled either by capillary action or by applying a vacuum to the electrode configuration. Light is then passed perpendicularly through the glass plates and the mini grid gold working electrode which is highly transparent (Figure 8.3).

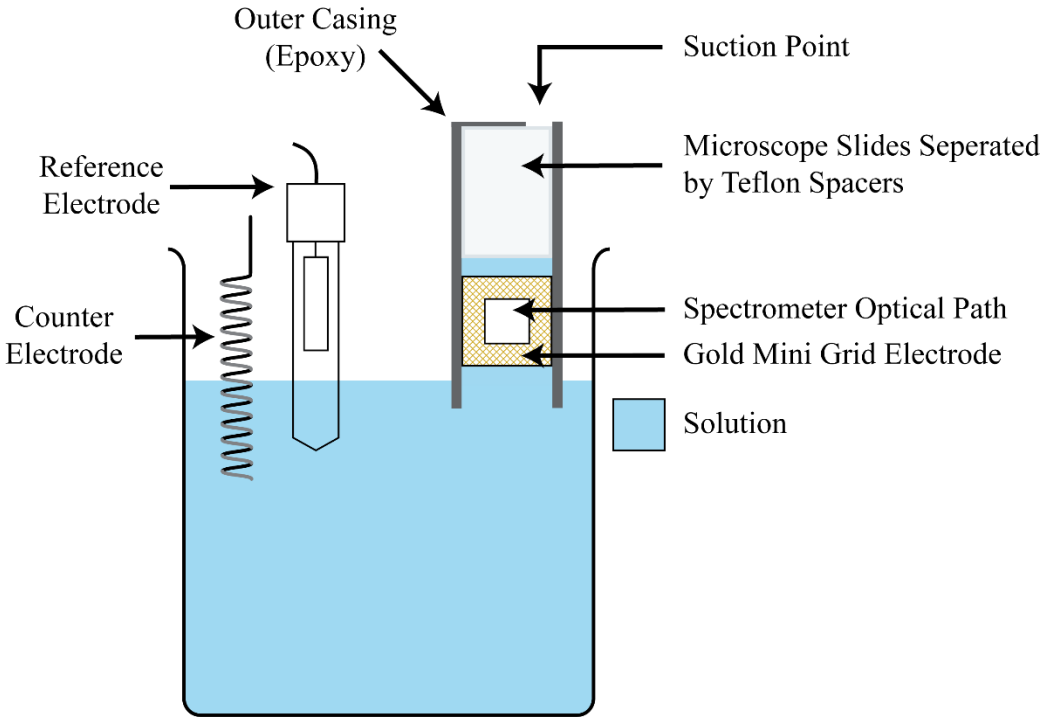

Figure 8.3: Illustration of an optically transparent thin layer electrode (OTTLE).

Large resistive currents prevent the use of OTTLEs for fast kinetic studies. However, quick conversion of electro-active species occurs due to the thin layer configuration. Diffusion is the only form of transport and allows for electrolysis of all electro-active species to be observed in seconds. This initial design of OTTLEs was used primarily for in situ spectral investigation of the evolution of electrolytic consumption of the electrolyte. Adaptation to the initial design has allowed for different applications. Problems can arise due to the solvent used with some organic solvents dissolving epoxy resin which is used to hold the microscope slides together. This would result in contamination of the sample under investigation and could lead to the leakage of

solution. Teflon has been used to avoid contact between the solvent and the sealant which can be prone to dissolving (Rhodes and Kadish, 1981). OTTLEs have been modified for anaerobic use (Lin and Kadish, 1985). The modification consisted of a vacuum tight thing layer cell with a removable mesh double platinum gauze thin layer electrode. Depending on the application (i.e. visible or UV light) the cell is made of either Pyrex or quartz with no epoxy resin or any other material prone to solvent dissolving used in its manufacture. The solution can access the chamber form all four edges resulting in IR drop being minimised. The platinum gauze is carefully folded and tightly compressed; the transparency of the gauze was found to be approximately 30%. The edges of the electrode are exposed to the bulk solution and must be accounted for during data analysis. To guarantee the current contribution was mainly due to the platinum mesh contained in the thin layer cell, an electrode with a size that the ratio of the surface of the edge to the surface of the gauze electrode of less than 5% was chosen. For a layer thickness of 0.2 mm a mesh electrode that was at least 2.6 mm by 1 cm was required. This type of electrode has the advantage of having a longer lifetime which allows for improved reproducibility of experiments.

This design has been utilized inside a flow cell (Oliveira-Brett, 1992). A thin layer electrode that restricts the solution to only contact the Teflon, glass or quartz and the electrodes has also been fabricated (Salbeck, 1993). The spacers and adhesive were replaced with Teflon brackets to set a gap between the microscope slides. The design is ideal for anaerobic conditions, the use of quartz allows for studies of systems within the UV region thus extending the spectral range. The cleaning process is also simplified due to the ease that the device can be assembled and dismantled.

The OTTLE design can be adapted to suit a variety of needs. Its major weakness being the high-uncompressed resistance due to the configuration of thin layer.

8.3.2 Back illumination

Back illumination is when light is shone directly through the electrode into the sample of interest. An electrode made of a glass support on which an antimony doped tin oxide film was deposited is an example of an optically transparent electrode (OTE). The electrode allows both ultraviolet and visible light to pass through and can be used for electrochemical and spectroscopic investigations. Light is passed through the sample and is analysed upon exiting the sample (Kuwana, 1964) (Figure 8.4).

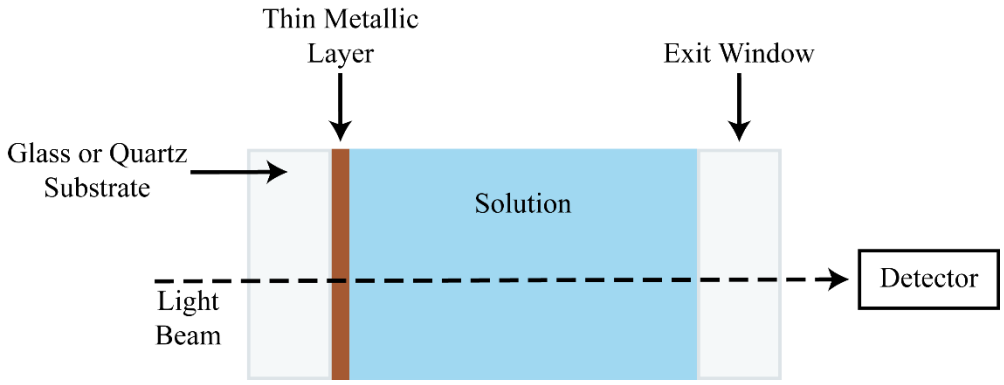

Figure 8.4: Experimental set-up for use of an optically transparent electrode.

OTEs are typically constructed of a thin metallic layer (metal or metal oxide) or a semiconductor deposited on a substrate, usually glass or quartz. Photochemistry is initiated via monochromatic light which passes through the electrode and into the solution of interest. Following this the light passes through an exit window and onto a detector where it is detected and analysed.

The thin metallic layers must be uniform, this is accomplished by applying a layer of metal usually in the region of 10 to 100 nm thick. Adhesion is improved by using a metal oxide undercoat. The electrode is then placed into an ultraviolet-visible cuvette where direct spectroscopic analysis of long lived and strongly coloured electro generated species.

OTEs have been adapted over the years resulting in a number of improvements. An example of this is the use of optically transparent carbon films (Anjo, Brown and Wang, 1993). Carbon film is deposited on a quartz rod which acts as a light guide. The flat end of the quartz rod acts as a working electrode and is in contact with a tube that contains both the electrolyte solution and the quasi-reference electrode. Another example is the use of carbon-mercury films (DeAngelis *et al.*, 1977). The carbon-mercury OTE has the same electrochemical properties of a conventional mercury film electrode. Other examples of metallic films used in OTE designs include gold, platinum or nickel. Thin films of semiconductor deposited on a transparent substrate can also be used but have proven difficult to fabricate.

Semiconductors have been used alongside OTEs, an example is the use of tin oxide/cadmium selenium OTEs (Nasr, Hotchandani and Kim, 1997) which is based on Kressin's design ((Kressin *et al.*, 1991). Advantages of this design over CdSe OTEs include the increased photon-to-current conversion efficiency, increased stability and smaller reversal of current. It was concluded that the improved properties is due to the favourable positioning of energy bands of SnO_2. An OTE combined with a piezoelectric quartz crystal for the study of photo-electrochemical process has been suggested (Xie, Pang and Shen, 1994).

An optically transparent electrode with a semiconductor film covered in a thin layer of an electro-chromic polymer was developed for electro chromic cell experiments (Hyodo, 1994).

The photo-galvanic is another example of an electrode system using back illumination. It is constructed of two identical parallel electrodes with the exception of one allowing light to enter the cell (semi-transparent) whilst the other is classified as a 'dark' electrode. Photo-galvanic solution is situated between the two electrodes with a layer of approximately 10^{-2}-10^{-1} cm thick. Two redox couples are present in the solution and usually consist of a dye and an inorganic couple such as Iron (III)/Iron (II), which can undergo electron transfer via photoexcitation. This process can be reversed by a thermal back reaction. This setup is used to capture the products of photochemically induced electron transfer electrochemically before the thermal back reaction takes place.

The conditions resulting in the maximum power obtainable from a thin layer photo-galvanic cell as well as the conditions which lead to the optimal efficacy of the cell have been investigated (Albery and Archer, 1978; Albery and Foulds, 1979).

Dyes used in electrochemical studies are usually placed in the solution of interest. As chemically modified electrodes developed, dye-modified electrodes for photo galvanic cells were fabricated on the assumption that as with chemically-modified electrodes (Hawn and Armstrong, 1978), they would result in an increase in the photo electrochemical response of the electrode in comparison to the current from the photoactive species in solution. Quickenden and Bassett, (1981) and Bauldreay and Archer, (1983) both found an increase in efficiency of chemically modified electrodes when compared to non-coated electrodes. Photo-galvanic cell analogues have been created using semiconductor colloids. Photoelectrochemical reduction of dyes such as thiazine, oxazine and some ruthenium (II) complexes has been shown on colloidal TiO_2 suspensions with bandgap excitation (Kamat, 1985; Hill and Archer, 1990; Nazeerudin *et al.*, 1993; McEvoy and Gratzel, 1994).

OTE can be used in photovoltaic cells where the electrode material absorbs the light. Typically, the electrode material used is a semiconductor where photogenerated holes or excited electrons can react with electrolyte redox species. It is important to consider the thickness of the SnO_2 film used; a larger thickness will result in an increase in the photocurrent. However, the migration of charges across the grain boundaries is a limiting factor for the generation of photocurrents in thicker films. A thin semiconductor film will result in an electrode that can be operated by either front or back illumination (Bedja, Hitchandani and Kamat, 1993, 1994). OTE/SnO_2 front illumination appeared to result in a higher incident photon-to-photocurrent efficiency than back illumination. This is due to a conducting layer of indium tin oxide placed between the glass plate and the semiconductor film absorbing the majority of the UV light and therefore prevents the excitation of SnO_2 particles. An optically transparent thin film iron oxide electrode, that was used for the photo-electrolysis of water, has had the same comparison made.

The conducting layer was SnO_2 and the back illumination was found to give similar photocurrents to front illumination.

A rotating optical disc ring electrode (RODRE) is another example of a back illuminated electrode (Johnson and Resnick, 1972; Albery and Bartlett, 1985). The RODRE has a disc that is formed by the light guide and a concentric platinum ring. The photoexcited species generated during illumination via light shone through the disc is detected by the platinum ring electrode. The construction is insulated with a Teflon cylinder with the exposed surface of the electrode in the plane of the ring.

Albery, Archer and Egdell, (1977) and Boxall and Albery, (2000) developed an optical rotating disc electrode. It consisted of a quartz rod that had been polished at both ends with one end coated with a layer of quasi metallic antimony-doped tin oxide resulting in a transparent disc electrode. The quartz rod is used to delivery light shone down it, through the disc electrode and into a solution of interest. Photoactive species present in the solution become excited which then diffused towards the electrode surface resulting in a photocurrent. Rotating the transparent disc electrode allows for the imposition of known transport by convection and diffusion onto the electroactive species. This set up has been used to investigate colloidal semiconductor particles (Boxall and Albery, 2000).

When light is shone through an electrode (back illumination) into a solution of interests, the solution may contain high concentrations of light absorbing species when compared to light shining through the solution (front illumination), resulting in a significant amount of the light being absorbed in the diffusion layer of the electrode. Such a setup results in a couple of problems. Firstly, a metal/semiconductor layer over the end of the light guide will reduce the intensity of the light entering the solution. In addition to this the band gap of semiconductor-based electrodes (3.2 eV for SnO_2) results in an upper limit on the energy of light transmittable through the electrode. Secondly, electrode surfaces become soiled with use and must be polished periodically. Polishing a semi-transparent electrode will remove the thin surface film damaging the electrode. These problems may be overcome with the use of a Micro Optical (disc) Ring Electrode (MORE). A MORE uses a fibre optic light guide surrounded by a concentric ring electrode. Light is shone through the fibre optic into a solution of interest resulting in photoexcited products being detected at the disc-ring inner edge. One advantage of the MORE is that the tip can be polished with no reduction in performance and no metal/semiconductor surface later exists to cause attenuation of the transmitted light intensity.

The use of a ring geometry electrode allows for a number of advantages. A thin ring configuration (an inner to outer diameter ratio of more than 0.91, Symanski and Bruckenstein, 1988) results in enhanced material flux that will expedite the detection of short lived reaction intermediates and make electron transfer step the rate determining step over a wider potential range than that observed for typical larger ring electrodes.

This allows for an improvement of the collection efficiency of the electro active species that has been photogenerated at the optical disc. It has been shown that under diffusion-controlled conditions the current density at the edges of the ring approached infinity asymptotically (Phillips, 1992). The collection efficiency is improved due to the edges of the ring being closer together in a thin ring setup when compared to a thicker ring with a similar inner ring radius. This is expected to improve the ability to detect short lived photogenerated species. The extant semi analytical mathematical solutions for how the conventional ring electrodes behave in the dark have been established meaning the use of a thin ring electrode in the MORE does not require mathematical characterisation. However, a significant disadvantage of using thin ring MOREs is that commercially available fibre optics with thin metal layers in the region of 10^{-6} to 10^{-5} are not available and therefore must be manufactured in house.

A MORE type device called GRiN (graphene ring nanoelectrode) was developed that utilized a graphene as the conducting layer. It was successful in exploiting the geometric and electrical properties of graphene to reliably characterise ring thickness. GRiNs were manufactured by dip coating chemically delaminated graphite oxide followed by a simple two step reduction process. This resulted in conducting nano layers based on a graphene material. The Grins were sized electrochemically, and by physical methods including atomic, lateral and conductive force microscopies. Ring thickness was found to range from 5-73 nm, with a ratio of inner to outer ring ratios in excess of 0.999 (Dickinson, 2013).

9 References

Ache, H. (1993) ‘Journal of Interdisciplinary Sciences’, *Journal of Interdisciplinary Sciences*, 18, p. 280.

Albery, W. and Archer, M. (1978) ‘No Title’, *Journal of Electroanalytical Chemistry*, 86, p. 1,18.

Albery, W., Archer, M. and Egdell, R. (1977) ‘No Title’, *Journal of Electroanalytical Chemistry*, 82, p. 199.

Albery, W. and Bartlett, P. (1985) ‘No Title’, *Chemistry Soc Faraday Trans*, p. 4647.

Albery, W. and Foulds, A. (1979) ‘No Title’, *Journal of Photochemistry and Photobiology A: Chemistry*, 10, p. 41.

Andrieux, F. P. L., Boxall, C. and O’Hare, D. (2006a) ‘The micro-optical ring electrode. 3: Transient photocurrent studies of photophysical-electrochemical and photophysical-chemical-electrochemical systems’, *Journal of Physical Chemistry B*, 110(32), pp. 16148–16156. doi: 10.1021/jp0622785.

Andrieux, F. P. L., Boxall, C. and O’Hare, D. (2006b) ‘The micro-optical ring electrode Part 2: Theory for the transport limited, steady-state photocurrent’, *Journal of Electroanalytical Chemistry*, 589(2), pp. 177–186. doi: 10.1016/j.jelechem.2005.12.002.

Anjo, D., Brown, S. and Wang, L. (1993) ‘No Title’, *Analytical Chemistry*, 65, p. 317.

Archer, M. (1975) ‘No Title’, *journal of Appl Electrochem*, 5, p. 17.

Baker, A. M. *et al.* (2017) ‘Cerium Ion Mobility and Diffusivity Rates in Perfluorosulfonic Acid Membranes Measured via Hydrogen Pump Operation’, *Journal of The Electrochemical Society*, 164(12), pp. F1272–F1278. doi: 10.1149/2.1221712jes.

Bard, A. J. and Faulkner, L. R. (2004) *Fundamentals and Applications Plasmonics : Fundamentals and Applications*, *JOHN WILEY & SONS, INC.* doi: 10.1016/j.aca.2010.06.020.

Bard and Faulkner (2001) *Electrochemcial Methods*.

Barisci, J. and Wallace, G. (1994) ‘No Title’, *Electroanalytical Chemistry*, 6, p. 209.

Barnard, S. and Walt, D. (1991) ‘American Chemcial Society’, *American Chemcial Society*, 201, p. 17.

Barnard, S. and Walt, D. (1992) ‘American Chemcial Society’, *American Chemcial Society*, 487, p. 310.

Bauldreay, J. and Archer, M. (1983) ‘No Title’, *Electrochimica Acta*, 28, p. 1515.

Bedja, I., Hitchandani, S. and Kamat, P. (1993) ‘No Title’, *Journal of Physical Chemistry*, 97, p. 11064.

Bedja, I., Hitchandani, S. and Kamat, P. (1994) ‘No Title’, *Journal of Physical Chemistry*, 98, p. 4133.

Bell, J. T. and Buxton, S. R. (1974) ‘Photoreduction of the uranyl ion with laser light and ethanol-I. Quantum yields and medium effects’, *Journal of Inorganic and Nuclear Chemistry*. Pergamon, 36(7), pp. 1575–1579. doi: 10.1016/0022-1902(74)80626-3.

Bell, J. T. and Buxton, S. R. (1975) ‘Photoreduction of the uranyl ion with laser light and ethanol-II. The effects of temperature and uranyl concentration on the uranyl-ethanol reaction’, *Journal of Inorganic and Nuclear Chemistry*. Pergamon, 37(6), pp. 1469–1474. doi: 10.1016/0022-1902(75)80792-5.

Bès, R. *et al.* (2018) ‘Laboratory-scale X-ray absorption spectroscopy approach for actinide research: Experiment at the uranium L3-edge’, *Journal of Nuclear Materials*. North-Holland, 507, pp. 50–53. doi: 10.1016/J.JNUCMAT.2018.04.034.

Bowling, R. *et al.* (1989) ‘No Title’, *Analytical Chemistry*, 61, p. 2763.

Boxall, C. and Albery, W. (2000) ‘No Title’, *Physical Chemistry Chemical Physics*, 2, p. 3631,3641,3651.

Brown, G., Birks, J. and Koval, C. (1992) ‘No Title’, *Analytical Chemistry*, 64, p. 427.

Buchachenko, A. L. and Khudyakov, I. V. (1991) ‘Magnetic and Spin Effects in Photoreduction of Uranyl Salts’, *Accounts of Chemical Research*, 24(6), pp. 177–183. doi: 10.1021/ar00006a004.

Burney, G. . and Harbour, R. . (1974) *Radiochemistry of neptunium*. Washington DC: The National Academies Press. Available at: https://www.osti.gov/servlets/purl/4242713/.

Burrows, H. D. *et al.* (1976) *Quenching of the luminescent state of the uranyl ion (UO22+) by metal ions: Evidence for an electron transfer mechanism, Journal of the Chemical Society, Faraday Transactions 1: Physical Chemistry in Condensed Phases*. doi: 10.1039/F19767200163.

Burrows, H. D. (1990) ‘Electron Transfer from Halide Ions to UO22+Excited-State Ions in Aqueous Solution: Formation and Decay of Dihalide Radical Anions’, *Inorganic Chemistry*. American Chemical Society, 29(8), pp. 1549–1554. doi: 10.1021/ic00333a021.

Burrows, H. D. and Kemp, T. J. (1974a) ‘The photochemistry of the uranyl ion’, *Chemical Society Reviews*, 3(2), pp. 139–165. doi: 10.1039/CS9740300139.

Burrows, H. D. and Kemp, T. J. (1974b) ‘The photochemistry of the uranyl ion’, *Chemical Society Reviews*, pp. 139–165. doi: 10.1039/CS9740300139.

Bursten, B. E., Rhodes, L. F. and Strittmatter, R. J. (1989) ‘Comprehensive Organometallic Chemistry’, *B. E.; Fang, A. J. Am. Chem. Soc*. American Chemical Society, 111(3), pp. 904–905. Available at: https://pubs.acs.org/sharingguidelines (Accessed: 12 September 2021).

cerium | Uses, Properties, & Facts | Britannica (2020) *Britannica*. Available at: https://www.britannica.com/science/cerium (Accessed: 31 March 2021).

Chi-Square Calculator (no date). Available at: https://www.mathsisfun.com/data/chi-square-calculator.html (Accessed: 13 December 2020).

Chimes, M. *et al.* (2018) ‘Nitrous acid-driven reduction of vanadium as a neptunium analogue’, *Progress in Nuclear Science and Technology*. The Atomic Energy Society of Japan, 5(0), pp. 37–40. doi: 10.15669/PNST.5.37.

Choppin, G. R. (2007) ‘Actinide speciation in the environment’, *Journal of Radioanalytical and Nuclear Chemistry*, 273(3), pp. 695–703. doi: 10.1007/s10967-007-0933-3.

Clark, D. L. *et al.* (1981) ‘XAFS Structural Determination of Np(VII). Evidence for a Trans Dioxo Cation Under Alkaline Solution Conditions’, *J. Am. Chem. Soc*, 23(7), pp. 5259–5260. Available at: https://pubs.acs.org/sharingguidelines (Accessed: 7 September 2021).

Clark, D. L. (2000) ‘The Chemical Complexities of Plutonium’, *Los Alamos Science*, 1(24), pp. 364–318. doi: 10.1103/PhysRevB.70.085418.

Cohen, C. and Weber, S. (1993) ‘Analytical Chemistry’, *Analytical Chemistry*, 65, p. 169.

DeAngelis, T. *et al.* (1977) ‘No Title’, *Analytical Chemistry*, 49, p. 1395.

Deaver, D. (1995) ‘No Title’, *Nature*, 377, p. 758.

Dickinson, J. W. (2013) *The Graphene Ring Nanoelectrode and its Application as a*.

Lancaster University.

Ding, C. *et al.* (2013) 'Vanadium flow battery for energy storage: Prospects and challenges', *Journal of Physical Chemistry Letters*, 4(8), pp. 1281–1294. doi: 10.1021/jz4001032.

Dittmar, A. *et al.* (1997) 'Sensors & Actuators B', *Sensors & Actuators B*, 44, p. 316.

Van Dyke, D. and Cheng, H. (1988) 'No Title', *Analytical Chemistry*, 60, p. 1256.

Van Dyke, D. and Cheng, H. (1989) 'No Title', *Analytical Chemistry*, 61, p. 633.

Elbicki, J., Morgan, D. and Weber, S. (1985) 'No Title', *Analytical Chemistry*, 57, p. 1746.

Engstrom, R., Nohr, P. and Vitt, J. (1994) 'No Title', *Physiochem. Engin. Aspects*, 93, p. 221.

Farid, M. . and Edelmann, F. T. (2012) *Lanthanides: Tetravalent Inorganic". Encyclopedia of Inorganic and Bioinorganic Chemistry*.

Fonseca, S. M. *et al.* (2004) 'Photooxidation of cellulose acetate and cellobiose by the uranyl ion', *Photochemical & Photobiological Sciences*. The Royal Society of Chemistry, 3(3), pp. 317–321. doi: 10.1039/B314671E.

Frost, M. J. (2006) 'Mohs scale of hardness', in *Mineralogy*. Kluwer Academic Publishers, pp. 283–284. doi: 10.1007/0-387-30720-6_84.

Gangwer, T. (1977) *Photochemistry relevant to nuclear waste separations: a feasibility study, Bnl-50715(Tid-4500)*. Available at: http://inis.iaea.org/Search/search.aspx?orig_q=RN:9383967.

George, S. A., Whittaker, A. M. and Stearns, D. M. (2011) 'Photoactivated uranyl ion produces single strand breaks in plasmid DNA', *Chemical Research in Toxicology*. NIH Public Access, 24(11), pp. 1830–1832. doi: 10.1021/tx200410x.

Gerber, M. S. (1993) 'A brief history of the PUREX and UO{sub 3} facilities'. Available at: https://www.osti.gov/biblio/10115226%0Ahttps://www.osti.gov/servlets/purl/10115226.

Good, R. and Sawyer, D. T. (1976) 'Vanadium(IV) Gluconate Complexes', *Inorganic Chemistry*, 15(6), pp. 1427–1431. doi: 10.1021/ic50160a035.

Gruen, D. M. and Mcbeth, R. L. (1962) 'Spectra of Oxidation States of Vanadium in LiCl-KCl Eutectic ABSORPTION SPECTRA OF THE II, III, IV AND V

OXIDATION STATES OF VANADIUM IN LiCl-KCl EUTECTIC. OCTAHEDRAL-TETRAHEDRAL TRANSFORMATIONS OF V(II) AND V(III)1'. Available at: https://pubs.acs.org/sharingguidelines (Accessed: 13 September 2021).

Gschneidner, K. . (2006) *Chapter 229: Applications of tetravalent cerium compounds"*.

Haapakka, K. and Kankare, J. (1982) 'No Title', *Analytical Chemistry*, 183, p. 253.

Hall, G. R. and Herniman, P. D. (1954) 'The separation and purification of americium-241 and the absorption spectra of tervalent and quinquevalent americium solutions', *Journal of the Chemical Society (Resumed)*, pp. 2214–2221. doi: 10.1039/JR9540002214.

Hawn, D. and Armstrong, N. (1978) 'No Title', *Journal of Physical Chemistry*, 82, p. 1288.

Hill, R. and Archer, M. (1990) 'No Title', *Journal of Photochemistry and Photobiology A: Chemistry*, 51, p. 45.

Hindman, J. C., Magnusson, L. B. and LaChapelle, T. J. (1949) 'The Oxidation States of Neptunium in Aqueous Solution', *Journal of the American Chemical Society*, 71(2), pp. 687–693. doi: 10.1021/ja01170a087.

Holleman, A. . (1985) *Lehrbuch der anorganischen Chemie*. Edited by E. Wiberg. Walter de Gruyter.

Horiba scientific (no date) *No Title*. Available at: https://www.horiba.com/uk/scientific/.

Howell, J. and Wightman, R. (1984) 'Analytical Chemistry', *Analytical Chemistry*, 56, p. 524.

Hyodo, K. (1994) 'No Title', *Electrochimica Acta*, 39, p. 265.

Johnson, D. and Resnick, E. (1972) 'No Title', *Analytical Chemistry*, 44, p. 637.

Kamat, P. (1985) 'No Title', *J.Chem.Soc.Faraday Trans*, 81, p. 509.

Kandrashkin, Y. E., Asano, M. S. and Van Der Est, A. (2006) 'Light-induced electron spin polarization in vanadyl octaethylporphyrin: II. Dynamics of the excited states', *Journal of Physical Chemistry A*, 110(31), pp. 9617–9626. doi: 10.1021/jp062037x.

Kern, D. M. H. and Orlemann, E. F. (1949) 'The Potential of the Uranium (V), Uranium (VI) Couple and the Kinetics of Uranium (V) Disproportionation in Perchlorate Media 1,2', *Journal of the American Chemical Society*, 71(6), pp. 2102–2106. doi: 10.1021/ja01174a055.

Kim, Y., Scarnulis, D. and Ewing, A. (1986) ‘Analytical Chemistry’, *Analytical Chemistry*, 58, p. 1782.

Kressin, A. *et al.* (1991) ‘No Title’, *Chem. Mater*, 3, p. 1015.

Kuhn, L., Weber, A. and SG, W. (1990) ‘Analytical Chemistry’, *Analytical Chemistry*, 62, p. 1631.

Kuwana, T. (1964) ‘No Title’, *Analytical Chemistry*, 36, p. 2023.

Lee, Y. and Bard, A. J. (2002) ‘Fabrication and characterization of probes for combined scanning electrochemical/optical microscopy experiments’, *Analytical Chemistry*, 74(15), pp. 3626–3633. doi: 10.1021/ac015705d.

Leung, P. K. *et al.* (2011) ‘Ce(III)/Ce(IV) in methanesulfonic acid as the positive half cell of a redox flow battery’, *Electrochimica Acta*, 56(5), pp. 2145–2153. doi: 10.1016/j.electacta.2010.12.038.

Liddle, S. T. (2015) ‘The Renaissance of Non-Aqueous Uranium Chemistry’, *Angewandte Chemie - International Edition*. Wiley-VCH Verlag, 54(30), pp. 8604–8641. doi: 10.1002/ANIE.201412168.

Lide, D. R. (2007) ‘CRC Handbook of Chemistry and Physics, 87th ed’, *Journal of the American Chemical Society*. American Chemical Society, 129(3), pp. 724–724. doi: 10.1021/ja069813z.

Lin, C. T. and Sutin, N. (1976) ‘Quenching of the luminescence of the tris(2,2′-bipyridine) complexes of ruthenium(II) and osmium(II). Kinetic considerations and photogalvanic effects’, *Journal of Physical Chemistry*. American Chemical Society, 80(2), pp. 97–105. doi: 10.1021/j100543a002.

Lin, X. and Kadish, K. (1985) ‘No Title’, *Analytical Chemistry*, 57, p. 1498.

Lind, J., Mereniji, G. and Erikan, T. (1983) ‘No Title’, *American Chemcial Society*, 105, p. 7655.

Lovley, D. R. *et al.* (1991) ‘Microbial reduction of uranium’, *Nature*, 350(6317), pp. 413–416. doi: 10.1038/350413a0.

Lubbers, J. *et al.* (1974) ‘No Title’, *Analytical Chemistry*, 46, p. 865.

Mao, Y. and Bakac, A. (1996) ‘Uranyl-Sensitized Photochemical Oxidation of Naphthalene by Molecular Oxygen. Role of Electron Transfer’. Available at: https://pubs.acs.org/sharingguidelines (Accessed: 21 September 2021).

Marra, J. C. *et al.* (2012) ‘Cerium as a Surrogate in the Plutonium Immobilized Form’,

in. John Wiley & Sons, Ltd, pp. 381–388. doi: 10.1002/9781118371435.ch36.

Marsac, R. *et al.* (2017) 'Aqueous chemistry of Ce (IV): estimations using actinide analogues To cite this version : HAL Id : insu-01588240 Aqueous chemistry of Ce (IV): estimations using actinide analogues', (Iv).

McEvoy, A. and Gratzel, M. (1994) 'No Title', *Sol.Ener.Mat & Sol. Cells*, 32, p. 221.

Meyer, T. J. *et al.* (1982) 'Photochemical Electron Transfer from Cerous Ions to the Lowest Excited State of Uranyl Ions In Aqueous Media, Studied by Laser Photolysis', *Spectroscopy and Photochemistry of Uranyl Compounds*. UTC, 86(1), p. 37. Available at: https://pubs.acs.org/sharingguidelines (Accessed: 22 September 2021).

Microscopic Cross-section | Definition & Examples | nuclear-power.net (2020). Available at: https://www.nuclear-power.net/nuclear-power/reactor-physics/nuclear-engineering-fundamentals/neutron-nuclear-reactions/microscopic-cross-section/ (Accessed: 31 March 2021).

Morss, L. (2020) *Uranium chemical element, britannica*. Available at: https://www.britannica.com/science/uranium (Accessed: 31 March 2021).

Mossier-Boss, P. and Lieberman, S. (1999) 'Electroanalytical Chemistry', *Electroanalytical Chemistry*, 460, p. 105.

Nagaishi, R. *et al.* (1996) 'Photoreduction of uranyl ion in aqueous solution. I. With ethanol in sulphuric acid solutions', *Journal of Photochemistry and Photobiology A: Chemistry*, 96(1–3), pp. 45–50. doi: 10.1016/1010-6030(95)04272-5.

Nagaishi, R. *et al.* (2002a) 'Photoreduction of the uranyl ion in aqueous solution: II. Alcohols in acid solutions', *Journal of photochemistry and photobiology. A, Chemistry*. Elsevier B.V, 146(3), pp. 157–161. doi: 10.1016/S1010-6030(01)00609-8.

Nagaishi, R. *et al.* (2002b) 'Photoreduction of the uranyl ion in aqueous solution II. Alcohols in acid solutions', *Journal of Photochemistry and Photobiology A: Chemistry*, 146(3), pp. 157–161. doi: 10.1016/S1010-6030(01)00609-8.

Nasr, C., Hotchandani, S. and Kim, W. (1997) 'No Title', *Journal Phys. Chem*, 101, p. 7480.

Natarajan, V. *et al.* (1992) 'Photochemical reduction of uranyl ion in nitric acid medium using a XeCl excimer laser', *Journal of Radioanalytical and Nuclear Chemistry Letters*. Kluwer Academic Publishers, 165(4), pp. 255–261. doi: 10.1007/BF02164764.

Nazeerudin, M. *et al.* (1993) 'No Title', *American Chemcial Society*, 115, p. 6382.

Oliveira-Brett, A. (1992) 'No Title', *Electroanalytical Chemistry*, 4, p. 911.

Park, T.-H. *et al.* (2018) ‘Absorption spectroscopic observation of interactions between neptunium and oxide ions in molten LiCl-KCl eutectic’, *Nuclear Science and Technology*, 5, pp. 44–47.

Pendley, B. and Abruna, H. (1990) ‘Analytical Chemistry’, *Analytical Chemistry*, 62, p. 782.

Pennarun, G. (1999) *The Micro-Optical Ring Electrode and its applications to study the electrochemistry and photochemistry of Methylene Blue*. University of Central Lancashire.

Pharr, C. *et al.* (1990) ‘No Title’, *Electroanalytical Chemistry*, (278), p. 119.

Phillips, C. (1992) ‘No Title’, *Journal of Electrochemistry Society*, 119, p. 2222.

Pourbaix, M. (1974) *Atlas of electrochemical equilibria in aqueous solutions,*. [1st Engli. Oxford, New York: Pergamon Press.

Quickenden, T. and Bassett, R. (1981) ‘No Title’, *Journal of Physical Chemistry*, 85, p. 2232.

Radioactivity (2018) *Radioactivity : Fission products*. Available at: https://www.radioactivity.eu.com/site/pages/Fission_Products.htm (Accessed: 31 March 2021).

Renshaw, J. C. *et al.* (2005) ‘Bioreduction of uranium: Environmental implications of a pentavalent intermediate’, *Environmental Science and Technology*, 39(15), pp. 5657–5660. doi: 10.1021/es048232b.

Rhodes, R. and Kadish, K. (1981) ‘No Title’, *Analytical Chemistry*, 53, p. 1539.

Riddle, C. L. and Demmer, R. (2020) ‘Colorimetric Detection Method for Actinides (CoDeAc)’. Available at: http://www.inl.gov (Accessed: 8 November 2021).

Riefkohl, J. *et al.* (1987) ‘Photoelectrochemistry with the Rotating Optical Disk Ring Electrode III. Thermal and Photoinduced Electron Transfer in Colloidal n-Ti02’, *Electrochemical SOC*, 134, p. 1679.

Rosenfeld-Grünwald, T. and Rabanl, J. (1980) ‘Quantum Yield and Electron-Transfer Reaction of the Lowest Excited State of Uranyl Ion1’, *J. Phys. Chem*, 84, pp. 2981–2985. Available at: https://pubs.acs.org/sharingguidelines (Accessed: 22 September 2021).

Salbeck, J. (1993) ‘No Title’, *Analytical Chemistry*, 65, p. 2169.

Sarakha, M., Bolte, M. and Burrows, H. D. (1997) ‘The photo-oxidation of 2,6-

dimethylphenol and monophenylphenols by uranyl ion in aqueous solution', *Journal of Photochemistry and Photobiology A: Chemistry*. Elsevier, 107(1–3), pp. 101–106. doi: 10.1016/S1010-6030(97)00064-6.

Sarsfield, M. J. *et al.* (2016) 'The Separation of 241Am from Aged Plutonium Dioxide for Use in Radioisotope Power Systems Using the AMPPEX Process', *Procedia Chemistry*, 21(1), pp. 140–147. doi: 10.1016/j.proche.2016.10.020.

Schnaars, D. D., Wu, G. and Hayton, T. W. (2011) 'Silylation of the Uranyl Ion Using B(C 6 F 5) 3-Activated Et 3 SiH', *Inorg. Chem*, 50, pp. 9642–9649. doi: 10.1021/ic201385h.

Schreiber, U. *et al.* (1996) 'Photosynthesis Research', *Photosynthesis Research*, 47, p. 103.

Schrepp, W. *et al.* (1983) 'Oxidation-State-Specific Detection of Uranium in Aqueous Solution by Photoacoustic Spectroscopy', *Appl. Phys. B*, 32, pp. 207–209.

Seaborg, G. T. D. L. (1990) *The elements beyond uranium*. Edited by W. D. Loveland. New York: Wiley.

Seitz, W. (1993) 'Journal of Molecular Structure', *Journal of Molecular Structure*, 292, p. 105.

Selvaduray, G., Goldstein, M. K. and Anderson, R. N. (1979) 'Survey of nuclear fuel reprocessing technologies', *Conservation and Recycling*, 3(2), pp. 93–134. doi: 10.1016/0361-3658(79)90002-X.

Sessler, J. L. *et al.* (2004) 'Hexaphyrin(1.0.1.0.0.0). A new colorimetric actinide sensor', *Tetrahedron*. Pergamon, 60(49), pp. 11089–11097. doi: 10.1016/j.tet.2004.08.055.

Shackleford, S. (2003) *No Ti Development of an EQCM-Based Sensor for Metal Ionstle*. University of Central Lancashire.

Smythe, W. (1951) 'Applied Physics', *Applied Physics*, 22, p. 1499.

Symanski, J. and Bruckenstein, S. (1988) 'No Title', *Journal of Electrochemistry Society*, 135, p. 198.

Szabo, A. (1887) 'Physical Chemsitry', *Physical Chemsitry*, 91, p. 3108.

Szunerits, S. and Walt, D. (2002) 'No Title', *Analytical Chemistry*, 74, p. 1716.

Takeuchi, T., Yokoyama, K. and Y, K. (1993) 'No Title', *Analytical Chemistry*, 276, p. 1993.

Tallman, D. (1994) ‘Analytical Chemistry’, *Analytical Chemistry*, 66, p. 557.

Tan, W., Shi, Z.-Y. and Kopelman, R. (1992) ‘Development of Submicron Chemical Fiber Optic Sensors’, *Anal. Chem*, 64, p. 2985. Available at: https://pubs.acs.org/sharingguidelines (Accessed: 12 September 2021).

Taylor, J. and Young, E. (1993) ‘Analytical Chemistry’, *Analytical Chemistry*, 65, p. 956.

Thompson, R. B. and Jones, E. R. (1993) ‘Enzyme-Based Fiber Optic Zinc Biosensor’, *Anal. Chem*, 65, pp. 730–734. Available at: https://pubs.acs.org/sharingguidelines (Accessed: 12 September 2021).

Tsionsky, M. *et al.* (1994) ‘Analytical Chemistry’, *Analytical Chemistry*, 66, p. 1747.

Tsushima, S. (2009) ‘Photochemical reduction of UO22+ in the presence of alcohol studied by density functional theory calculations’, *Inorganic Chemistry*. American Chemical Society, 48(11), pp. 4856–4862. doi: 10.1021/ic900066z.

Veliscek-Carolan, J. (2016) ‘Separation of actinides from spent nuclear fuel: A review’, *Journal of Hazardous Materials*. Elsevier B.V., 318, pp. 266–281. doi: 10.1016/j.jhazmat.2016.07.027.

Verma, C. and Bhowmik, B. (1992) ‘No Title’, *Chem. Phys. Lip*, 62, p. 225.

Vitt, J. and Johnson, D. (1991) ‘No Title’, *Journal of Electrochemistry Society*, 138, p. 1637.

Wang, W.-D., Bakac, A. and Espenson, J. H. (1995) ‘Uranium(VI)-Catalyzed Photooxidation of Hydrocarbons with Molecular Oxygen’, *Inorg. Chem*, 34, pp. 6034–6039. Available at: https://pubs.acs.org/sharingguidelines (Accessed: 21 September 2021).

Weik, M. H. and Weik, M. H. (2000) ‘Electrochemical Series’, *Computer Science and Communications Dictionary*, pp. 489–489. doi: 10.1007/1-4020-0613-6_5901.

Wightman, R. and Wipf, D. (1989) *electroanalytical chemistry vol 15*. 15th edn. New York: Marcel Dekker.

Williams, C. W. *et al.* (1997) ‘The Coordination Geometry of Np(VII) in Alkaline Solution’, *J. Appl. Electrochem*, 119(4), pp. 4346–4347. doi: 10.1021/ja005640g.

World Nuclear (2020) *Processing of Used Nuclear Fuel - World Nuclear Association*, *World Nuclear Association*. Available at: https://www.world-nuclear.org/information-library/nuclear-fuel-cycle/fuel-recycling/processing-of-used-nuclear-fuel.aspx (Accessed: 31 March 2021).

World Nuclear Association (2017) *MOX, Mixed Oxide Fuel - World Nuclear Association, World Nuclear Association*. Available at: https://www.world-nuclear.org/information-library/nuclear-fuel-cycle/fuel-recycling/mixed-oxide-fuel-mox.aspx (Accessed: 31 March 2021).

World Nuclear Association (2018) 'What is Uranium? How Does it Work - World Nuclear Association', *World Nuclear Association*. Available at: https://www.world-nuclear.org/information-library/nuclear-fuel-cycle/introduction/what-is-uranium-how-does-it-work.aspx (Accessed: 31 March 2021).

World Nuclear Association (2020) *Nuclear Fuel Cycle Overview - World Nuclear Association, Nuclear Fuel Cycle Overview*. Available at: https://www.world-nuclear.org/information-library/nuclear-fuel-cycle/introduction/nuclear-fuel-cycle-overview.aspx (Accessed: 31 March 2021).

Xie, Q., Pang, X. and Shen, D. (1994) 'No Title', *Electrochimica Acta*, 39, p. 727.

Yamada, S. (1992) 'No Title', *Analytical Chemistry*, 264, p. 1.

Yong, L. *et al.* (2013) 'SCIENCE CHINA Chemistry Photocatalysis with visible-light-active uranyl complexes', 56, pp. 1671–1681. doi: 10.1007/s11426-013-4965-y.

Yusov, A. B. and Shilov, V. P. (2000) 'Photochemistry of f-element ions', *Russian Chemical Bulletin*, 49(12), pp. 1925–1953.

Zak, J. and Kuwana, T. (1983) 'Electroanalytical Chemistry', *Electroanalytical Chemistry*, 150, p. 645.

Zeng, Y. K. *et al.* (2015) 'A comparative study of all-vanadium and iron-chromium redox flow batteries for large-scale energy storage', *Journal of Power Sources*, 300, pp. 438–443. doi: 10.1016/j.jpowsour.2015.09.100.